Centro de Investigación Científica y de Educación Superior de Ensenada, Baja California

Programa de Posgrado en Ciencias en Electrónica y Telecomunicaciones

Robust control synthesis of mechanical systems under unilateral constraints with an application to a biped robot

Thesis

to partially fulfil the requirements needed to obtain the degree of

Doctor in Science

Presents:

Oscar Eduardo Montaño Godinez

Ensenada, Baja California, México

2016

Thesis defended by

Oscar Eduardo Montaño Godinez

and approved by the following committee

Dr. Yury Orlov

Codirector of the Committee

Dr. Yannick Aoustin

Codirector of the Committee

Dr. Joaquín Álvarez Gallegos

Dr. Luis Alejandro Márquez Martínez

Dr. Bernard Brogliato

Dr. Miguel Ángel Alonso Arevalo

Coordinator of the Graduate Program in Electronics and Telecommunications

Dr. Rufina Hernández Martínez

Director of Graduate Studies

Resumen de la tesis que presenta Oscar Eduardo Montaño Godinez como requisito parcial para la obtención del grado de Doctor en Ciencias en Electrónica y Telecomunicaciones con orientación en Instrumentación y Control.

Robust control synthesis of mechanical systems under unilateral constraints with an application to a biped robot

Resumen aprobado por:

Dr. Yury Orlov	Dr. Yannick Aoustin
Codirector de Tesis	Codirector de Tesis

El objetivo principal de este trabajo es el control robusto de sistemas mecánicos híbridos, operando bajo restricciones unilaterales de co-dimensión uno. Condiciones suficientes para la existencia de una solución local del problema de control $\mathcal{H}_\infty$, son dadas en términos de la solución adecuada de desigualdades diferenciales de Hamilton–Jacobi-Isaacs, acopladas a una condición adicional que aparece en la reinicialización de la planta en lazo cerrado. La síntesis de controladores $\mathcal{H}_\infty$ por retroalimentación de salida es desarrollada en el contexto hibrído, abordando el fenómeno de colisión. Primero, la regulación y la estabilización orbital de un péndulo simple, chocando contra una barrera, ilustra las capacidades de la metodología propuesta, usando retroalimentación de posición. Para tal ilustración, un modelo de referencia fue diseñado mediante la realización de un estudio de bifurcación para una modificación híbrida del famoso oscilador de Van der Pol, usando el bien conocido método de secciones de Poincaré, y determinando el conjunto de parámetros de amortiguamiento que permiten la generación de un movimiento periódico. Para agregar valor práctico a esta investigación, se aborda la sintesís de un control de seguimiento de una trayectoria de marcha para un robot bípedo complejo con pies actuados. Finalmente, la teoría desarrollada es extendida hacia la estabilización orbital de sistemas mecánicos subactuados sujetos a restricciones unilaterales con grado de subactuación uno, y posteriormente aplicada a un bípedo subactuado que periódicamente toca el suelo. Tanto en el ejemplo ilustrativo como en ambas aplicaciones, se observa un buen desempeño a pesar de las imperfecciones en las mediciones y la presencia de perturbaciones externas, afectando la fase de movimiento libre, y de incertidumbres que ocurren en la fase de colisión.

Palabras Clave: **Control robusto, restricciones unilaterales, estabilización orbital, robot bípedo**

Abstract of the thesis presented by Oscar Eduardo Montaño Godinez as a partial requirement to obtain the Doctor in Science degree in Electronics and Telecommunications, with orientation to Instrumentation and Control.

Robust control synthesis of mechanical systems under unilateral constraints with an application to a biped robot

Abstract approved by:

Dr. Yury Orlov	Dr. Yannick Aoustin
Thesis Co-Director	Thesis Co-Director

The primary concern of the work is robust control of hybrid mechanical systems under unilateral constraints of co-dimension one. Sufficient conditions for a local solution of the underlying $\mathcal{H}_\infty$ control problem to exist are given in terms of the appropriate solvability of Hamilton–Jacobi–Isaacs partial differential inequalities, coupled to an extra condition on the plant reset in the closed-loop. Nonlinear $\mathcal{H}_\infty$ output feedback synthesis is thus developed in the hybrid setting, covering collision phenomena. First, the regulation and orbital stabilization of a simple pendulum, impacting a barrier, illustrate the capability of the proposed approach via position feedback design. A reference model for such an illustration is designed by performing a bifurcation study for a hybrid modification of the popular Van der Pol oscillator, using the well-known method of Poincaré sections, and determining the set of damping parameters that allows to obtain a periodic motion. To add a practical value to the present investigation, the tracking synthesis of a walking gait is then addressed for a complex bipedal robot with actuated feet. Finally, the developed theory is extended towards the orbital stabilization of underactuated mechanical systems subject to unilateral constraints with underactuation degree one, and then applied to an underactuated bipedal robot periodically touching the ground. In our illustrative example and both applications, good performances are achieved despite imperfect measurements, and the presence of both external disturbances affecting the collision-free motion phase and uncertainties that occur in the collision phase.

Keywords: **Robust control, unilateral constraints, orbital stabilization, biped robot**

Dedication

To Rosario, Francisco

César and Edgar

Acknowledgements

Firstly, I would like to express my sincere gratitude to my advisors Dr. Yury Orlov and Dr. Yannick Aoustin, for their patience and guidance.

I would like to thank the Centro de Investigación Científica y de Educación Superior de Ensenada, for all the support I received during these last four years. Also, thanks to the Consejo Nacional de Ciencia y Tecnología (CONACyT), for providing me the means to complete my doctorate studies.

To the members of my thesis committee, Dr. Joaquin Alvarez Gallegos, Dr. Luis Alejandro Marquez Martinez, and Dr. Bernard Brogliato, I express my gratitude for all the support they gave me during the development of this work. In addition, a very special thank you to Dr. Christine Chevallereau and Dr. Claude Moog, for their valuable comments and discussions.

My sincere thanks to my friends and colleges, Alberto, Antonio, Lilia, Susy, Pepe, Veronica, Maxime, Vincent, Marija, Fang, Hendry, for the great times spent together. To Diana, for all her support and advice, which she always provided selflessly. To Lalo, for his invaluable help and friendship. And Miriam, my friend, my ally, thank you for always being there when I needed you.

Finally, thanks to my parents, Rosario and Francisco, and to my brothers, Cesar and Alex, for their trust, their love, and for being my greatest motivation and inspiration. None of this would have been possible without you. Thank you!

Table of Contents

Page

Table of Contents (continues)

Table of Contents (continues)

Table of Contents (continues)

List of Figures

Figure Page

List of Figures (continues)

List of Figures (continues)

List of Figures (continues)

List of Figures (continues)

Figure Page

List of Figures (continues)

List of Figures (continues)

List of Tables

Chapter 1. Introduction

Significant research interest has been devoted to the stability analysis and control synthesis of switched systems subject to input, state, and output constraints. The progress made in the area relied on different tools such as multiple Lyapunov functions (El-Farra *et al.*, 2005), and predictive control (Mhaskar *et al.*, 2006) among others. More recently, barrier Lyapunov functions (functions which grow to infinity when their arguments approach the domain boundaries) have been involved into the tracking control synthesis of nonlinear switched systems with output constraints (Su *et al.*, 2012; Niu and Zhao, 2013a,b; Li *et al.*, 2014). Sliding mode control of switched single-input, output-constrained systems have also been brought into play (Richter, 2011). In addition, robustness of linear switched systems subject to actuator constraints has been studied in (Zhang *et al.*, 2012) in terms of the $\mathcal{L}_2$-gain, using the LMI-optimization approach. A piece-wise linear $\mathcal{H}_\infty$ control synthesis was developed for switched systems with output constraints in (Rodrigues and Boukas, 2006), relying again on the LMI-optimization.

Switched dynamic systems governed by continuous differential equations and difference equations, provided that the switch between such equations is defined according to output and/or time constraints, are typically referred to as hybrid systems. Such systems have also attracted a lot of attention due to the wide variety of their applications and due to the need of special analysis tools for this type of systems. The interested reader may refer to the relevant works by Goebel *et al.* (2009); Hamed and Grizzle (2013); Naldi and Sanfelice (2013); and Nesic *et al.* (2013), to name a few. Particularly, the disturbance attenuation problem for hybrid dynamic systems has been addressed by Haddad *et al.* (2005); Nesic *et al.* (2013, 2008) where impulsive control inputs were admitted to counteract/compensate disturbances/uncertainties at time instants of instantaneous changes of the underlying state. It should be noted, however, that even in the state feedback design, a pair of independent Riccati equations (separately coming from continuous and discrete dynamics) was required to possess a solution that satisfies both equations. A restrictive condition was thus involved on the feasibility of the proposed synthesis. Moreover, the physical implementation of impulsive control inputs was impossible in many practical situations (e.g., while controlling walking biped robots).

Thus motivated, the present investigation intends to introduce a new control strategy, which is feasible under certain conditions and which avoids using impulsive control inputs. The control objective in question is to asymptotically stabilize the undisturbed hybrid system, while also attenuating external disturbances. The work focuses on impact hybrid systems, which are recognized as dynamic systems under unilateral constraints (Brogliato, 1999). Since the dynamic systems with unilateral constraints possess nonsmooth solutions, which arise due to hitting the constraints, a challenging problem is to extend the popular nonlinear $\mathcal{H}_\infty$ approach (Basar and Bernhard, 1995; Isidori and Astolfi, 1992; Van Der Schaft, 1991) to this kind of dynamic systems. It is worth noticing that the Lyapunov characterization of integral Input-to-State Stability (iISS), recently developed by Hespanha *et al.* (2008) for impulsive systems with state-independent impacts, could form a basis for such an extension. However, choosing this route would call for further generalization of iISS concept to hybrid systems (possibly under unilateral constraints) with state-dependent impacts.

The $\mathcal{H}_\infty$ approach, that has recently been developed by Orlov and Aguilar (2014) towards nonsmooth mechanical applications with hard-to-model friction forces and backlash effects, is extended in Chapter 2 in the presence of unilateral constraints. Such an extension, is further generalized to multi-link mechanical systems with unilateral constraints of co-dimension 1. The general case of unilateral constraints of higher co-dimensions, possibly, resulting in ill-posed dynamics (Brogliato, 1999; Bentsman *et al.*, 2012), remains beyond the scope of the present investigation.

Both the full information case with perfect state measurements and the incomplete information case with output disturbance-corrupted measurements are first addressed and specified for n-DOF fully actuated mechanical manipulators. An essential feature, adding the value to the present investigation, is that not only standard external disturbances, but also their discrete-time counterparts are attenuated with the proposed synthesis. It is worth noticing that this is in contrast to the control algorithms, developed so far (cf. that of Ames *et al.* (2012)) where the perfect knowledge of the restitution rule is assumed at the collision time instants.

To facilitate the exposition capabilities of the developed synthesis and its robustness features, Chapter 4 illustrates a simple 1-DOF nonlinear testbed of an impacting pendulum that captures all the essential features of the general treatment under unilateral constraints. In addition to the numerical study, made for the position feedback regulation of this testbed, two different scenarios are proposed and tested side by side for the pendulum position feedback tracking of an impact reference model, generating a stable limit cycle. In the first scenario, an impact reference output to follow is constructed off-line based on the impact Van der Pol oscillator (that will be commented on the next subsection) (Akhmet and Turan, 2014). In the second scenario, the same reference output is updated on-line to synchronize its impacts to the time instants when the plant hits the unilateral constraint. As theoretically predicted, the disturbance attenuation is actually enforced, and good performance of the closed-loop system is concluded from the numerical study being conducted for the former scenario. However, the disturbance-free closed-loop system proves to be unstable because of the potential impact desynchronization (Biemond *et al.*, 2013). In the latter scenario, the reference trajectory tracking is tested under on-line synchronization of the reference velocity jumps to the collision time instants of the plant. Simulation runs are additionally conducted for this scenario to support the theory that the closed-loop system is capable of retaining attractive robustness features while also presenting the asymptotic stability in the disturbance-free environment.

1.1 Impact Oscillators

An essential ingredient of the illustration of Chapter 4 lies in the design of a hybrid reference model capable of generating a sustained periodic motion. The motivation behind designing such a hybrid reference model can be found, for example, in robotics (Aoustin and Formalsky, 2003; Chevallereau *et al.*, 2004b) where a biped is required to generate a stable cyclic gait along the ground to be viewed as a natural unilateral constraint.

Research interest to the orbital stabilization of mechanical systems is inspired from applications where the natural operation mode is periodic. For these systems the orbital stabilization paradigm differs from typical formulations of output tracking where the reference trajectory to follow is known *a priori*. The control objective for the orbital stabilization (e.g., periodic balancing for a walking biped (Chevallereau *et al.*, 2003) or trajectory planning for industrial robot manipulators (Ellekilde and Perram, 2005)), is twofold. Firstly, the closed-loop system should generate its own limit cycle, similar to that produced by a nonlinear (e.g., Van der Pol) oscillator. Secondly, it should be capable of moving from one orbit to another by modifying the orbit parameters such as the frequency and/or the amplitude.

Impact oscillators have attracted significant research interest, mainly due to variety of their applications such as the works by Goyder and Teh (1989); Hogan (1989); Ehrich (1991) to name a few. This kind of systems also presents different types of complex phenomena (see, e.g., the works by (Bernardo *et al.*, 2008a; Kuznetsov, 2013; Leine and Nijmeijer, 2013; Makarenkov and Lamb, 2012, p.208), and references quoted therein). For the simple case of forced linear oscillators, the powerful method of Poincaré sections has been successfully utilized by varying one of the parameters of the hybrid model (typically, the frequency of an external driving force) for determining the frontier between different dynamic behaviors such as double-period bifurcations and chaos (Lee, 2005; Ikeda *et al.*, 2012). Grazing bifurcations have been studied in the work of Fredriksson and Nordmark (1997), based on the Poincaré map, and in Chillingworth (2002), using singularity theory. Both techniques have been involved to analyze the dynamics near grazing points of general mechanical oscillators where the limit cycle just touches the constraint (impact surface).

In recent works (Akhmet, 2005; Akhmet and Turan, 2014), the perturbation theory was applied to analyze the Hopf bifurcations in hybrid dynamic systems with state-dependent resets and in the impact Van der Pol oscillator, in particular. The proposed perturbation-based approach, however, appeared to be rather tricky and restrictive since it was based on the separation of the nonlinear dynamics in a nominal system that possessed an explicit solution, and sufficiently small nonlinear terms. As a matter of fact, this led only to a local analysis of the periodic behavior in a small region, thus not allowing to analyze the bifurcation phenomena far from the nominal system, possessing explicit solutions.

Chapter 3 aims to give a deeper insight on the behavior of the (modified) Van der Pol oscillator subject to a unilateral constraint that has been used *ad hoc* in the works by Montano *et al.* (2013); Dutra *et al.* (2003) to generate periodic bipedal locomotion with impacts due to ground constraints. By applying Poincaré stability analysis of periodic orbits in hybrid mechanical systems (Aoustin and Formalsky, 1999; Chevallereau *et al.*, 2004b; Grizzle *et al.*, 1999), it is numerically revealed that dependent on the damping value ε, the constrained Van der Pol oscillator either mimics its unconstrained version features, exhibiting both an asymptotically stable hybrid limit cycle, and an unstable equilibrium, or it possesses an asymptotically stable equilibrium only.

A numerical study is additionally performed to determine the bifurcation value of the damping parameter ε where the limit cycle disappears. Once this value is obtained, a proper reference model is designed and used to provide a reference to track for the numerical example in Chapter 4.

1.2 Bipedal Robots Applications

Bipedal robots form a subclass of legged robots. Their design is naturally inspired from the functional mobility of the human body. On the practical side, the study of mechanical legged locomotion has been motivated by its potential use as means of locomotion in rough terrains, but in particular, the interest arises from diverse sociological and commercial interests, ranging from the desire to replace humans in hazardous occupations (de-mining, nuclear power plant inspection, military interventions, etc.), to the restoration of motion in the disabled (Westervelt *et al.*, 2007).

For practical implementation, a good mechanical design and a good modeling, play a very important role in achieving good performance. However, in real world applications, bipedal robots are subject to many sources of uncertainty during walking; these could include a push from a human, an unexpected gust of wind, geometric perturbations of the terrain heights, or parametric uncertainties of non-modeled friction forces (Dai and Tedrake, 2013). For this reasons, the design of feedback control systems, capable of attenuating the effect of these uncertainties is critical to achieve the desired walking gait.

For simplicity, the complete model of the biped robot considered in this work consists of two parts: the differential equations describing the dynamics of the robot during the single support phase (one foot swinging on the air, the other staying as a pivot on the ground), and an impulse model of the contact event (the impact between the swing leg and the ground, which is modeled as a contact between two rigid bodies as in the work by Westervelt *et al.* (2007)). This simplified model permits the utilization of the theory developed in Chapter 2 so as to achieve disturbance attenuation in these complex and highly nonlinear models.

In addition, the actuation at the ankles allow us to define two different problems: 1) if the ankles are actuated, the biped is **fully actuated** during the single support phase, because there will be as many actuators as degrees of freedom at the legs (rotations around the feet, rotations at the knees, and the rotations around the hip); 2) if the ankles are not actuated, the biped is **underactuated** during the single support, because there will be less actuators than degrees of freedom, since the rotation around the foot on the ground is not controlled directly by an actuator. Both problems will be tackled in Chapters 5 and 7, respectively.

Other robust control techniques, such as sliding modes control, have been designed for this kind of systems (see *e.g.*, the works by Raibert *et al.* (1993), Manamani *et al.* (1997), Nikkhah *et al.* (2007), Aoustin *et al.* (2010), Oza *et al.* (2014). While providing both finite-time convergence to a desired reference trajectory and disturbance rejection, these approaches also entail the well-known problem of chattering in the actuators. This further motivates the study of robust control techniques such as the one presented in this work, which attenuate the effect of disturbances while avoiding undesirable and harmful effects on both the actuators, and the joints.

1.3 Orbital Stabilization of Bipedal Locomotion

Stability of bipedal locomotion has been a recent topic of research. For example, in the work by Westervelt *et al.* (2004), the authors stabilized a planar underactuated biped around a periodic orbit, but instead of a sliding mode or finite-time converging controller, the authors preferred to use a decoupled PD control law for its robustness to noise. Hamed *et al.* (2014) proposed a control strategy to exponentially stabilize an underactuated biped using a time-invariant continuous-time controller; however, the effects of external disturbances were not explicitly taken into account for the synthesis of the controller, and a perfect knowledge of the complete state vector was assumed. In the works by Chevallereau *et al.* (2009) and Hamed and Grizzle (2014), event based controllers were developed to robustly stabilize periodic orbits for underactuated biped systems. Also, based on the Poincaré map, Hobbelen and Wisse (2007) introduced the gait sensitivity norm as a measure of the robustness cycle limits in bipedal walkers. Miossec and Aoustin (2005) inserted a double support to reinforce the stability of the walking gait of an underactuated biped and studied the stability of the dynamics not controlled during the single support phase, considering a perfect tracking of the references of the other joint angles of the biped.

In this regard, two major drawbacks should be mentioned with the methods based on the Poincaré map analysis. On one hand, it is hardly possible to include uncertainties into the free-motion phase, since the analysis is made only on the selected Poincaré section. On the other hand, it is difficult to represent the Poincaré map in the closed form since it relies on finding the analytical solution to the differential equations that describe the motion of the system. As stated by Morris and Grizzle (2005), numerical schemes can be used to compute the return map, to find its fixed points, and to estimate eigenvalues for determining exponential stability. However, the numerical computations are usually time-intensive, and performing them iteratively as part of a system design process can be cumbersome. A more important drawback is that numerical computations are not insightful for a fixed point of the Poincaré map to exist and to possess desired stability properties as these computations, made *a priori*, do not allow one to tune the controller gains in the closed loop.

The orbital stability analysis has recently been addressed using the moving Poincaré section approach (Leonov, 2006). In contrast to the standard Poincaré analysis, dealing with a single transversal surface at a fixed point, the moving Poincaré section method involves a family of transversal surfaces at each point on the cyclic trajectory. The linearized dynamics on the foliation of these surfaces are governed by a linear time-varying and periodic system, whose dimension is less than the original system by one. Therefore, asymptotic orbital stability of the desired motion can be studied by analyzing the stability of this auxiliary transversal system. Coupled to the virtual holonomic constraint approach, the transverse linearization has proved to be a powerful method for orbital stabilization around desired periodic motions (see the works by Shiriaev *et al.* (2008); Freidovich *et al.* (2008); Shiriaev and Freidovich (2009); La Hera *et al.* (2013) and references cited therein).

Thus motivated, Chapters 6 and 7 are devoted to the derivation of sufficient conditions for a new output feedback control strategy, that would result in the asymptotic orbital stabilization of the underactuated and undisturbed hybrid system of interest, while also guaranteeing the $\mathcal{L}_2$-gain of its disturbed version to be less than an appropriate disturbance attenuation level γ.

The $\mathcal{H}_\infty$ approach extended to fully actuated systems under unilateral constraints in Chapter 2, is generalized in Chapter 6 to an underactuated mechanical system with collisions. As in the fully actuated case, a local synthesis of an underactuated system is derived in the presence of unilateral constraints by means of two coupled Riccati equations that appear in solving the $\mathcal{H}_\infty$ state feedback and output injection designs for the linearized system viewed beyond the system constraints.

To illustrate capabilities of the proposed synthesis it is further developed in Chapter 7 to the orbital stabilization of an underactuated planar bipedal robot under ground unilateral constraints, and subject to external disturbances in the over-all hybrid dynamical system. Due to the existence of a free-motion, and a transition phase, the bipedal robot represents a hybrid system whose desired orbit to track is actually required to be attained at a sufficiently rapid rate, before occurring the next contact between the swing leg and the ground (Morris and Grizzle, 2005). The underactuation degree of the robot is one during the single support phase. The effects of the disturbances during the single support phase, and during the impact phase, are studied.

Finally, it is worth mentioning that in the recent work of Dai and Tedrake (2012), and Dai and Tedrake (2013), a hybrid $\mathcal{H}_\infty$ control approach was developed by defining an $\mathcal{L}_2$-gain from ground perturbations to deviations from the nominal limit cycle. In contrast to the work of Dai and Tedrake (2013), the present work demonstrates good robustness features of the developed orbital synthesis against both external disturbances, affecting the collision-free motion phase, and against uncertainties that occur in the collision phase, while using only the available measurements of the plant variables. Along with the theoretical development of the nonsmooth orbital $\mathcal{H}_\infty$ synthesis under unilateral constraints, these robustness features, numerically justified on a biped emulator (Aoustin *et al.*, 2010), form the novelty of this work.

1.4 Notation

The notation used throughout this work is rather standard. The argument t^+ is used to denote the right-hand side value $\mathbf{x}(t^+)$ of a trajectory $\mathbf{x}(t)$ at an impact time instant t whereas $\mathbf{x}(t^-)$ stands for the left-hand side value of the same; by default, $\mathbf{x}(t)$ is reserved for $\mathbf{x}(t^-)$, thus implying an underlying trajectory to be continuous on the left. Vectors are represented by bold, lowercase letters, whereas matrices are represented by bold, uppercase letters.

1.5 General Objective

The main objective of this work, is to develop the framework for addressing the problem of nonlinear $\mathcal{H}_\infty$-control for mechanical systems under unilateral constraints on the position, with bounded exogeneous disturbances on both the continuous and discrete dynamics, and in the measurements.

1.5.1 Specific Objectives

To accomplish the above mentioned general objective, the following specific objectives were set:

- Synthetize $\mathcal{H}_\infty$ controllers for mechanical systems under unilateral constraints in the position, considering the control action only between impacts.
- The robust controller will be synthetized via output feedback.
- Validate the proposed scheme using numerical simulations for a 6 degrees-of-freedom planar biped robot.
- Extend the proposed scheme to the underactuated scenario (underactuation degree 1), to orbitally stabilize a 5-link, planar biped without feet.
- Validate the proposed scheme using numerical simulations for a 32 degrees-of-freedom biped robot, Romeo, from the company Aldebaran.

1.6 Structure of the Work

In Chapter 2, the $\mathcal{H}_\infty$-control problem is stated for the hybrid model of interest, which is subject to a unilateral constraint, and sufficient conditions for a local solution of the underlying problem to exist are derived, to synthesize an output feedback controller. Chapter 3 presents a bifurcation study of a hybrid version of the Van der Pol oscillator, so it can be used as a reference model for mechanical systems subject to unilateral constraints. Capabilities of the developed synthesis are illustrated in Chapter 4, in numerical experiments made for the regulation, and orbital stabilization, of an impact pendulum testbed. Chapter 5 presents the results of the application of the developed synthesis to the benchmark application of a seven-link bipedal robot with feet. A locally stabilizing $\mathcal{H}_\infty$ controller, ensuring orbital asymptotical stabilization, and disturbance attenuation for underactuated mechanical systems subject to unilateral constraints, of underactuation degree one, is presented in Chapter 6. This controller is then generalized in Chapter 7, for an underactuated biped, walking in the saggital plane, and its capabilities are illustrated on an emulator. Finally, general conclusions, contributions, and future work are collected in Chapter 8.

Chapter 2. Nonlinear $\mathcal{H}_\infty$ Output Feedback Synthesis Under Unilateral Constraints

The objective of this chapter is to present the hybrid model of interest, which is subject to a unilateral constraint, and the $\mathcal{H}_\infty$-control problem associated with it. Then, sufficient conditions for a local solution of such underlying problem to exist are derived, so an output feedback controller can be synthesized, and further applied to n-DOF mechanical manipulators subject to unilateral constraints.

2.1 Problem Statement

Given a scalar time-varying unilateral constraint $F(\mathbf{x_1}, t) \geq 0$, consider a non-autonomous nonlinear system, evolving within the above constraint, which is governed by continuous dynamics of the form

$$\begin{aligned} \dot{\mathbf{x}}_1 &= \mathbf{x}_2 \\ \dot{\mathbf{x}}_2 &= \mathbf{\Phi}(\mathbf{x}_1, \mathbf{x}_2, t) + \mathbf{\Psi}_1(\mathbf{x}_1, \mathbf{x}_2, t)\mathbf{w} + \mathbf{\Psi}_2(\mathbf{x}_1, \mathbf{x}_2, t)\mathbf{u} \end{aligned} \tag{1}$$

$$\mathbf{z} = \mathbf{h_1}(\mathbf{x}_1, \mathbf{x}_2, t) + \mathbf{k_{12}}(\mathbf{x}_1, \mathbf{x}_2, t)\mathbf{u} \tag{2}$$

$$\mathbf{y} = \mathbf{h_2}(\mathbf{x}_1, \mathbf{x}_2, t) + \mathbf{k_{21}}(\mathbf{x}_1, \mathbf{x}_2, t)\mathbf{w} \tag{3}$$

beyond the surface $F(\mathbf{x_1}, t) = 0$ when the constraint is inactive, and by the algebraic relations

$$\begin{aligned} \mathbf{x}_1(t_i^+) &= \mathbf{x}_1(t_i^-) \\ \mathbf{x}_2(t_i^+) &= \boldsymbol{\mu}_0(\mathbf{x}_1(t_i), \mathbf{x}_2(t_i^-), t_i) + \boldsymbol{\omega}(\mathbf{x}_1(t_i), \mathbf{x}_2(t_i^-), t_i)\mathbf{w_i^d} \end{aligned} \tag{4}$$

$$\mathbf{z_i^d} = \mathbf{x}_2(t_i^+) \tag{5}$$

at *a priori* unknown collision time instants $t = t_i,\ i = 1, 2, \ldots$, when the system trajectory hits the surface $F(\mathbf{x_1}, t) = 0$. Without loss of generality, the unilateral constraint is assumed to be centered in the origin, that is, $F(0, t) = 0$ for all $t \in \mathbb{R}$.

In the above relations, $\mathbf{x}^\top = [\mathbf{x}_1^\top, \mathbf{x}_2^\top] \in \mathbb{R}^{2n}$ represents the state vector with components $\mathbf{x}_1 \in \mathbb{R}^n$, and $\mathbf{x}_2 \in \mathbb{R}^n$; $\mathbf{u} \in \mathbb{R}^n$ is the control input of dimension n; $\mathbf{w} \in \mathbb{R}^l$ and $\mathbf{w_i^d} \in \mathbb{R}^q$ collect exogenous signals affecting the motion of the system (external forces, including impulsive ones, as well as model and measurement imperfections). The variable $\mathbf{y} \in \mathbb{R}^p$ is the only available measurement of the state of the system whereas the variables $\mathbf{z} \in \mathbb{R}^m$ and $\mathbf{z_i^d} \in \mathbb{R}^n$ represent the outputs of the system to be controlled. Since impulsive control actions were ruled out, the post-impact value $\mathbf{x}_2(t)$ of the state component subject to the instantaneous change was chosen as a discrete output function $\mathbf{z_i^d}$.

Throughout this work, the matrix functions $\mathbf{\Phi}$, $\mathbf{\Psi_1}$, $\mathbf{\Psi_2}$, $\mathbf{h_1}$, $\mathbf{k_{12}}$, $\mathbf{k_{21}}$, F, $\boldsymbol{\mu}_0$, and $\boldsymbol{\omega}$ are of appropriate dimensions, which are continuously differentiable in their arguments, and uniformly bounded in t. Admitting these functions to be time-varying is particularly invoked to deal with tracking problems where the plant description is given in terms of the state deviation from the reference trajectory to track (Brogliato *et al.*, 1997). In addition, the origin is assumed to be an equilibrium of the unforced system (1)-(5), that is, for all t, one has $\mathbf{\Phi}(\mathbf{0}, \mathbf{0}, t) = \mathbf{0}$, $\mathbf{h_1}(\mathbf{0}, \mathbf{0}, t) = \mathbf{0}$, $\mathbf{h_2}(\mathbf{0}, \mathbf{0}, t) = \mathbf{0}$, and $\boldsymbol{\mu}_0(\mathbf{0}, \mathbf{0}, t) = \mathbf{0}$.

Clearly, the above system (1)-(5) is an affine control system of the vector relative degree $[2, \ldots, 2]^\top$, and it governs a wide class of mechanical systems with impacts. Since the control input $\mathbf{u}$ has the same dimension as that of the generalized position $\mathbf{x}$, the present investigation is confined to the fully actuated case, though it could readily be extended to the over-actuated case with a correct choice of the control inputs. The treatment in the underactuated case is also possible using the virtual constraint approach (Aoustin and Formalsky, 2003; Westervelt *et al.*, 2007) whenever it is applicable (e.g., for the undegraduation degree one similar to that of Montano *et al.* (2016)).

If interpreted in terms of mechanical systems, equation (1) describes the continuous dynamics before the underlying system hits the reset surface $F(\mathbf{x_1}, t) = 0$, which depends on the position and time variables only. In turn, the restitution law, given by equation (4), is a physical law for the instantaneous change of the velocity when the resetting surface is hit. Thus, the position is not instantaneously changed at the collision time instants whereas the post-impact velocity $\mathbf{x}_2(t^+)$ is a function of both the pre-impact state $(\mathbf{x}_1(t), \mathbf{x}_2(t^-))$, and a discrete perturbation $\mathbf{w_d}$ accounting for inadequacies of the restitution law.

For later use, the notion of an admissible controller is specified for the underlying system. Consider a causal dynamic feedback controller of the same structure

$$\begin{aligned} \dot{\boldsymbol{\xi}}_{\mathbf{1}} &= \boldsymbol{\xi}_2, \quad \dot{\boldsymbol{\xi}}_2 = \boldsymbol{\eta}(\boldsymbol{\xi}, \mathbf{y}, t) \\ \boldsymbol{\xi}(t_j^+) &= \boldsymbol{\nu}(\boldsymbol{\xi}(t_j^-), \mathbf{y}(t_j^-), t_j) \\ \mathbf{u} &= \boldsymbol{\theta}(\boldsymbol{\xi}, t) \end{aligned} \tag{6}$$

as that of the plant, and with the internal state $\boldsymbol{\xi} = [\boldsymbol{\xi}_1, \boldsymbol{\xi}_2]^\top \in \mathbb{R}^{2s}$, with the time instants $t = t_j,\ j = 1, 2, \ldots,$ which are not necessarily coinciding with the collision time instants in the plant equations (1)-(5), and with uniformly bounded in t functions $\boldsymbol{\eta}(\boldsymbol{\xi}, \mathbf{y}, t)$, $\boldsymbol{\nu}(\boldsymbol{\xi}, \mathbf{y}, t)$, and $\boldsymbol{\theta}(\boldsymbol{\xi}, t)$ of class C^1 such that $\boldsymbol{\eta}(\mathbf{0}, \mathbf{0}, t) = \mathbf{0}$, $\boldsymbol{\nu}(\mathbf{0}, \mathbf{0}, t) = \mathbf{0}$, and $\boldsymbol{\theta}(\mathbf{0}, t) = \mathbf{0}$ for all t. Such a controller is said to be a locally *admissible controller* if and only if the undisturbed closed-loop system (1)-(5), (6) with $\mathbf{w}, \mathbf{w}_\mathbf{i}^\mathbf{d} = \mathbf{0}$ is uniformly asymptotically stable.

The $\mathcal{H}_\infty$-control problem of interest consists in finding a locally admissible controller (if any) such that the $\mathcal{L}_2$-gain of the disturbed system is less than a certain $\gamma > 0$, that is the inequality

$$\int_{t_0}^{T} \|\mathbf{z}(t)\|^2 \mathrm{d}t + \sum_{i=1}^{N_T} \|\mathbf{z}_\mathbf{i}^\mathbf{d}\|^2 \le \gamma^2 \left[\int_{t_0}^{T} \|\mathbf{w}(t)\|^2 \mathrm{d}t + \sum_{i=1}^{N_T} \|\mathbf{w}_\mathbf{i}^\mathbf{d}\|^2 \right] + \sum_{k=0}^{N_T} \beta_k(\mathbf{x}(t_k^-), \boldsymbol{\xi}(t_k^-), t_k) \tag{7}$$

holds for some positive definite functions $\beta_k(\mathbf{x}, \boldsymbol{\xi}, t)$, $k = 0, \ldots, N_T$, for all $T > 0$ and a natural N_T such that $t_{N_T} \le T < t_{N_T+1}$, for all piecewise continuous disturbances $\mathbf{w}(t)$ and discrete ones $\mathbf{w}_\mathbf{i}^\mathbf{d},\ i = 1, 2, \ldots,$ for which the state trajectory of the closed-loop system starting from an initial point $(\mathbf{x}(t_0), \boldsymbol{\xi}(t_0)) = (\mathbf{x_0}, \boldsymbol{\xi}_\mathbf{0}) \in \mathcal{U}$ remains in some neighborhood $\mathcal{U} \in \mathbb{R}^{2(n+s)}$ of the origin for all $t \in [t_0, T]$.

It is worth noticing that the above $\mathcal{L}_2$-gain definition is consistent with the notion of dissipativity, introduced by Willems (1972), and Hill and Moylan (1980), and with iISS notion Hespanha *et al.* (2008). It represents a natural extension to hybrid systems (see, e.g. the works by Nesic *et al.* (2008), Yuliar *et al.* (1998), Lin and Byrnes (1996), and Baras and James (1993)). To facilitate the exposition the underlying system, chosen for treatment, has been pre-specified with the post-impact velocity value $\mathbf{x}_2(t)$ in the discrete output (5) to be controlled. The general case of a certain function $\boldsymbol{\kappa}(\mathbf{x}_2(t))$ of the post-impact velocity value in the discrete output (5) can be treated in a similar manner because the $\mathcal{L}_2$-gain inequality (7) is flexible in the choice of positive definite functions $\beta_k(\mathbf{x}, \boldsymbol{\xi}, t)$, $k = 0, \ldots, N_T$.

2.2 Output Feedback Synthesis Under Unilateral Constraints

In this section, we present sufficient conditions for the solution of the underlying disturbance attenuation problem to exist. For later use, the continuous dynamics (1) are rewritten in the form

$$\dot{\mathbf{x}} = \mathbf{f}(\mathbf{x}, t) + \mathbf{g_1}(\mathbf{x}, t)\mathbf{w} + \mathbf{g_2}(\mathbf{x}, t)\mathbf{u} \tag{8}$$

whereas the restitution rule is represented as follows

$$\mathbf{x}(t_i^+) = \boldsymbol{\mu}(\mathbf{x}(t_i^-), t_i) + \boldsymbol{\Omega}(\mathbf{x}(t_i^-), t_i)\mathbf{w_i^d},\ i = 1, 2, \ldots \tag{9}$$

with $\mathbf{x}^\top = [\mathbf{x}_1^\top, \mathbf{x}_2^\top]$, $\mathbf{f}^\top(\mathbf{x}, t) = [\mathbf{x}_2^\top, \boldsymbol{\Phi}^\top(\mathbf{x}, t)]$, $\mathbf{g_1}^\top(\mathbf{x}, t) = [\mathbf{0}, \boldsymbol{\Psi}_1^\top(\mathbf{x}, t)]$, $\mathbf{g}_2^\top(\mathbf{x}, t) = [\mathbf{0}, \boldsymbol{\Psi}_2^\top(\mathbf{x}, t)]$, $\boldsymbol{\mu}^\top(\mathbf{x}, t) = [\mathbf{x}_1^\top, \boldsymbol{\mu}_0^\top(\mathbf{x}, t)]$, and $\boldsymbol{\Omega}^\top(\mathbf{x}, t) = [\mathbf{0}, \boldsymbol{\omega}(\mathbf{x}, t)]$. To simplify the synthesis to be developed, and to provide reasonable expressions for the controller design, the standard assumptions

$$\mathbf{h_1}^\top \mathbf{k_{12}} \equiv \mathbf{0}, \quad \mathbf{k_{12}}^\top \mathbf{k_{12}} \equiv \mathbf{I}, \quad \mathbf{k_{21}} \mathbf{g_1}^\top \equiv \mathbf{0}, \quad \mathbf{k_{21}} \mathbf{k_{21}}^\top \equiv \mathbf{I}, \tag{10}$$

are brought from the work of Isidori and Astolfi (1992) into play. Relaxing these assumptions is indeed possible, but it would substantially complicate the formulas to be worked out.

2.2.1 Non-local State-space Solution

Let $B_\delta^{2n} \in \mathbb{R}^{2n}$ be a ball of radius $\delta > 0$, centered around the origin. Given $\gamma > 0$, a solution to the problem in question is derived under the hypotheses, specified below in a domain $\mathbf{x} \in B_\delta^{2n}, \boldsymbol{\xi} \in B_\delta^{2n}, t \in \mathbb{R}$ of interest:

H1) the norm of the matrix function $\boldsymbol{\omega}$ is upper bounded by $\frac{\sqrt{2}}{2}\gamma$, that is,

$$\|\boldsymbol{\omega}(\mathbf{x},t)\| \leq \frac{\sqrt{2}}{2}\gamma. \tag{11}$$

H2) there exists a positive definite function $R(\mathbf{x})$ and a piece-wise smooth, positive definite, decrescent in t function $V(\mathbf{x},t)$, with $\mathbf{x}(t_0) \in B_\delta^{2n}$, such that the constrained Hamilton–Jacobi–Isaacs inequality

$$\frac{\partial V}{\partial t} + \frac{\partial V}{\partial \mathbf{x}}(\mathbf{f}(\mathbf{x},t) + \mathbf{g_1}(\mathbf{x},t)\boldsymbol{\alpha_1} + \mathbf{g_2}(\mathbf{x},t)\boldsymbol{\alpha_2}) + \mathbf{h_1}^\top\mathbf{h_1} + \boldsymbol{\alpha_2}^\top\boldsymbol{\alpha_2} - \gamma^2\boldsymbol{\alpha_1}^\top\boldsymbol{\alpha_1} \leq -R(\mathbf{x}), \tag{12}$$

subject to $V(\mathbf{x},t^+) = V(\boldsymbol{\mu}(\mathbf{x},t),t^-)$ on the surface $F(\mathbf{x}_1,t) = 0$, holds for almost all $t \in \mathbb{R}$ with

$$\boldsymbol{\alpha_1}(\mathbf{x},t) = \frac{1}{2\gamma^2}\mathbf{g}_1^\top(\mathbf{x},t)\left(\frac{\partial V}{\partial \mathbf{x}}\right)^\top, \quad \boldsymbol{\alpha_2}(\mathbf{x},t) = -\frac{1}{2}\mathbf{g}_2^\top(\mathbf{x},t)\left(\frac{\partial V}{\partial \mathbf{x}}\right)^\top;$$

H3) there exist i) a uniformly bounded in t function $\boldsymbol{\nu}(\xi,\mathbf{y},t)$ of class C^1, ii) a continuous uniformly bounded function $G(t)$, iii) a positive semidefinite function $Q(\mathbf{x},\boldsymbol{\xi})$ with $Q(\mathbf{0},\boldsymbol{\xi})$ being positive definite, and iv) a smooth, positive semidefinite, decrescent in t function $W(\mathbf{x},\boldsymbol{\xi},t)$ with $W(\mathbf{0},\boldsymbol{\xi},t)$ being positive definite such that the constrained Hamilton-Jacobi-Isaacs inequality

$$\frac{\partial W}{\partial t} + \begin{pmatrix} \frac{\partial W}{\partial \mathbf{x}} & \frac{\partial W}{\partial \boldsymbol{\xi}} \end{pmatrix} \mathbf{f_e}(\mathbf{x},\boldsymbol{\xi},t) + \mathbf{h_e}^\top\mathbf{h_e} - \gamma^2\boldsymbol{\psi}^\top\boldsymbol{\psi} \leq -Q(\mathbf{x},\boldsymbol{\xi}), \tag{13}$$

subject to $W(\mathbf{x},\boldsymbol{\xi},t^+) = W(\boldsymbol{\mu}(\mathbf{x},t),\boldsymbol{\nu}(\boldsymbol{\xi},\mathbf{h_2}(\mathbf{x},t),t^-)$ on the surface $F(\mathbf{x}_1,t) = 0$, holds for almost all $t \in \mathbb{R}$ with

$$\mathbf{f_e}(\mathbf{x},\boldsymbol{\xi},t) = \begin{pmatrix} \mathbf{f}(\mathbf{x},t) + \mathbf{g_1}(\mathbf{x},t)\boldsymbol{\alpha_1}(\mathbf{x},t) + \mathbf{g_2}(\mathbf{x},t)\boldsymbol{\alpha_2}(\boldsymbol{\xi},t) \\ \mathbf{f}(\boldsymbol{\xi},t) + \mathbf{g_1}(\boldsymbol{\xi},t)\boldsymbol{\alpha_1}(\boldsymbol{\xi},t) + \mathbf{g_2}(\boldsymbol{\xi},t)\boldsymbol{\alpha_2}(\boldsymbol{\xi},t) + \mathbf{G}(t)(\mathbf{h_2}(\mathbf{x},t) - \mathbf{h_2}(\boldsymbol{\xi},t)) \end{pmatrix}$$

$$\mathbf{h_e}(\mathbf{x},\boldsymbol{\xi},t) = \boldsymbol{\alpha_2}(\xi,t) - \boldsymbol{\alpha_2}(\boldsymbol{x},t),$$

$$\boldsymbol{\psi}(\mathbf{x},\boldsymbol{\xi},t) = \frac{1}{2\gamma^2}\mathbf{g_e}^\top(\mathbf{x},t)\begin{pmatrix} \left(\frac{\partial W}{\partial \mathbf{x}}\right)^\top \\ \left(\frac{\partial W}{\partial \boldsymbol{\xi}}\right)^\top \end{pmatrix},$$

$$\mathbf{g_e}(\mathbf{x},t) = \begin{pmatrix} \mathbf{g_1}(\mathbf{x},t) \\ \mathbf{G}(t)\mathbf{k_{21}}(\mathbf{x},t) \end{pmatrix};$$

H4) Hypotheses H2) and H3) are satisfied with the functions $V(\mathbf{x},t)$ and $W(\mathbf{x},\boldsymbol{\xi},t)$, which decrease on the constraint $F(\mathbf{x}_1,t)=0$ along the directions $\boldsymbol{\mu}(\mathbf{x},t)$ and $\boldsymbol{\nu}(\boldsymbol{\xi},\mathbf{h_2}(\mathbf{x},t),t)$, that is, the inequalities

$$V(\mathbf{x},t) \geq V(\boldsymbol{\mu}(\mathbf{x},t),t), \tag{14}$$

$$W(\mathbf{x},\boldsymbol{\xi},t) \geq W(\boldsymbol{\mu}(\mathbf{x},t),\boldsymbol{\nu}(\boldsymbol{\xi},\mathbf{h_2}(\mathbf{x},t),t),t) \tag{15}$$

hold in the domains of V and W whenever $F(\mathbf{x}_1,t)=0$.

The following result is in force.

Theorem 2.1 *Given $\gamma > 0$, suppose that hypotheses H1)-H3) are satisfied for system* (1)-(5) *in a domain $\mathbf{x} \in B_\delta^{2n}, \boldsymbol{\xi} \in B_\delta^{2n}, t \in \mathbb{R}$ with functions $V(x,t)$ and $W(x,\xi,t)$. Then, the closed-loop system* (1)-(5)*, driven by the dynamic controller*

$$\begin{aligned} \dot{\boldsymbol{\xi}} = \mathbf{f}(\boldsymbol{\xi},t) + \mathbf{g_1}(\boldsymbol{\xi},t)\boldsymbol{\alpha_1}(\boldsymbol{\xi},t) + \mathbf{g_2}(\boldsymbol{\xi},t)\boldsymbol{\alpha_2}(\boldsymbol{\xi},t) + \mathbf{G}(t)(\mathbf{y}(t) - \mathbf{h_2}(\boldsymbol{\xi},t)) \\ \boldsymbol{\xi}(t_i^+) = \boldsymbol{\nu}(\boldsymbol{\xi}(t_i^-),\mathbf{y}(t_i^+),t_i) \\ \mathbf{u} = \boldsymbol{\alpha_2}(\boldsymbol{\xi},t), \end{aligned} \tag{16}$$

locally possesses a $\mathcal{L}_2$-gain less than γ. Once Hypothesis H4) is satisfied as well, the function

$$U(\mathbf{x},\boldsymbol{\xi},t) = V(\mathbf{x},t) + W(\mathbf{x},\boldsymbol{\xi},t) \tag{17}$$

constitutes a Lyapunov function of the disturbance-free closed-loop system (1)-(5)*,* (16) *the uniform asymptotic stability of which is thus additionally guaranteed.*

Remark 2.1 *It should be noted that since the influence of the disturbance $\mathrm{w}^{\mathbf{d}}$, acting at the transition phase* (4)*, cannot be attenuated by an admissible non-impulsive control input the best disturbance attenuation level γ of Theorem 2.1 is limited by Hypothesis H1).*

2.2.1.1 Proof of Theorem 2.1

The proof of Theorem 2.1 is preceded with an instrumental lemma which extends the powerful Lyapunov approach to impact systems. The following result specifies (Haddad *et al.*, 2006, Theorem 2.4) to the present case with $x_1 = x$ and $x_2 = t$.

Lemma 2.1 *Consider the unforced ($\mathbf{u} = 0$) disturbance-free ($\mathbf{w} = \mathbf{0},\ \mathbf{w_i^d} = \mathbf{0},\ i = 1, 2, \ldots$) system* (8)*,* (9) *with the assumptions above. Assume that there exists a positive definite decrescent function $V(\mathbf{x}, t)$ such that its time derivative, computed along* (8)*, is negative definite whereas $V(\mathbf{x}, t) \geq V(\boldsymbol{\mu}(\mathbf{x}, t), t)$ for all $t \in \mathbb{R}$ and all $\mathbf{x} \in \mathbb{R}^{2n}$ such that $F(\mathbf{x}_1, t) = 0$. Then the system is uniformly asymptotically stable.*

Proof of Theorem 2.1. Since the proof follows the same line of reasoning as that used in Orlov (2009) for the impact-free case, here we provide only a sketch. Similar to the proof of (Orlov, 2009, Theorem 7.1), let us differentiate function (17) along the disturbed closed-loop system (1)-(5), and estimate it between collision time instants (Orlov, 2009, p.138):

$$\frac{\mathrm{d}U}{\mathrm{d}t} \leq -\|\mathbf{z}(t)\|^2 + \gamma^2\|\mathbf{w}\|^2 - R(\mathbf{x}) - Q(\mathbf{x}, \boldsymbol{\xi}) - \gamma^2\|\mathbf{w} - \boldsymbol{\alpha_1}(\mathbf{x}, t) - \boldsymbol{\psi}(\mathbf{x}, \boldsymbol{\xi}, t)\|^2, \qquad t \in (t_k, t_{k+1}), \quad k = 0, 1, \ldots. \tag{18}$$

Then, integrating (18) from t_k to $t_{k+1},\ k = 0, 1, \ldots,$ yields

$$\int_{t_k}^{t_{k+1}} [\gamma^2\|\mathbf{w}\|^2 - \|\mathbf{z}(t)\|^2]\mathrm{d}t \geq \int_{t_k}^{t_{k+1}} [R(\mathbf{x}(t)) + Q(\mathbf{x}(t), \boldsymbol{\xi}(t))]\mathrm{d}t + \int_{t_k}^{t_{k+1}} \frac{\mathrm{d}U(\mathbf{x}(t), \boldsymbol{\xi}(t), t)}{\mathrm{d}t}\mathrm{d}t + \gamma^2 \int_{t_k}^{t_{k+1}} \|\mathbf{w}(t) - \boldsymbol{\alpha_1}(\mathbf{x}(t), t) - \boldsymbol{\psi}(\mathbf{x}(t), \boldsymbol{\xi}(t), t)\|^2\mathrm{d}t > 0. \tag{19}$$

Taking (17) into account and skipping positive terms in the right-hand side of (19), it follows that

$$\int_{t_0}^{T} (\gamma^2\|\mathbf{w}\|^2 - \|\mathbf{z}(t)\|^2)\mathrm{d}t \geq U(\mathbf{x}(T), \boldsymbol{\xi}(T), T) + \sum_{i=1}^{N_T}[V(\mathbf{x}(t_i^+), t_i) - V(\mathbf{x}(t_i^-), t_i)] + \sum_{i=1}^{N_T}[W(\mathbf{x}(t_i^+), \boldsymbol{\xi}(t_i^+), t_i) - W(\mathbf{x}(t_i^-), \boldsymbol{\xi}(t_i^-), t_i)] - U(\mathbf{x}(t_0), \boldsymbol{\xi}(t_0), t_0). \tag{20}$$

Since the functions V and W are smooth by hypotheses H2) and H3), the following relations

$$\begin{aligned}|V(\mathbf{x}(t_i^-),t_i)-V(\mathbf{x}(t_i^+),t_i)| &\le L_i^V\|\mathbf{x}(t_i^-)-\mathbf{x}(t_i^+)\| \le L_i^V[\|\mathbf{x}(t_i^-)\|+|\mathbf{x}(t_i^+)\|]\\ |W(\mathbf{x}(t_i^-),\boldsymbol{\xi}(t_i^-),t_i)-W(\mathbf{x}(t_i^+),\boldsymbol{\xi}(t_i^-),t_i)| &\le L_i^W[\|\mathbf{x}(t_i^-)-\mathbf{x}(t_i^+)\|+\|\boldsymbol{\xi}(t_i^-)-\boldsymbol{\xi}(t_i^+)\|]\\ &\le L_i^W[\|\mathbf{x}(t_i^-)\|+\|\mathbf{x}(t_i^+)\|+\|\boldsymbol{\xi}(t_i^-)\|+\|\boldsymbol{\xi}(t_i^+)\|]\end{aligned} \tag{21}$$

hold true, with $L_i^V > 0$ and $L_i^W > 0$ being local Lipschitz constants of V and W in the domain $B_\delta^{2n} \subset \mathbb{R}^{2n}$. Relations (20) and (21), coupled together, result in the inequality

$$\int_{t_0}^{T}(\gamma^2\|\mathbf{w}\|^2-\|\mathbf{z}(t)\|^2)\mathrm{d}t \ge -\sum_{i=1}^{N_T}[2(L_i^V+L_i^W)\|\mathbf{x}(t_i^-)\|+2L_i^W\|\boldsymbol{\xi}(t_i^-)\|]-U(\mathbf{x}(t_0),\boldsymbol{\xi}(t_0),t_0), \tag{22}$$

thus being verified in the domain $B_\delta^{2n} \subset \mathbb{R}^{2n}$. Apart from this, inequality

$$\begin{aligned}\sum_{i=1}^{N_T}\|\mathbf{z_i^d}\|^2 = \sum_{i=1}^{N_T}\|\mathbf{x_2}(t_i^+)\|^2 \le 2\sum_{i=1}^{N_T}\|\boldsymbol{\mu_0}(\mathbf{x}(t_i^-),t_i)\|^2+2\sum_{i=1}^{N_T}\|\boldsymbol{\omega}(\mathbf{x}(t_i^-),t_i)\mathbf{w_i^d}\|^2 \le\\ 2\sum_{i=1}^{N_T}\|\boldsymbol{\mu_0}(\mathbf{x}(t_i^-),t_i)\|^2+\gamma^2\sum_{i=1}^{N_T}\|\mathbf{w_i^d}\|^2\end{aligned} \tag{23}$$

is ensured by Hypothesis H1). Thus, combining (22)-(23), one derives

$$\begin{aligned}\int_{t_0}^{T}\|\mathbf{z}(t)\|^2\mathrm{d}t+\sum_{i=1}^{N_T}\|\mathbf{z_i^d}\|^2 \le U(\mathbf{x}(t_0),\boldsymbol{\xi}(t_0),t_0)+\gamma^2\left[\int_{t_0}^{T}\|\mathbf{w}(t)\|^2\mathrm{d}t+\sum_{i=1}^{N_T}\|\mathbf{w_i^d}\|^2\right]+\\ 2\sum_{i=1}^{N_T}\|\boldsymbol{\mu_0}(\mathbf{x}(t_i^-),t_i)\|^2+\sum_{i=1}^{N_T}[(2L_i^V+2L_i^W)\|\mathbf{x}(t_i^-)\|+2L_i^W\|\boldsymbol{\xi}(t_i^-)\|],\end{aligned} \tag{24}$$

that is, the disturbance attenuation inequality (7) is established with the positive definite functions

$$\begin{aligned}&\beta_0(\mathbf{x}(t_0),\boldsymbol{\xi}(t_0),t_0)=U(\mathbf{x}(t_0),\boldsymbol{\xi}(t_0),t_0),\\ &\beta_i(\mathbf{x}(t_i),\boldsymbol{\xi}(t_i),t_i)=(2L_i^V+2L_i^W)\|\mathbf{x}(t_i^-)\|+2L_i^W\|\boldsymbol{\xi}(t_i^-)\|+2\|\boldsymbol{\mu_0}(\mathbf{x}(t_i^-),t_i)\|^2,\\ &\qquad i=1,\dots,N.\end{aligned} \tag{25}$$

To complete the proof it remains to establish the asymptotic stability of the undisturbed version of the closed-loop system (1)-(5),(16). Indeed, the negative definiteness (18) of the time derivative of the Lyapunov function (17) between the collision time instants, coupled to Hypothesis H4), ensures that Lemma 2.1 is applicable to the undisturbed version of the closed-loop system (1)-(5),(16). By applying Lemma 2.1, the required asymptotic stability is thus validated. Theorem 2.1 is proved. ■

2.3 Application to Impact Mechanical Systems

The proposed synthesis is now specified for the tracking problem stated for a mechanical manipulator, composed of free-motion phases governed by

$$\mathbf{D}(\mathbf{q})\ddot{\mathbf{q}} + \mathbf{H}(\mathbf{q}, \dot{\mathbf{q}}) = \mathbf{D}_{\boldsymbol{\tau}}\boldsymbol{\tau} + \mathbf{w_1} \tag{26}$$

beyond a unilateral time-invariant constraint $F_0(\mathbf{q}) = 0$ where

$$F_0(\mathbf{q}) > 0, \tag{27}$$

whereas these free-motion phases are separated by transition phases according to the restitution rule

$$\mathbf{q}(t_i^+) = \mathbf{q}(t_i^-) \tag{28}$$

$$\dot{\mathbf{q}}(t_i^+) = \phi(\mathbf{q}(t_i))\dot{\mathbf{q}}(t_i^-) + \mathbf{w_i^d} \tag{29}$$

when the state trajectory hits the surface

$$F_0(\mathbf{q}(t_i)) = 0, \quad i = 1, 2, \dots. \tag{30}$$

Hereinafter, $\mathbf{q}, \dot{\mathbf{q}} \in \mathbb{R}^n$ are generalized position and velocity vectors, the control input $\boldsymbol{\tau} \in \mathbb{R}^n$ is a vector of external torques, $\mathbf{w_1} \in \mathbb{R}^n$ is an external disturbance, $\mathbf{w_i^d},\ i = 1, 2, \dots$ are discrete perturbations of the velocity restitution rule (29) at *a priori unknown* time instants t_i;, $\phi(\mathbf{q}) \in \mathbb{R}^{n\times n}$ is a position-dependent restitution matrix; $\mathbf{H}(\mathbf{q}, \dot{\mathbf{q}}) \in \mathbb{R}^n$ is the vector of Coriolis, centrifugal and gravitational torques, the inertia matrix $\mathbf{D}(\mathbf{q})$, and the actuation matrix $\mathbf{D}_\tau$, are of appropriate dimensions. $\mathbf{D}(\mathbf{q})$ is symmetric and positive definite, $\mathbf{D}_\tau$ is invertible and is composed of zero and unit values (thus considering only fully actuated mechanical systems); the scalar function $F_0(\mathbf{q})$ relies on the unilateral constraint, imposed on the robot. As a matter of fact, $\mathbf{D}(\mathbf{q})$, $\mathbf{H}(\mathbf{q}, \dot{\mathbf{q}})$, and $\phi(\mathbf{q})$ are smooth functions in their arguments.

In what follows, the research is confined to the tracking control problem where the output to be controlled is given in terms of the state deviation from a reference trajectory $\mathbf{q}^{\mathbf{r}}(t)$, and it is composed of the continuous-time component

$$\mathbf{z} = \begin{bmatrix} \mathbf{0} \\ \rho_p(\mathbf{q} - \mathbf{q}^{\mathbf{r}}) \\ \rho_v(\dot{\mathbf{q}} - \dot{\mathbf{q}}^{\mathbf{r}}) \end{bmatrix} + \begin{bmatrix} \mathbf{I} \\ \mathbf{0} \\ \mathbf{0} \end{bmatrix} \mathbf{u} \tag{31}$$

with positive weight coefficients ρ_p, ρ_v, and its discrete counterpart

$$\mathbf{z}^{\mathbf{d}}_{\mathbf{i}} = \dot{\mathbf{q}}(t_i^+) - \dot{\mathbf{q}}^{\mathbf{r}}(t_i^+) \tag{32}$$

whereas the available measurement

$$\mathbf{y} = \mathbf{q} - \mathbf{q}^{\mathbf{r}} + \mathbf{w_0} \tag{33}$$

is affected by the measurement error $\mathbf{w_0}(t)$. To respect (10), the output to be controlled has been pre-specified in the form (31), where the zero symbol stand for the zero matrix, and $\mathbf{I}$ stands for the identity matrix, both of appropriate dimensions.

The reference trajectory $\mathbf{q}^{\mathbf{r}}(t)$ to be tracked is a periodic trajectory subject to an impact that occurs when the reference trajectory achieves the surface $F_0(\mathbf{q}^{\mathbf{r}}) = 0$. The restitution law during this impact phase is given by

$$\dot{\mathbf{q}}^{\mathbf{r}}(t_i^+) = \phi(\mathbf{q}^{\mathbf{r}}(t_i))\dot{\mathbf{q}}^{\mathbf{r}}(t_i^-), \;\; i = 1, 2, \ldots . \tag{34}$$

This trajectory may be constructed off-line with *a priori* known impact instants $t_i, \; i = 1, 2, \ldots .$

2.3.1 Hybrid Error Dynamics

Let us now introduce the state deviation vector $\mathbf{x} = (\mathbf{x}_1, \mathbf{x}_2)^\top$ where $\mathbf{x}_1(t) = \mathbf{q}(t) - \mathbf{q}^\mathbf{r}(t)$, and $\mathbf{x}_2(t) = \dot{\mathbf{q}}(t) - \dot{\mathbf{q}}^\mathbf{r}(t)$. Then, rewriting the state equations (26)-(30),(31)-(33) in terms of the errors $\mathbf{x_1}$ and $\mathbf{x_2}$ yields the continuous dynamics

$$\begin{aligned}\dot{\mathbf{x}}_\mathbf{1} &= \mathbf{x_2}\\ \dot{\mathbf{x}}_\mathbf{2} &= \mathbf{D^{-1}}(\mathbf{x_1} + \mathbf{q^r})[-\mathbf{H}(\mathbf{x_1} + \mathbf{q^r}, \mathbf{x_2} + \dot{\mathbf{q}}^\mathbf{r}) + \mathbf{D}_{\boldsymbol{\tau}}\boldsymbol{\tau} + \mathbf{w_1}] - \ddot{\mathbf{q}}^\mathbf{r}\end{aligned} \tag{35}$$

of the error system.

The transitions occur in the error dynamics according to the following scenarios:

T1) The reference trajectory reaches its predefined impact time instant $t = t^k,\ k = 1, 2, \ldots$ when it hits the unilateral constraint whereas the plant remains beyond this constraint, that is, $F_0(\mathbf{q^r}(t^k)) = 0$, $F_0(\mathbf{x_1}(t^k) + \mathbf{q^r}(t^k)) \neq 0$;

T2) The plant hits the unilateral constraint at $t = t^j,\ j = 1, 2, \ldots$ while the reference trajectory is beyond this constraint, that is, $F_0(\mathbf{q^r}(t^j)) \neq 0$, $F_0(\mathbf{x_1}(t^j) + \mathbf{q^r}(t^j)) = 0$;

T3) Both the reference trajectory and the plant hits the unilateral constraint at the same time instant $t = t^l,\ l = 1, 2, \ldots$ (what can deliberately be enforced by modifying the pre-specified reference trajectory on-line), that is, $F_0(\mathbf{q^r}(t^l)) = 0$, $F_0(\mathbf{x_1}(t^l) + \mathbf{q^r}(t^l)) = 0$.

These scenarios are illustrated in Figure 1. Transition errors are then represented as follows.

Scenario T1:

$$\begin{aligned}\mathbf{x_1}(t^{k+}) &= \mathbf{x_1}(t^{k-})\\ \mathbf{x_2}(t^{k+}) &= \boldsymbol{\mu}^1(\mathbf{x}(t^{k-}), t^k) + \mathbf{w^d_k},\end{aligned} \tag{36}$$

provided that $F_0(\mathbf{q^r}(t^k)) = 0$ and $F_0(\mathbf{x_1}(t^k) + \mathbf{q^r}(t^k)) \neq 0,\ k = 1, 2, \ldots$;

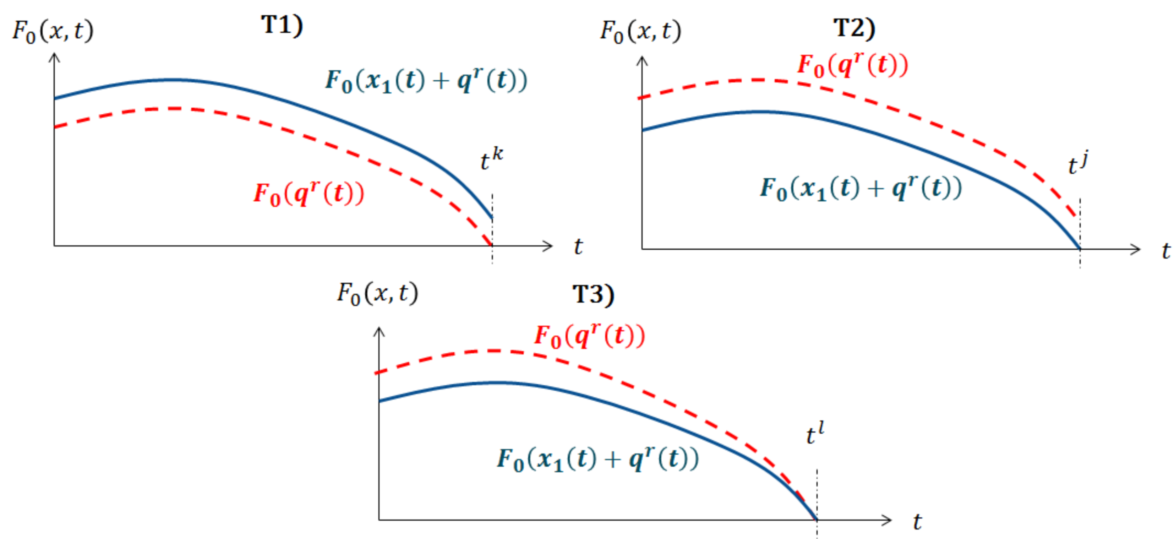

Figure 1: The three different scenarios for the transitions in the error dynamics.

Scenario T2:

$$\begin{aligned} \mathbf{x_1}(t^{j+}) &= \mathbf{x_1}(t^{j-}) \\ \mathbf{x_2}(t^{j+}) &= \boldsymbol{\mu}^2(\mathbf{x}(t^{j-}), t^j) + \mathbf{w_j^d}, \end{aligned} \tag{37}$$

provided that $F_0(\mathbf{q^r}(t^j)) \neq 0$ and $F_0(\mathbf{x_1}(t^j) + \mathbf{q^r}(t^j)) = 0,\ j = 1, 2, \ldots$;

Scenario T3:

$$\begin{aligned} \mathbf{x_1}(t^{l+}) &= \mathbf{x_1}(t^{l-}) \\ \mathbf{x_2}(t^{l+}) &= \boldsymbol{\mu}^3(\mathbf{x}(t^{l-}), t^l) + \mathbf{w_l^d},\ l = 1, 2, \ldots \end{aligned} \tag{38}$$

provided that $F_0(\mathbf{q^r}(t^l)) = 0$ and $F_0(\mathbf{x_1}(t^l) + \mathbf{q^r}(t^l)) = 0,\ l = 1, 2, \ldots$

where $\mathbf{w_k^d}$, $\mathbf{w_j^d}$, $\mathbf{w_l^d}$ are discrete perturbations, counting for restitution inadequacies, and functions $\boldsymbol{\mu}^1$, $\boldsymbol{\mu}^2$, and $\boldsymbol{\mu}^3$ are given by

$$\boldsymbol{\mu}^1(\mathbf{x}, t) = \mathbf{x_2} + [\mathbf{I} - \phi(\mathbf{q^r}(t))]\dot{\mathbf{q}}^{\mathbf{r}}(t^-) \tag{39}$$

$$\boldsymbol{\mu}^2(\mathbf{x}, t) = \phi(\mathbf{x_1} + \mathbf{q^r}(t))[\mathbf{x_2} + \dot{\mathbf{q}}^{\mathbf{r}}(t^-)] - \dot{\mathbf{q}}^{\mathbf{r}}(t^-) \tag{40}$$

$$\boldsymbol{\mu}^3(\mathbf{x}, t) = \phi(\mathbf{x_1} + \mathbf{q^r}(t)[\mathbf{x_2} + \dot{\mathbf{q}}^{\mathbf{r}}(t^-)] - \phi(\mathbf{q^r}(t))\dot{\mathbf{q}}^{\mathbf{r}}(t^-). \tag{41}$$

To put the previous equations into the form (4), it suffices to set

$$F(\mathbf{x},t) = F_0(\mathbf{x_1} + \mathbf{q^r}(t)), \quad \boldsymbol{\omega}(\mathbf{x},t) = \mathbf{I}, \tag{42}$$

and specify the function $\boldsymbol{\mu_0}(\mathbf{x},t)$ by means of

$$\boldsymbol{\mu_0}(\mathbf{x},t) = \begin{cases} \boldsymbol{\mu}^1(\mathbf{x},t) \text{ if } F_0(\mathbf{q^r}(t)) = 0, \;\; F_0(\mathbf{x_1} + \mathbf{q^r}) \neq 0 \\ \boldsymbol{\mu}^2(\mathbf{x},t) \text{ if } F_0(\mathbf{q^r}(t)) \neq 0, \;\; F_0(\mathbf{x_1} + \mathbf{q^r}) = 0 \\ \boldsymbol{\mu}^3(\mathbf{x},t) \text{ if } F_0(\mathbf{q^r}(t)) = 0, \;\; F_0(\mathbf{x_1} + \mathbf{q^r}) = 0. \end{cases} \tag{43}$$

Clearly, the functions $\boldsymbol{\mu_0}(\mathbf{x},t), \boldsymbol{\omega}(\mathbf{x},t), F(\mathbf{x},t)$, thus specified, meet the assumptions, imposed on the generic system (1)-(5) to be twice continuously differentiable in the state domain for all t, and to be piece wise continuous, and uniformly bounded in t, for all state variables $\mathbf{x}$ in some neighborhood around the origin.

2.3.2 Pre-Feedback Design and Controller Synthesis

In the case where only the generalized positions of the mechanical system are available for measurements, the pre-feedback design

$$\boldsymbol{\tau} = \mathbf{D}_{\boldsymbol{\tau}}{}^{-1}[\mathbf{D}(\mathbf{q^r})\ddot{\mathbf{q}}^{\mathbf{r}} + \mathbf{H}(\mathbf{q^r}, \dot{\mathbf{q}}^{\mathbf{r}}) + \mathbf{u}] \tag{44}$$

computes the Coriolis, centrifugal, and gravitational torques on the reference trajectories rather than those occurring in the plant. Thus, the position feedback controller to be constructed consists of a disturbance attenuator $\mathbf{u}$, internally stabilizing the biped around the desired trajectory, and the remainder, which is responsible for the compensation of the torques associated with the reference trajectory.

Substituting the position pre-feedback (44) into (35) yields the impact-free error dynamics in the form

$$
\begin{aligned}
\dot{\mathbf{x}}_1 =& \mathbf{x}_2 \\
\dot{\mathbf{x}}_2 =& \mathbf{D}^{-1}(\mathbf{x}_1 + \mathbf{q}^r)[-\mathbf{H}(\mathbf{x}_1 + \mathbf{q}^r, \mathbf{x}_2 + \dot{\mathbf{q}}^r) + \mathbf{D}(\mathbf{q}^r)\ddot{\mathbf{q}}^r + \mathbf{H}(\mathbf{q}^r, \dot{\mathbf{q}}^r) + \mathbf{u} + \mathbf{w}_1] - \ddot{\mathbf{q}}^r
\end{aligned}
\tag{45}
$$

These error dynamics represent a particular form of the generic system (2)-(3), (8)-(9), when specified with (42)-(43), and

$$
\mathbf{f}(\mathbf{x}, t) = \begin{bmatrix} \mathbf{x}_2 \\ \mathbf{D}^{-1}(\mathbf{x}_1 + \mathbf{q}^r)[-\mathbf{H}(\mathbf{x}_1 + \mathbf{q}^r, \mathbf{x}_2 + \dot{\mathbf{q}}^r) + \mathbf{D}(\mathbf{q}^r)\ddot{\mathbf{q}}^r + \mathbf{H}(\mathbf{q}^r, \dot{\mathbf{q}}^r)] - \ddot{\mathbf{q}}^r \end{bmatrix} \tag{46}
$$

$$
\mathbf{g}_1(\mathbf{x}, t) = \begin{bmatrix} \mathbf{0} & \mathbf{0} \\ \mathbf{0} & \mathbf{D}^{-1}(\mathbf{x}_1 + \mathbf{q}^r) \end{bmatrix}, \ \mathbf{h}_1(\mathbf{x}, t) = \begin{bmatrix} \mathbf{0} \\ \rho_p \mathbf{x}_1 \\ \rho_v \mathbf{x}_2 \end{bmatrix}, \tag{47}
$$

$$
\mathbf{g}_2(\mathbf{x}, t) = \begin{bmatrix} \mathbf{0} \\ \mathbf{D}^{-1}(\mathbf{x}_1 + \mathbf{q}^r) \end{bmatrix}, \ \mathbf{k}_{12}(\mathbf{x}, t) = \begin{bmatrix} \mathbf{I} \\ \mathbf{0} \\ \mathbf{0} \end{bmatrix}, \tag{48}
$$

$$
\mathbf{h}_2(\mathbf{x}, t) = \begin{bmatrix} \mathbf{x}_1^\top & \mathbf{0} \end{bmatrix}^\top, \ \mathbf{k}_{21}(\mathbf{x}, t) = \begin{bmatrix} \mathbf{I} & \mathbf{0} \end{bmatrix}, \ \boldsymbol{\omega}(\mathbf{x}, t) = \mathbf{I}, \ \mathbf{w} = [\mathbf{w}_0^\top \mathbf{w}_1^\top]^\top. \tag{49}
$$

In the sequel, the generic nonlinear $\mathcal{H}_\infty$ synthesis of Theorem 2.1 is specified for the position feedback tracking of the unilaterally constrained mechanical manipulator in question, and it is given in terms of appropriate local solutions of the constrained Hamilton–Jacobi–Isaacs inequalities (12), (13) .

2.3.3 Local State-space Solution

In the manipulator position measurement case (46)-(49) the difficulty of solving the constrained Hamilton–Jacobi–Isaacs PDIs (12), (13) is circumvented by approximating their local solutions by those to the corresponding Riccati equations. The latter equations appear in solving the $\mathcal{H}_\infty$ control problem for the linearized system which is given by

$$\dot{\mathbf{x}} = \mathbf{A}(t)\mathbf{x} + \mathbf{B_1}(t)\mathbf{w} + \mathbf{B_2}(t)\mathbf{u}, \tag{50}$$

$$\mathbf{z} = \mathbf{C_1}(t)\mathbf{x} + \mathbf{D_{12}}(t)\mathbf{u}, \tag{51}$$

$$\mathbf{y} = \mathbf{C_2}(t)\mathbf{x} + \mathbf{D_{21}}(t)\mathbf{w}, \tag{52}$$

within impact-free time intervals (t_{i-1}, t_i), where t_0 is the initial time instant, $t_i,\ i = 1, 2, \ldots$ are the collision time instants, and

$$\begin{aligned} \mathbf{A}(t) &= \left.\frac{\partial \mathbf{f}(\mathbf{x},t)}{\partial \mathbf{x}}\right|_{\mathbf{x}=\mathbf{0}},\ \mathbf{B_1}(t) = \mathbf{g_1}(0,t), \mathbf{B_2}(t) = \mathbf{g_2}(0,t),\ \mathbf{C_1}(t) = \left.\frac{\partial \mathbf{h_1}(\mathbf{x},t)}{\partial \mathbf{x}}\right|_{\mathbf{x}=\mathbf{0}}, \\ \mathbf{C_2}(\mathbf{x})(t) &= \begin{bmatrix} \mathbf{x_1} & \mathbf{0} \end{bmatrix},\ \mathbf{D_{12}}(t) = \mathbf{k_{12}}(0,t),\ \mathbf{D_{21}}(\mathbf{x})(t) = \begin{bmatrix} \mathbf{I} & \mathbf{0} \end{bmatrix}. \end{aligned} \tag{53}$$

By the time-varying strict bounded real lemma (Orlov and Aguilar, 2014, p.46), the following conditions are necessary and sufficient for the linear $\mathcal{H}_\infty$ control problem (50)-(52) to possess a solution: given $\gamma > 0$,

C1) there exists a positive constant ε_0 such that the differential Riccati equation

$$\begin{aligned} -\dot{\mathbf{P}}_\varepsilon(t) &= \mathbf{P}_\varepsilon(t)\mathbf{A}(t) + \mathbf{A}^\top(t)\mathbf{P}_\varepsilon(t) + \mathbf{C_1}^\top(t)\mathbf{C_1}(t) \\ &+ \mathbf{P}_\varepsilon(t)\left[\frac{1}{\gamma^2}\mathbf{B_1}\mathbf{B_1}^\top - \mathbf{B_2}\mathbf{B_2}^\top\right](t)\mathbf{P}_\varepsilon(t) + \varepsilon\mathbf{I} \end{aligned} \tag{54}$$

has a uniformly bounded symmetric positive definite solution $\mathbf{P}_\varepsilon(t)$ for each $\varepsilon \in (0, \varepsilon_0)$;

C2) while being coupled to (54), the differential Riccati equation

$$\begin{aligned} \dot{\mathbf{Z}}_\varepsilon(t) &= \mathbf{A}_\varepsilon(t)\mathbf{Z}_\varepsilon(t) + \mathbf{Z}_\varepsilon(t)\mathbf{A}_\varepsilon^\top(t) + \mathbf{B_1}(t)\mathbf{B_1}^\top(t) \\ &+ \mathbf{Z}_\varepsilon(t)\left[\frac{1}{\gamma^2}\mathbf{P}_\varepsilon\mathbf{B_2}\mathbf{B_2}^\top\mathbf{P}_\varepsilon - \mathbf{C_2}^\top\mathbf{C_2}\right](t)\mathbf{Z}_\varepsilon(t) + \varepsilon\mathbf{I}, \end{aligned} \tag{55}$$

has a uniformly bounded symmetric positive definite solution $\mathbf{Z}_\varepsilon(t)$ with $\mathbf{A}_\varepsilon(t) = \mathbf{A}(t) + \frac{1}{\gamma^2}\mathbf{B_1}(t)\mathbf{B_1}^\top(t)\mathbf{P}_\varepsilon(t)$.

Next result asserts that these conditions, if coupled to a certain monotonicity condition, are also sufficient for a local solution to the nonlinear $\mathcal{H}_\infty$ control problem to exist under unilateral constraints.

Theorem 2.2 *Consider the nonlinear system* (1)-(5)*, specified with* (46)-(49)*. Let conditions C1) and C2) be satisfied for some* $\gamma > 0$*. Then hypotheses H2) and H3) hold locally around the origin* $(\mathbf{x}, \boldsymbol{\xi}) = (0, 0)$ *with*

$$V(\mathbf{x}, t) = \mathbf{x}^\top \mathbf{P}_\varepsilon(t)\mathbf{x} \tag{56}$$

$$R(\mathbf{x}) = \frac{\varepsilon}{2}\|\mathbf{x}\|^2 \tag{57}$$

$$W(\mathbf{x}, \boldsymbol{\xi}, t) = \gamma^2(\mathbf{x} - \boldsymbol{\xi})^\top \mathbf{Z}_\varepsilon^{-\mathbf{1}}(t)(\mathbf{x} - \boldsymbol{\xi}) \tag{58}$$

$$Q(\mathbf{x}, \boldsymbol{\xi}) = \frac{\varepsilon}{2}\gamma^2 \inf_{t\in\mathbb{R}} \|\mathbf{Z}_\varepsilon^{-\mathbf{1}}(t)\|^2\|\mathbf{x} - \boldsymbol{\xi}\|^2 \tag{59}$$

$$G(t) = \mathbf{Z}_\varepsilon(t)\mathbf{C_2}^\top(t) \tag{60}$$

$$\boldsymbol{\nu}(\xi, \mathbf{y}, t) = \begin{bmatrix} \mathbf{y}^\top & \boldsymbol{\mu}_0^\top(\xi, t) \end{bmatrix}^\top, \tag{61}$$

and the closed-loop system, driven by the output feedback

$$\begin{aligned} \dot{\boldsymbol{\xi}} =& \mathbf{f}(\boldsymbol{\xi}, t) + \mathbf{Z}_\varepsilon(t)\mathbf{C_2}^\top(t)[\mathbf{y}(t) - \mathbf{h_2}(\boldsymbol{\xi}, t)] \\ &+ \left[\frac{1}{\gamma^2}\mathbf{g_1}(\boldsymbol{\xi}, t)\mathbf{g_1}^\top(\boldsymbol{\xi}, t) - \mathbf{g_2}(\boldsymbol{\xi}, t)\mathbf{g_2}^\top(\boldsymbol{\xi}, t)\right]\mathbf{P}_\varepsilon(t)\boldsymbol{\xi} \end{aligned}$$

$$\boldsymbol{\xi}(t_i^+) = \boldsymbol{\nu}(\boldsymbol{\xi}(t_i^-), \boldsymbol{y}(t_i^-), t_i) \tag{62a}$$

$$\mathbf{u} = -\mathbf{g_2}(\boldsymbol{\xi}, t)^\top \mathbf{P}_\varepsilon(t)\boldsymbol{\xi}, \tag{62b}$$

locally possesses a $\mathcal{L}_2$*-gain less than* γ *provided that Hypothesis H1) holds as well. Moreover, the disturbance-free closed-loop system* (1)-(5), (62) *is uniformly asymptotically stable provided that Hypothesis H4) is satisfied with the quadratic functions* (56) *and* (58)*.*

Proof. Following the line of reasoning used in the proof of (Orlov and Aguilar, 2014, Theorem 24), hypotheses H2), and H3) are verified to locally hold with (56)-(61). Then by applying Theorem 2.1, the validity of Theorem 2.2 is concluded. ∎

Remark 2.2 *Since the restitution rule* (29)*, chosen for treatment, comes with the identity disturbance multiplier* $\boldsymbol{\omega}(\mathbf{x}, t) = \mathbf{I}$ *the best disturbance attenuation level is limited by*

Hypothesis H1) (see Remark 2.1), which holds if and only if

$$\gamma \geq \sqrt{2} \tag{63}$$

within the present framework. To ensure a better closed-loop performance one should prescribe a realistic multiplier $\boldsymbol{\omega}(\mathbf{x}, t)$ *at the transition phase* (4) *to be infinitesimal at low plant velocities.*

To conclude this section, it is worth noticing that the quadratic forms (56), (58), used in Theorem 2.2, are the simplest ones, yielding local solutions of the Hamilton–Jacobi–Isaacs PDIs (12), (13). These solutions, relying on the differential Riccati equations (54), (55), result in the constructive nonlinear output feedback design (62), which is based on the linearization of the the Hamilton–Jacobi–Isaacs PDIs rather than on the linearization of the plant equations. Remarkably, the resulting nonlinear synthesis is of the same level of complexity as that of the linear $\mathcal{H}_\infty$ synthesis.

Alternative forms, taking for instance care of the (kinetic plus potential) system energy, are indeed possible to locally solve the Hamilton–Jacobi–Isaacs inequalities (12), (13). The compensation of nonlinear (Coriolis, centrifugal, and/or gravitational) forces is typically argued in this way provided that the state feedback is available (see e.g., Chen *et al.* (1994); Aghabalaie *et al.* (2010) for synthesis of unconstrained manipulators). It is however widely accepted (Ortega *et al.*, 2013, p.65) that attenuating (which is presumed by the nonlinear design of Theorem 2.2) instead of compensating the nonlinear terms enhances the system robustness against parametric uncertainties. The closed-loop performance comparison under the afore mentioned local solutions of the Hamilton–Jacobi–Isaacs PDIs remains beyond the scope of the present investigation, and it will not be addressed in this work.

2.3.4 State Feedback Synthesis

In the full-information case, where the perfect state measurement is available, a pre-feedback controller of the form

$$\boldsymbol{\tau} = \mathbf{D}_{\boldsymbol{\tau}}{}^{-1}[\mathbf{D}(\mathbf{q})(\ddot{\mathbf{q}}^{\mathrm{r}} + \mathbf{u}) + \mathbf{H}(\mathbf{q}, \dot{\mathbf{q}})] \tag{64}$$

is designed to simplify the subsequent state feedback synthesis. The controller to be constructed consists of a disturbance attenuator $\mathbf{u}$, internally stabilizing the biped around the desired trajectory, and the remainder, which is responsible for the trajectory compensation, and for the compensation of the Coriolis, centrifugal, and gravitational torques.

By substituting (64) into (35), the error dynamics between impacts are simplified to

$$\begin{aligned}\dot{\mathbf{x}}_{\mathbf{1}} =& \mathbf{x}_{\mathbf{2}} \\ \dot{\mathbf{x}}_{\mathbf{2}} =& \mathbf{D}^{-\mathbf{1}}(\mathbf{x}_{\mathbf{1}} + \mathbf{q}^{\mathrm{r}})\mathbf{w}_{\mathbf{1}} + \mathbf{u}\end{aligned} \tag{65}$$

Thus, the error dynamics are represented in the generic form (1)-(5), being specified with

$$\mathbf{f}(\mathbf{x}, t) = \begin{bmatrix} \mathbf{x}_2 \\ \mathbf{0} \end{bmatrix}, \ \mathbf{g}_{\mathbf{1}}(\mathbf{x}, t) = \begin{bmatrix} \mathbf{0} \\ \mathbf{D}^{-\mathbf{1}}(\mathbf{x}_{\mathbf{1}} + \mathbf{q}^{\mathrm{r}}) \end{bmatrix}, \tag{66}$$

$$\mathbf{g}_{\mathbf{2}}(\mathbf{x}, t) = \begin{bmatrix} \mathbf{0} \\ \mathbf{I} \end{bmatrix}, \ \mathbf{h}(\mathbf{x}) = \begin{bmatrix} \mathbf{0} \\ \rho_p \mathbf{x}_1 \\ \rho_v \mathbf{x}_2 \end{bmatrix}, \ \mathbf{k}_{\mathbf{12}}(\mathbf{x}) = \begin{bmatrix} \mathbf{I} \\ \mathbf{0} \\ \mathbf{0} \end{bmatrix}. \tag{67}$$

Finally, Theorem 2.2 is simplified to the static feedback design

$$\mathbf{u} = -\mathbf{g}_{\mathbf{2}}(\mathbf{x}, t)^{\top} \mathbf{P}_{\varepsilon}(t) \mathbf{x}, \tag{68}$$

and it is summarized as follows.

Theorem 2.3 *Let Hypothesis H1), and Condition C1) be satisfied for some $\gamma > 0$. Then the closed-loop system* (1)-(5)*, specified with* (66)-(67)*, and driven by the state feedback* (68)*, locally possesses a $\mathcal{L}_2$-gain less than γ. Moreover, the disturbance-free closed-loop* *system proves to be uniformly asymptotically stable provided that the function* $V(\mathbf{x},t) = \mathbf{x}^\top \mathbf{P}_\varepsilon(t)\mathbf{x}$ *locally satisfies inequality* (14).

Proof. Since the proof follows the same line of reasoning as that of Theorems 2.1, and 2.2 here we provide only a sketch. Similar to the proof of (Orlov, 2009, Theorem 7.1), let us consider the function $V(\mathbf{x},t)$, whose time derivative, computed along the disturbed closed-loop system (1)-(5) between collision time instants $t \in (t_k, t_{k+1}), \quad k = 0, 1, \ldots,$ is estimated from H2) as follows (Orlov, 2009, p.138):

$$\frac{\mathrm{d}V}{\mathrm{d}t} \leq -\|\mathbf{z}\|^2 + \gamma^2\|\mathbf{w}\|^2 - R(\mathbf{x}). \tag{69}$$

Then, integrating (69) from t_k to $t_{k+1},\ k = 0, 1, \ldots,$ yields

$$\int_{t_k}^{t_{k+1}} [\gamma^2\|\mathbf{w}\|^2 - \|\mathbf{z}\|^2]\mathrm{d}t \geq \int_{t_k}^{t_{k+1}} R(\mathbf{x}(t))\mathrm{d}t + \int_{t_k}^{t_{k+1}} \frac{\mathrm{d}V(\mathbf{x}(t),t)}{\mathrm{d}t}\mathrm{d}t > 0. \tag{70}$$

Skipping positive terms in the right-hand side of (70), it follows that

$$\int_{t_0}^{T} (\gamma^2\|\mathbf{w}\|^2 - \|\mathbf{z}\|^2)\mathrm{d}t \geq V(\mathbf{x}(T),T) + \sum_{i=1}^{N_T}[V(\mathbf{x}(t_i^-),t_i) - V(\mathbf{x}(t_i^+),t_i)] - V(\mathbf{x}(t_0),t_0). \tag{71}$$

Since the function V is smooth by Hypothesis H2), the following relation

$$|V(\mathbf{x}(t_i^-),t_i) - V(\mathbf{x}(t_i^+),t_i)| \leq L_i^V|\mathbf{x}(t_i^-) - \mathbf{x}(t_i^+)| \tag{72}$$

holds true with $L_i^V > 0$ being a local Lipschitz constant of V, in the ball of radius $\|\mathbf{x}(t_i^+)\|$, centered around $\mathbf{x}(t_i^-)$. Relations (71) and (72), coupled together, result in

$$\int_{t_0}^{T} (\gamma^2\|\mathbf{w}\|^2 - \|\mathbf{z}\|^2)\mathrm{d}t \geq -\sum_{i=1}^{N_T}[2(L_i^V)\|\mathbf{x}(t_i^-)\| - V(\mathbf{x}(t_0),t_0) \tag{73}$$

Apart from this, inequality

$$\sum_{i=1}^{N_T}\|\mathbf{z_i^d}\|^2 = \sum_{i=1}^{N_T}\|\mathbf{x_2}(t_i^+)\|^2 \leq \sum_{i=1}^{N_T}[2\|\mu_\mathbf{0}\|^2] + 2\sum_{i=1}^{N_T}[\|\omega\mathbf{w_d^i}\|^2] \leq \gamma^2\sum_{i=1}^{N_T}\|\mathbf{w_d^i}\|^2 + \sum_{i=1}^{N_T}[2\|\mu_\mathbf{0}\|^2] \tag{74}$$

is ensured by H1). Thus, combining (73)-(74), one derives

$$\begin{aligned}\int_{t_0}^{T}\|\mathbf{z}\|^2\mathrm{d}t+\sum_{i=1}^{N_T}\|\mathbf{z_i^d}\|^2&\le V(\mathbf{x}(t_0),t_0)+\sum_{i=1}^{N_T}[2\|\mu_\mathbf{0}\|^2]\\+\gamma^2\left[\int_{t_0}^{T}\|\mathbf{w}\|^2\mathrm{d}t+\sum_{i=1}^{N_T}\|\mathbf{w_d^i}\|^2\right]&+\sum_{i=1}^{N_T}[(2L_i^V)\|\mathbf{x}(t_i^-)\|,\end{aligned} \tag{75}$$

that is, the disturbance attenuation inequality (7) is established with

$$\begin{aligned}\beta_0(\mathbf{x}(t_0),t_0)&=V(\mathbf{x}(t_0),t_0),\\ \beta_i(\mathbf{x}(t_i),t_i)&=(2L_i^V)\|\mathbf{x}(t_i^-)\|+2\|\mu_\mathbf{0}(\mathbf{x}(t_i^-),t_i)\|^2\end{aligned} \tag{76}$$

with $i=1,\dots,N.$ To complete the proof it remains to establish the asymptotic stability of the undisturbed ($\mathbf{w}=\mathbf{0},\ \mathbf{w_d^i}=\mathbf{0},\ i=1,2,\dots$) version of the closed-loop system (1)-(5),(68). To do that, we can use Lemma 2.1. Indeed, according to this result, Hypothesis H1), and the negative definiteness (69) of the time derivative of the Lyapunov function $V(\mathbf{x},t)$ between the collision time instants, ensure that the system is uniformly asymptotically stable. Since the compliance of C1) is established, Hypothesis H2) locally holds with $V(\mathbf{x},t)=\mathbf{x}^\top\mathbf{P}_\varepsilon\mathbf{x}$ due to (Orlov and Aguilar, 2014, Theorem 24), thus yielding this result local. This completes the proof. ■

2.3.5 Remarks on the Synthesis of Autonomous and Periodic Systems

For the regulation of the autonomous systems (1)-(5), all functions in (46)-(49) and (50)-(52) are time-independent, and the differential Riccati equations (54) and (55) degenerate to the algebraic Riccati equations with $\dot{\mathbf{P}}_\varepsilon(t)=0$ and $\dot{\mathbf{Z}}_\varepsilon(t)=0$.

For the periodic tracking of period T with periodic impact instants $t_{i+1}=t_i+T,\ i=1,2,\dots$, all functions in (46)-(49) and (50)-(52) are time-periodic, and Theorem 2.2 admits a time-periodic synthesis (62) which is based on appropriate periodic solutions $\mathbf{P}_\varepsilon(t)$ and $\mathbf{Z}_\varepsilon(t)$ of the periodic differential Riccati equations (54) and (55). It should be noted that $P_\varepsilon(t_{i+1}^+)=P_\varepsilon(t_i^+),\ Z_\varepsilon(t_{i+1}^+)=Z_\varepsilon(t_i^+)$ due to the periodicity, and conditions (14), (15) of

Hypothesis H4) are then specified to the boundary conditions

$$\mathbf{x}^\top \mathbf{P}_\varepsilon(t_2^-)\mathbf{x} \geq \boldsymbol{\mu}^\top(\mathbf{x}, t_1^+))\mathbf{P}_\varepsilon(t_1^+)\boldsymbol{\mu}(\mathbf{x}, t_1^+)), \tag{77}$$

$$(\mathbf{x}-\xi)^\top \mathbf{Z}_\varepsilon(t_2^-)(\mathbf{x}-\xi) \geq [\boldsymbol{\mu}(\mathbf{x}, t_1^+) - \boldsymbol{\mu}(\xi, t_1^+)]^\top \mathbf{Z}_\varepsilon(t_1^+)[\boldsymbol{\mu}(\mathbf{x}, t_1^+) - \boldsymbol{\mu}(\xi, t_1^+)] \tag{78}$$

on the Riccati equations (54), (55). Capabilities of the resulting regulation and tracking synthesis are subsequently illustrated in a simple testbed.

2.4 Conclusions

In this chapter, sufficient conditions for a local solution of the $\mathcal{H}_\infty$ output feedback tracking problem to exist are obtained in terms of the appropriate solvability of an independent inequality on discrete disturbance factor that occurs in the restitution rule, and three coupled inequalities, involving two Hamilton-Jacobi-Isaacs inequalities. The former inequality ensures that the closed-loop impulse dynamics (when the state trajectory hits the unilateral constraint) are ISS whereas the latter inequalities, arising in the continuous-time state feedback and, respectively, output injection designs, should impose the desired iISS property on the continuous closed-loop dynamics between impacts.

Chapter 3. Periodic motion generation under unilateral constraints : hybrid Van der Pol oscillator

The primary concern of this chapter is to design a hybrid reference model based on the Van der Pol oscillator, that would generate a stable limit cycle under unilateral constraints. Similar to the unconstrained case, such a model could be used in the model reference adaptive control to synthesize the closed-loop system producing its own limit cycle.

The Van der Pol oscillator, governed by the second order nonlinear differential equation

$$\ddot{x} + \varepsilon[x^2 - \rho^2]\dot{x} + \mu^2 x = 0 \tag{79}$$

with positive parameters $\varepsilon,\ \rho,\ \mu$ is of fundamental value in nonlinear oscillation theory. It possesses (see, e.g., Khalil (2002)) a stable limit cycle that attracts all other solutions except a unique equilibrium point, being the origin $(x, \dot{x}) = (0, 0)$. Figure 2a, drawn from Khalil (2002), depicts typical phase trajectories and limit cycle of a generic Van der Pol oscillator. With the value ε, escaping to zero, the nonlinear Van der Pol oscillator degenerates to the linear one, which possesses the center (non-asymptotically stable equilibrium) and harmonic orbits of amplitude and frequency dependent on the initial conditions. Such a phenomenon, when under small parametric variations a stable limit cycle degenerates to a (possibly, asymptotically) stable equilibrium, is referred to as Poincaré-Andronov-Hopf bifurcation, or simply Hopf bifurcation (Hale and Koçak, 2012, p.208).

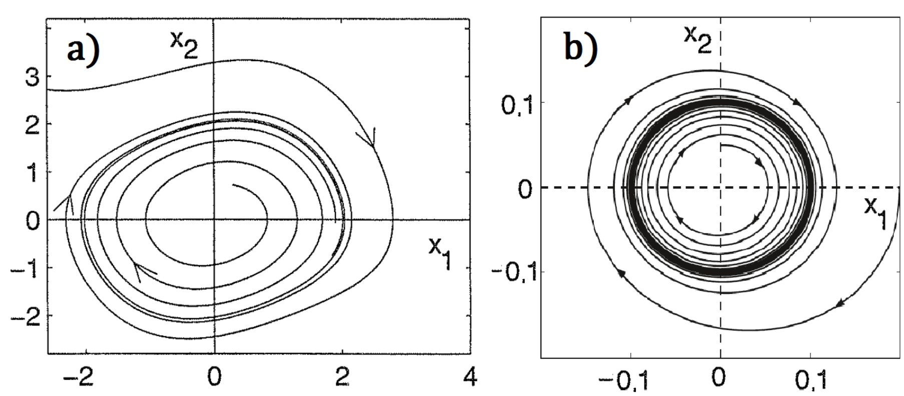

Figure 2: a) Phase portrait of the Van der Pol Oscillator (79). **b) Phase portrait of the modified the Van der Pol Oscillator** (80).

To re-shape the generated limit cycle geometry to an appropriate form of an ellipse (or a circle, in particular) the following Van der Pol modification

$$\dot{x}_1 = x_2, \;\; \dot{x}_2 = -\varepsilon\left[\left(x_1^2 + \frac{x_2^2}{\mu^2}\right) - \rho^2\right] x_2 - \mu^2 x_1 \tag{80}$$

was proposed Roup and Bernstein (2001) where the state vector $x = (x_1, x_2)^\top$ consists of the position x_1 of the oscillator and its velocity x_2. It was shown Orlov *et al.* (2004) that the proposed modification still belongs to a class of damped systems, its limit cycle, which inherits the stability property from its original version, is explicitly governed by the ellipse equation

$$x_1^2 + \frac{x_2^2}{\mu^2} = \rho^2, \tag{81}$$

and it is remarkably generated by harmonic oscillations

$$\dot{x}_1 = x_2, \; \dot{x}_2 = -\mu^2 x_1, \tag{82}$$

initialized on ellipse (81). Thus, while being initialized outside the origin, the modified Van der Pol oscillator (80) produces stable harmonic oscillations of the magnitude ρ and frequency μ, respectively, with the transient limit cycle speed (damping) ε. The phase portrait of the modified Van der Pol oscillator with the parameters $\rho = 0.01, \mu = 1, \varepsilon = 1000$ is reproduced from Orlov *et al.* (2004) in Figure 2b. Due to the above features, the Van der Pol modification (80) has become extremely suited for its use in the model reference adaptive control (Roup and Bernstein, 2001; Orlov *et al.*, 2008; Santiesteban *et al.*, 2008) where the desired magnitude and frequency of the resulting oscillation are on-line manipulatable.

3.1 The Constrained Van der Pol Oscillator

In the sequel, the dynamics of the modified Van der Pol oscillator (80) are studied under the unilateral constraint $x_1 \geq 0$. The present investigation aims to determine if such a constrained Van der Pol model is still capable of generating a limit cycle. Along with numerical analysis of the limit cycle to exist, Hopf bifurcation is revealed for the constrained Van der Pol modification under a nontrivial value of the parameter ε, yet corresponding to nonlinear dynamics. This is in contrast to the unconstrained nonlinear Van der Pol oscillator which exhibits the Hopf bifurcation just for the trivial parameter value $\varepsilon = 0$ when it degenerates to the linear oscillator.

As pointed out, the modified Van der Pol model of interest operates under the unilateral position constraint $x_1 \geq 0$. Once a model trajectory hits the constraint surface

$$S = \{x \in \mathbb{R}^2 : x_1 = 0 \cup x_2 \leq 0\} \tag{83}$$

at a collision time instant t, the underlying model instantaneously resets its velocity according to the elastic restitution law

$$x_1(t^+) = x_1(t^-), \;\; x_2(t^+) = -ex_2(t^-), \text{ if and only if } \; x(t) \in S \tag{84}$$

with the restitution parameter $e \in (0, 1)$. Hereinafter, $x_1(t^-)$ and $x_2(t^-)$ stand for the pre-impact states (position and velocity, respectively) before hitting the constraint surface (83), whereas $x_1(t^+)$ and $x_2(t^+)$ are for the post-impact states after the reset. Beyond the constraint, the continuous dynamics are governed by (80) whenever $x(t) \notin S$.

Remark 3.1 *The model* (80)*,* (83)*,* (84) *can be viewed as a complementary system (Heemels and Brogliato, 2003) by introducing the complementarity condition* $0 \leq x_1 \perp \lambda \geq 0$*, where* λ *represents a slack variable (e.g. a contact force in mechanical systems). For simplicity, an instantaneous reset in the states, given by* (84) *is considered, with no further interaction of the trajectories with the resetting surface* (83)*, so* (80)*,* (83)*,* (84) *is analyzed as a hybrid system. An extension of this work, considering the associated complementarity problem, is interesting and calls for further research.*

3.2 Existence of a Constrained Limit Cycle

Similar to the constraint-free Van der Pol oscillator, the above model (80), (83), (84) possesses an equilibrium in the origin that is straightforwardly verified by inspection. The question then arises whether the constrained oscillator (80), (83), (84) generates a stable limit cycle as well. To address this question the present section employs the well-known features of the Poincaré map to derive sufficient conditions of the constrained stable limit cycle to exist. Potential Zeno dynamics with finite impact-accumulation points (similar to those of bouncing ball Liberzon (2003)) are actually admitted, but their finite-time stability is not specifically treated as the present investigation focuses on the asymptotic stability only.

Without loss of generality, the subsequent stability analysis of the constrained Van Der Pol model (80), (83), (84) is confined to initial conditions $x^0 = (0, v_0)^T$ with $v_0 > 0$; otherwise, one could readily re-initialize the model with such initial conditions by reconstructing the continuous dynamics in the backward time. With this in mind, let $x(v_0;t) = (x_1(v_0;t), x_2(v_0;t))^T$ denote a trajectory of (80), (83), (84), initialized at $x_1(v_0;0) = 0, x_2(v_0;0) = v_0 > 0$, and let t_k, $k = 1, 2, \ldots$ stand for the collision time instants when this trajectory resets its velocity. Dependent on the oscillator parameter values, the following alternative scenarios are heuristically in order.

S1) Inequalities

$$x_2(v_0;t_1^+) < v_0,\ x_2(v_0;t_{k+1}^+) < x_2(v_0;t_k^+) \tag{85}$$

hold for all $k = 1, 2, \ldots$, and all $v_0 > 0$.

S2) There exists a scalar $x^* > 0$ such that inequalities (85) hold for all $k = 1, 2, \ldots$, and all $v_0 > x^*$, whereas the inverse inequalities

$$x_2(v_0;t_1^+) > v_0,\ x_2(v_0;t_{k+1}^+) > x_2(v_0;t_k^+) \tag{86}$$

hold for all $k = 1, 2, \ldots$, and all $v_0 \in (0, x^*)$.

It should be pointed out that Scenario S2) is the only possible option for the constraint-free Van der Pol oscillator (80) provided that $t_k,\ k = 1, 2, \ldots$ stand for the time instants when the state trajectory meets the vertical semi-axis $x_1 = 0, x_2 > 0$. Indeed, to reproduce this conclusion it suffices (see (Orlov, 2009, Section 2.3.3) for details) to differentiate the function

$$V(x) = \frac{1}{2}x_1^2 + \frac{1}{2\mu^2}x_2^2 \tag{87}$$

along the trajectories of (80) to obtain that

$$\dot{V}(x) = \frac{\varepsilon}{\mu^2}[\rho^2 - (x_1^2 + \frac{x_2^2}{\mu^2})]x_2^2 \tag{88}$$

thereby yielding

$$\dot{V}(x) \begin{cases} > 0, & if \;\; (x_1^2 + \frac{x_2^2}{\mu^2} < \rho), x_2 \neq 0 \\ < 0, & if \;\; (x_1^2 + \frac{x_2^2}{\mu^2} > \rho), x_2 \neq 0 \\ = 0, & if \;\; (x_1^2 + \frac{x_2^2}{\mu^2} - \rho)x_2^2 = 0 \end{cases} \tag{89}$$

Then, Scenario S2), properly modified for the constraint-free oscillator (80), follows from (89). Remarkably, the same function (87) is no longer useful to detect a limit cycle of the constrained oscillator (80), (83), (84), because its instantaneous change $\Delta V(x(v_0; t_k)) = V(x(v_0; t_k^+)) - V(x(v_0; t_k^-))$ at the collision time instants t_k, $k = 1, 2, \ldots$ is governed by the elastic restitution law (84) with $e \in (0, 1)$, and therefore it remains negative definite, since $\Delta V(x(v_0; t_k)) = \frac{1}{2\mu^2}[x_2^2(v_0; t_k^+) - x_2^2(v_0; t_k^-)] = \frac{e^2-1}{2\mu^2} x_2^2(v_0; t_k^-) < 0$ regardless of whether the initial condition x^0 is inside or outside the ellipse equation (81). This is in contrast to the sign variation (89) of the time derivative (88).

The following result might be viewed as a counterpart of the Poincaré-Bendixon criterion for the constrained oscillator (80), (83), (84).

Theorem 3.1 *Consider the constrained Van der Pol oscillator* (80), (83), (84) *with a priori fixed parameters* $\rho, \mu, \varepsilon > 0$ *and* $e \in (0, 1)$. *i) under Scenario S1) its globally asymptotically stable in the origin. ii) Under Scenario S2) it possesses a stable limit cycle* γ^* *generated by the trajectory* $x(x^*; t)$, *with* $x^0 = (0, x^*)^T$ *such that any trajectory of* (80), (83), (84), *initialized beyond the origin, converges to* γ^*.

Proof. To begin with, let us assume that Scenario S1) holds. Then given an initial condition $x^0 = (0, v_0)$ at $t = 0$ with $v_0 > 0$, the pre-impact and post-impact velocity values monotonically converge to some $\tilde{x}_* \geq 0$, and $\tilde{x}^* \geq 0$, respectively, that is,

$$\lim_{k\to\infty} x_2(v_0; t_k^-) = \tilde{x}_*, \; \lim_{k\to\infty} x_2(v_0; t_k^+) = \tilde{x}^* \tag{90}$$

where the restitution rule (84), and inequality (85) were taken into account. Since the time derivative (88) of the Lyapunov function (87) of the unconstrained oscillator remains monotonic between the impact time instants, the stability of the constrained Van der Pol oscillator (80) is then concluded.

Moreover, due to the continuous dependence of the trajectories $\gamma_k(v_0) = \{x(v_0;t),\ t \in (t_k, t_{k+1})\},\ k = 1, 2, \ldots$ on its initial values $x(v_0;t_k^+)$ at $t = t_k$, it follows that $x(v_0;t_{k+1}^-) \to x(\tilde{x}^*;t_1^-)$ as $k \to \infty$. Then by employing (84), one concludes that

$$\lim_{k\to\infty} x_2(v_0;t_{k+1}^+) = x_2(\tilde{x}^*;t_1^+). \tag{91}$$

Since S1) ensures that $x_2(\tilde{x}^*;t_1^+) < \tilde{x}^*$ whenever $\tilde{x}^* > 0$ convergence (91) would not contradict to the second convergence in (90) in the case that $\tilde{x}^* = 0$. Thus, according to (90), the post-impact velocity values $x_2(v_0;t_k^+)$ escape to zero as $k \to \infty$, and relying again on the continuous dependence of the trajectories $\gamma_k(v_0) = \{x(v_0;t),\ t \in (t_k, t_{k+1})\},\ k = 1, 2, \ldots$ on the values $x(v_0;t_k^+)$ at $t = t_k$, the global asymptotic stability of (80), (83), (84) is established in the origin under Scenario S1), which is illustrated in Fig. 3a.

The proof of the asymptotic stability of the limit cycle γ^* under Scenario S2) follows the same line of reasoning. In this case, convergence (90) holds for some $\tilde{x}^* \geq x^*$ if $v_0 > x^*$, and for some $\tilde{x}^* \leq x^*$ if $v_0 < x^*$. In turn, convergence (91) does not contradict to convergence (90) if and only if $x_2(\tilde{x}^*;t_1^+) = \tilde{x}^* = x^*$. Thus, Scenario S2) results in a limit cycle γ^*, generated by the initial condition $x_1(0) = 0, x_2(0) = x^*$, and this cycle is asymptotically stable due to the continuous dependence of the trajectory plots $\gamma_k(v_0) = \{x(v_0;t),\ t \in (t_k, t_{k+1})\},\ k = 1, 2, \ldots$ on the initial values $x(v_0;t_k^+)$ at $t = t_k$. This scenario is illustrated in Fig. 3b. This completes the proof. ■

Remark 3.2 *For the case of* $e = 0$*, the trajectories of* (80)*,* (83)*,* (84) *reach the origin after the first impact. Since the origin is an equilibrium point, the system stays at rest there for all* $t > t_1$*. For the case of* $e = 1$*, Scenario S2) is in order, and* (87) *is again useful to detect a limit cycle, since* $\Delta V(x(v_0;t_k)) = 0$ *at the collision time instants* t_k*, and it easily follows that the limit cycle is given by* (81) *restricted to* $x_1 > 0$*.*

Theorem 3.1 admits a useful interpretation in terms of the Poincaré map of the trajectories of (80), (83), (84) where the Poincaré section is set at each post-reset instant. With this in mind, the value of $x(t_k^+)$ after each reset can be viewed as a discrete system of the

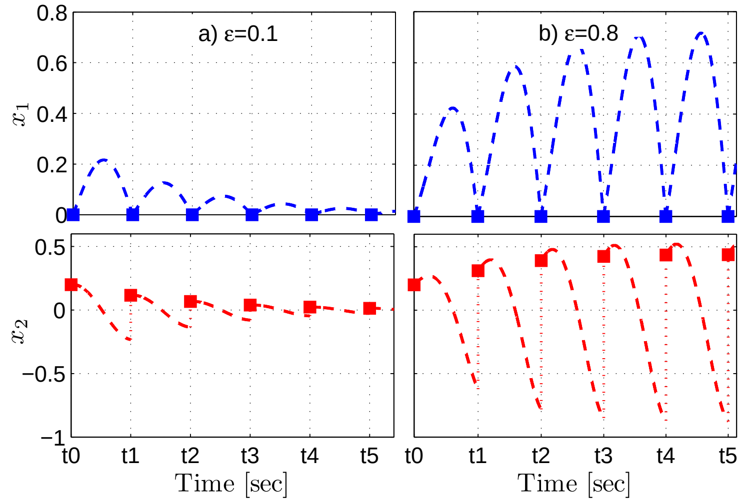

Figure 3: State dynamics under an initial condition $x^0 = (0, 0.2)^T$. The squares denote the post-impact positions and velocities at time instants t_k. For $\varepsilon = 0.1$, the sequence of $x_2(0.2; t_k^+)$ is observed to fall into Scenario S1). To the contrary, for $\varepsilon = 0.8$, Scenario S2) is brought into play.

form

$$x_2(t_{k+1}^+) = F(x_2(t_k^+)) \tag{92}$$

where F represents the map from the previous post-reset state to the next one. Since by Theorem 3.1, inequalities (85)-(86) ensure the existence of a fixed point x^* of the map (92), then the eigenvalues of the gradient ∇F of this map are all inside the unit circle, and neither of them has an imaginary part because the sequence $x_2(t_k^+),\ k = 1, 2, \ldots$ cannot traverse x^*. In Section 3.4, this observation will numerically be applied to the stability analysis of a limit cycle generated by the constrained Van der Pol oscillator (80), (83), (84).

3.3 Numerical Analysis of Phenomenological Behaviors

In this section, different behaviors of the constrained Van der Pol oscillator (80), (83), (84) are numerically analyzed. To facilitate the exposition, the magnitude and frequency parameters are pre-specified with $\rho = \mu = 1$, while the restitution parameter is set to $e = 0.5$. The investigation is thus focused on the Hopf bifurcation which is relevant to variations of the damping parameter ε only. An event-driven algorithm is utilized, as described in Heemels and Brogliato (2003), and the simulations were performed using Simulink®, by means of the Dormand-Prince method, with a fixed step of $1\ mS$.

Using the results of the previous section, inequalities (85) and (86) are successfully applied to search for an asymptotically stable limit cycle, or to verify the asymptotic stability of the origin according to Theorem 3.1.

From the numerical experiments performed, two cases are carried out. First, the trajectories of the system in question are shown to fall into Scenario S1) for rather low values of ε. Second, the system trajectories are shown to fit Scenario S2) for rather high values of ε. The values of ε are then delimited, so as to detect a hypothetical critical point of the Hopf bifurcation.

3.3.1 Case Study: Low Transient Speed

The transient speed parameter was initially set to $\varepsilon = 0.3$. Figure 4a depicts a solution of the constrained Van der Pol oscillator (80), (83), (84), initialized at $x^0 = (0, 0.8)^T$, which escapes to the origin.

It can readily be identified from Fig. 4a that the post-impact velocities $x_2(t_k^+)$ at the collision time instants when the trajectory hits the surface $x_1 = 0$ form a sequence that monotonically decreases towards the origin, thus complying with inequality (85), and after several iterations, the oscillator continues to converge towards the origin of the phase plane, This phenomenon is observed for various initial conditions, thereby supporting the global asymptotic stability of the constrained Van Der Pol oscillator. Successive numerical experiments made for lower values of the transient speed parameter established that the oscillator remained globally asymptotically stable for $\varepsilon < 0.3$.

3.3.2 Case Study: High Transient Speed

The value $\varepsilon = 1$ was numerically tested to be high enough to generate an asymptotically stable limit cycle.

Figure 4b shows the solution of (80), (83), (84), using two different initial conditions $x^0 = (0, 1.2)^T$, and $x^0 = (0, 0.2)^T$. The trajectory, starting from the top, is observed to form a monotonically decreasing sequence of the post-impact velocity values $x_2(t_k^+)$, converging to a value x^*. Inequality (85) is thus numerically verified in this case. In turn, the trajectory starting from a lower value, is observed to form a monotonically increasing sequence of $x_2(t_k^+)$, also converging to x^*. Inequality ((86) is thus respected, too. By Theorem 3.1, both trajectories approach a limit cycle. Numerical tests were also performed using several higher values $\varepsilon > 1$ of the transient speed parameter, and all of the tests demonstrated the generation of attractive limit cycles.

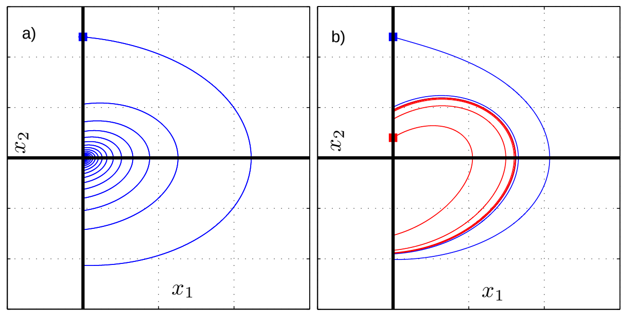

Figure 4: Phase trajectories of (80)**,** (83)**,** (84) **for different values of the transient speed parameter** ε**: a)** $\varepsilon = 0.3$**, b)** $\varepsilon = 1$**. The squares denote the initial condition of each trajectory.**

3.3.3 Bifurcation of Limit Cycles

Subsequent numerical experiments intended to enclose the bifurcation value $\varepsilon = \varepsilon_c$ within a smaller range, yielding $0.4 < \varepsilon_c < 0.5$. Motivated by these results, the next section numerically applies the method of Poincaré to better approximate the critical parameter value ε_c, when the Hopf bifurcation takes place.

3.4 Poincaré Analysis of Stability of Limit Cycles

In this section, the method of Poincaré is applied to analyze which scenario is in play. The Poincaré section of (92) is determined just after a reset of the system (80), (83), (84) for taking into account both, the continuous and discrete dynamics. This map involves the solution of the differential equation of the continuous dynamics (80), and the restitution law (84). Since the former is hardly possible to obtain, the present development relies on the numerical integration step by step like that of Goswami *et al.* (1996).

To verify that (80), (83), (84) possesses a periodic solution, only the one-dimensional map of x_2 is analyzed, since the post-reset value of the position x_1 is equal to zero due to the choice of the restitution surface.

As in section 3.3.2, the fixed parameters are $e = 0.5, \mu = 1, \rho = 1$, and the stability of the limit cycle, shown in Fig. 4b, is analyzed under $\varepsilon = 1$. The Cobweb plot, which is well-recognized to be a useful tool of investigating the qualitative behavior of one-dimensional maps Waugh (1964), is presented in Fig. 5a for the same value of ε. The fixed points of (92) are typically obtained as the intersections of this map with the identity map.

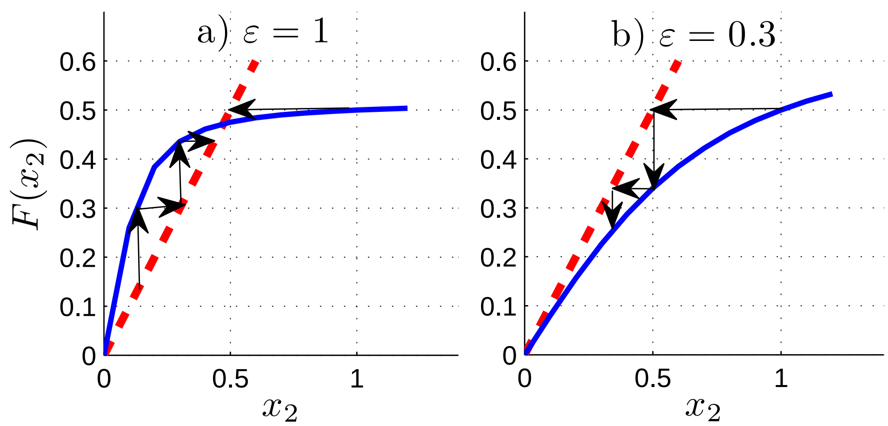

Figure 5: The Cobweb plots of the Poincaré map (92) **with** $\varepsilon = 1$ **and** $\varepsilon = 0.3$**. Solid line is for the Poincaré map** $F(x_2)$**, dashed line is for the identity map. The arrows illustrate a) the attractivity of the nonzero fixed point (black square) for** $\varepsilon = 1$**, and b) the attractivity of the origin for** $\varepsilon = 0.3$**.**

Apart from the unstable equilibrium $x_2 = 0$, there is another intersection, that corresponds to an asymptotically stable fixed point x^*, denoted in Fig. 5a by the black square. Indeed, the arrows at the Cobweb plot indicate the evolution of the Poincaré map from an arbitrary initial condition of $x_2(t_0) = v_0 > 0$ so that all the trajectories evolve away from zero while approaching this fixed point x^*. Thus, Scenario S2) is in order and Theorem 3.1 ensures the existence and asymptotic stability of the limit cycle, generated by the trajectory, initialized at $x_1 = 0, x_2 = x^*$. To locally analyze the stablity of the fixed point x^*, the eigenvalues of the gradient of the Poincaré map F are numerically computed as follows Goswami *et al.* (1996).

The Taylor series approximation of the map F, governed by (92), is expressed as:

$$F(x^* + \delta x^*) \approx F(x^*) + (\nabla F)\delta x^*. \tag{93}$$

where δx^* is a small deviation from the fixed point x^*, and ∇F represents the gradient of F. Since x^* is a fixed point of the map, (93) can be rewritten as

$$F(x^* + \delta x^*) \approx x^* + (\nabla F)\delta x^*. \tag{94}$$

The fixed point x^* of the map F is asymptotically stable if the Poincaré map of the perturbed state is closer to the fixed point. This property can be viewed as the contraction of the phase space around the limit cycle Goswami *et al.* (1996). This means that the magnitude of the eigenvalues of ∇F at the fixed point x^* are strictly less than one. From (94), the gradient is expressed as

$$\nabla F = [F(x^* + \delta x^*) - x^*] = \Upsilon\Omega^{-1}(\delta x^*)^{-1} \tag{95}$$

Thus, ∇F is computed according to (95) by applying a deviation Ω from the fixed point (via deviating the initial value of x_2) for the numerical derivation of the resulting value $\Upsilon = x_2(t_{k+1}^+)$.

Following this procedure with a certain deviation $\Omega = 0.228$, the value $\Upsilon = 0.018$ is then obtained for $\varepsilon = 1$. Since the computed eigenvalue $\lambda(\nabla F) = 0.079$ is inside of the unit circle, the asymptotic stability of x^* is established. Also, due to the fact that $\lambda(\nabla F)$ does not have an imaginary part, Scenario S2) is in force, so that Theorem 3.1 ensures that the limit cycle of the constrained Van der Pol oscillator (80), (83), (84), depicted in Fig. 4b, is asymptotically stable, too.

The asymptotic stability of the origin is illustrated in Fig. 4a for $\varepsilon = 0.3$, and it is determined by means of the Cobweb plot of (92), depicted in Fig. 5b. In this case, the only fixed point of the map is the origin, and, as indicated by the black arrows, the map evolves towards the origin, thus resulting in the asymptotic stability of the origin. The same conclusion is obtained with ∇F, centered in the origin, the eigenvalue of which is less than the unity.

The proposed analysis reveals a fixed point of (92) to exist, thus ensuring the existence of a limit cycle. Figure 6 shows the intersections of the Poincaré map (92) with the identity map, for several values of ε. It can be observed that while decreasing ε towards zero, there is no longer an intersection of the Poincaré map with the identity map, so there is no fixed point of (92) other than the origin. Using the same tools as before, the Cobweb plot straightforwardly demonstrates that the origin is attractive, as predicted based on the eigenvalues of ∇F, located inside the unit circle for low values of ε. Thus, Scenario S1) remains in order, and the asymptotic stability of the origin is concluded from Theorem 3.1.

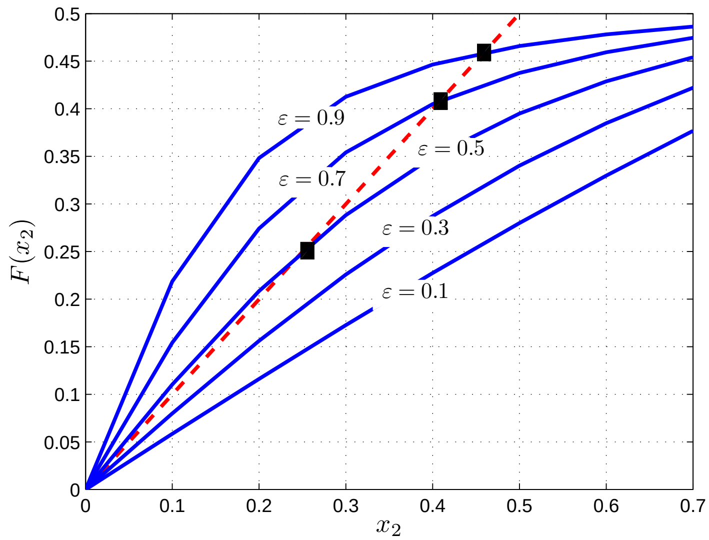

Figure 6: Intersections of the Poincaré map (92) **with the identity map for different values of** ε**. Dashed line is for the identity map, black square is for the fixed points of the maps.**

Figure 7 plots the fixed point x^*, computed for different values of ε. This figure clearly illustrates the Hopf bifurcation of (80), (83), (84) occurring at the critical transient speed value $\varepsilon_c \approx 0.43$.

Figures 8-9 additionally illustrate that for a value $\varepsilon = 1$, higher that the bifurcation point, $x_2(t_k^+)$ converges to a fixed point as k goes to infinity, thus ensuring the convergence of the dynamics of (80), (83), (84) to a limit cycle, whereas for a value $\varepsilon = 0.3$, lower than the bifurcation point, $x_2(t_k^+)$ escapes to zero, thus ensuring that the asymptotic stability of (80), (83), (84) around the equilibrium point.

3.5 Conclusions

In this chapter, the Van der Pol oscillator is analyzed under unilateral constraints. Opposed to the unrestricted case, where a Hopf bifurcation occurs when the oscillator degenerates

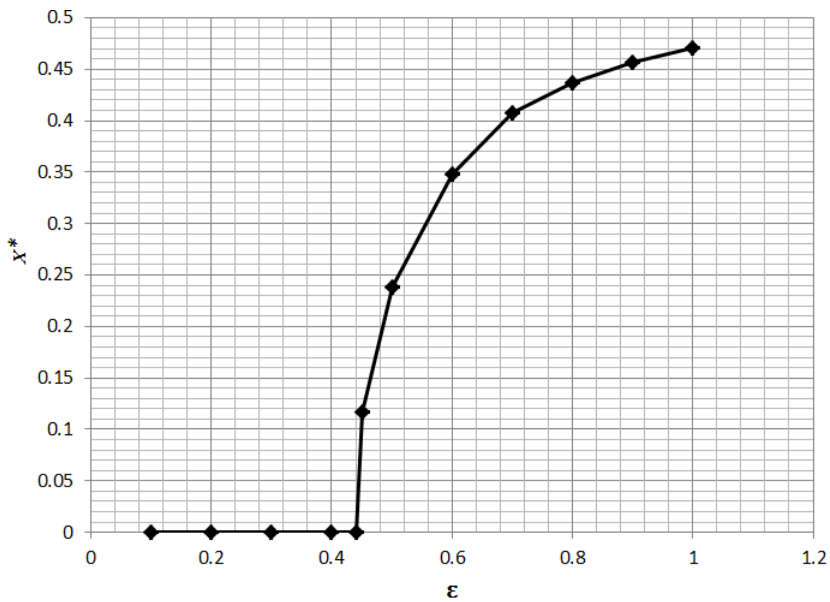

Figure 7: Bifurcation diagram for the constrained Van der Pol oscillator: fixed point x^* of the Poincaré map (92) **vs ε. The Hopf bifurcation occurs at $\varepsilon \approx 0.43$.**

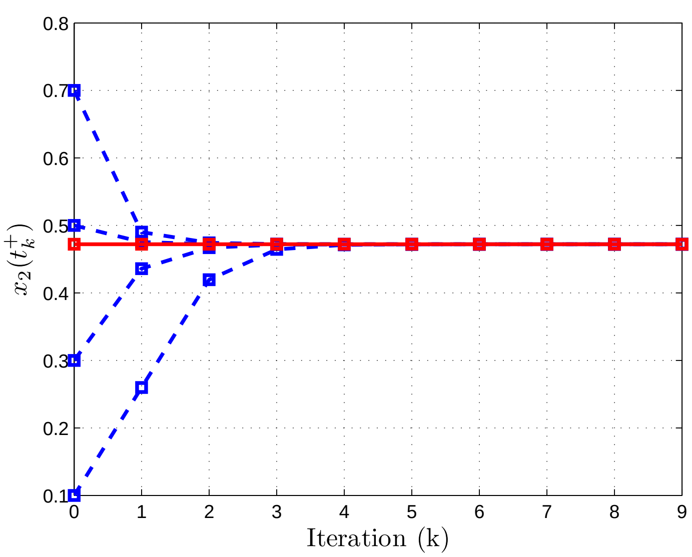

Figure 8: Evolution of $x_2(t_k^+)$ at each resetting event k under $\varepsilon = 1$ for different initial velocities $v_0 = 0.1$, $v_0 = 0.3$, $v_0 = 0.5$, $v_0 = 0.7$. The solid line indicates the fixed point towards which $x_2(t_k^+)$ converge.

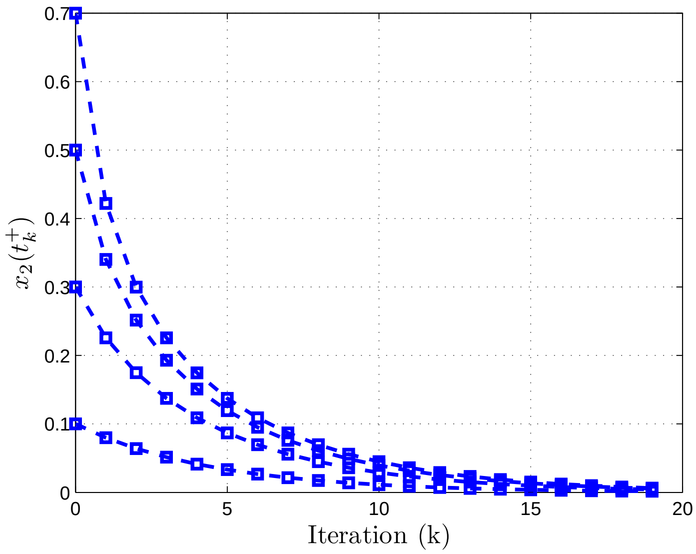

Figure 9: Evolution of $x_2(t_k^+)$ at each resetting event k under $\varepsilon = 0.3$ for different initial velocities $v_0 = 0.1$, $v_0 = 0.3$, $v_0 = 0.5$, $v_0 = 0.7$.

to a linear oscillator for the trivial parameter value $\varepsilon = 0$, the restricted version is shown to exhibit a Hopf bifurcation for a non trivial transient speed parameter $\varepsilon_c > 0$. Existence and stability of the limit cycle is finally ensured via the well-known method of Poincaré sections. These results will be used in the following chapter, to provide to a simple impacting mechanical system a reference model to be robustly tracked by means of the $\mathcal{H}_\infty$ theory developed in Chapter 2.

Chapter 4. Model reference tracking of limit cycle: A case study

The objective of this chapter is to illustrate the effectiveness of the synthesis developed in Chapter 2, with a simple example that captures all the essential features of the general treatment under unilateral constraints. Regulation and tracking problems are explored using output feedback designs and numerical simulations are presented to discuss the performance of the closed-loop system.

4.1 Pendulum-barrier model

A simple testbed of an impacting pendulum is depicted in Fig. 10, where the free motion of the pendulum is confined by the barrier located at the positive vertical axis. For the free-motion dynamics $q \in (0, 2\pi)$, the plant equation reads

$$(ml^2 + J)\ddot{q} = -mgl\sin(q) - k\dot{q} + \tau + w_1 \tag{96}$$

where q is the angle made by the pendulum with the vertical, m is the mass of the pendulum, l is the distance to the center of mass, J is the moment of inertia of the pendulum about the center of mass, g is the gravity acceleration, k is a viscous friction coefficient, τ is the control torque, and w_1 stands for non-modeled external force such as dry friction. For the transition phase at the unstable equilibrium $q = 0$, the restitution rule is given by

$$q^+ = q^-, \quad \dot{q}^+ = -e\dot{q}^- + w_i^d, \quad e \in [0, 1]. \tag{97}$$

The variables $w_i^d,\ i = 1, 2, \dots$ are introduced to account for model inadequacies and restitution uncertainties. A similar velocity restitution occurs at $q = 2\pi$ however for certainty the subsequent local synthesis is confined to the free-motion domain $q \in (0, \pi)$ within the right half-plane.

To address position feedback tracking of a reference trajectory $q^r(t)$, the state error variables

$$x_1 = q - q^r,\ x_2 = \dot{q} - \dot{q}^r \tag{98}$$

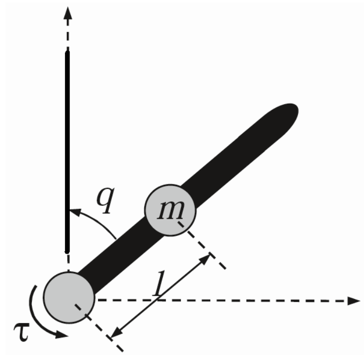

Figure 10: Pendulum-barrier system

and the position measurement

$$y = x_1 + w_0 \tag{99}$$

are involved where w_0 is the measurement noise. Inspired from (44), the pre-feedback control law

$$\tau = (ml^2 + J)\ddot{q}^r + k\dot{q}^r + mgl\sin q^r + (ml^2 + J)u, \tag{100}$$

is composed of a controller u to be designed and the rest being a trajectory compensator. Then, setting $\mathbf{x} = (x_1, x_2)^\top$, $\mathbf{w} = (w_0, w_1)^\top$, and rewriting the system (96)-(100) in terms of the tracking error variables, one derives the free-motion phase error dynamics

$$\dot{\mathbf{x}} = \underbrace{\begin{bmatrix} x_2 \\ -\frac{mgl}{ml^2+J}\sin(x_1 + q^r) - \frac{k}{ml^2+J}x_2 + \frac{mgl}{ml^2+J}\sin(q^r) \end{bmatrix}}_{\mathbf{f}(\mathbf{x},t)} + \underbrace{\begin{bmatrix} 0 & 0 \\ 0 & \frac{1}{m} \end{bmatrix}}_{\mathbf{g}_1} \mathbf{w} + \underbrace{\begin{bmatrix} 0 \\ 1 \end{bmatrix}}_{\mathbf{g}_2} u \tag{101}$$

within the constraint $F_0(\mathbf{x}, t) = x_1 + q^r(t) > 0$, and the transition phase error system

$$\mathbf{x}^+ = \begin{bmatrix} x_1^- \\ \mu_0(\mathbf{x}, t) \end{bmatrix} + \begin{bmatrix} 0 \\ 1 \end{bmatrix} w_i^d \tag{102}$$

on the constraint surface $F_0(\mathbf{x}, t) = x_1 + q^r(t) = 0$ where

$$\mu_0(\mathbf{x}, t) = \begin{cases} x_2 + (1+e)\dot{q}^r & \text{if } F_0(q^r(t)) = 0, \quad F_0(x_1 + q^r) \neq 0 \\ -e(x_2 + \dot{q}^r) - \dot{q}^r & \text{if } F_0(q^r(t)) \neq 0, \quad F_0(x_1 + q^r) = 0 \\ -ex_2 & \text{if } F_0(q^r(t)) = 0, \quad F_0(x_1 + q^r) = 0, \end{cases} \tag{103}$$

is obtained by specifying (34)-(43) to the present case.

In terms of the tracking errors, the variables to be controlled are specified in the form

$$\mathbf{z} = \underbrace{\begin{bmatrix} 0 & 0 \\ \rho_p & 0 \\ 0 & \rho_v \end{bmatrix}}_{\mathbf{h_1}} \mathbf{x} + \underbrace{\begin{bmatrix} 1 \\ 0 \\ 0 \end{bmatrix}}_{\mathbf{D_{12}}} u \tag{104}$$

$$z_i^d = -ex_2^- + w_i^d, \tag{105}$$

complying with (10).

4.2 Output Feedback Regulation

To begin with, the tracking of the pendulum-barrier system is treated in a particular case of the trivial reference trajectory degenerated to the origin $q^r = 0$, $\dot{q}^r = 0$, $\ddot{q}^r = 0$ while the pre-feedback (100) is simplified to the form $\tau = (ml^2 + J)u$ with no trajectory compensation. In this case, the robust regulation to the origin is synthesized in accordance with Theorem 2.2, the applicability of which to the pendulum-barrier error system (101)-(105) is verified as follows.

First, the generic time-invariant terms (53) in the Riccati equations (54)-(55) are specified according to (101)-(105), and then conditions C1) and C2) of Theorem 2.2 are verified by following the well-known iteration procedure (Orlov and Aguilar, 2014, Section 6.2.1). For this purpose, a constant positive semidefinite solution of the corresponding time-invariant equation (54) subject to $\varepsilon = 0$ is obtained by iterating on γ to approach the infimal achievable level $\gamma_{min} \approx 1.01$. The value $\gamma = 2$ is subsequently selected to avoid an undesired high-gain controller design that would appear for a value of γ close to the infimal $\gamma_{min} \approx 1.01$. With $\gamma = 2$, the value $\varepsilon = 0.01$ is determined by iterating on ε to ensure that the corresponding perturbed Riccati equation (54) possesses a constant positive definite solution

$$\mathbf{P}_\varepsilon = \begin{bmatrix} 3.6682 & 0.1020 \\ 0.1020 & 0.7234 \end{bmatrix}, \quad \mathbf{Z}_\varepsilon = \begin{bmatrix} 0.0678 & -0.0027 \\ -0.0027 & 0.3306 \end{bmatrix} \tag{106}$$

which is obtained using MATLAB®.

After that, inequality (63) of Hypothesis H1), required by Theorem 2.2, is straightforwardly verified for the afore-given value $\gamma = 2$.

Finally, to verify Hypothesis H4) of Theorem 2.2, it suffices to note that only scenario T3) is in force for the position feedback regulation. With this in mind, employing (103) yields the following state restitution

$$\begin{bmatrix} x_1^+ \\ x_2^+ \end{bmatrix} = \mu(x_1^-, x_2^-) = \begin{bmatrix} 0 \\ -ex_2^- \end{bmatrix}, \begin{bmatrix} \xi_1^+ \\ \xi_2^+ \end{bmatrix} = \nu(\xi_1^-, \xi_2^-, y) = \begin{bmatrix} 0 \\ -e\xi_2^- \end{bmatrix} \tag{107}$$

in the disturbance-free case when the pendulum touches the constraint $x_1 = 0$. Thus, inequality (14) of Hypothesis H4) is presently simplified to

$$V(\mathbf{x}^-) = P_{22}(x_2^-)^2 \geq P_{22}e^2(x_2^-)^2 = V(\mu(\mathbf{x}^-)) \tag{108}$$

with the quadratic function

$$V(\mathbf{x}, t) = \mathbf{x}^\top \mathbf{P}_\varepsilon \mathbf{x} = \begin{bmatrix} x_1 & x_2 \end{bmatrix} \begin{bmatrix} P_{11} & P_{12} \\ P_{12} & P_{22} \end{bmatrix} \begin{bmatrix} x_1 \\ x_2 \end{bmatrix} = x_1^2 P_{11} + 2P_{12}x_1x_2 + P_{22}x_2^2 \tag{109}$$

specified with (106). Clearly, (108) holds true for any admissible restitution parameter $e \in [0, 1]$, regardless of any positive definite matrix P_ε.

In addition, inequality (15) of Hypothesis H4) is verified by applying the same line of reasoning to the quadratic function

$$\begin{aligned} W(\mathbf{x}, \boldsymbol{\xi}, t) = \gamma^2(\mathbf{x} - \boldsymbol{\xi})^\top \mathbf{Z}_\varepsilon^{-1}(\mathbf{x} - \boldsymbol{\xi}) = \gamma^2 \begin{bmatrix} x_1 - \xi_1 & x_2 - \xi_2 \end{bmatrix} \begin{bmatrix} Y_{11} & Y_{12} \\ Y_{12} & Y_{22} \end{bmatrix} \begin{bmatrix} x_1 - \xi_1 \\ x_2 - \xi_2 \end{bmatrix} \\ = \gamma^2 \left[Y_{11}(x_1 - \xi_1)^2 + 2Y_{12}(x_1 - \xi_1)(x_2 - \xi_2) + Y_{22}(x_2 - \xi_2)^2 \right]. \end{aligned} \tag{110}$$

The resulting inequality (15), specified with (106), (107), (110), and given by

$$\begin{aligned} W(\mathbf{x}^-, \boldsymbol{\xi}^-) = \gamma^2 \left[Y_{11}(x_1^- - \xi_1^-)^2 + 2Y_{12}(x_1^- - \xi_1^-)(x_2^- - \xi_2^-) + Y_{22}(x_2^- - \xi_2^-)^2 \right] \geq \\ \gamma^2 Y_{22} e^2 (x_2^- - \xi_2^-)^2 = W(\boldsymbol{\mu}(\mathbf{x}^-), \boldsymbol{\nu}(\boldsymbol{\xi}^-, \mathbf{y}^-)), \end{aligned} \tag{111}$$

holds true provided that the matrix

$$\begin{bmatrix} Y_{11} & Y_{12} \\ Y_{12} & (1-e^2)Y_{22} \end{bmatrix} \tag{112}$$

is positive definite. Thus, an extra condition

$$(1-e^2)Y_{11}Y_{22} - Y_{12}^2 = 44.6122(1-e^2) - 0.0145 > 0 \tag{113}$$

which is equivalent to

$$e^2 < 0.9997 \tag{114}$$

is to be imposed on the restitution parameter.

Since the corresponding matrix

$$\mathbf{Y} = Z_{\varepsilon}^{-1} = \begin{bmatrix} Y_{11} & Y_{12} \\ Y_{12} & Y_{22} \end{bmatrix} = \begin{bmatrix} 14.7449 & 0.1205 \\ 0.1205 & 3.0256 \end{bmatrix} \tag{115}$$

is positive definite (because $\mathbf{Z}_{\varepsilon}$ is so) inequality (113) is definitely satisfied for the trivial parameter $e = 0$. If however, (114) happens to be invalid for a pre-specified restitution value $e \in (0, 1)$ one should iteratively increase γ until the corresponding relation (114) holds. In the numerical simulations of the next section, the restitution value $e = 0.5$ is pre-specified to meet condition (113), and Theorem 2.2 is then applied to the robust stabilization of the impacting pendulum under the unilateral constraint.

4.2.1 Numerical Results

The performance of the closed-loop system, driven by the controller, designed according to Theorem 2.2, is numerically illustrated in the sequel. The parameters, used in the simulation, are presented in Table 1.

From Fig. 11 that depicts the disturbance-free regulation errors, and the velocity estimation error, escaping to zero, one concludes that the pendulum-barrier system is actually regulated to the barrier. The monotonically decreasing evolution (between and across the

Table 1: Simulation parameters for the regulation problem

Param	Value	Param	Value
g	$9.81\ Nm/s^2$	J	1
k	$1\ N/(rad/s)$	ε	0.01
m	$1\ kg$	l	$1\ m$
e	0.5	w_1	$0.1q_2 + 0.1sign(q_2)\ Nm$
ρ_p	1	w_2	$0.1\sin(1.5t)\ rad$
ρ_v	1	w_i^d	$0.2q_2\ rad/s$
$q(0)$	$1\ rad$	$\dot{q}(0)$	$-0.2\ rad/s$
$\xi_1(0)$	$0.1\ rad$	$\xi_2(0)$	$-0.1\ rad/s$

impacts) of the quadratic Lyapunov function (17), specified with (56), (58) and the Riccati matrices (106), is presented in Fig. 12. Figure 13 shows that while the disturbing friction force w_1, the measurement perturbation w_2 and deviation w_i^d in the restitution coefficient are added to pendulum-barrier testbed (see Table 1 for their numerical values) these disturbances are actually attenuated by the controller designed. In addition, Fig. 14 demonstrates that the output of the system remains bounded to match the $\mathcal{L}_2$-gain inequality (7).

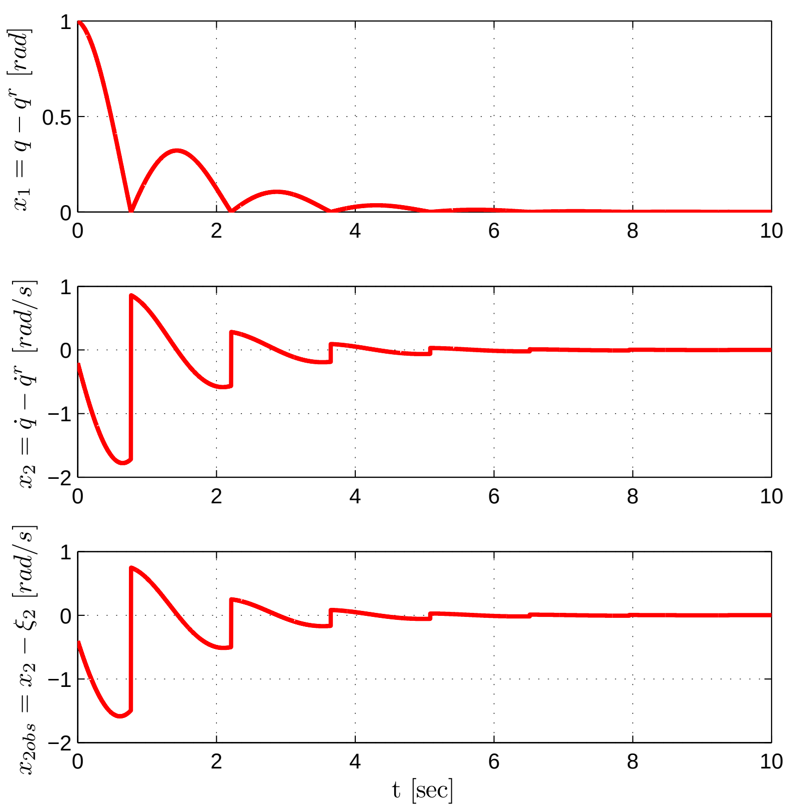

Figure 11: Position and velocity errors for the undisturbed case for the regulation problem.

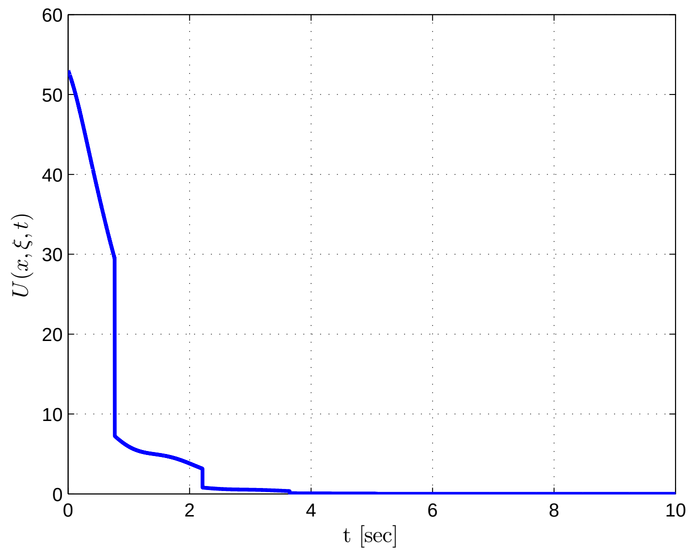

Figure 12: Lyapunov function evolution in the disturbance-free case of the regulation problem.

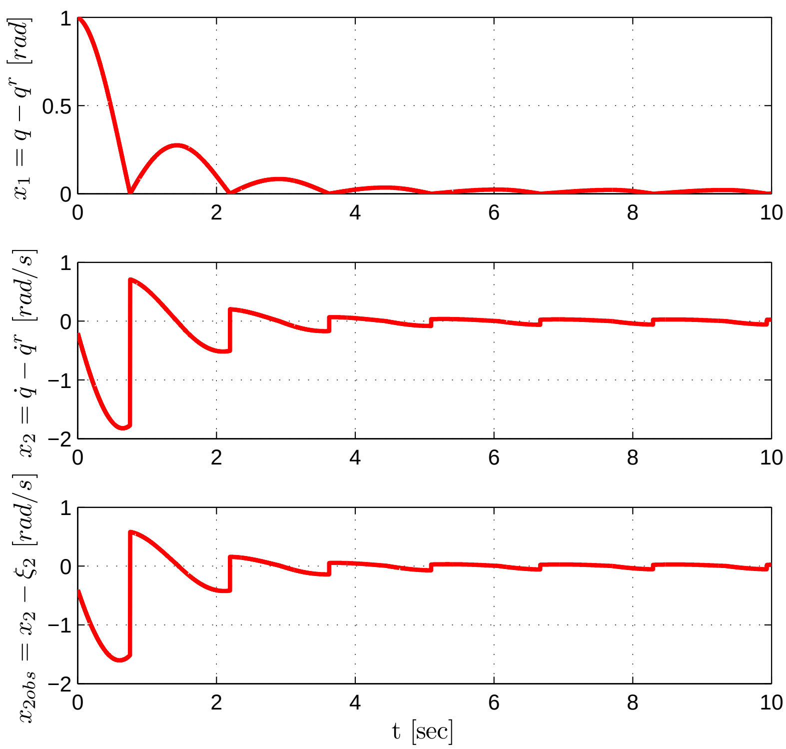

Figure 13: Position and velocity errors for the disturbed case for the regulation problem.

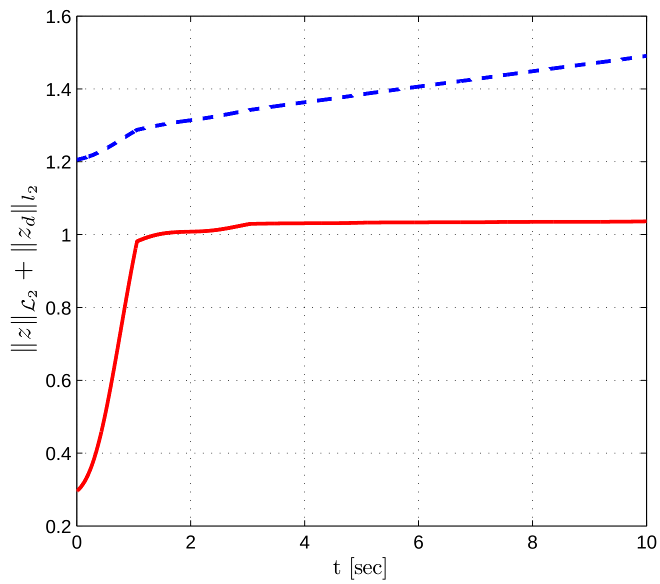

Figure 14: $\mathcal{L}_2$-gain behavior for $\gamma = 2$: $\|z\|^2_{L_2} + \|z^d\|^2_{l_2}$ (solid line) vs. $\gamma^2[\|w\|^2_{L_2} + \|w_i^d\|^2_{l_2}] + \Sigma_{k=0}^{N}\beta_k$ (dashed line).

4.3 Position Feedback Tracking

In the remainder, the $\mathcal{H}_\infty$-orbitally stabilizing output feedback synthesis is developed using a hybrid version of the Van der Pol oscillator, generating a stable limit cycle to follow.

4.3.1 Periodic Trajectory Generation

The periodic trajectory to follow is generated by specifying the hybrid Van der Pol oscillator (80), (83), (84) developed in Chapter 3 as follows:

Free-motion phase ($q^r > 0$)

$$\ddot{q}^r = -\left[(q^r)^2 + (\dot{q}^r)^2 - 1\right]\dot{q}^r - q^r \tag{116}$$

Transition phase ($q^r = 0$)

$$q^r(t_i^+) = q^r(t_i^-), \quad \dot{q}^r(t_i^+) = -e\dot{q}^r(t_i^-) \tag{117}$$

where q^r represents the desired position, $\dot{q}^r$ the velocity, $t_i,\ i = 1, 2, \ldots$ are impact instants when the oscillator hits the constraint $q^r = 0$, and the oscillator parameters have been set to $\varepsilon = 1$, $\mu = 1$ and $\rho = 1$.

Solving the fixed point equation (92) numerically yields

$$\dot{\mathbf{q}}^{r^*} = [1.012]^\top. \tag{118}$$

It follows from the Poincaré analysis of section 3.4 that the hybrid Van der Pol oscillator (116)-(117), initialized in the locally asymptotically stable fixed point (118) of the Poincaré map (92), generates an asymptotically stable limit cycle. Being numerically simulated, this limit cycle proves to be of period

$$T_r = 3.183. \tag{119}$$

4.3.2 Controller Synthesis

The position feedback synthesis is based on Theorem 2.2, which is now applied to the error dynamics (99), (101)-(105), driven by (100), for ensuring robust tracking of the desired trajectory, governed by (116)-(117). By substituting the right-hand side of (116) into (100) for $\ddot{q}^r$, the pre-feedback controller (100), fed by the output of the impact Van der Pol reference model (116)-(117), is represented in the form

$$\tau = (ml^2 + J)[-\left((q^r)^2 + (\dot{q}^r)^2 - 1\right)\dot{q}^r - q^r] + k\dot{q}^r + mgl\sin q^r + (ml^2 + J)u, \tag{120}$$

As to the error restitution rule, it is actually given by (103).

The applicability of Theorem 2.2 to the present case is verified by following the same line of reasoning used in the regulation case. Being coupled to (53), the Riccati equations

(54)-(55) are presently specified with

$$\mathbf{A}(t)=\begin{bmatrix}0 & 1\\ -\frac{mgl}{ml^2+J}\cos(x_1+q^r) & \frac{k}{ml^2+J}\end{bmatrix},\ \mathbf{B_1}(t)=\begin{bmatrix}0 & 0\\ 0 & \frac{1}{ml^2+J}\end{bmatrix},\ \mathbf{B_2}(t)=\begin{bmatrix}0\\ 1\end{bmatrix},$$

$$\mathbf{C_1}(t)=\begin{bmatrix}0 & 0\\ \rho_p & 0\\ 0 & \rho_v\end{bmatrix},\ \mathbf{C_2}(t)=\begin{bmatrix}1 & 0\end{bmatrix}, \tag{121}$$

which are identified from the plant dynamics (101)-(105), (99). In the above relations, the reference trajectory $q_r(t)$ to follow is a periodic function, which is numerically computed on the period time interval $[0, T_r]$ with T_r, given in (119), by solving the hybrid Van der Pol oscillator equations (116)-(117), initialized at the fixed point (118) of the corresponding Poincaré map.

To verify conditions C1) and C2) in the periodic case (see Section 2.3.5 for remarks on the periodicity) a T_r-periodic positive definite solution $\mathbf{P}_\varepsilon(t)$, $\mathbf{Z}_\varepsilon(t)$ of the periodic system (54)-(55) is then derived, by iterating on the initial conditions $\mathbf{P}_\varepsilon(0)$, $\mathbf{Z}_\varepsilon(0),$ for a sufficiently large γ, and for a sufficiently small ε. The following restitution rules

$$\mathbf{P}_\varepsilon(T_r^+)=\begin{bmatrix}P_{11}(T_r^-) & -\frac{1}{e}P_{12}(T_r^-)\\ -\frac{1}{e}P_{12}(T_r^-) & \frac{1}{e^2}P_{22}(T_r^-)\end{bmatrix} \tag{122}$$

$$\mathbf{Z}_\varepsilon(T_r^+)=Y^{-1}(T_r^+)=\begin{bmatrix}Y_{11}(T_r^-) & -\frac{1}{e}Y_{12}(T_r^-)\\ -\frac{1}{e}Y_{12}(T_r^-) & \frac{1}{e^2}Y_{22}(T_r^-)\end{bmatrix}^{-1} \tag{123}$$

are deliberately imposed on such periodic solutions at the period time instant T_r to ensure that the quadratic functions

$$V(\mathbf{x},t) = \mathbf{x}^\top \mathbf{P}_\varepsilon(t)\mathbf{x} = \begin{bmatrix} x_1 & x_2 \end{bmatrix} \begin{bmatrix} P_{11}(t) & P_{12}(t) \\ P_{12}(t) & P_{22}(t) \end{bmatrix} \begin{bmatrix} x_1 \\ x_2 \end{bmatrix} = x_1^2 P_{11}(t) + 2x_1x_2P_{12}(t) + x_2^2 P_{22}(t) \tag{124}$$

$$\begin{aligned} W(\mathbf{x},\boldsymbol{\xi},t) &= \gamma^2(\mathbf{x}-\boldsymbol{\xi})^\top \mathbf{Z}_\varepsilon^{-\mathbf{1}}(\mathbf{t})(\mathbf{x}-\boldsymbol{\xi}) \\ &= \gamma^2 \begin{bmatrix} x_1-\xi_1 & x_2-\xi_2 \end{bmatrix} \begin{bmatrix} Y_{11}(t) & Y_{12}(t) \\ Y_{12}(t) & Y_{22}(t) \end{bmatrix} \begin{bmatrix} x_1-\xi_1 \\ x_2-\xi_2 \end{bmatrix} \\ &= \gamma^2 \left[(x_1-\xi_1)^2 Y_{11}(t) + 2(x_1-\xi_1)(x_2-\xi_2)Y_{12}(t) + (x_2-\xi_2)^2 Y_{22}(t)\right], \end{aligned} \tag{125}$$

computed along the plant trajectories $\mathbf{x}(t), \boldsymbol{\xi}(t)$, remain continuous at $t = T_r$. Indeed, relations (122), (123) ensure the desired continuity properties

$$\begin{aligned} &(x_1^-)^2 P_{11}(t_i^-) + 2(x_1^-)(x_2^-)P_{12}(t_i^-) + (x_2^-)^2 P_{22}(t_i^+) \geq \\ &(x_1^-)^2 P_{11}(t_i^+) - 2e(x_1^-)(x_2^-)P_{12}(t_i^+) + e^2(x_2^-)^2 P_{22}(t_i^+) \end{aligned} \tag{126}$$

$$\begin{aligned} &\gamma^2\left[(x_1^- - \xi_1^-)^2 Y_{11}(t_i^-) + 2(x_1^- - \xi_1^-)(x_2^- - \xi_2^-)Y_{12}(t_i^-) + (x_2^- - \xi_2^-)^2 Y_{22}(t_i^-)\right] \geq \\ &\gamma^2\left[(x_1^- - \xi_1^-)^2 Y_{11}(t_i^-) - 2e(x_1^- - \xi_1^-)(x_2^- - \xi_2^-)Y_{12}(t_i^-) + e^2(x_2^- - \xi_2^-)^2 Y_{22}(t_i^+)\right]. \end{aligned} \tag{127}$$

of the quadratic functions (124), (125), thereby automatically complying with relations (77)-(78) of Hypothesis H4).

By iterating on γ, the infimal achievable level $\gamma_{min} \approx 10$ is approached. The value $\gamma = 15$ is however selected to avoid an undesirable high-gain controller design which would appear for a value of γ close to the optimum $\gamma_{min} \approx 10$. With $\gamma = 15$, the corresponding Riccati equations (54)-(55), specified with (121), and complying with (122), (123), are properly solved with positive definite periodic solutions $\mathbf{P}_\varepsilon$, $\mathbf{Z}_\varepsilon$ under the value $\varepsilon = 0.01$, which is obtained by iterating on ε. These solutions are illustrated in Fig. 15.

After that, the value $\gamma = 15$ is straightforwardly verified to meet Hypothesis H1) with $\omega = 1$, corresponding to the present investigation. Thus, Theorem 2.2 ensures that the underlying closed-loop system possesses $\mathcal{L}_2$-gain less than $\gamma = 15$.

Since the impact instants of the reference trajectory are not in general synchronized with the plant impact instants (unless the reference initial state coincides with that of the

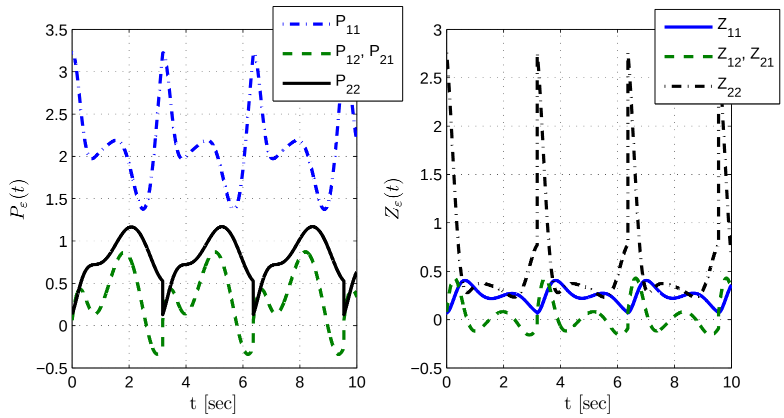

Figure 15: Plot of the periodic, positive definite and symmetric solutions of the Riccati equations (54)**-**(55)**.**

plant), any of the three scenarios T1)-T3) may occur according to the adopted state error restitution rule (103). Therefore, Hypothesis H4) is generally ruled out by the resulting synthesis which proves to be incapable to asymptotically stabilize the closed-loop system, even in the disturbance-free case as is well-known from Biemond *et al.* (2013). Nevertheless, the proposed controller does attenuate external disturbances, restitution uncertainties, and measurement noise as established by Theorem 2.2 before, and while being numerically tested, the performance of the closed-loop system is observed to be acceptable.

4.3.3 Numerical results

The simulation results, shown in Figs. 16-20, were performed under the same circumstances of Section 4.2.1, using the parameters from Table 1 and additional parameters from Table 2, where it can be noticed that the reference trajectory is initialized on the limit cycle. The disturbance-free case is presented in Figs. 16-18. These figures exhibit peaking phenomena since the plant velocity jumps do not match the reference velocity jumps (as clearly observed in Fig. 17), thus falling into either Scenario T1 or T2 of Section 2.3.1. The Lyapunov candidate function (17), specified with (56), (58), and the solutions $\mathbf{P}_\varepsilon$, $\mathbf{Z}_\varepsilon$, is thus monotonically decreasing just between impacts while exhibiting undesired increments at the impact time instants (see Fig. 18), and the asymptotic stability proof is no longer applicable to the disturbance-free case under both Scenarios T1 and T2. Despite the discrepancy in the impact instants of the plant velocity and of the reference

Table 2: Simulation parameters for the tracking problem

Param	Value	Param	Value
$q(0)$	$0.1\ rad$	$\dot{q}(0)$	$-0.1\ rad/s$
$\xi_1(0)$	$0.1\ rad$	$\xi_2(0)$	$0.1\ rad/s$
$q^r(0)$	$0\ rad$	$\dot{q}^r(0)$	$1.012\ rad/s$

velocity, the $\mathcal{L}_2$-gain inequality (7) is still guaranteed by Theorem 2.2, and good behavior of the closed-loop system with the tracking errors, approaching zero between the impact instants, is concluded from Fig. 16 in the disturbance-free case. From Figs. 19 and 20, good performance is also concluded for the periodic tracking synthesis despite the added disturbances, affecting the free-motion (due to friction), and transition phases (due to uncertainty in the restitution coefficient).

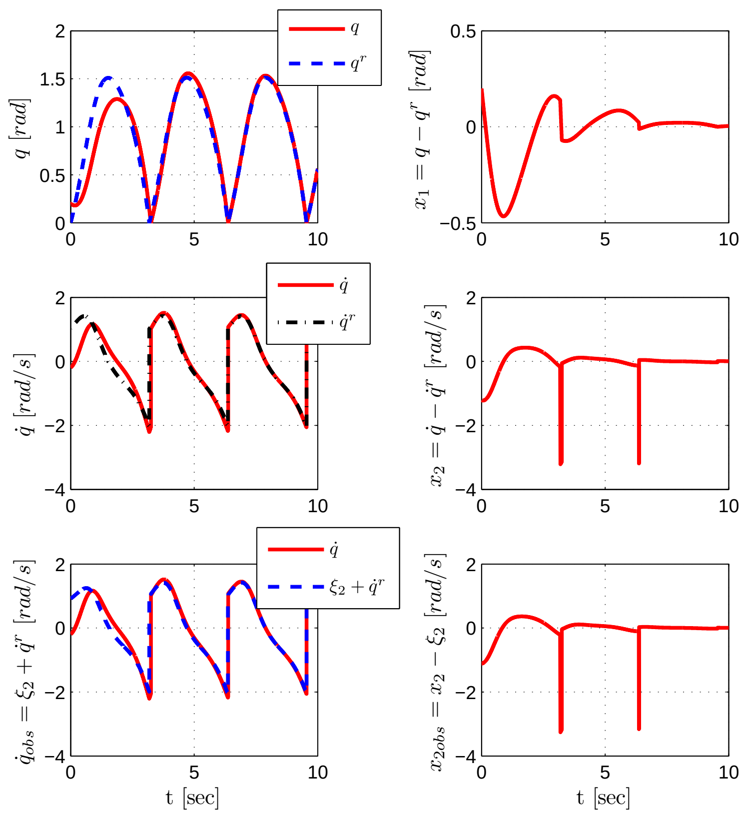

Figure 16: Plots of the position, plant velocity, estimated velocity, tracking errors, and velocity estimation error in the disturbance-free case.

Finally, the estimated velocity $\dot{q}_{obs} = \xi_2 + \dot{q}^r$, and the observation error $x_{2obs} := x_2 - \xi_2$, are compared in Figs. 16 and 19 for the disturbed and undisturbed cases, respectively. One can observe that if disturbances are not applied, the filter adequately tracks the system velocity between the impact times (Fig. 16), whereas a reasonably small observation

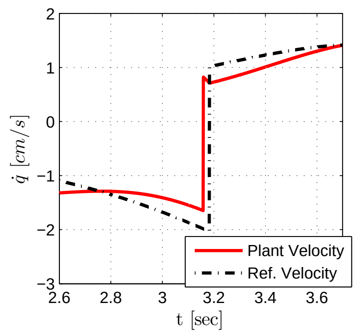

Figure 17: Desynchronization of the reference trajectory with the plant trajectory for the undisturbed case.

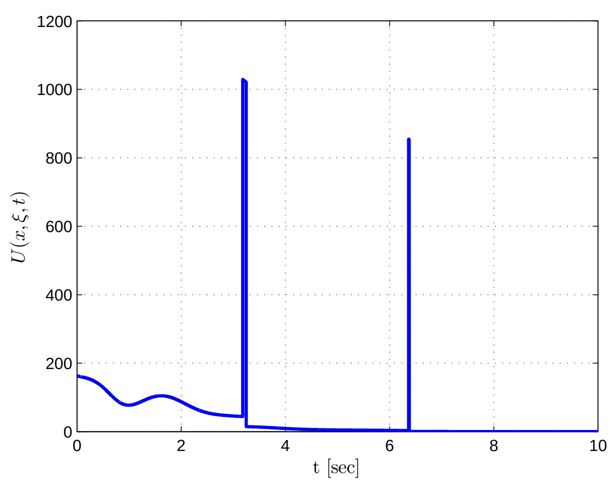

Figure 18: Lyapunov function evolution in the disturbance-free case of the desynchronized tracking.

error persists in the disturbed case (Fig. 19), such that good tracking performance is achieved.

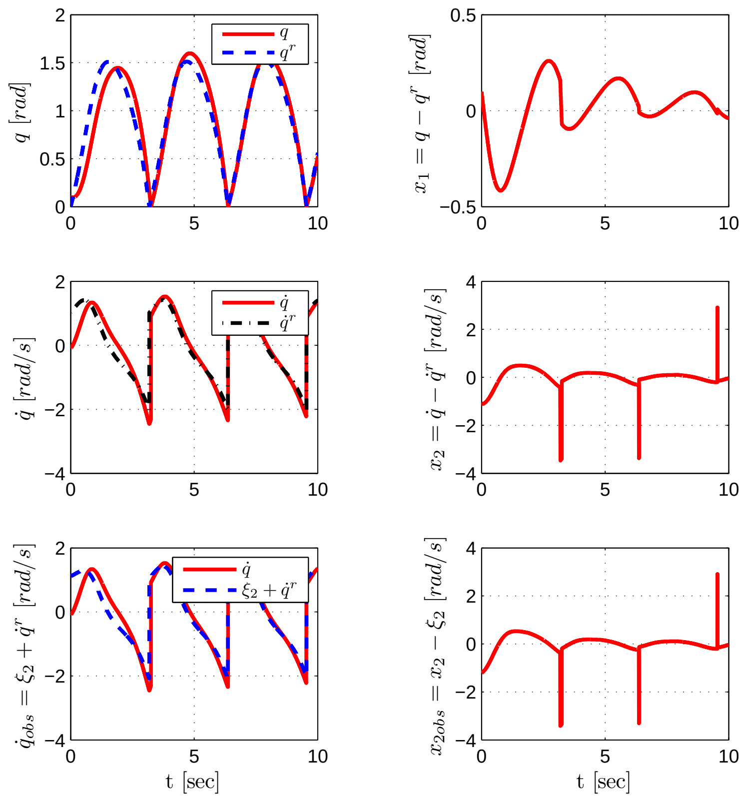

Figure 19: Plots of the position, plant velocity, estimated velocity, tracking errors, and velocity estimation error for the disturbed case.

4.3.4 Impact Synchronization via Online Reference Model Reset

The results of section 4.3.3 clearly exemplify that in hybrid systems with state-triggered jumps, the jump times of the plant and the reference trajectory are in general not coinciding. During the time interval caused by this jump-time mismatch, the tracking error is large, even in the undisturbed case, as shown in Fig. 16. Since this behavior also occurs for arbitrarily small initial errors, the error dynamic displays unstable behavior in the sense of Lyapunov, as illustrated by Fig. 18. This is behavior is known in the literature as ”peaking”. It is expected to occur in all hybrid systems with state-triggered jumps when considering tracking or observer design problems (Biemond *et al.*, 2013), and imposes a difficulty in guaranteeing that the norm of the tracking error converges to zero. This prob-

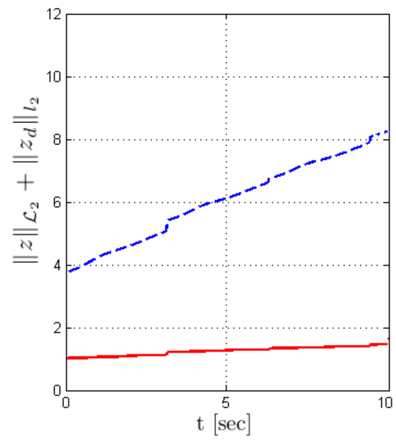

Figure 20: $\mathcal{L}_2$-gain behavior without online reference model reset: $\|z\|^2_{L_2} + \|z^d\|^2_{l_2}$ (solid line) vs. $\gamma^2[\|w\|^2_{L_2} + \|w_i^d\|^2_{l_2}] + \Sigma_{k=0}^{N}\beta_k$ (dashed line) with $\gamma = 2$.

lem has been tackled by Biemond *et al.* (2013) by formulating a different notion of tracking, that considers the behavior shown in Fig. 16 as a proper solution, since the jump times of the plant converge to the jump times of the reference and the distance between the plant and reference trajectories converges to zero during time intervals without jumps. In (Robles and Sanfelice, 2011) the authors consider an exosystem generating the reference trajectory with jumps and force the impact instants of the reference trajectory and the plant to occur at the same time. In (Sanfelice *et al.*, 2014), inspired by the idea of treating time in time-varying systems as a state, the authors embed the given reference trajectory into an extended hybrid system, imposing conditions on the state representing tracking of the given reference trajectory.

In this work, to suppress the peaking phenomena, depicted in Fig. 16 which destroys the asymptotic stability of the disturbance-free closed loop system, the reference model is now reset online, as it is shown in the block-diagram of Fig. 21. The idea behind such a reset is in using the same hybrid Van der Pol reference model of Section 4.3.1, but instead of using its own unilateral constraint $q^r = 0$, the reset event is synchronized with the impact of the plant ($q = 0$), so as to generate an asymptotically-stable limit cycle on the resulting full order dynamics. Thus, the restitution law (117) is modified to

$$q^r(t_i^+) = 0, \quad \dot{q}^r(t_i^+) = -e\dot{q}^r(t_i^-), \quad \text{if and only if } q(t_i) = 0. \tag{128}$$

The pre-feedback controller (120), and the same controller u, synthesized in Section 4.3.2, are now coupled to the Van der Pol reference model, thus modified. Hypotheses H1) - H3) hold, and it remains to show that H4) is additionally satisfied in the present case. Since the reference trajectory is reset when the plant hits the constraint, Scenario T3 is now in order, and due to (103), the error transition phase is governed by $x_2^+ = -ex_2^-$. Since the solutions of (54)-(55) are chosen to comply with the boundary conditions (77)-(78), H4) is thus established with V and W, specified in (56) and (58), respectively. This verifies the applicability of Theorem 2.2, by virtue of which, the properly specified dynamical controller (62) enforces the disturbance-free pendulum-barrier system to asymptotically track the reference trajectory while also attenuating external disturbances.

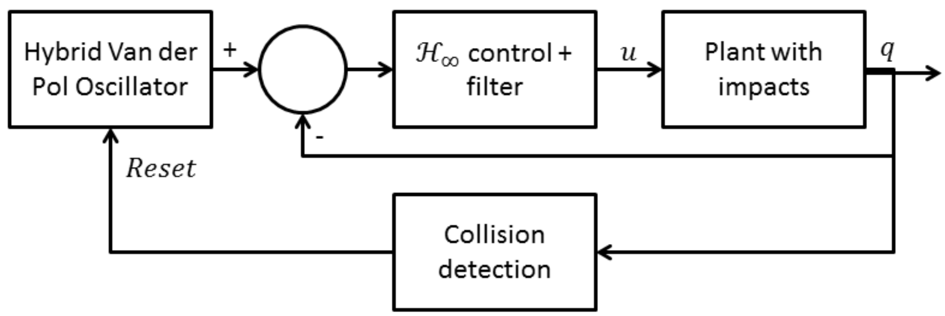

Figure 21: Block-diagram of online Van der Pol reference model reset

.

To demonstrate that the closed-loop system (62), (96), (97), (116), (128), generates an asymptotically-stable limit cycle, the Poincaré analysis of Section 3.4 is revisited, using the Poincaré map

$$\tilde{\Gamma}(\zeta_k) = \zeta_{k+1} \tag{129}$$

associated with the Poincaré section $q = 0$, while considering the post-impact values $\zeta_k = [q_k, \dot{q}_k, \xi_k, q_k^r, \dot{q}_k^r]$ at the impact instants t_k, $k = 1, 2, \ldots$. The fixed point

$$\zeta^* = [0, 1.012, 0, 0, 0, 1.012]$$

of the Poincaré map $\tilde{\Gamma}$ and the eigenvalues

$$eig(\nabla\tilde{\Gamma}) = [0, 0.6961, 0, 0.0045, 0, -0.7706] \tag{130}$$

of the gradient $\nabla\tilde{\Gamma}$ around the fixed point are numerically computed. The asymptotic stability of the limit cycle, matching to the fixed point of the Poincaré map $\tilde{\Gamma}$, is then established

Table 3: Simulation parameters for the tracking problem with impact synchronization

Param	Value	Param	Value
$q(0)$	$0.1\ rad$	$\dot{q}(0)$	$-0.2\ rad/s$
$\xi_1(0)$	$0.1\ rad$	$\xi_2(0)$	$-0.1\ rad/s$
$q^r(0)$	$0.2\ rad$	$\dot{q}^r(0)$	$1.5\ rad/s$

by observing that eigenvalues (130) of the gradient $\nabla\tilde{\Gamma}$ are inside of the unit circle.

4.3.4.1 Numerical results

Figures 22-26 demonstrate the numerical results performed using the parameters of Tables 1 and 3, while the synthesized tracking controller is coupled to the Van der Pol reference model, whose online reset adaptation is synchronized with the plant impacts, and is initialized at a value outside of the limit cycle. It can be seen from Fig. 22 that in the disturbance-free case, the position, velocity, and estimation errors, tend to zero. The asymptotic stability of the origin of the closed-loop system can additionally be observed from Fig. 23, where the plotted Lyapunov function (17), specified with (56), (58), and the solutions $\mathbf{P}_\varepsilon$, $\mathbf{Z}_\varepsilon$, monotonically goes to zero. The asymptotic stability of the limit cycle, theoretically predicted by the Poincaré analysis, is illustrated in Fig. 24, where the plant trajectory (dashed line) converges to a periodic orbit (solid line).

The simulations, performed in the disturbed case, are reflected in Fig. 25 that depicts the plots of the position and velocity tracking errors as well as the plot of the velocity estimation error. It is seen that after the transitory, the errors remain small and bounded. As seen in Fig. 26, this ensures that the plant trajectory evolves around the periodic orbit.

It is worth noticing that in both disturbed and undisturbed cases, the peaking phenomena depicted in the error plots of Fig. 16, which coincide with the desynchronized impact instants of the plant and of the reference model, disappear from the velocity tracking and velocity estimation errors of Figs. 22 and 25, where the reference model resets are synchronized with the plant impact instants. Thus, the superiority of the synthesis with the online reference model reset adaptation is concluded.

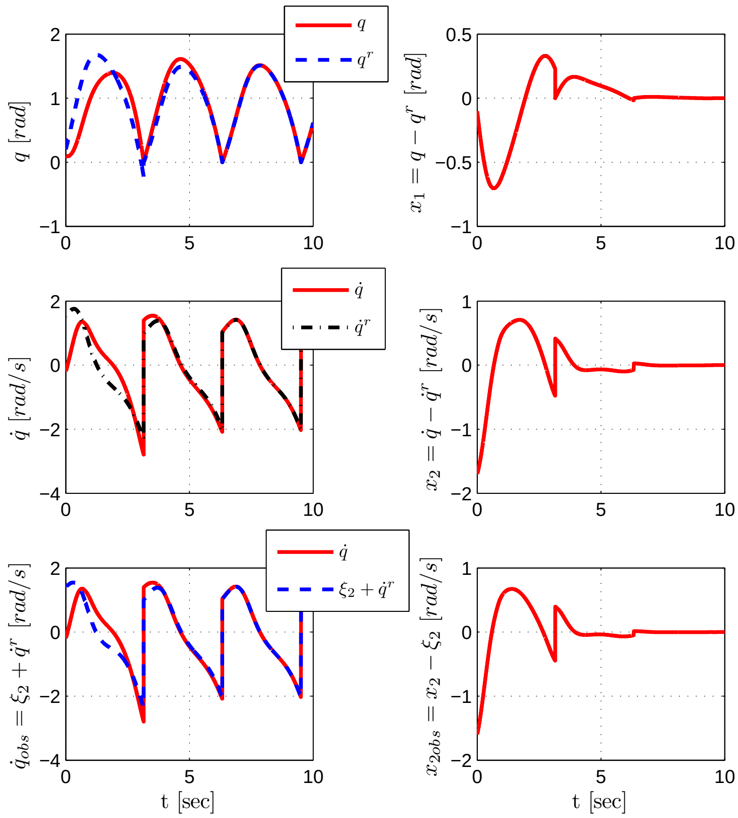

Figure 22: Plots of the position, plant velocity, estimated velocity, tracking errors, and velocity estimation error in the disturbance-free case when the online reset adaptation of the Van der Pol reference model is enforced.

.

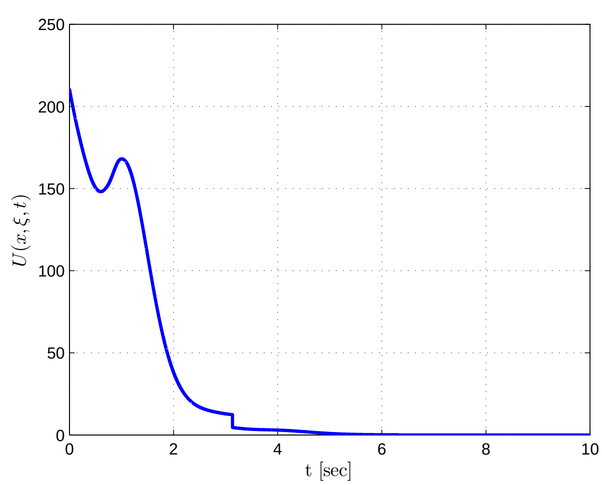

Figure 23: Lyapunov function evolution in the disturbance-free case of the synchronized tracking.

.

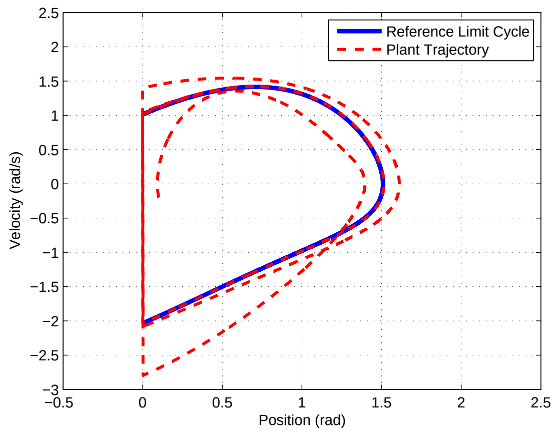

Figure 24: Limit cycle of the synchronized impact Van der Pol Oscillator and a closed-loop plant trajectory, approaching it: the disturbance-free case

.

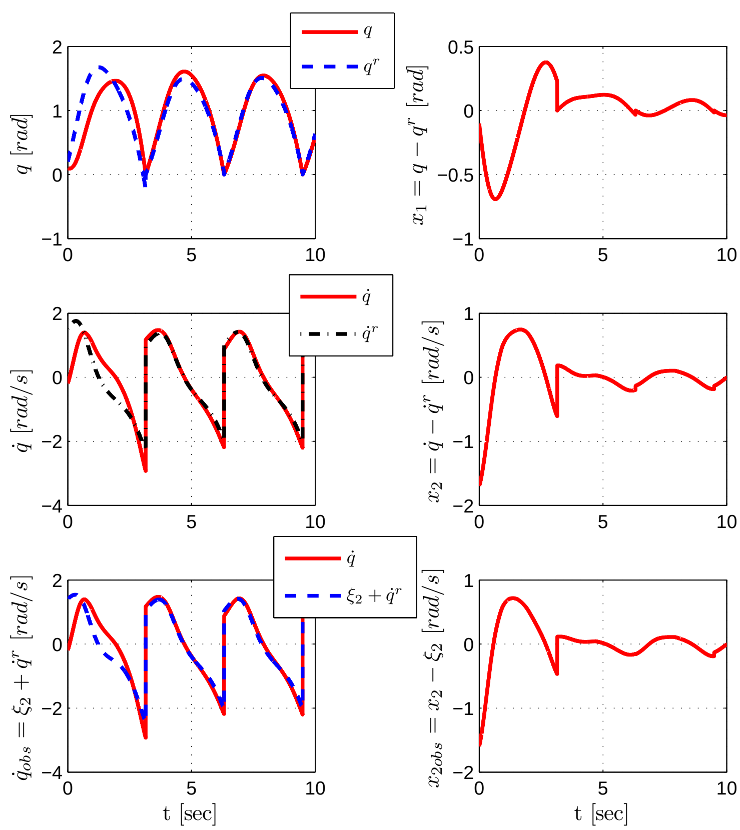

Figure 25: Plots of the position, plant velocity, estimated velocity, tracking errors, and velocity estimation error in the disturbed case when the reference model is reset online.

.

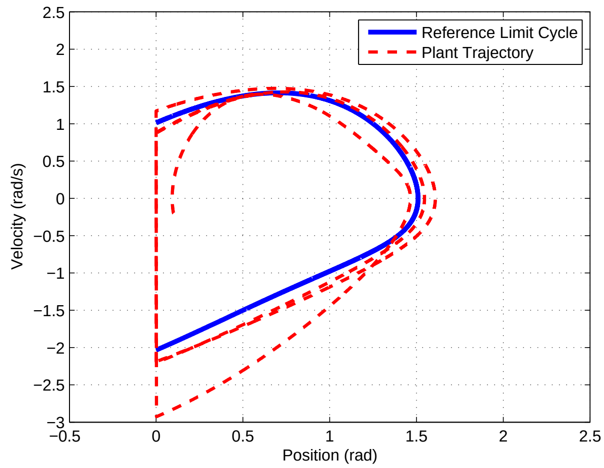

Figure 26: Limit cycle of the synchronized impact Van der Pol Oscillator and a closed-loop plant trajectory, evolving around it in the presence of disturbances.

4.4 Conclusions

In this chapter, the effectiveness of the design procedure developed so far is supported in the numerical study made for a benchmark (pendulum-barrier) system. The reference trajectory to follow is generated by an impact Van der Pol oscillator, possessing an asymptotically-stable limit cycle. The desired disturbance attenuation is satisfactorily achieved under external disturbances during the free-motion phase, and in the presence of uncertainties in the transition phase. An online reference-model reset adaptation is additionally applied so as to synchronize the impacts of the plant with those of the reference model, thereby enhancing the performance of the closed-loop system.

Chapter 5. Periodic Locomotion of Biped with Feet

Theoretical results developed so far are now supported in the numerical study made for the robust trajectory tracking of a seven-link bipedal robot with feet, and a 32-DOF fully-actuated biped robot. The capabilities of the $\mathcal{H}_\infty$ tracking controller are illustrated with a simulation study, and a trajectory adaptation method is proposed to guarantee asymptotic stability of the closed-loop system.

5.1 Trajectory Tracking of a Planar Biped with Feet

The bipedal robot considered in this section is walking on a rigid and horizontal surface. It is modeled as a planar biped, which consists of a torso, hips, two legs with knees and feet. The walking gait takes place in the sagittal plane and is composed of single support phases and impacts which occur between two rigid bodies (see Chevallereau *et al.* (2003) for more details).

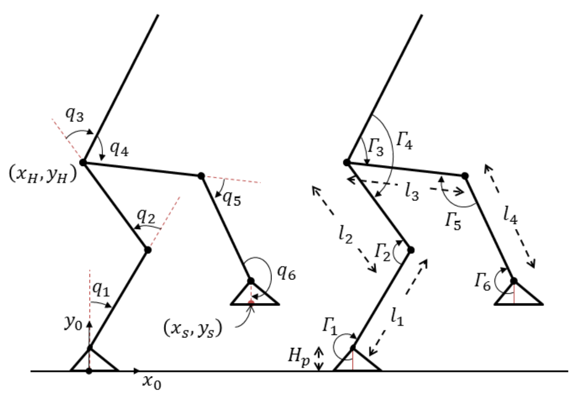

Figure 27: Seven-link bipedal robot

5.1.1 Dynamic Model in Single Support

The dynamic model of the biped, can be written as follows (Hurmuzlu *et al.*, 2004):

$$\mathbf{D_e}(\mathbf{q_e})\ddot{\mathbf{q}}_\mathbf{e} + \mathbf{C_e}(\mathbf{q_e}, \dot{\mathbf{q}}_\mathbf{e}) + \mathbf{G_e}(\mathbf{q_e}) = \mathbf{D}_{\mathbf{e}\boldsymbol{\tau}}\boldsymbol{\tau} + \mathbf{J}^\top \begin{pmatrix} \mathbf{R_1} \\ \mathbf{R_2} \end{pmatrix} + \mathbf{D_w}\mathbf{w_1} \tag{131}$$

with $\mathbf{J} = (\mathbf{J_1}, \mathbf{J_2})^\top$, the complementarity condition

$$0 \leq F(\mathbf{q_e}) \perp \mathbf{R_2} \geq \mathbf{0} \tag{132}$$

and the constraint equations

$$\mathbf{J_i}\ddot{\mathbf{q}}_\mathbf{e} + \dot{\mathbf{J}}_\mathbf{i}\dot{\mathbf{q}}_\mathbf{e} = \mathbf{0}, \text{ for } \text{ i} = 1 \text{ to } 2 \tag{133}$$

where $\mathbf{q_e} = (q_1, q_2, q_3, q_4, q_5, q_{p_1}, q_{p_2}, x_H, y_H)^\top$ the 9×1 vector of generalized coordinates, $\mathbf{D_e}$ is the symmetric, positive definite 9×9 inertia matrix, $\mathbf{D_{e\tau}}$ and $\mathbf{D_w}$ are 9×6 constant matrices composed of zeros and ones, and $\boldsymbol{\tau} = (\tau_1, \tau_2, \tau_3, \tau_4, \tau_{p_1}, \tau_{p_2})^\top$ is the 6×1 vector of joint torques (see figure 27). Term $\mathbf{C_e}(\mathbf{q_e}, \dot{\mathbf{q}}_\mathbf{e})$ is the 9×1 vector of centrifugal and Coriolis forces, while $\mathbf{G_e}(\mathbf{q_e})$ is the 9×1 vector of gravity forces; $\mathbf{R_1}$ and $\mathbf{R_2}$ represent the reaction forces on foot 1 and foot 2, respectively, while $\mathbf{J_1}$ and $\mathbf{J_2}$ are 3×9 Jacobian matrices converting these efforts to the corresponding joint torques, and $\mathbf{w_1}$ is the 6×1 vector of external disturbances. Equations (131)-(132), in addittion to a restitution law to be defined later, form a Lagrangian Complementarity System, which can be interpreted as a specific class of hybrid dynamical systems (for more information about of this class of dynamical systems, see the work by Heemels and Brogliato (2003) and the references cited therein).

In the single support phase, considering a flat foot contact of the stance foot with the ground (i.e. there is no take off, no rotation, and no sliding during this phase), there exists the orthogonal matrix $\mathbf{J}^\perp$ (6×9), such that left multiplying it by (131) we obtain

$$\mathbf{D}(\mathbf{q})\ddot{\mathbf{q}} + \mathbf{H}(\mathbf{q}, \dot{\mathbf{q}}) = \mathbf{D}_\tau \boldsymbol{\tau} + \mathbf{w_1} \tag{134}$$

where $\mathbf{q} = (q_1, q_2, q_3, q_4, q_5, q_6)^\top$ the 6×1 vector of generalized coordinates, $\mathbf{D}$ is the symmetric, positive definite 6×6 inertia matrix, $\mathbf{D}_\tau$ is a 6×6 constant and nonsingular matrix; $\boldsymbol{\tau} = (\boldsymbol{\tau}_1, \boldsymbol{\tau}_2, \boldsymbol{\tau}_3, \boldsymbol{\tau}_4, \boldsymbol{\tau}_5, \boldsymbol{\tau}_6)^\top$ is the 6×1 vector of joint torques (see Fig. 27); the term $\mathbf{H}(\mathbf{q}, \dot{\mathbf{q}})$ is the 6×1 vector of the centrifugal, Coriolis and gravity forces; and $\mathbf{w_1}$ is the 6×1 vector of external disturbances. Also, assuming an instanteneous impact, a switching of the swing leg and the support leg is made, so (134) holds throughout the walking gait; in this sense, the coordinate q_6 represents q_{p1} or q_{p2}, depending on the support leg. This kind of switching is not new, and can be seen in the literature (see for example Djoudi *et al.*

(2005) and Hurmuzlu *et al.* (2004)).

To validate that (134) is an appropriate representation of the biped during the single support phase, it is necessary to verify the following conditions (Djoudi *et al.*, 2005):

1. To ensure that there is no take-off of the support foot, the normal component of the force reaction exerted by the ground must be positive only, that is

$$R_{1x} > 0$$

2. To ensure that the support feet does not slide, the tangential force must be inside the friction cone, that is

$$-\mu R_{1z} < R_{1x} < \mu R_{1z}$$

   where μ represents the positive friction coefficient.

3. To ensure the no rotation of the support foot, the Zero Moment Point (ZMP), defined as that point on the ground at which the net moment of the inertial forces and the gravity forces has no component along the horizontal axes (Vukobratović and Borovac, 2004), should rest inside the support foot sole.

These conditions are verified during the numerical study using model (131). If at least one of these conditions is not satisfied, the conditions to construct (134) are not met and thus it is not valid. Thus, the reference trajectories are designed taking these conditions as restrictions.

5.1.2 Impact Model

Now, assuming a flat foot contact of the swing foot with the ground, the double support phase is instantaneous, and it can be modeled through passive impact equations, that is, impulsive torques are applied in the interlink joints (Formalskii, 2009). An impact appears at a time $t = T_I$ when the swing leg touches the ground.

To simplify the analysis, we shall make the reasonable assumptions that the impact is passive, absolutely inelastic, and that the legs do not slip (Tlalolini *et al.*, 2010), so the following equations:

$$\mathbf{J_1}\dot{\mathbf{q}}_{\mathbf{e}}^{-} = \mathbf{0} \tag{135}$$

$$\mathbf{J_2}\dot{\mathbf{q}}_{\mathbf{e}}^{+} = \mathbf{0} \tag{136}$$

hold. This means that the feet perfectly stick on the ground after the shock, thus avoiding multiple impacts. Given these conditions, the ground reactions can be viewed as impulsive forces. The algebraic equations allowing one to compute the jumps of the velocities, can be obtained through integration of the dynamic equations of the motion, taking into account the ground reactions during an infinitesimal time interval from T_I^- to T_I^+ around an instantaneous impact. The torques supplied by the actuators at the joints, the centrifugal, Coriolis, and gravity forces have finite values, thus not influencing an impact.

The impact is assumed to be with complete surface of the foot sole touching the ground. This means that the velocity of the swing foot impacting the ground is zero after impact. After an impact, the right foot (previous stance foot) takes off the ground, so the vertical component of the velocity of the taking-off foot must be directed upwards right after an impact, and the impulsive ground reaction in this foot is equal to zero. Thus, the impact dynamic model can be represented as follows (Haq *et al.*, 2012):

$$\begin{aligned} \dot{\mathbf{q}}_{\mathbf{e}}^{+} =& (\mathbf{I} - \mathbf{D}_{\mathbf{e}}^{-1}\mathbf{J}_{\mathbf{2}}^{\top}(\mathbf{J_2}\mathbf{D}_{\mathbf{e}}^{-1}\mathbf{J}_{\mathbf{2}}^{\top})^{-1}\mathbf{J_2})\dot{\mathbf{q}}_{\mathbf{e}}^{-} + \mathbf{w}_{\mathbf{ei}}^{\mathbf{d}} \\ \dot{\mathbf{q}_e^{+}} =& \phi_e(\mathbf{q_e})\dot{\mathbf{q}_e^{-}} + \mathbf{w}_{\mathbf{ei}}^{\mathbf{d}} \end{aligned} \tag{137}$$

where $\dot{\mathbf{q}}_{\mathbf{e}}^{-}$ is the velocity of the robot before the impact and $\dot{\mathbf{q}}_{\mathbf{e}}^{+}$ is the velocity after the impact; $\phi_e(\mathbf{q_e})$ represents a restitution law that determines the relations between the velocities before and after the impacts; $\mathbf{q_e}$ is the configuration of the robot at the impact instant. The additive term $\mathbf{w}_{\mathbf{ei}}^{\mathbf{d}}$ is introduced to account for inadequacies in this restitution law. Thus, equation (137) renders the complementarity system (131)-(136) complete.

Considering $\dot{q}_{p1}^{-} = 0$, $\dot{q}_{p2}^{+} = 0$, and combining (135)-(137), it is possible to pre-multiply (137) by $\mathbf{J}^{\perp}$ so as to obtain the following expression:

$$\dot{\mathbf{q}}^{+} = \phi(\mathbf{q})\dot{\mathbf{q}}^{-} + \mathbf{w}_{\mathbf{i}}^{\mathbf{d}} \tag{138}$$

Also, considering the reference frame x_0, y_0 shown in Fig. 27, and since we are assuming flat foot contact with the ground, the time-invariant unilateral constraint $F_0(\mathbf{q}) \geq 0$ is determined by the height of the swing foot's sole (point (x_s, y_s) in Fig. 27) being represented as a function of the generalized coordinates of the implicit-contact model (134):

$$\begin{aligned} F_0(\mathbf{q}) = H_p + l_1\cos(q_1) + l_2\cos(q_1+q_2) - l_3\cos(q_1+q_2+q_3+q_4) - \\ l_4\cos(q_1+q_2+q_3+q_4+q_5) + H_p\cos(q_1+q_2+q_3+q_4+q_5+q_6) \end{aligned} \tag{139}$$

With all the assumptions taken above, equations (134), (138), (139) define a hybrid model that falls directly into our studied setting.

A specific trajectory design, which is invoked to generate a desired cyclic motion of the biped, is explained next.

5.1.3 Periodic Motion Planning

Using an off-line optimization (Haq *et al.*, 2012), the walking gait, which is composed of single support phases and impacts, is determined by the reference trajectory whose position $\mathbf{q}^{\mathrm{r}}(t)$, and velocity $\dot{\mathbf{q}}^{\mathrm{r}}(t)$, satisfy the conditions of contact.

The control task is to drive the biped in such a manner that each joint angle follows its own reference trajectory. According to the adopted off-line optimization (Haq *et al.*, 2012), the periodic reference minimizes the integral of the norm of the torque vector for a given distance. For the underlying biped with the parameters drawn from Haq *et al.* (2012), the walking velocity was selected to be $0.5\ m/s$ with the duration of one step being chosen $0.53\ s$. Since the impact is instantaneous and passive, the controller acts during the single support phase only. The restitution law of this reference trajectory is governed by (34).

5.1.4 Numerical Study

The proposed synthesis is further tested on the seven-link biped emulator, constructed in Haq *et al.* (2012), where the well-known constraint (complementarity)-based approach (Rengifo *et al.*, 2011; Acary and Brogliato, 2008; Brogliato, 2000) is utilized to simulate the biped contact with the ground. The latter approach belongs to the family of time-stepping approaches and it is often invoked for biped dynamics simulations (see, e.g., the works by Van Zutven *et al.* (2010); Hurmuzlu *et al.* (2004); Yunt and Glocker (2005)). To simulate a discrete disturbance, the velocities after an impact occurs are modified $5\ \%$ from the values given by the restitution rule (29), thus representing uncertainty on this rule.

5.1.4.1 State Feedback $\mathcal{H}_\infty$ Tracking Control Synthesis Using Reference Trajectory Adaptation

The reference trajectory tracking synthesis of Sect. 2.3, being applied to the seven-link biped, is first tested under the complete knowledge of the state vector. To respect Condition C1 of Theorem 2.3 for the error system (65), the controlled output (31) is specified with $\rho_p = 500$ and $\rho_v = 1$, and then, following the standard $\mathcal{H}_\infty$ design procedure (see, e.g., (Orlov and Aguilar, 2014, Section 6.2.1)), the disturbance attenuation level, and the perturbation parameter, are set to $\gamma = 470$ and $\epsilon = 0.01$ to ensure an appropriate solvability of the perturbed differential Riccati equation (54), corresponding to (53), (66)-(67). Next, hypothesis H1) of Theorem 2.3 is then straightforwardly verified with γ, thus specified, and with $\boldsymbol{\omega}$, being an identity matrix. Finally, to comply with the last condition of Theorem 2.3 (inequality (14) of Section 2.2.1) to be verified at the impact time instants, the reference trajectory, designed in section 5.1.3, is adapted on-line in such a manner that the state error dynamics possess no jumps. Thus, inequality (14) becomes redundant for the adapted trajectory because only trivial transitions with $\boldsymbol{\mu}_{\mathbf{0}}(\mathbf{x},t) = 0$ are feasible in accordance with Scenario 3 of Section 2.3.1.

The importance of the synchronization of impacts between the plant and the reference trajectory, for mechanical systems under unilateral constraints, has been explained in Section 4.3.4. This synchronization is achieved in our biped application by adapting the reference trajectory, as illustrated in Fig.28 for the first joint q_1. Provided that the impact is detectable (e.g., by using a force or touch sensor) it happens that either the reference trajectory hits the constraint before the plant does, or the plant hits the constraint before the reference trajectory does. In the former scenario, the reference trajectory is continuously extrapolated until the plant collision occurs whereas in the latter scenario, the reference

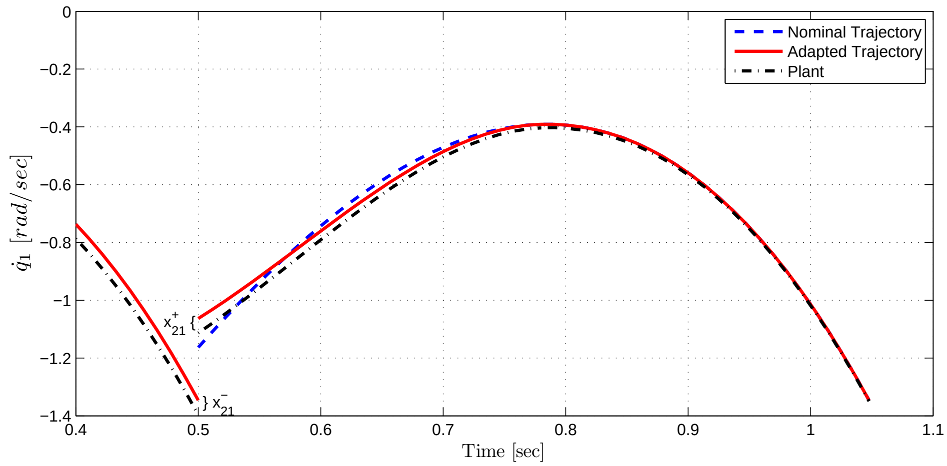

Figure 28: Reference velocity adaptation for the first joint, with an impact at $t^l = 0.5$. After the impact, the initial value of the adapted velocity is such that the pre-impact ($x_{21}(t^l-) = \dot{q}_1(t^l-) - \dot{q}_1^r(t^l-)$) and post-impact ($x_{21}(t^l+) = \dot{q}_1(t^l+) - \dot{q}_1^r(t^l+)$) tracking errors are the same, and at the middle of the step, the adapted reference velocity reaches the nominal one.

trajectory is restarted on-line once the plant collision is detected. Either way, both the plant trajectory and the adapted reference trajectory exhibit impacts at the same time instants. By adaptation, the nominal reference trajectory, and the adapted one, are equivalent before a collision. The position and velocity tracking errors are measured, and once the impact of the plant is detected, the adapted trajectory is updated on-line in such a manner that the new post-impact error, x_{21}^{+} in Fig.28, coincides with the error measured before the impact ($x_{21}(t^l-)$ in Fig.28), thereby rendering the evolution of the error to exhibit no jump. Following the idea of Grishin *et al.* (1994), a new polynomial is defined for the adapted trajectory, that starts from this imposed condition, and will join the nominal reference trajectory at the middle of the step with the same velocity, and will continue to be the same until the end of the step. While the reference trajectory is recalculated after the impact, the perturbed differential Riccati equation (54) is also updated, and its corresponding solution is recomputed on-line.

5.1.4.2 Numerical Results

To illustrate the performance issues of the developed stable bipedal gait synthesis, numerical simulations were performed for a laboratory prototype whose parameters were drawn from Haq *et al.* (2012). The contact constraints presented in Section 5.2.1 were verified on-line so as to confirm the validity of (26)-(30).

The undisturbed system was then simulated, using initial conditions different from zero:

$$\mathbf{q_0} =[0.1962, 0.2262, -0.0766, -0.1337, -0.1661, 0.0500]^\top$$
$$\dot{\mathbf{q}}_\mathbf{0} =[-1.0633, -0.6369, 0.3775, -0.3968, -1.4030, -1.4264]^\top,$$

so the plant is started away from the reference trajectory. Figure 29 shows three representative joints positions of the undisturbed system for twelve consecutive steps. It can be seen that these joints possess periodic trajectories. Using the reference trajectory adaptation method proposed, the velocity error is smooth and goes to zero, instead of presenting the peaking phenomena described in Biemond *et al.* (2013). This is clearly observed in Fig.30). Since there are no jumps in the velocity error, the Lyapunov function monotonically decreases to zero, as shown in Fig.31). Figure 32 depicts the resulting heights of the feet. The periodicity of these heights is a good indicator of a stable motion for the walking gait. In Fig.32, legends ”P1” and ”P3” represent the ”toe” of the right foot and left foot, respectively; similarly, ”P2” and ”P4” represent the ”heel” of the right foot and left foot.

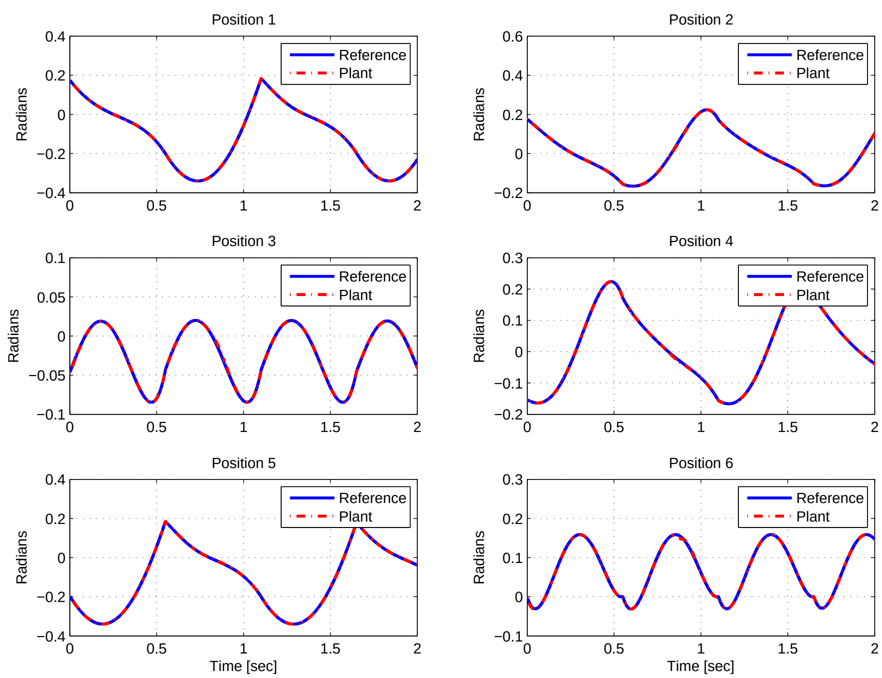

Figure 29: Joints positions for the undisturbed system: the tracking error is zero for all joints

The robustness of the tracking controller (68) was tested by involving a resultant disturbance force $F_{xw} = 80\ N$ in the horizontal plane, applied to the hip of the robot. Such a force was used for the duration of $0.07\ s$ to simulate a disturbance effect. This force,

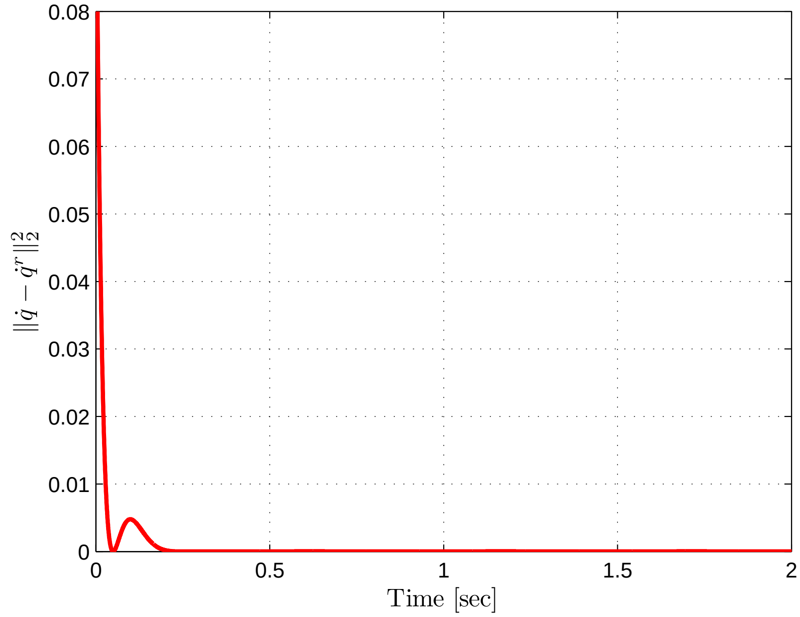

Figure 30: Velocity error $\|\dot{\mathrm{q}} - \dot{\mathrm{q}}^{\mathrm{r}}\|^2$ for the undisturbed system.

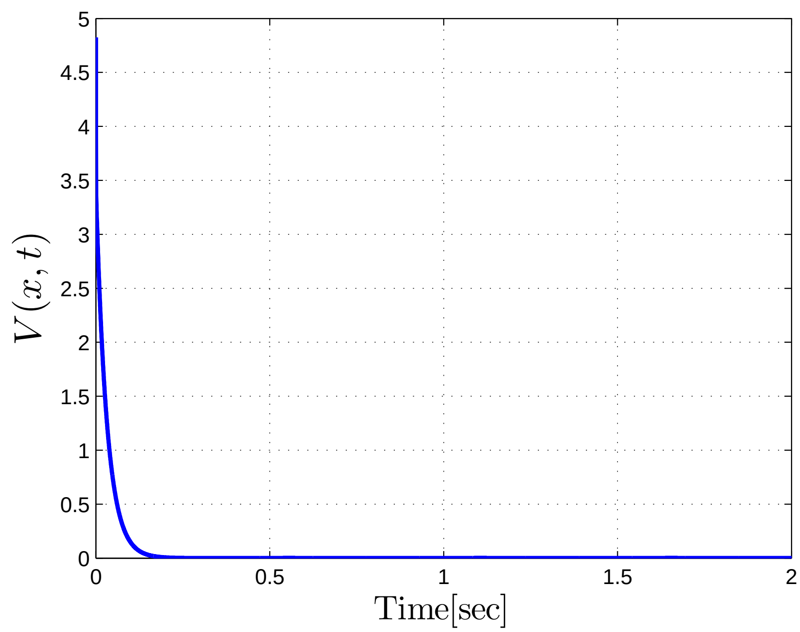

Figure 31: Lyapunov function for the undisturbed system, with nonzero initial conditions.

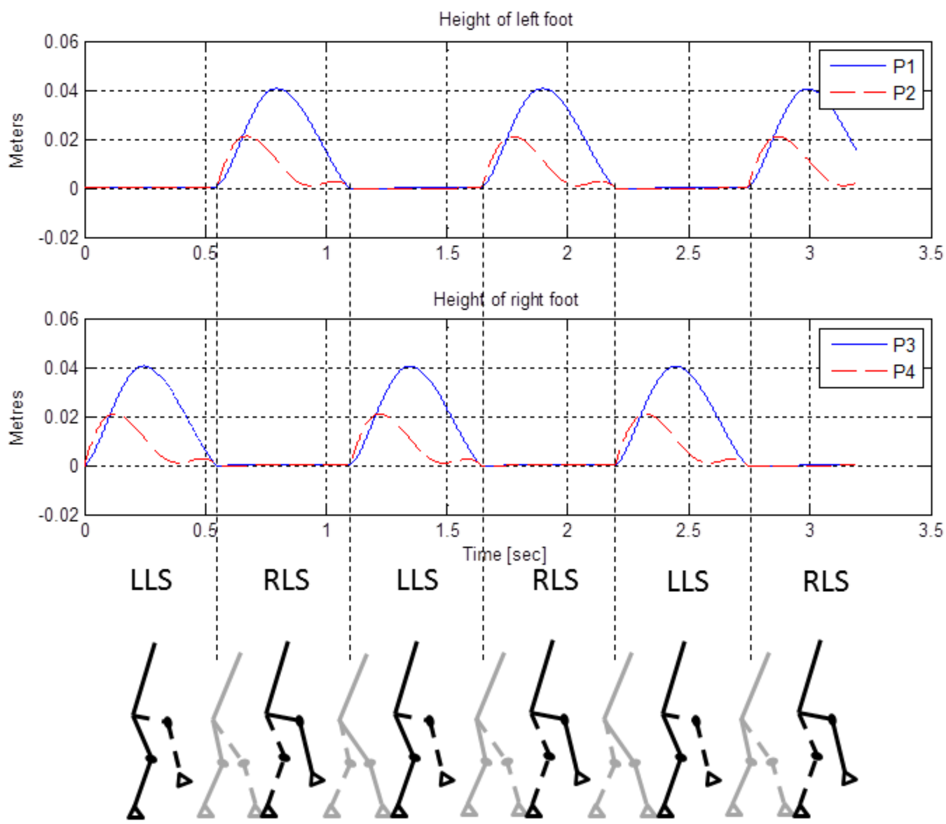

Figure 32: Feet height in the walking gait, representing a stable motion with left leg support (LLS) phases followed by right leg support (RLS) phases, separated by impacts.

applied at $0.8\ s$ in the first cycle of the biped, represented a disturbance in the continuous phase of the dynamics (26).

The effect of the disturbance is observed in Figs.33-35. The disturbance attenuation is readily concluded from Fig.33 where the effect of the disturbance is quickly attenuated by the controller. This effect is not evident in the feet heights plot, but the corresponding location of the Zero Moment Point (ZMP), depicted in Fig.34, directly reflects the disturbance effect which does not however influence on the stability of the walking gait because (see Haq *et al.* (2012) for details) the ZMP location remains inside the support foot area between the toe and the heel. As predicted, the torques do not exhibit jumps due to the trajectory adaptation. In addition, one can observe from Fig.35 that while attenuating the applied disturbance, the torques remain within the actuator limitations ($\pm 150\ Nm$). Once the discrete disturbance disappears the biped returns to its desired gait. Good robustness features are thus concluded from Figs.32-35.

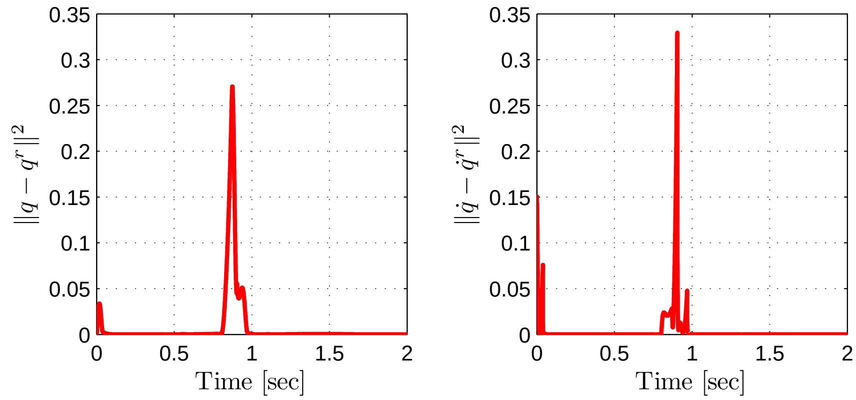

Figure 33: Position and velocity errors $\|\mathrm{q} - \mathrm{q}^{\mathrm{r}}\|^2$ and $\|\dot{\mathrm{q}} - \dot{\mathrm{q}}^{\mathrm{r}}\|^2$ of the disturbed system. The effect of the disturbance is evident at $0.8\ sec$, and it is quickly attenuated by the controller.

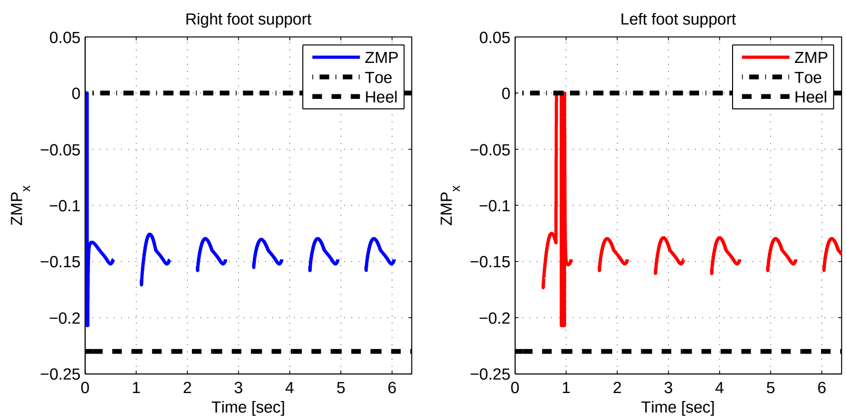

Figure 34: Zero moment point (ZMP) location along the x-axis for each foot during its support phase. It is seen that the ZMP is always located between the toe and the heel of the supporting foot, so the walk is stable Haq *et al.* (2012).

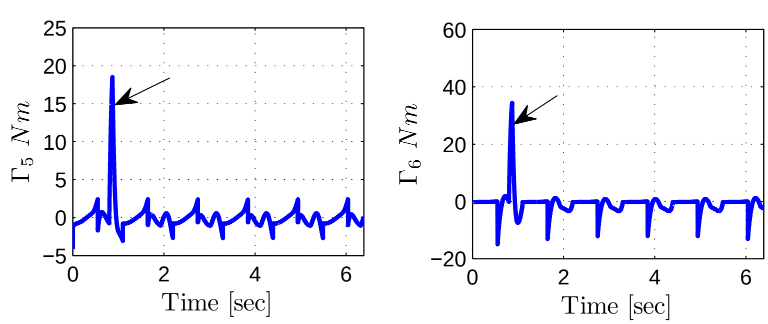

Figure 35: Torques appearing in joints 5 and 6, where the effects of the disturbance, pointed out by the arrows, are evident.

5.1.4.3 Numerical Comparison to a PD Controller

For the sake of comparison, a PD controller was brought into play. Such a controller was designed using the outer-loop pre-feedback linearization (64), applied to (26). The standard inner-loop state feedback $\mathcal{H}_\infty$ controller was then synthesized for the resulting double integrator

$$\mathbf{\dot{x}_1} = \mathbf{x_2}, \quad \mathbf{\dot{x}_2} = \mathbf{u} + \mathbf{w_n} \tag{140}$$

where the additive term $\mathbf{w_n} = \mathbf{D^{-1}}(\mathbf{x_1} + \mathbf{q^r})\mathbf{w_1}$ was viewed as an external disturbance to be attenuated. For providing a fair comparison, the PD controller

$$\mathbf{u} = -\mathbf{K_p}\mathbf{x_1} - \mathbf{K_v}\mathbf{x_2}, \tag{141}$$

which was designed in this way, relied on the same output (31) to be controlled and the same parameters $\rho_p = 500$, $\rho_v = 1$, $\gamma = 470$, and $\epsilon = 0.01$, used before while applying the developed nonlinear $\mathcal{H}_\infty$ control synthesis under unilateral constraints. Thus, the PD controller (141) was designed with the constant matrices $[\mathbf{K_p}, \mathbf{K_v}] = \mathbf{B_2^\top}\mathbf{P}_\varepsilon$ where $\mathbf{P}_\varepsilon$ solved the algebraic Riccati equation (54) with $\mathbf{\dot{P}}_\varepsilon = \mathbf{0}$.

The comparison results with the time-varying disturbance force $F_{xw} = 15\sin(2t) + 15\ N$, applied to the hip are shown in Fig.36, where the position tracking errors are presented for both controllers. As a matter of fact, the discrete disturbances, caused by the discrepancy between the velocity restitution, used in the synthesis of the underlying controllers, and that modeled for the biped, persisted in these simulations as well. It is evident from this figure that the tracking errors are bounded (so the biped still achieves walking), but the errors, exhibited with the PD-controller implementation, are higher than those, corresponding to the $\mathcal{H}_\infty$ controller, thereby yielding an improvement on the precision of the task for the nonlinear $\mathcal{H}_\infty$ synthesis vs. the linear (PD) one. From Fig.37, it can be seen that after $6.13\ s$, the cumulative position tracking error, generated by the developed nonlinear periodic $\mathcal{H}_\infty$ tracking controller, is approximately 26% less than that generated by the PD controller. Thus, a better performance of the proposed synthesis is concluded in comparison to the standard linear $\mathcal{H}_\infty$ PD design coupled to the pre-feedback linearization.

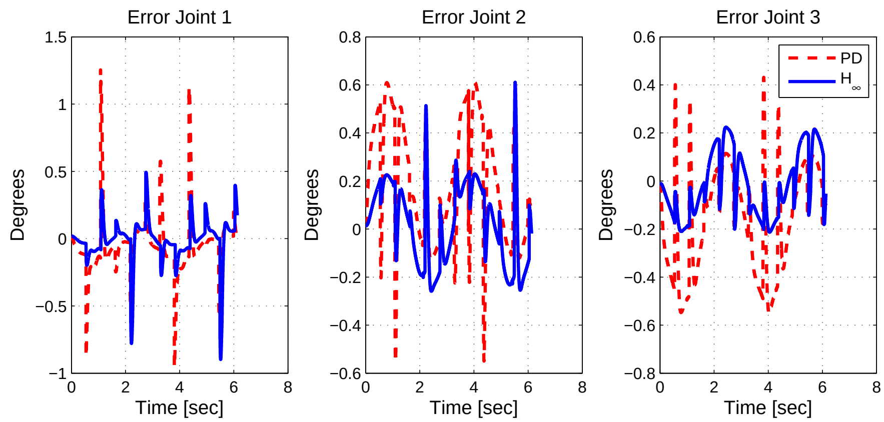

Figure 36: Tracking error comparison of the nonlinear $\mathcal{H}_\infty$ controller (solid lines) vs. the linear $\mathcal{H}_\infty$ PD controller (dashed lineas) for the first three joints.

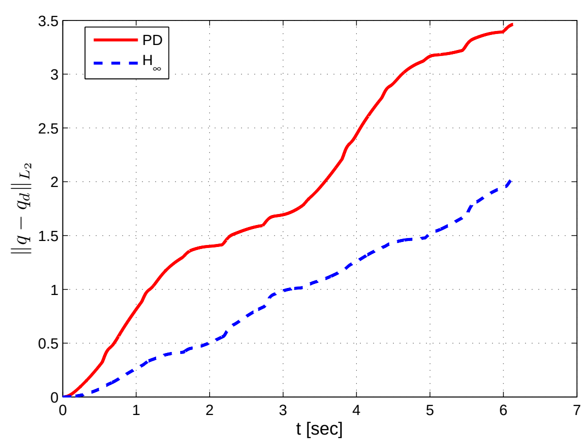

Figure 37: Cumulative error comparison of the nonlinear $\mathcal{H}_\infty$ controller (solid lines) vs. the linear $\mathcal{H}_\infty$ PD controller (dashed lines).

5.1.4.4 Disturbance Attenuation via Position Feedback Synthesis

In what follows, the results of section 2.3.3, specified in terms of the angular deviations of the biped, are applied to robustly track the time-reference trajectory $\mathbf{q}^{\mathbf{r}}(t)$, constructed in Section 5.1.3. Only imperfect position measurements are assumed to be available.

The parameters in (31), required to design the differential Riccati equations (54)-(55), were selected by specifying certain values of ρ_p and ρ_v. Then, an iteration procedure on γ was applied to the periodic differential Riccati equations for carrying out its periodic, symmetric and positive definite solutions.

The controller parameters, properly solving (54)-(55), were thus set to $\rho_p = 2500$, $\rho_v = 400$, and $\epsilon = 0.01,$ and the value $\gamma = 800$ was then straightforwardly verified to meet Condtions C1) and C2) with $\boldsymbol{\omega}$ being an identity matrix.

Thus, Theorem 2.2 proved to be applicable to the error system (1)-(5), specified with (42)-(43), (46)-(49). By applying Theorem 2.2, the control law (62) renders a local solution to the robust tracking problem for the biped with the desired trajectory $\mathbf{q}^{\mathbf{r}}(t)$ to follow.

5.1.4.5 Numerical Results

In the simulation runs made for the position feedback synthesis, neither adaptation nor extrapolation of the reference trajectory is used. Despite external disturbance, and non-zero initial conditions ($\mathbf{q_0}$ and $\dot{\mathbf{q}}_\mathbf{0}$ were set to the same values as in Section 5.1.4.2), good tracking of the reference trajectory is still achieved in the closed-loop, and all the joints exhibit stable periodic motions. However, since the impact instants of the reference trajectory, and those of the plant are not equal (see Fig.38, where the impact instant mismatching is illustrated during the first impact), the velocity errors generate the peaking phenomena provoked by the mismatching impacts. This is illustrated by the velocity errors in Fig.39, where the peaks are bounded by the magnitude value 18. Thus, the Lyapunov function is not a strictly decreasing function. In spite of that, good performance of the closed-loop error dynamics, driven by the proposed nonlinear $\mathcal{H}_\infty$ position feedback, is still achieved, as shown in the sequel.

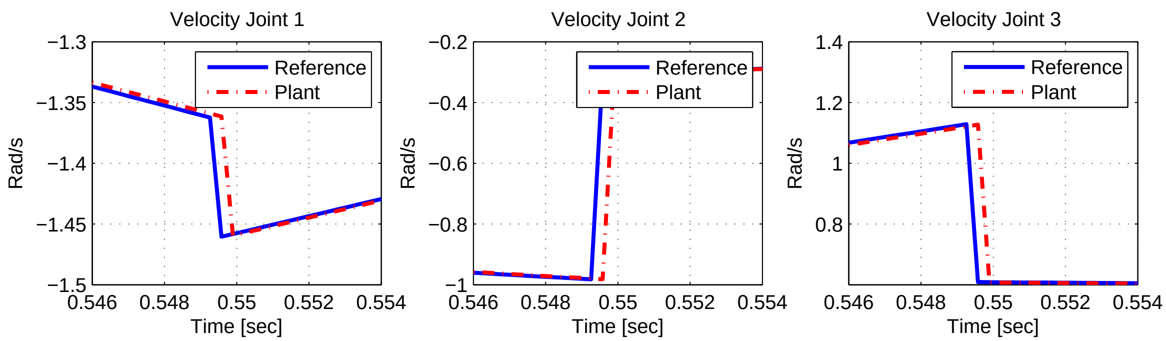

Figure 38: Difference in the first impact instant between the reference trajectory and the disturbed plant with non-zero initial conditions.

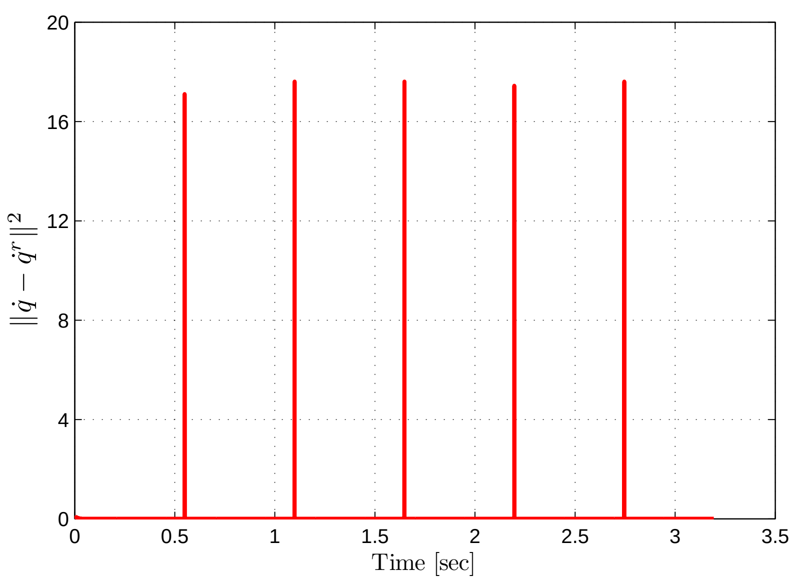

Figure 39: Disturbed velocity error $\|\dot{\mathrm{q}} - \dot{\mathrm{q}}^{\mathrm{r}}\|^2$ with non-zero initial conditions whose bounded peaks are due to the difference in the impact instants of the reference trajectory and of the plant.

The robustness of the tracking controller (62) was tested by involving a resultant disturbance force $F_{xw} = 10\ N$ in the horizontal plane, applied to the hip of the robot. Such a force was used for the duration of $0.07\ s$ to simulate a disturbance effect. The effect of F_{xw} represented a disturbance in the continuous phase of the dynamics (26) as it started from $1.2\ s$ during the second cycle of the biped which belonged to the continuous phase of the trajectory. In turn, the position measurements were counted with the sinusoidal disturbance $15\sin(t)$.

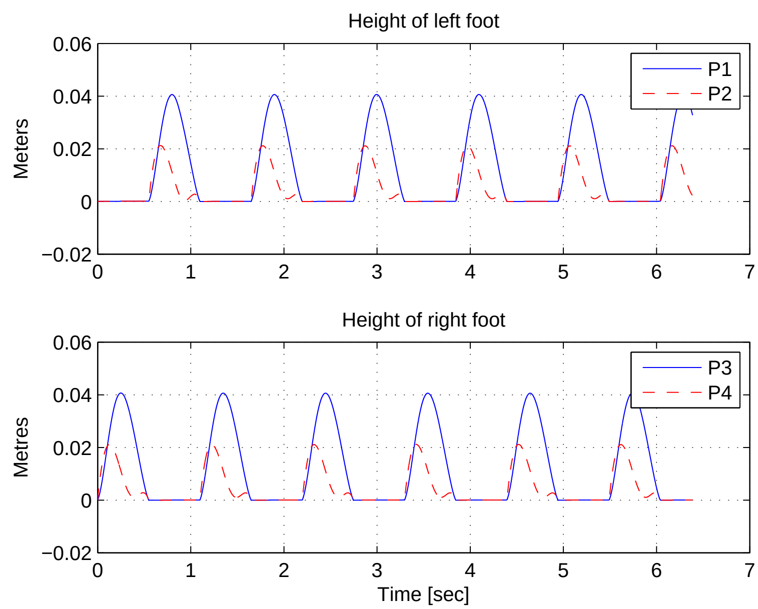

Figure 40: Feet height in the walking gait under disturbances in the swing and impact phases, and under measurement errors.

Figure 40 shows the heights of the feet for twelve consecutive steps with a periodic behavior, yielding a stable walking gait. From Fig.41, one can observe that the state filter used presents very small estimation errors, even in the presence of the disturbances in the continuous dynamics and in the measurements. As predicted for non-adapted reference trajectories, there appear torque peaks at each impact instant (see Fig.43 for the torque that occurs in joint 5) which have been saturated to meet the admissible torque limitations of $\pm 150\ Nm$). Once the disturbance F_{xw} disappears the biped returns close to its desired gait because the position tracking error decreases immediately afterwards, as depicted in Fig.42. Thus, in spite of the disturbances, resulting in mismatching between impact instants of the non-adapted reference trajectory and those of the biped, good performance and desired robustness features of the nonlinear $\mathcal{H}_\infty$ position feedback synthesis are concluded from Figs.40-43.

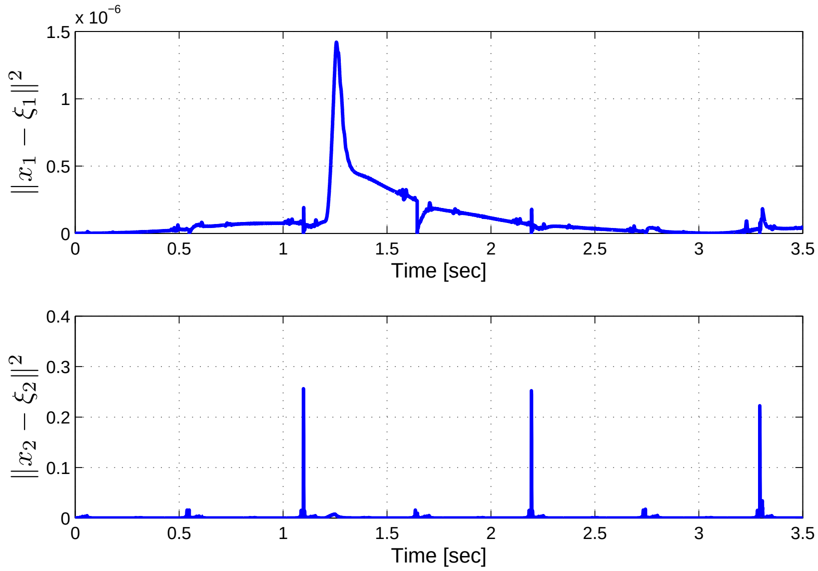

Figure 41: Filter estimation errors $\|\mathbf{x_1} - \boldsymbol{\xi_1}\|^2$ and $\|\mathbf{x_2} - \boldsymbol{\xi_2}\|^2$ for the disturbed system with an evident effect of the continuous disturbance at $1.2\ sec$

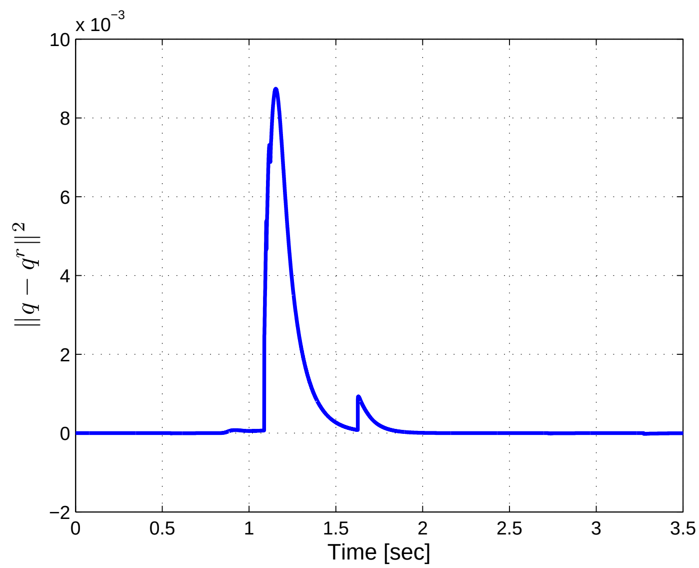

Figure 42: Disturbed position error $\|\mathbf{q} - \mathbf{q^r}\|^2$ with an evident effect of the continuous disturbance at $1.2\ sec$**.**

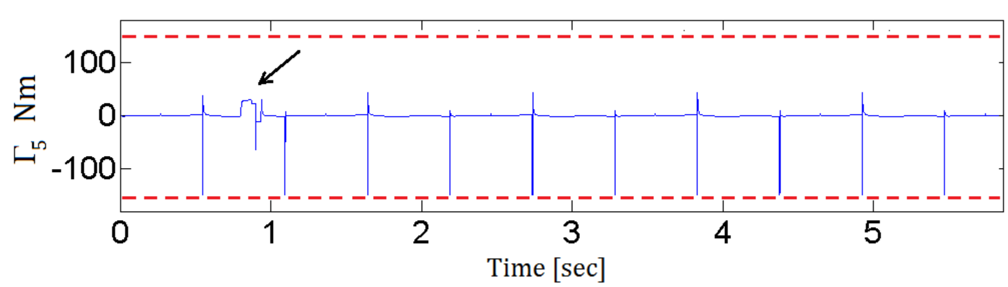

Figure 43: The disturbed torque of joint 5: the dashed lines indicate the maximum and minimum allowed torques, the arrow points to the disturbance effect.

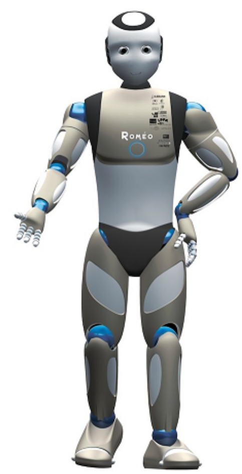

Figure 44: 32-DOF Robot Romeo, of Aldebaran Robotics.

5.2 Trajectory Tracking of a 3D Biped with Feet

The bipedal robot considered in this section is walking on a rigid and horizontal surface. It consists of the 32-DOF robot Romeo, of Aldebaran Robotics, depicted in Fig. 44. Similar to the planar biped form the previous section, the walking gait takes place in the sagittal plane and is composed of single support phases and impacts.

5.2.1 Dynamic Model in Single Support

The configuration of the biped robot in single support can be described only by the vector $\mathbf{q} = (q_0, q_1, \ldots, q_{32})^\top$. We use the modified Denavit-Hartenberg notation (Khalil and Kleinfinger, 1986) to define the frame position for each joint (see Fig. 45). To define the geometric structure of the biped we assume that the link 0 (stance foot) is the base of the bipedal robot while the link 12 (swing foot) is the terminal link. Considering the torso, head and arms, one obtains a tree structure. To take into account explicitly the contact with the ground, we have to add six more variables to describe the position and orientation of the frame 0 with respect to a fixed Galilean frame R_g. Thus, we can define the position, velocity, and acceleration vectors, $\mathbf{X} = (\mathbf{X_0}^\top, \boldsymbol{\alpha_0}^\top, \mathbf{q}^\top)^\top$, $\mathbf{V} = ({}^0\mathbf{V}_0^\top, {}^0\boldsymbol{\omega}_0^\top, \dot{\mathbf{q}}^\top)^\top$, and $\dot{\mathbf{V}} = ({}^0\dot{\mathbf{V}}_0^\top, {}^0\dot{\boldsymbol{\omega}}_0^\top, \ddot{\mathbf{q}}^\top)^\top$. $\mathbf{X_0}$ and $\boldsymbol{\alpha_0}$ are the position and orientation variables of frame R_0, while ${}^0\mathbf{V}_0$ and ${}^0\boldsymbol{\omega}_0$ are the linear and angular velocities of R_0, with respect to the Galilean

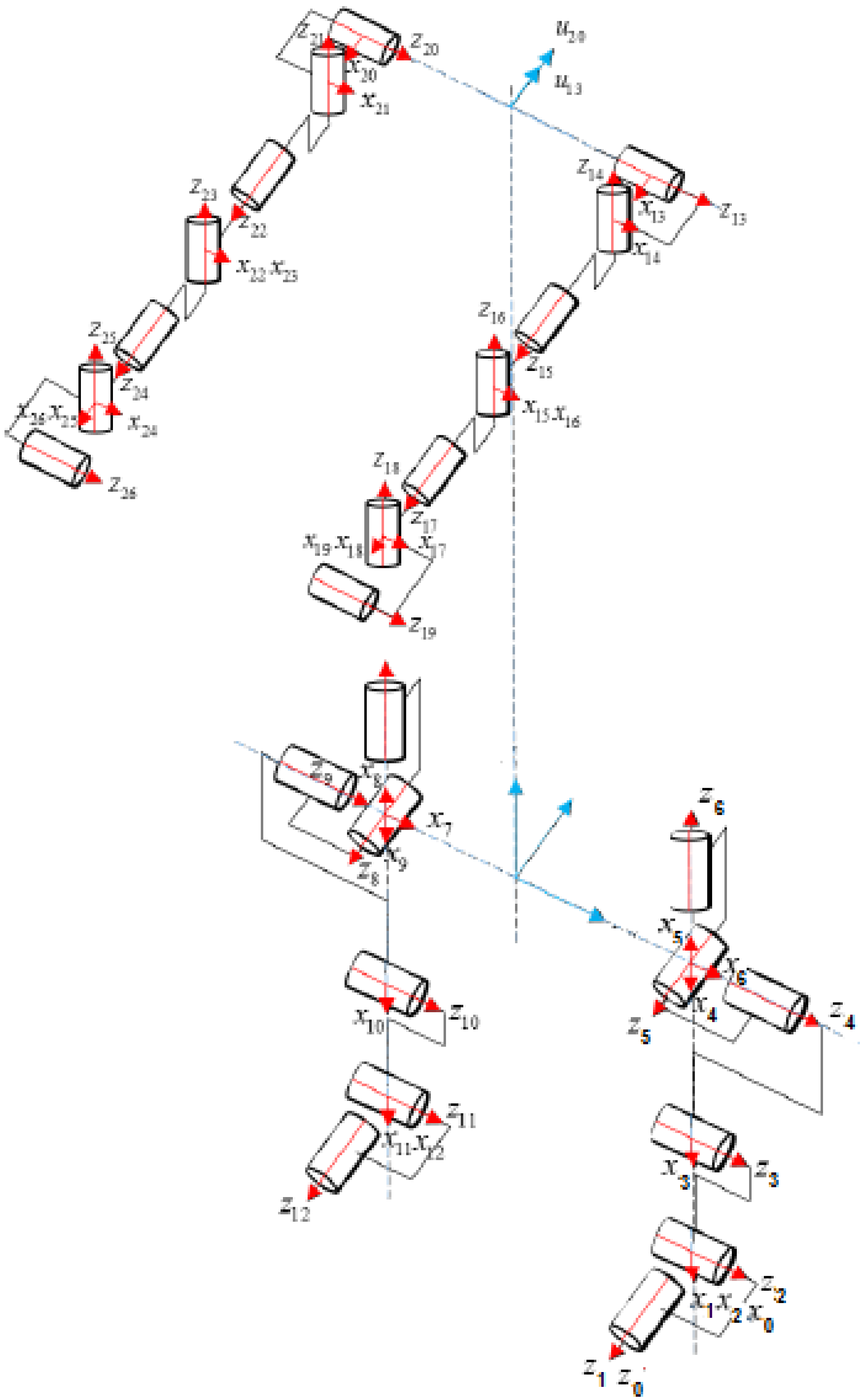

Figure 45: Frames placement for the main limbs; the remaining 6 frames not appearing belong to the hands (2 frames) and the neck and head (4 frames), thus completing the 32 degrees of freedom. The zero frame R_0 is attached to the left foot.

frame. Therefore, the complete dynamic model of the biped can be written as follows:

$$\mathbf{D_e}(\mathbf{X})\dot{\mathbf{V}} + \mathbf{C_e}(\mathbf{X}, \mathbf{V}) + \mathbf{G_e}(\mathbf{X}) = \mathbf{D_{e\tau}}\boldsymbol{\tau} + \mathbf{J_1}^\top\mathbf{R_1} + \mathbf{J_2}^\top\mathbf{R_2} + \mathbf{D_w}\mathbf{w_1}, \tag{142}$$

with the complementarity condition

$$0 \leq F(\mathbf{X}) \perp \mathbf{R_2} \geq \mathbf{0} \tag{143}$$

and the constraint equation

$$\mathbf{J_1}\dot{\mathbf{V}} = \mathbf{0}, \tag{144}$$

where $\mathbf{D_e}$ is the symmetric, positive definite 38×38 inertia matrix; $\mathbf{D_{e\tau}}$ and $\mathbf{D_w}$ are 38×32 constant matrices, composed of zeros and ones; $\boldsymbol{\tau} = (\tau_1, \ldots, \tau_{32})^\top$ is the 32×1 vector of joint torques; terms $\mathbf{C_e}(\mathbf{X}, \mathbf{V})$, and $\mathbf{G_e}(\mathbf{X})$ are the 38×1 vector of the centrifugal and Coriolis forces, and the 38×1 vector of gravity forces, respectively; $\mathbf{w_1}$ is the 32×1 vector of external disturbances; $\mathbf{R_1}$ and $\mathbf{R_2}$ represent the reaction forces on foot 1 and foot 2, respectively, whereas $\mathbf{J_1}$ and $\mathbf{J_2}$ are 6×38 Jacobian matrices converting these efforts to the corresponding joint torques. Equations (142)-(143), in addition to a restitution law to be defined later, form a Lagrangian Complementarity System.

Due to the difficulty of the analytic calculation of the dynamic model (142), it is numerically computed by means of the Newton-Euler algorithm (Luh *et al.*, 1980), which is based on recursive calculations associated to the choice of the reference frames from Fig. 44b. Then, matrices $\mathbf{D_e}$, $\mathbf{C_e}(\mathbf{X}, \mathbf{V})$ and $\mathbf{G_e}(\mathbf{X})$ can be easily and rapidly computed using the method of Walker and Orin (1982). The same algorithm also allows to find the ground reaction forces.

In the single support phase, considering a flat foot contact of the support foot with the ground, and assuming no take off, no sliding and no rotation of the support foot, the model (142)-(144) can be reduced to:

$$\mathbf{D}(\mathbf{q})\ddot{\mathbf{q}} + \mathbf{H}(\mathbf{q}, \dot{\mathbf{q}}) = \mathbf{D}_\tau\boldsymbol{\tau} + \mathbf{w_1} \tag{145}$$

where $\mathbf{D}_\tau$ is the symmetric, positive definite 32×32 inertia matrix, $\boldsymbol{\tau} = (\boldsymbol{\tau}_1, \ldots, \boldsymbol{\tau}_{32})^\top$ is the 32×1 vector of joint torques. The term $\mathbf{H}(\mathbf{q}, \dot{\mathbf{q}})$ is the 32×1 vector of the centrifugal, Coriolis and gravity forces.

These conditions are verified during the numerical study using model (142). If at least one of these conditions are not satisfied, the conditions to construct (145) are not met and thus it is not valid. Thus, the reference trajectories are designed taking these conditions as restrictions.

5.2.2 Impact Model

The impact is assumed to be inelastic with complete surface of the foot sole touching the ground. This means that the velocity of the swing foot impacting the ground is zero after impact. The double support phase is instantaneous and it can be modeled through passive impact equations. An impact appears at a time $t = T_I$ when the swing leg touches the ground.

Since the impact is assumed to be passive, absolutely inelastic, and that the legs do not slip (Tlalolini *et al.*, 2010), the following equations:

$$\mathbf{J_1 V^-} = \mathbf{0} \tag{146}$$

$$\mathbf{J_2 V^+} = \mathbf{0} \tag{147}$$

hold. This means that the feet perfectly stick on the ground after the shock, thus avoiding multiple impacts. Given these conditions, the ground reactions can be viewed as impulsive forces. The algebraic equations, allowing one to compute the jumps of the velocities, can be obtained through integration of the dynamic equations of the motion, taking into account the ground reactions during an infinitesimal time interval from T_I^- to T_I^+ around an instantaneous impact.

The impact is assumed to be with complete surface of the foot sole touching the ground. This means that the velocity of the swing foot impacting the ground is zero after impact. After an impact, the right foot (previous stance foot) takes off the ground, so the vertical component of the velocity of the taking-off foot must be directed upwards right after an impact and the impulsive ground reaction in this foot equals zeros. Thus, the impact dynamic model can be represented as follows (Tlalolini *et al.*, 2010):

$$\begin{aligned}\mathbf{V}^{+} =& (\mathbf{I} - \mathbf{D_e^{-1}}\mathbf{J_2^{\top}}(\mathbf{J_2}\mathbf{D_e^{-1}}\mathbf{J_2^{\top}})^{-1}\mathbf{J_2})\mathbf{V}^{-} + \mathbf{w_{ei}^{d}} \\ \mathbf{V}^{+} =& \phi_e(\mathbf{X})\mathbf{V}^{-} + \mathbf{w_{i}^{d}}\end{aligned} \tag{148}$$

where $\mathbf{V}^{-}$ is the velocity of the robot before the impact, and $\mathbf{V}^{+}$ is the velocity after the impact; $\phi_e(\mathbf{X})$ represents a restitution law that determines the relations between the velocities before, and after the impacts; $\mathbf{X}$ is the configuration of the robot at the impact. The additive term $\mathbf{w_{ei}^{d}}$ is introduced to account for inadequacies in this restitution law. Thus, equation (148) renders the complementarity system (142)-(147) complete.

As done for the 2D example, by considering that the support foot velocity is zero before the impact, and the swing foot velocity is zero after the impact, and combining (146)-(148), it is possible to obtain the following expression:

$$\dot{\mathbf{q}}^{+} = \phi(\mathbf{q})\dot{\mathbf{q}}^{-} + \mathbf{w_{i}^{d}} \tag{149}$$

Also, considering the reference frame x_0, y_0, z_0 shown in Fig. 44b, and since we are assuming flat foot contact with the ground, the time-invariant unilateral constraint $F_0(\mathbf{q}) \geq 0$ is determined by the height of the swing foot's sole.

If all the assumptions mentioned above are met, equations (145), (149) define a hybrid system that can controlled using the methodology developed in this work.

5.2.3 Periodic Motion Planning

Since a walking biped gait is a periodical phenomenon, our objective is to design a cyclic biped gait. A complete walking cycle is composed of two phases: a single support phase, and a double support phase, which is modeled through passive impact equations. The single support phase begins with one foot which stays on the ground while the other foot swings from the rear to the front. The double support phase is assumed instantaneous. This means that when the swing leg touches the ground the stance leg takes off. The reference trajectories, allowing a symmetric step, are obtained by an off-line optimization, minimizing a Sthenic criteria, as presented in the work of Tlalolini *et al.* (2010).

5.2.4 State Feedback $\mathcal{H}_\infty$ Synthesis Using Trajectory Adaptation

Since the structure of the simplified model (145) is the same as a mechanical manipulator subject to unilateral constraints (presented in Chapter 2), the results from section 2.3.4 can be used, despite the complexity of the biped model. Therefore, the pre-feedback (64) and Theorem 2.3 are applied to the hybrid system (145), (149), to provide a robust controller capable of attenuating external disturbances around the reference walking gait. In addition, the idea of trajectory adaptation presented in section 5.1.4.1 is implemented in this control design, so as to suppress the peaking phenomena and guarantee asymptotic stability.

To solve the Riccati equation (54) for the error system (65) the controlled output (31) is specified with $\rho_p = 3500$ and $\rho_v = 500$, and then, following the standard $\mathcal{H}_\infty$ design procedure (see, e.g., (Orlov and Aguilar, 2014, Section 6.2.1)), the disturbance attenuation level and the perturbation parameter are set to $\gamma = 200$ and $\epsilon = 0.01$ to ensure an appropriate solvability of the perturbed differential Riccati equation (54).

5.2.5 Numerical Results

To illustrate the performance issues of the developed stable bipedal gait synthesis numerical simulations were performed for a laboratory prototype whose parameters were drawn from the Aldebaran's Romeo documentation. The contact constraints presented in section 5.2.1 were verified on-line to confirm the validity of (145), (149). Similar to the planar biped, the numerical scheme used for these simulations was a time-stepping, constraint-based approach (Rengifo *et al.*, 2011).

It can be seen that these joints possess a periodic trajectory. Figure 46 depicts the resulting heights of the feet for the undisturbed case. As presented for the planar biped, the periodicity of these heights is a good indicator of a stable motion for the walking gait.

In Fig.46, legends ”P1” and ”P4” represent the corners corresponding to the ”toe” of the foot, whereas ”P2” and ”P3” represent the corners of the ”heel” of the foot.

As a next step, a persistent disturbance of $10\sin(t)\ Nm$ was applied to the hip, while the velocities after the impact are deviated $5\ \%$ from their nominal values (given by (149)), thus considering disturbances on both the single support and impact phases. Six joints among the 32 were selected to clearly illustrate the effect of this disturbance (both ankles, knees, and hip joints). This is depicted in Fig. 47, where the error is small and bounded, and the robot maintains an stable walking gait. The torques for these joints are shown in Fig. 48, where they stay between the buondaries of $\pm 150\ Nm$. Despite the disturbances, good performance of the closed-loop error dynamics, driven by the proposed nonlinear $\mathcal{H}_\infty$ state feedback, is still achieved.

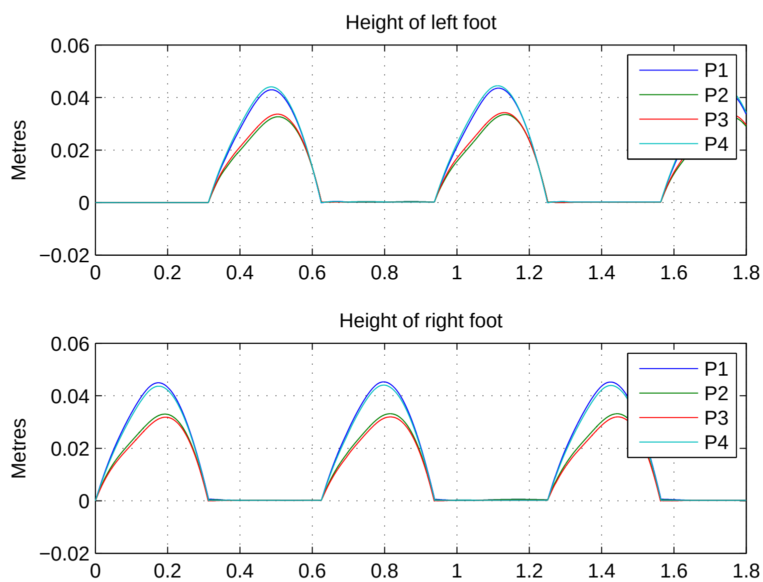

Figure 46: Feet heights for 6 steps for Romeo, representing a stable motion

5.3 Conclusions

The effectiveness of the synthesis procedure developed in Chapter 2, which is based on solving disturbed differential Riccati equations, corresponding to the linearized system, is supported in numerical studies, made side by side, for state and position feedback designs of stable gaits of a seven-link biped and a 32-DOF fully actuated biped robot. The desired

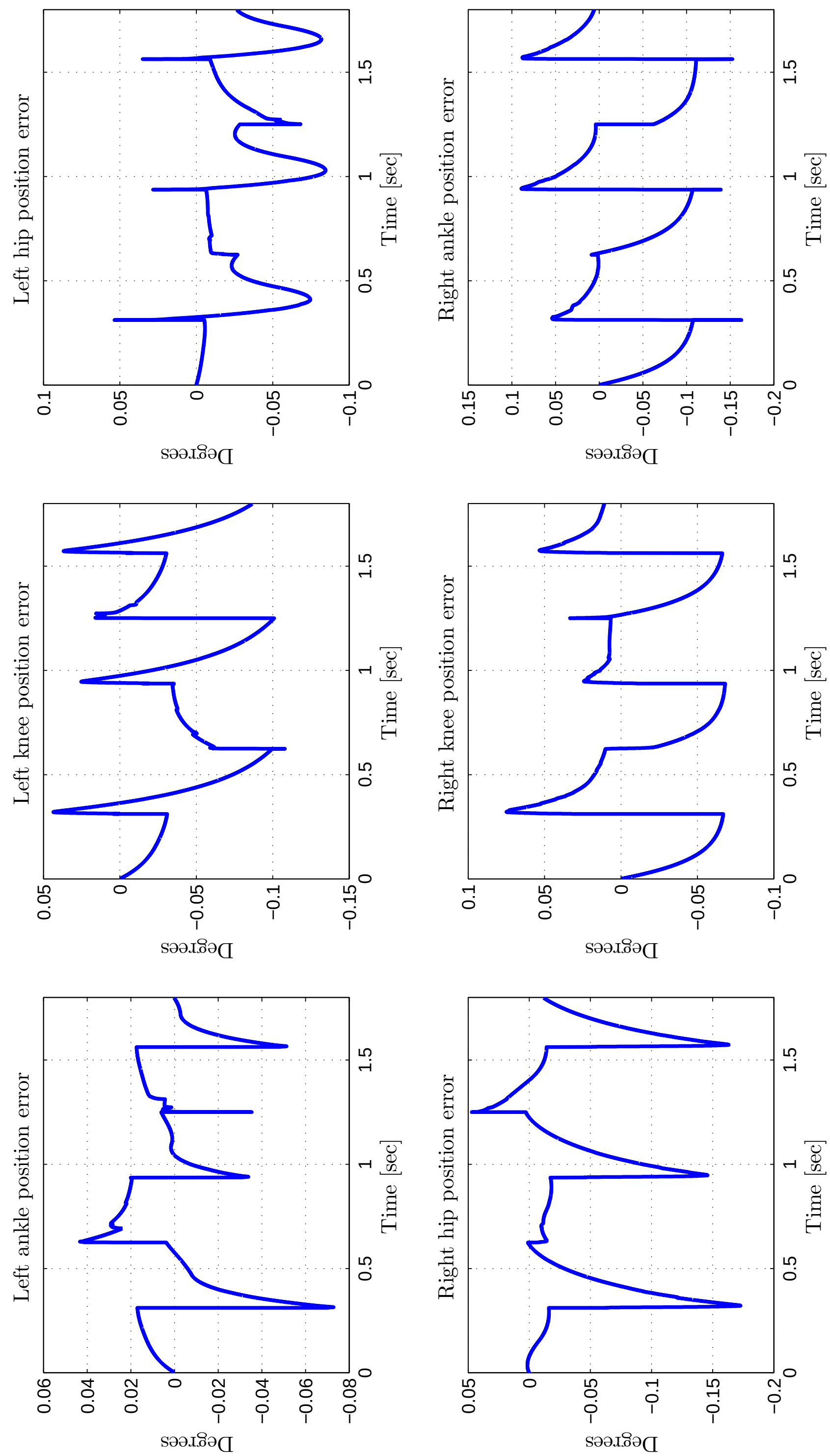

Figure 47: Joints errors for left and right hips, knees, and ankles, under a persistent continuous disturbance ($10\sin(t)\ Nm$) applied on the hip.

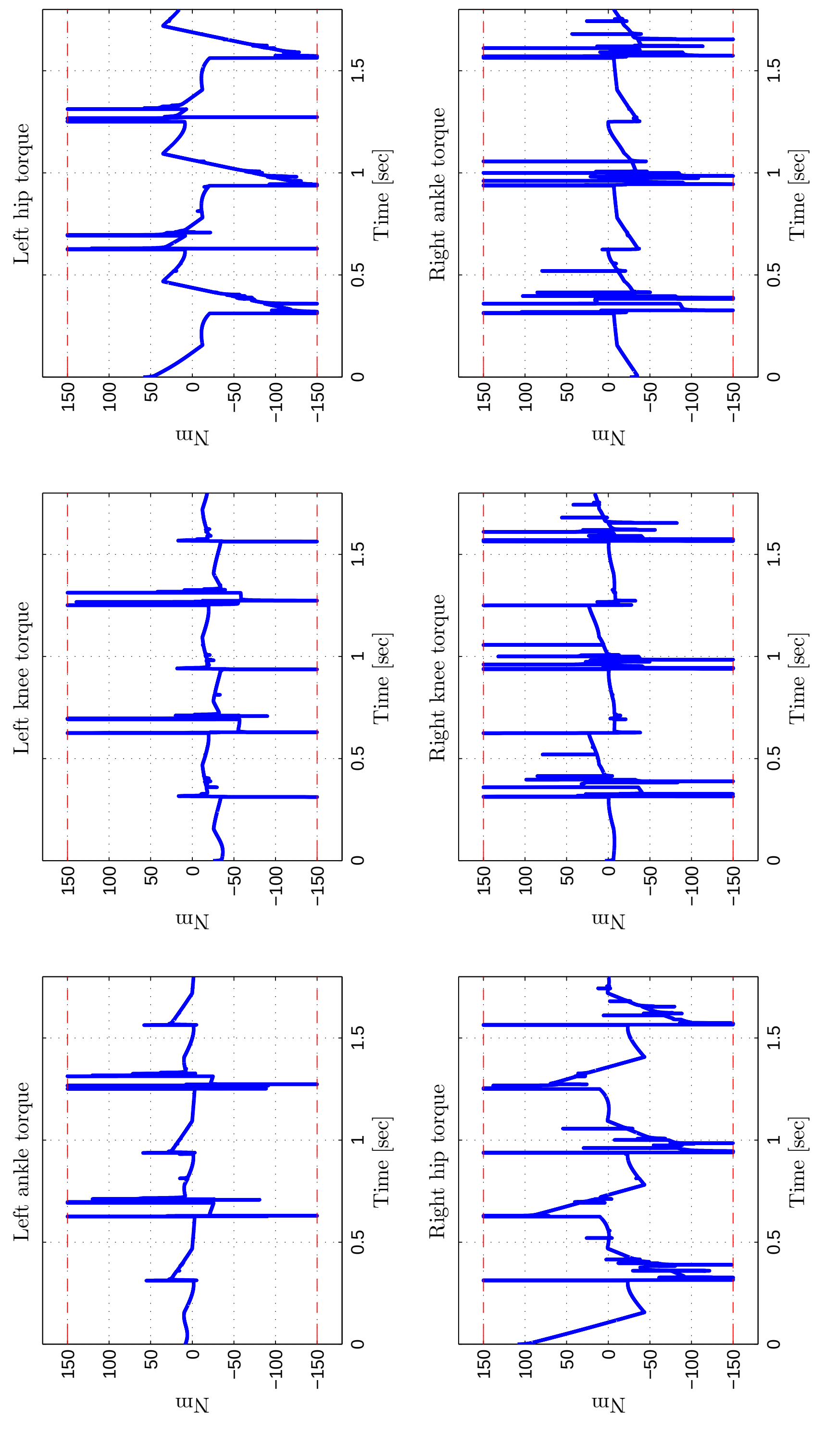

Figure 48: Torques for left and right hips, knees, and ankles, under a persistent continuous disturbance ($10\sin(t)\ Nm$) applied on the hip.

disturbance attenuation is satisfactorily achieved under external disturbances during the free-motion phase, and in the presence of uncertainty in the transition phase.

Chapter 6. Nonlinear $\mathcal{H}_\infty$ Control of Underactuated Mechanical Systems Operating Under Unilateral Constraints

This chapter is devoted to the extension of the $\mathcal{H}_\infty$ approach, developed for fully actuated systems under unilateral constraints in Chapter 2, towards underactuated mechanical systems, of underactuation degree one, with collisions. Sufficient conditions for a new output feedback control strategy are presented, that would result in the asymptotic orbital stabilization of the underactuated and undisturbed hybrid system of interest, while also guaranteeing the $\mathcal{L}_2$-gain of its disturbed version to be less than an appropriate disturbance attenuation level γ.

Given a scalar unilateral constraint $F(q) \geq 0$ of class C^1, consider a nonlinear system, evolving within the above constraint, which is governed by continuous dynamics of the form

$$\mathbf{D}(\mathbf{q})\ddot{\mathbf{q}} + \mathbf{C}(\mathbf{q}, \dot{\mathbf{q}})\dot{\mathbf{q}} + \mathbf{G}(\mathbf{q}) = \mathbf{B}\boldsymbol{\Gamma} + \mathbf{w_c} \tag{150}$$

out of the surface $F(q) = 0$ when the constraint is inactive, and by the algebraic relations

$$\begin{bmatrix} \mathbf{q}^+ \\ \dot{\mathbf{q}}^+ \end{bmatrix} = \psi(\mathbf{q}^-, \dot{\mathbf{q}}^-) + \boldsymbol{\omega}(\mathbf{q}^-, \dot{\mathbf{q}}^-)\mathbf{w_d} \tag{151}$$

when the system trajectory hits the surface $F(q) = 0$. The vectors $\mathbf{q} \in \mathbb{R}^n$ and $\dot{\mathbf{q}} \in \mathbb{R}^n$ are generalized positions and velocities, respectively, $\mathbf{D}$ is a $n \times n$ symmetric, positive definite inertia matrix, $\mathbf{B}$ is a $n \times (n-k)$ constant matrix, whose entries are either 0 or 1, depending if a variable is actuated or not. The vector $\boldsymbol{\Gamma} \in \mathbb{R}^{n-k}$ with $1 \leq k < n$ is the vector of joint torques (thus covering underactuated systems); ψ represents the impact equation; $\mathbf{w_c} \in \mathbb{R}^n$ represents external disturbances affecting the continuous dynamics, whereas $\mathbf{w_d} \in \mathbb{R}^s$ represents disturbances affecting the impact equation (151) (see Fig. 49). The vector $\mathbf{C}(\mathbf{q}, \dot{\mathbf{q}})\dot{\mathbf{q}}$ stands for centrifugal and Coriolis forces while $\mathbf{G}(\mathbf{q})$ stands for the gravity forces. This chapter will focus in mechanical systems of underactuation degree 1 during their locomotion, so $k = 1$.

Let us consider that a certain task is achieved by carrying out a feasible trajectory $\mathbf{q}_\star$ of the hybrid mechanical system (150)-(151), and this feasible trajectory will describe a

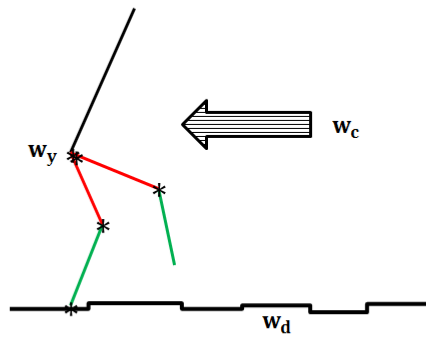

Figure 49: Disturbances present in bipedal locomotion

periodic orbit, given by

$$\mathcal{O}_\star = \{(\mathbf{q}, \dot{\mathbf{q}}) \in \mathbb{R}^{2n} : \mathbf{q} = \mathbf{q}_\star(\theta), \dot{\mathbf{q}} = \dot{\mathbf{q}}_\star(\theta, \dot{\theta})\} \tag{152}$$

where θ is called a phasing variable, and is a scalar quantity, which is strictly monotonic on the periodic orbit. Let $\theta_\star$ denote the evolution of θ corresponding to the periodic orbit $\mathcal{O}_\star$, then $\theta_\star|_t = \theta_\star|_{(t+T_s)}$, where $T_s > 0$ stands for the period of the motion.

As presented in the work of Hamed *et al.* (2014), now lets consider a controller $\mathbf{\Gamma}$ of the form

$$\mathbf{\Gamma} = \mathbf{\Gamma}_\star + \mathbf{u}, \tag{153}$$

where $\mathbf{\Gamma}_\star$ is a feedforward term corresponding to the periodic orbit $\mathcal{O}_\star$, and $\mathbf{u}$ is a feedback control law that internally stabilizes the closed-loop system system (150)-(151) to a feasible trajectory $\mathbf{q}_\star(\theta)$. Thus the existence of the periodic orbit $\mathcal{O}_\star$ as well as the existence of the feedforward term $\mathbf{\Gamma}_\star$ are postulated *a priori*.

Therefore, the orbital stabilization problem in question is to find an appropriate control action $\mathbf{\Gamma}$ such that the solutions of the undisturbed version of(150), (151), initiated in a neighborhood of the desired orbit $\mathcal{O}_\star$, defined by (152), asymptotically approach the compact set $\mathcal{O}_\star$, and for the disturbed version, attenuate the effect of the disturbances on the continuous dynamics (150) and the restitution law (151).

6.1 Background Materials

In this section, the virtual holonomic constraint approach is presented as well as the concepts of transverse coordinates and transverse linearization are. Coupled together, these results form a basis of attenuating disturbances in mechanical systems of underactuation degree one ($k = 1$).

6.1.1 Virtual Constraint Approach and Transverse Coordinates

The virtual holonomic constraint (VHC) approach is a powerful analytical tool of planning periodic motions in underactuated mechanical systems Shiriaev *et al.* (2005). Along with the system representation (150)-(151) in the generalized coordinates

$$q_1 = q_1(t), \ldots, q_n = q_n(t), \quad t \in [0, T_s], \tag{154}$$

an alternative time independent representation can be given in the parametric form

$$q_1 = \phi_1(\theta), \ldots, q_n = \phi_n(\theta), \quad \theta \in [\theta_0, \theta_f] \tag{155}$$

to be valid along a desired orbit, specified with functions $\phi_i(\cdot)$, $i = 1, \ldots, n$, which are functions of a parameter θ. Identities (155) are known as virtual holonomic constraints since they express algebraic relations among the generalized coordinates. The parameter θ can be chosen as one of the generalized coordinates (Shiriaev *et al.*, 2005) or as a linear combination of them (Westervelt *et al.*, 2007).

The dynamics of (150) in the new coordinates (155) can now be obtained by introducing the time derivatives $\dot{q}_i = \phi_i'\dot{\theta}$, $\ddot{q}_i = \phi_i''\dot{\theta}^2 + \phi_i'\ddot{\theta}$, $i = 1, \ldots, n$ into the Euler-Lagrange equation (150), where $\phi_i' = \frac{\partial \phi_i}{\partial \theta}$, and $\phi_i'' = \frac{\partial^2 \phi_i}{\partial \theta^2}$. The resulting equation is then governed by

$$\mathbf{D}(\mathbf{\Phi}(\theta)) \left[\mathbf{\Phi}'(\theta)\ddot{\theta} + \mathbf{\Phi}''\dot{\theta}^{\mathbf{2}}\right] + \mathbf{C}\left(\mathbf{\Phi}(\theta), \mathbf{\Phi}'(\theta)\dot{\theta}\right)\mathbf{\Phi}'(\theta)\dot{\theta}^{\mathbf{2}} + \mathbf{G}(\mathbf{\Phi}(\theta)) = \mathbf{B}(\mathbf{\Phi}(\theta))\mathbf{\Gamma} \tag{156}$$

where

$$\mathbf{\Phi}(\theta) = [\phi_1(\theta), \ldots, \phi_n(\theta)]^\top \tag{157}$$

$$\mathbf{\Phi}'(\theta) = [\phi_1'(\theta), \ldots, \phi_n'(\theta)]^\top \tag{158}$$

$$\mathbf{\Phi}''(\theta) = [\phi_1''(\theta), \ldots, \phi_n''(\theta)]^\top. \tag{159}$$

Since the present development is confined to mechanical systems (150) of underactuation degree 1, there exists a nontrivial matrix function $\mathbf{B}^\perp(q) \in \mathbb{R}^{1\times n}$ such that $\mathbf{B}^\perp(\mathbf{q})\mathbf{B}(\mathbf{q}) = \mathbf{0}$. Therefore, multiplying (156) by $\mathbf{B}^\perp(\mathbf{q})$ from the left, one arrives at the reduced second order dynamics along the holonomic constraints (155):

$$\bar{\alpha}(\theta)\ddot{\theta} + \bar{\beta}(\theta)\dot{\theta}^2 + \bar{\gamma}(\theta) = 0 \tag{160}$$

where

$$\bar{\alpha}(\theta) = \mathbf{B}^\perp(\mathbf{\Phi}(\theta))\mathbf{D}(\mathbf{\Phi}(\theta))\mathbf{\Phi}'(\theta) \tag{161}$$

$$\bar{\beta}(\theta) = \mathbf{B}^\perp(\mathbf{\Phi}(\theta))[\mathbf{C}(\mathbf{\Phi}(\theta), \mathbf{\Phi}'(\theta)\dot{\theta}) + \mathbf{D}(\mathbf{\Phi}(\theta))\mathbf{\Phi}''] \tag{162}$$

$$\bar{\gamma}(\theta) = \mathbf{B}^\perp(\mathbf{\Phi}(\theta))\mathbf{G}(\mathbf{\Phi}(\theta)). \tag{163}$$

For underactuated mechanical systems under unilateral constraints, (160) should be accompanied with the reset law

$$\begin{bmatrix} \theta^+ \\ \dot{\theta}^+ \end{bmatrix} = \Delta_\theta(\theta^-, \dot{\theta}^-) \tag{164}$$

where Δ_θ translates the jumps of the mechanical system (150), (151) to the jumps of the reduced dynamics (160).

The reduced system (160), (164) is referred to as the hybrid zero dynamics (Westervelt *et al.*, 2003; Ames *et al.*, 2012), and its solutions (if any) represent motions that, under some technical assumptions, can be imposed on the system by a proper feedback synthesis.

An appropriate periodic solution $\mathbf{q}_\star(t) = \mathbf{q}_\star(t + T_s)$ of (150)-(151) can be found by the use of a nonlinear dynamic optimization (see, e.g. the works by Aoustin and Formalsky (2003); Westervelt *et al.* (2007)), where the motion is defined by basis functions (normally polynomials) $\mathbf{q}_{\star}(t)$ whose coefficients are to be specified to optimize some criteria, energy for example. A feasible solution of the hybrid zero dynamics (160), (164) can thus be obtained. The resulting procedure constitutes a widely used methodology of the reference trajectory design in bipedal robotics, and it is the approach adopted in this paper. Other methods to generate periodic solutions can be found, for example, in Arai *et al.* (1998); Bullo and Lynch (2001); Mettin *et al.* (2007).

Clearly, the knowledge of $\mathbf{q}_{\star}(t)$ allows one to construct n-scalar functions $\phi_1(\theta), \ldots, \phi_n(\theta)$ that parametrize the same periodic solution $\mathbf{q}_{\star}(\mathbf{t})$ by the scalar variable θ. Given these VHCs, the $n+1$ quantities

$$\theta, \;\; \eta_1 = q_1 - \phi_1(\theta), \ldots, \eta_n = q_n - \phi_n(\theta) \tag{165}$$

can be viewed as redundant generalized coordinates for the underactuated system (150)-(151) so that one of them, can be expressed as a function of the other coordinates. Without loss of generality, η_n is assumed to be so, and the new independent coordinates are

$$\boldsymbol{\eta} = \eta_1, \ldots, \eta_{n-1}{}^{\top} \in \mathbb{R}^{n-1} \quad \text{and} \quad \theta \in \mathbb{R} \tag{166}$$

whereas the last equality in (165) can be rewritten as

$$q_n = \phi_n(\theta) + h(\boldsymbol{\eta}, \theta) \tag{167}$$

with some smooth scalar function $h(\boldsymbol{\eta}, \theta)$. Hence, the coordinate transformation (165), (167) comes with the Jacobian matrix

$$\mathbf{L}(\theta, \boldsymbol{\eta}) = \begin{bmatrix} \mathbf{I}_{n-1} & \mathbf{0}_{(n-1)\times 1} \\ \frac{\partial h}{\partial \boldsymbol{\eta}} & \frac{\partial h}{\partial \theta} \end{bmatrix} + [\mathbf{0}_{\mathbf{n}\times(\mathbf{n-1})}, \boldsymbol{\Phi}'(\theta)]. \tag{168}$$

Provided that the Jacobian matrix is not singular in a vicinity of the desired orbit, a one-to-one relation is locally established between the first order derivatives of the new coordinates $(\boldsymbol{\eta}, \theta)^{\top}$, and those of the original coordinates q as

$$\dot{\mathbf{q}} = \mathbf{L}(\boldsymbol{\eta}, \theta)[\dot{\boldsymbol{\eta}}, \dot{\theta}]^{\top}. \tag{169}$$

Then, by substituting the relations $q_i = \eta_i - \phi_i(\theta)$, $1 \leq i \leq (n-1)$, $q_n = \phi_n(\theta) + h(\boldsymbol{\eta}, \theta)$, (169), (168), their derivatives $\dot{q}_i(\theta, \boldsymbol{\eta})$, $1 \leq i \leq (n-1)$, $\dot{q}_n(\theta, \boldsymbol{\eta})$ into (150), the state equations, governing the dynamics of $\boldsymbol{\eta}$, are obtained as follows

$$\ddot{\boldsymbol{\eta}} = \mathbf{R}(\boldsymbol{\eta}, \dot{\boldsymbol{\eta}}, \theta, \dot{\theta}) + \mathbf{N_1}(\boldsymbol{\eta}, \theta)\mathbf{w} + \mathbf{N_2}(\boldsymbol{\eta}, \theta)\boldsymbol{\Gamma}. \tag{170}$$

Moreover, one can introduce a control transformation

$$\boldsymbol{\Gamma} = \mathbf{v} + \boldsymbol{\Gamma}_\star \tag{171}$$

where $\boldsymbol{\Gamma}_\star$ is the nominal input along the nominal target trajectory $\theta = \theta_\star$, $\dot{\theta} = \dot{\theta}_\star$, $\boldsymbol{\eta} = 0$, $\dot{\boldsymbol{\eta}}$. Then, combining (170) and (171) yields the dynamics of the $\boldsymbol{\eta}$ variables in the form

$$\ddot{\boldsymbol{\eta}} = \bar{\mathbf{R}}(\boldsymbol{\eta}, \dot{\boldsymbol{\eta}}, \theta, \dot{\theta}) + \mathbf{N_1}(\theta, \boldsymbol{\eta})\mathbf{w} + \mathbf{N_2}(\theta, \boldsymbol{\eta})\mathbf{v} \tag{172}$$

where the function $\bar{\mathbf{R}} = \mathbf{R}(\boldsymbol{\eta}, \dot{\boldsymbol{\eta}}, \theta, \dot{\theta}) + \mathbf{N_2}(\theta, \boldsymbol{\eta})\boldsymbol{\Gamma}_\star$ is nullified along the desired orbit. To fully describe the dynamics in the new coordinates (165), it remains to incorporate the plant dynamics of θ. Following (Shiriaev *et al.*, 2005), the local dynamics of (150) are given by

$$\begin{aligned} \bar{\alpha}(\theta)\ddot{\theta} + \bar{\beta}(\theta)\dot{\theta}^2 + \bar{\gamma}(\theta) = g_I(\boldsymbol{\eta}, \dot{\boldsymbol{\eta}}, \theta, \dot{\theta}, \ddot{\theta})I \\ + g_\eta(\boldsymbol{\eta}, \dot{\boldsymbol{\eta}}, \theta, \dot{\theta}, \ddot{\theta})\boldsymbol{\eta} + g_{\dot{\eta}}(\boldsymbol{\eta}, \dot{\boldsymbol{\eta}}, \theta, \dot{\theta}, \ddot{\theta})\dot{\boldsymbol{\eta}} + g_v(\boldsymbol{\eta}, \dot{\boldsymbol{\eta}}, \theta, \dot{\theta}, \ddot{\theta})\mathbf{v} \\ + g_w(\boldsymbol{\eta}, \dot{\boldsymbol{\eta}}, \theta, \dot{\theta}, \ddot{\theta})\mathbf{w} \end{aligned} \tag{173}$$

$$\ddot{\boldsymbol{\eta}} = \bar{\mathbf{R}}(\boldsymbol{\eta}, \dot{\boldsymbol{\eta}}, \theta, \dot{\theta}) + \mathbf{N_1}(\theta, \boldsymbol{\eta})\mathbf{w} + \mathbf{N_2}(\theta, \boldsymbol{\eta})\mathbf{v} \tag{174}$$

where the functions $g_I(\cdot)$, $g_\eta(\cdot)$, $g_{\dot{\eta}}(\cdot)$, $g_v(\cdot)$ and $g_w(\cdot)$ are smooth matrix functions of appropriate dimensions, and are nullified for $\boldsymbol{\eta} = \dot{\boldsymbol{\eta}} = \mathbf{0}$, while I is a solution of the differential equation

$$\dot{I} = \dot{\theta}\left[\frac{2}{\alpha(\theta)}g - \frac{2\beta(\theta)}{\alpha(\theta)}I\right] \tag{175}$$

with $g(\cdot) = g_I(\cdot)I + g_\eta(\cdot)\boldsymbol{\eta} + g_{\dot{\eta}}(\cdot)\dot{\boldsymbol{\eta}} + g_v(\cdot)\mathbf{v} + g_w(\cdot)\mathbf{w}$.

The *transversal coordinates* to the periodic motion are given by the $(2n-1)$-dimensional vector

$$\mathbf{x}_\perp = [I, \boldsymbol{\eta}, \dot{\boldsymbol{\eta}}]^\top, \tag{176}$$

which can be introduced in a vicinity of the solution

$$\eta_1 = \eta_{\star 1} = 0, \ldots, \eta_{n-1} = \eta_{\star(n-1)} = 0, \quad \theta = \theta_\star. \tag{177}$$

The choice of these transverse coordinates allows one to introduce a moving Poincaré section $S(\tau)$, which is determined in a time interval $[0, T_s]$. These sections are transversal to the target trajectory at each instant of time and at each point of the motion, and are illustrated in Fig. 50 (see (Leonov, 2006) for more details on moving Poincaré sections). In particular, the conserved quantity I, playing an important role in the transversal dynamics, is shown (Shiriaev *et al.*, 2008) to directly relate to the Euclidean distance from the orbit, generated by the reference trajectory $\theta_\star(t)$, to the actual plant trajectory for every $t \in [0, T_s]$.

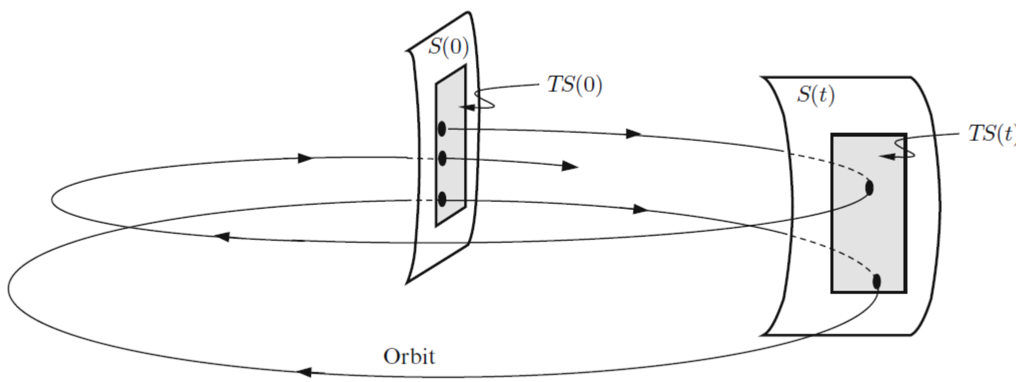

Figure 50: Moving Poincaré section for the periodic trajectory ($\theta_\star, \dot{\theta}_\star$), where $TS(\cdot)$ denotes the tangent space.

The underactuated orbital stabilization problem can now be treated, using the $\mathcal{H}_\infty$-control synthesis for fully actuated systems operating under unilateral constraints, that has been developed in Chapter 2.

6.2 Orbital synthesis via nonlinear $\mathcal{H}_\infty$-control

Between impacts, combining (175), (172), one arrives to the nonlinear dynamics of the transverse coordinates (176), defined by a nonlinear time-variant system of the form

$$\dot{\mathbf{x}}_\perp = \mathbf{f}(\mathbf{x}_\perp, t) + \mathbf{g_1}(\mathbf{x}_\perp, t)\mathbf{w} + \mathbf{g_2}(\mathbf{x}_\perp, t)\mathbf{v} \tag{178}$$

To complete this model, one needs to complement (178) with its corresponding impact map. This can be done by applying the instantaneous transformation proposed in (Freidovich *et al.*, 2008), that allows to introduce the impact law as

$$\mathbf{x}_\perp^+ = \mathcal{F}\mathbf{x}_\perp^- + \mathbf{w}_\perp^{\mathbf{d}} \tag{179}$$

with

$$\mathcal{F} = \mathbf{P}^+_{\mathbf{n(0)}} \mathrm{d}\bar{\mathbf{F}} \mathbf{P}^-_{\mathbf{n(T_s)}} \tag{180}$$

$$\mathbf{P}^+_{\mathbf{n(0)}} = \mathbf{L_c}(0)\left(\mathbf{I} - \frac{\mathbf{n}(0)\mathbf{n}^\top(0)}{\mathbf{n}^\top(0)\mathbf{n}(0)}\right) \tag{181}$$

$$\mathbf{P}^-_{\mathbf{n(T_s)}} = \left(\mathbf{I} - \frac{\mathbf{n}(T_s)\mathbf{m}^\top(T_s)}{\mathbf{n}^\top(T_s)\mathbf{m}}\right)\begin{bmatrix} \mathbf{L_c}(T_s) \\ \mathbf{n}^\top(T_s) \end{bmatrix}^{-1}\begin{bmatrix} \mathbf{I} \\ \mathbf{0} \end{bmatrix} \tag{182}$$

where $\bar{\mathbf{F}}$ is the map from the pre-impact states $(\mathbf{q}^-, \dot{\mathbf{q}}^-)$ to the post-impact states $(\mathbf{q}^+, \dot{\mathbf{q}}^+)$, T_s is the period of the target trajectory, $\mathbf{I}$ is an identity matrix of the appropriate dimensions (not to be confused with the scalar I, which is the solution of (175)), $w_\perp^d$ accounts for inaccuracies in the restitution law, $\mathbf{m}$ is a normal vector to the linearization of the switching surface, $\mathbf{n}(t) = [\dot{\mathbf{q}}_\star^\top(t), \ddot{\mathbf{q}}_\star(t)]^\top$ and $\mathbf{L_c}(\cdot)$ defines the Jacobian matrix of the coordinate transformation

$$[\Delta I, \Delta\boldsymbol{\eta}^\top, \Delta\dot{\boldsymbol{\eta}}^\top]^\top = \mathbf{L_c}(t)[\Delta\mathbf{q}^\top, \Delta\dot{\mathbf{q}}^\top]^\top \tag{183}$$

that relates the linear parts of the increments of the transverse coordinates and the linear parts of increments of the generalized coordinates, which in turn can be computed from the relations (165) and the formulas

$$\left.\frac{\partial I}{\partial \theta}\right|_{\substack{\theta=\theta_\star(t)\\ \dot\theta=\dot\theta_\star(t)}} = -2\ddot{\theta}_\star(t), \quad \left.\frac{\partial I}{\partial \dot\theta}\right|_{\substack{\theta=\theta_\star(t)\\ \dot\theta=\dot\theta_\star(t)}} = 2\dot{\theta}_\star(t). \tag{184}$$

For more details on this formulation, see the works by Freidovich *et al.* (2008); Freidovich and Shiriaev (2009).

Clearly, (178)-(179) define a hybrid nonlinear system that can be stabilized using the nonlinear $\mathcal{H}_\infty$ control theory presented before. The following result is now presented.

Theorem 6.1 *Consider the nonlinear time-variant hybrid system* (178)-(179)*. Let Hypothesis H1), inequality* (14)*, and condition C1) be satisfied with some $\gamma > 0$ (see sections 2.2.1 and 2.3.3). Then the transverse system* (178)-(179) *driven by the state feedback*

$$\mathbf{v} = -\mathbf{g_2}^\top \mathbf{P}_\varepsilon(s(\theta))\mathbf{x}_\perp \tag{185}$$

locally possesses a $\mathcal{L}_2$-gain less than γ, where $s(\theta)$ is an index parametrizing the particular leaf of the moving Poincaré section, to which the vector $x_\perp$ belongs at time moments t, that is, a smooth function that satisfies the identity $s(\theta_\star) = t$ for all $t \in [0, T_s]$. Moreover, the disturbance-free closed-loop transverse system (178)-(179), (185) *is uniformly asymptotically stable, which renders the desired orbit* (152) *orbitally asymptotically stable.*

Proof. The proof can be obtained by applying Theorem 2.3 to the nonlinear hybrid system (178)-(179). ∎

The solution $\mathbf{P}_\varepsilon(t)$ of the differential Riccati equation (54), subject to the boundary condition (77), relies on the transverse linearization (53) of the nonlinear dynamics (178) along the desired motion (177), after an output to be controlled (51) has been defined.

6.3 Conclusions

The robust $\mathcal{H}_\infty$ output feedback synthesis was developed for underactuated mechanical systems with unilateral constraints. Once a nominal feasible periodic trajectory to follow has been prescribed for the system, the analysis of the transversal dynamics allowed to determine sufficient conditions for attenuating the plant disturbances around the prescribed trajectory. This result will be used in the next chapter to orbitally stabilize a five-link underactuated biped.

Chapter 7. Orbital Stabilization of an Underactuated Bipedal Gait via $\mathcal{H}_\infty$ Control

The objective of this chapter is to extend the results of the previous chapter to the robust orbital stabilization of an underactuated bipedal robot, considering that only imperfect position measurements are available for feedback. The capabilities of the resulting synthesis are illustrated in simulation runs made on an emulator, for several disturbance scenarios.

7.1 Model of a Planar Five-Link Bipedal Robot

The bipedal robot considered in this section is walking on a rigid and horizontal surface. It is modeled as a planar biped, which consists of a torso, hips, two legs with knees but no actuated ankles (see Fig. 51). The walking gait is composed of single support phases and impacts. The complete model of the biped robot consists of two parts: the differential equations describing the dynamics of the robot during the swing phase, and an impulse model of the contact event (the impact between the swing leg and the ground is modeled as a contact between two rigid bodies as in the work of Chevallereau *et al.* (2003)). It is assumed that the only measurements available are the joints positions, since no velocity sensors are used. During the single-support phase, the degree of underactuation is equal

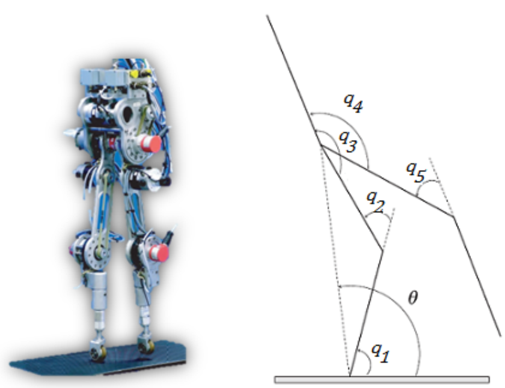

Figure 51: Left: Five-link bipedal planar robot Rabbit

to one. Let us assume the stance leg tip is acting as a pivot on the ground, that is, there is no slipping and no take off of the stance leg tip. Then the biped's model in single support phase between successive impacts can be written as:

$$\begin{pmatrix} D_{11} & \mathbf{D_{12}} \\ \mathbf{D_{21}} & \mathbf{D_{22}} \end{pmatrix} \begin{pmatrix} \ddot{q}_1 \\ \ddot{\mathbf{q}}_\mathbf{a} \end{pmatrix} + \begin{pmatrix} H_1 \\ \mathbf{H_2} \end{pmatrix} = \begin{pmatrix} 0 \\ \mathbf{\Gamma} \end{pmatrix} + \begin{pmatrix} w_1 \\ \mathbf{w_2} \end{pmatrix} \tag{186}$$

where $\mathbf{q} = (q_1, q_2, q_3, q_4, q_5)^\top$ is the 5×1 vector of generalized coordinates, $\mathbf{q_a} = (q_2, q_3, q_4, q_5)^\top$ the 4×1 vector of actuated joint angles, $\mathbf{\Gamma} = (\Gamma_1, \Gamma_2, \Gamma_3, \Gamma_4)^\top$ is the 4×1 vector of joint torques (see Fig. 51), $\mathbf{H} = \mathbf{C}(\mathbf{q}, \dot{\mathbf{q}})\dot{\mathbf{q}} + \mathbf{G}(\mathbf{q}) = [H_1, \mathbf{H_2}^\top]^\top$, and $\mathbf{w_c}$ is the 5×1 vector of disturbances, with components w_1, and $\mathbf{w_2}$, representing the disturbances in the under-actuated and actuated subsystems, respectively. D_{11} and H_1 are scalars, $\mathbf{D_{12}}$ is a 1×4 vector, $\mathbf{D_{21}}$ and $\mathbf{H_2}$ are 4×1 vectors, and $\mathbf{D_{22}}$ is a 4×4 matrix.

The double support phase is instantaneous, so an impact appears when the swing leg tip touches the ground, at an *a priori* unknown collision time instant $t = T_I$; for this time the swing leg touches the ground. It is assumed that the impact is passive, absolutely inelastic, and that the legs do not slip. The corresponding algebraic equations for the velocities jumps, that is, the restitution law (151), can be obtained through integration of biped's equations of motions, taking into account the ground reactions, for the infinitesimal time from T_I^- to T_I^+. Its analytic expression can be found in (Djoudi *et al.*, 2005).

Model (150) was written taking into account implicitly the contact between the stance leg and the ground, without take-off nor sliding. Since just after the impact, the legs exchange their role, the former swing leg must now become the stance leg and vice versa, a change of coordinates after the impact is necessary. This coordinate swap is included as part of the impact map (Chevallereau *et al.*, 2003). The overall bipedal robot model can be expressed as a nonlinear system with impulse effects (150)-(151), with $F(q)$ being the altitude of the swing leg tip, and $\mathbf{w_d}$ accounts for external disturbances in the impact phase, such as modelling errors, uneven ground, etc.

7.2 Motion Planning

The control of the biped for the walking gait, consists in tracking a reference trajectory $(\mathbf{q}_\star(\theta)^\top, \dot{\mathbf{q}}_\star(\theta, \dot{\theta})^\top)^\top$. The under-actuation characteristic of the biped in single support phase has to be taken into account because it is not possible to prescribe the five generalized coordinates independently of the biped's dynamic with only four torques. An instantaneous double support phase is considered. Also, in steady state, the motion is symmetric with respect to the two legs. The trajectory is then obtained using a nonlinear dynamics optimization (Chevallereau *et al.*, 2003; Miossec and Aoustin, 2006; Tlalolini *et al.*, 2011), briefly described below.

First, the well known approach of virtual constraints (Grizzle *et al.*, 2001; Aoustin and Formalsky, 2003; Westervelt *et al.*, 2007) was used for the definition of the motion. These virtual constraints are imposed as reference trajectories over the actuated coordinates $\mathbf{q_a}$, and they are chosen to be functions of the geometric variable

$$\theta = q_1 + 0.5q_2 \tag{187}$$

instead of time (Aoustin *et al.*, 2006). This variable θ represents the angle of the line connecting the stance leg end to the hip against the floor, and is strictly monotonic along each step. These functions are chosen as Bézier polynomials of fifth order (Bezier, 1972).

Two of the coefficients of the Bézier polynomial are selected on the basis of achieving invariance of the biped's hybrid zero dynamics (160), (164) (see (Westervelt *et al.*, 2007, Corollary 6.1, p.143)). The choice of the remaining free parameters in the Bézier polynomials to design the walking gait is stated as a parameter optimization problem.

The objective is to minimize a sthenic criterion (whose cost function roughly represents electric motor energy per distance traveled) to reduce the torques peak demands over a step. In addition, the solution of this optimization problem takes into account a set of nonlinear constraints: there is no take off of the support leg end; the support leg end does not slide on the floor; the swing leg end height ensures that a contact with the ground will appear only at the end of the step; and a fixed walking rate. For more details, the interested reader can consult the work by Westervelt *et al.* (2004). This parameter optimization problem may be solved with any number of the numerical optimization tools available. In our case, the optimization problem was solved with MATLAB's constrained nonlinear optimization tool *fmincon*.

7.3 $\mathcal{H}_\infty$ Control synthesis

The objective of this section is to apply the results of Section 6.2 to orbitally stabilize the underactuated bipedal robot to the desired motion presented in the previous section, supposing that both positions and velocities are measured. Afterwards, assuming that only positions are available for measurements, $\mathcal{H}_\infty$ output feedback synthesis is involved to estimate the missing velocities.

7.3.1 State Feedback Synthesis

The control objective for the 5-link bipedal robot is to design a nonlinear $\mathcal{H}_\infty$ position feedback controller that follows a pre-specified periodic motion

$$\mathbf{q}_\star(\theta) = \mathbf{\Phi}(\theta) = [\phi_1(\theta), \phi_2(\theta), \phi_3(\theta), \phi_4(\theta), \phi_5(\theta)]^\top \tag{188}$$

$$\dot{\mathbf{q}}_\star(\theta, \dot{\theta}) = \mathbf{\Phi}'(\theta) = \frac{\partial \mathbf{\Phi}(\theta)}{\partial \theta}\dot{\theta} \tag{189}$$

$$\ddot{\mathbf{q}}_\star(\theta, \dot{\theta}, \ddot{\theta}) = \mathbf{\Phi}''(\theta) = \frac{\partial \mathbf{\Phi}(\theta)}{\partial \theta}\dot{\theta}^2 + \frac{\partial^2 \mathbf{\Phi}(\theta)}{\partial \theta^2}\ddot{\theta} \tag{190}$$

Let us define the error variables

$$\eta_1 = q_2 - \phi_2(\theta), \dots \; \eta_4 = q_5 - \phi_5(\theta) \tag{191}$$

and the error vector $\boldsymbol{\eta} = [\eta_1, \dots, \eta_4]^\top$. Introducing the control transformation

$$\mathbf{\Gamma} = \left(\mathbf{H_2} - \frac{\mathbf{D_{21}}}{D_{11}}H_1\right) + \mathbf{D_T}(\mathbf{\Phi_a''}(\theta) + \mathbf{v}), \tag{192}$$

specified with $\mathbf{D_T} = \mathbf{D_{22}} - \frac{\mathbf{D_{21}}\mathbf{D_{12}}}{D_{11}}$ and $\mathbf{\Phi_a''}(\theta) = [\phi_2''(\theta), \dots, \phi_5''(\theta)]^\top$, the dynamics (172) can be represented in the form of the disturbed double integrator

$$\ddot{\boldsymbol{\eta}} = \mathbf{v} + \mathbf{D_T^{-1}}\mathbf{w_2}, \tag{193}$$

where $\mathbf{w_2}$ is the disturbance, affecting the actuated subsystem of (186).

By left-multiplying (186) by the ortogonal matrix $\mathbf{B}^\perp(\mathbf{q}) = [1, 0, 0, 0, 0]$, and combining it with (190), one can obtain the dynamics (160), (164) as follows

$$\ddot{\theta} = \frac{-\left(\frac{D_{11}}{2}\frac{\partial^2\phi_2(\theta)}{\partial\theta^2} + \mathbf{D_{12}}\frac{\partial^{\mathbf{2}}\mathbf{\Phi_a}(\theta)}{\partial\theta^{\mathbf{2}}}\right)\dot{\theta}^2 - H_1}{D_{11}\left(1 - \frac{1}{2}\frac{\partial\phi_2(\theta)}{\partial\theta}\right) + \mathbf{D_{12}}\frac{\partial\mathbf{\Phi_a}(\theta)}{\partial\theta}} \tag{194}$$

$$\begin{bmatrix} \theta^+ \\ \dot{\theta}^+ \end{bmatrix} = \Delta_\theta(\theta^-, \dot{\theta}^-) = \theta \circ \psi(\mathbf{q}_\star(\theta)^-, \dot{\mathbf{q}}_\star(\theta)^-) \tag{195}$$

with $\mathbf{\Phi_a}(\theta) = [\phi_2(\theta), \ldots, \phi_5(\theta)]^\top$.

From (194), one can clearly identify the terms $\bar{\alpha}(\theta)$, $\bar{\beta}(\theta)$ and $\bar{\gamma}(\theta)$. The denominator term of (194), which corresponds to $\bar{\alpha}(\theta)$ in (160), is a virtual inertia of the biped with respect to the contact point between the leg tip and the ground (Chevallereau *et al.*, 2003). This virtual inertia term can cross zero during a walking gait. However the optimization algorithm of getting the reference trajectory $\mathbf{q_{a\star}}(\theta)$ involves a constraint that ensures this term to be non-zero.

Therefore, by using the transverse coordinates $\mathbf{x}_\perp = [I.\boldsymbol{\eta}^\top, \dot{\boldsymbol{\eta}}^\top]^\top$, one can rewrite the biped dynamics in the form (178), (179), being specified with

$$\mathbf{f}(\mathbf{x}_\perp, t) = \begin{bmatrix} -\frac{2\dot{\theta}\bar{\beta}(\theta)}{\bar{\alpha}(\theta)} I \\ \dot{\boldsymbol{\eta}} \\ \mathbf{0} \end{bmatrix}, \tag{196}$$

$$\mathbf{g_1}(\mathbf{x}_\perp, t) = \begin{bmatrix} \frac{2\dot{\theta}}{\bar{\alpha}(\theta)} & \mathbf{0_{1\times 4}} \\ \mathbf{0_{4\times 1}} & \mathbf{0_{4\times 4}} \\ \mathbf{0_{4\times 1}} & \mathbf{D_T^{-1}} \end{bmatrix}, \tag{197}$$

$$\mathbf{g_2}(\mathbf{x}_\perp, t) = \begin{bmatrix} \frac{2\dot{\theta}}{\bar{\alpha}(\theta)}(D_{11}\mathbf{K}_\perp - \mathbf{D_{12}}) \\ \mathbf{0_{4\times 4}} \\ \mathbf{I_{4\times 4}} \end{bmatrix}, \tag{198}$$

$$\mathbf{K}_\perp = \left[\frac{1}{2}, 0, 0, 0\right], \tag{199}$$

$$\mathcal{F} = \mathbf{P}^+_{\mathbf{n(0)}} \mathrm{d}\psi(\mathbf{q}, \dot{\mathbf{q}}) \mathbf{P}^-_{\mathbf{n(T_s)}} \tag{200}$$

with θ, $\dot{\theta}$ taken along the predefined solution of (194), and the matrices $\mathbf{P}^+_{\mathbf{n(0)}}$, $\mathbf{P}^-_{\mathbf{n(T_s)}}$ come from the instant transformation (180)-(182) applied to the restitution function $\psi(\mathbf{q}^{-}, \dot{\mathbf{q}}^{-})$ (Freidovich *et al.*, 2008). The matrices $\mathbf{0_{n\times m}}$ and $\mathbf{I_{n\times m}}$ represent zero and identity matrices of dimensions $n \times m$.

It remains to define the output to be controlled (2). Inspired by the work of Isidori and Astolfi (1992), such an output can be written as

$$\mathbf{z} = \left[\begin{array}{cccc} \mathbf{0_{1\times 4}} & \rho_0 I & \rho_1 \boldsymbol{\eta}^\top & \rho_2 \dot{\boldsymbol{\eta}}^\top \end{array} \right]^\top + \mathbf{v}^\top \left[\begin{array}{cc} \mathbf{I_{4\times 4}} & \mathbf{0}^\top_{\mathbf{9\times 4}} \end{array} \right]^\top \tag{201}$$

which satisfies (10), with ρ_0, ρ_1, ρ_2 being positive scalars. Finally, the controller $\mathbf{v}$ can be synthesized by applying Theorem 6.1 to the transverse system (178), (179) specified with (196)-(200), considering the output (201).

Since the feedback transformation (192), and the $\mathcal{H}_\infty$ controller (185) make use of the measurements of positions and velocities, in the next section, the output feedback synthesis is developed so as to estimate the non-measured velocities.

7.3.2 Output feedback synthesis

According to (150)-(151), the desired periodic motion corresponding to the orbit $\mathcal{O}_\star$ is governed by

$$\mathbf{D}(\mathbf{q}_\star)\ddot{\mathbf{q}}_\star + \mathbf{H}(\mathbf{q}_\star, \dot{\mathbf{q}}_\star) = \mathbf{B}\boldsymbol{\Gamma}^{\mathrm{s}}_\star. \tag{202}$$

The input torque $\boldsymbol{\Gamma}^{\mathrm{s}}_\star$ is designed as (192), which forces the dynamics of (150), (151), (171), (185) to stay on the periodic orbit $\mathcal{O}_\star$ when the system is started on $\mathcal{O}_\star$. Since $\boldsymbol{\Gamma}^{\mathrm{s}}_\star$ relies on the measurement of the generalized positions and velocities (the latter not available), $\boldsymbol{\Gamma}$ is substituted by the dynamic controller

$$\boldsymbol{\Gamma} = \boldsymbol{\Gamma}^{\mathrm{s}}_\star + \mathbf{u}(\boldsymbol{\xi}, t) \tag{203}$$

where $\mathbf{u}(\boldsymbol{\xi}, t)$ has the form (6), and its internal state $\boldsymbol{\xi}$ provides an estimation of the non-measured variables. This can be done by defining the state vectors $\mathbf{x_1} = \mathbf{q} - \mathbf{q}_\star$, $\mathbf{x_2} = \dot{\mathbf{q}} - \dot{\mathbf{q}}_\star$, and combining (150), (153) and (202), the error dynamics can be rewritten as

$$\begin{aligned}\dot{\mathbf{x}}_\mathbf{1} &= \mathbf{x}_\mathbf{2}\\ \dot{\mathbf{x}}_\mathbf{2} &= \mathbf{D}(\mathbf{x}_\mathbf{1}+\mathbf{q}_\star)^{-\mathbf{1}}[\mathbf{D}(\mathbf{q}_\star)\ddot{\mathbf{q}}_\star+\mathbf{H}(\mathbf{q}_\star,\dot{\mathbf{q}}_\star)-\mathbf{H}(\mathbf{x}_\mathbf{1}+\mathbf{q}_\star,\mathbf{x}_\mathbf{2}+\dot{\mathbf{q}}_\star)+\mathbf{B}\mathbf{u}+\mathbf{w}_\mathbf{c}]-\ddot{\mathbf{q}}_\star\end{aligned} \tag{204}$$

with an output to be controlled (2) inspired by the work of Isidori and Astolfi (1992), which satisfies (10) and can be written as

$$\mathbf{z} = \rho_3 \begin{bmatrix} \mathbf{0}_{\mathbf{1}\times\mathbf{4}} & x_{1_2} & x_{1_3} & x_{1_4} & x_{1_5} \end{bmatrix}^\top + \mathbf{u}^\top \begin{bmatrix} \mathbf{I}_{\mathbf{4}\times\mathbf{4}} & \mathbf{0}_{\mathbf{4}\times\mathbf{4}} \end{bmatrix}^\top \tag{205}$$

where $x_{1_i} = q_i - q_{i\star}$, $i = 2,3,4,5$ (so only the actuated coordinates error $\mathbf{q_a} - \mathbf{q_{a\star}}$ is considered), ρ_3 is a positive scalar, and with the set of measurements

$$\mathbf{y} = \mathbf{x}_\mathbf{1} + \mathbf{w}_\mathbf{y} \tag{206}$$

where $\mathbf{w_y}$ is a 5×1 vector of measurement disturbances (for a practical application, to estimate the absolute orientation, and thus q_1 and θ, the use of an inertial measurement unit is introduced at Section 7.4.2). The generic system (1)-(5) can be specified with

$$\begin{aligned}\mathbf{f}(\mathbf{x},t) = &\begin{bmatrix} \mathbf{x}_2 \\ \mathbf{D}(\mathbf{x}_\mathbf{1}+\mathbf{q}_\star)^{-\mathbf{1}}[\mathbf{H}(\mathbf{q}_\star,\dot{\mathbf{q}}_\star)+\mathbf{D}(\mathbf{q}_\star)\ddot{\mathbf{q}}_\star] \end{bmatrix}\\ + &\begin{bmatrix} \mathbf{0}_{\mathbf{5}\times\mathbf{1}} \\ -\mathbf{D}(\mathbf{x}_\mathbf{1}+\mathbf{q}_\star)^{-\mathbf{1}}[\mathbf{H}(\mathbf{x}_\mathbf{1}+\mathbf{q}_\star,\mathbf{x}_\mathbf{2}+\dot{\mathbf{q}}_\star)]-\ddot{\mathbf{q}}_\star \end{bmatrix}\end{aligned} \tag{207}$$

$$\mathbf{g}_\mathbf{1}(\mathbf{x},t) = \begin{bmatrix} \mathbf{0}_{\mathbf{5}\times\mathbf{5}} & \mathbf{0}_{\mathbf{5}\times\mathbf{5}} \\ \mathbf{0}_{\mathbf{5}\times\mathbf{5}} & \mathbf{D}(\mathbf{x}_\mathbf{1}+\mathbf{q}_\star)^{-\mathbf{1}} \end{bmatrix}, \tag{208}$$

$$\mathbf{g}_\mathbf{2}(\mathbf{x},t) = \begin{bmatrix} \mathbf{0}_{\mathbf{5}\times\mathbf{4}} \\ \mathbf{D}(\mathbf{x}_\mathbf{1}+\mathbf{q}_\star)^{-\mathbf{1}}\mathbf{B} \end{bmatrix}, \ \mathbf{h}_\mathbf{1}(\mathbf{x}) = \begin{bmatrix} \mathbf{0}_{\mathbf{4}\times\mathbf{1}} \\ \rho_1\mathbf{K}_\mathbf{o}\mathbf{x}_1 \end{bmatrix}, \tag{209}$$

$$\mathbf{k}_{\mathbf{12}}(\mathbf{x}) = \begin{bmatrix} \mathbf{I}_{\mathbf{4}\times\mathbf{4}} \\ \mathbf{0}_{\mathbf{4}\times\mathbf{4}} \end{bmatrix}, \ \mathbf{K}_\mathbf{o} = \begin{bmatrix} \mathbf{0}_{\mathbf{4}\times\mathbf{1}} & \mathbf{I}_{\mathbf{4}\times\mathbf{4}} \end{bmatrix}, \tag{210}$$

$$\mathbf{h}_\mathbf{2}(\mathbf{x}) = \mathbf{x}_\mathbf{1}, \ \mathbf{k}_{\mathbf{21}}(\mathbf{x}) = \begin{bmatrix} \mathbf{I}_{\mathbf{5}\times\mathbf{5}} & \mathbf{0}_{\mathbf{5}\times\mathbf{5}} \end{bmatrix}, \tag{211}$$

$$\boldsymbol{\mu}(\mathbf{x},t) = \psi(\mathbf{x_1}+\mathbf{q}_\star, \mathbf{x_2}+\dot{\mathbf{q}}_\star) - \psi(\mathbf{q}_\star, \dot{\mathbf{q}}_\star), \tag{212}$$

$$F(\mathbf{x},t) = F_0(\mathbf{x_1}+\mathbf{q}_\star), \quad \boldsymbol{\omega}(\mathbf{x},t) = \mathbf{I_{5\times 5}} \tag{213}$$

where the function $F_0(\mathbf{q})$ is given by the swing foot height.

If the output (2) specified with (210) is driven to zero, the system will be driven to the zero dynamics manifold

$$\mathcal{Z} = \{(\mathbf{q},\dot{\mathbf{q}}) | \mathbf{q_a} = \mathbf{q_{a\star}}(\theta), \dot{\mathbf{q}}_\mathbf{a} = \frac{\partial \mathbf{q_{a\star}}(\theta)}{\partial\theta}\dot{\theta}\} \tag{214}$$

and the dynamic behavior of θ (restriction dynamics) will be given by the hybrid zero dynamics (194), (195).

Finally, the last theorem of this work is presented below.

Theorem 7.1 *Let conditions C1)-C2), and hypotheses H1) and H4) (see Chapter 2) be satisfied for the hybrid system* (1)-(5) *specified with* (207)-(213). *Then, the dynamic control* (62a)-(62b) *is a solution to the $\mathcal{H}_\infty$-control problem for the closed-loop mechanical system* (150)-(151)*,* (203)*.*

Proof. The proof can be obtained by applying Theorem 2.2 to the hybrid system (1)-(5) specified with (207)-(213). ■

This method has been successfully implemented to orbitally stabilize periodic orbits in unrestricted mechanical systems of underactuation degree 1 (see Meza-Sanchez *et al.* (2011)).

Thus, in the disturbed case, even if the output (2), (205) is not driven to zero, the $\mathcal{L}_2$-gain (7) of the system is still locally less than the specified value γ, keeping the output bounded around zero.

It is important to remark that $\dot{\theta}$ and $\ddot{\theta}$, necessaries to define the desired velocities $\dot{\mathbf{q}}_\star$ and accelerations $\ddot{\mathbf{q}}_\star$, need to be estimated, since only position measurements are considered; this estimation is effectuated using the states from (62a).

This result will be used in the next section to robustly stabilize a planar and underactuated biped robot on a desired periodic orbit.

7.4 Numerical tests

The parameters considered in this section are those of "Rabbit" (Chevallereau *et al.*, 2003). Here the application of the control law (203) is considered to track a geometrical-reference trajectory defined using a virtual constraints approach. The period and the length of the nominal walking gait, which is obtained by optimization, are $0.56\ s$ and $0.45\ m$. The average walking velocity is $0.80\ m \cdot s^{--1}$. This cyclic walking gait was tested in closed loop for several steps.

The control synthesis is performed in two steps. The first step consists in designing the state feedback control (185), (192) via the application of Theorem 6.1 to the transverse dynamics (178), (179), specified with (196)-(200). The matrices $\mathbf{A}$, $\mathbf{B_1}$, $\mathbf{B_2}$, and $\mathbf{C_1}$, used in (54) come from the transverse linearization (50), (51) of this transversal system. By iterating on γ and ε, a minimal value γ_{min} is to be found among all γ such that on the period T_s, (54) possesses a positive definite solution $\mathbf{P}_\varepsilon(t)$ for some $\varepsilon > 0$ provided that relation (77) holds true for the solution values at the initial time instant t_0, and at the first impact time instant $t_1 = t_0 + T_s$. Then, this solution should be continued to the right with the periodicity T_s. Since generally speaking, $\mathbf{P}_\varepsilon(t_0) \neq \mathbf{P}_\varepsilon(t_1)$, the resulting T_s-periodic function $\mathbf{P}_\varepsilon(t)$ is expected to undergo discontinuities at the impact time instants $t_i = t_0 + iT_s,\ i = 1, 2, \ldots$. Specifying the values $\rho_0 = 1$, $\rho_1 = 200$, $\rho_2 = 10$, and following the above iteration procedure, a value $\gamma_{min} \approx 8000$ is found for $\varepsilon = 0.001$. To avoid dealing with high controller gains, the value $\gamma = 10000$ is subsequently used in the simulation runs.

Figure 52 illustrates the eigenvalues of the periodic solution $\mathbf{P}_\varepsilon(t)$, thus obtained. It is observed from the figure that the periodic eigenvalues, also undergoing discontinuities at the impact time instants, remain positive definite along the period. The positive definiteness of $\mathbf{P}_\varepsilon(t)$ is thus confirmed for all $t \geq 0$.

The second step consists of the design of the output feedback synthesis (203), where $\mathbf{\Gamma}^{\mathbf{s}}_{\star}$ is the state feedback control (192) designed in the previous step, and $\mathbf{u}(\boldsymbol{\xi}, t)$ is calculated applying Theorem (7.1) to the hybrid system (1)-(5) specified with (207)-(213). The

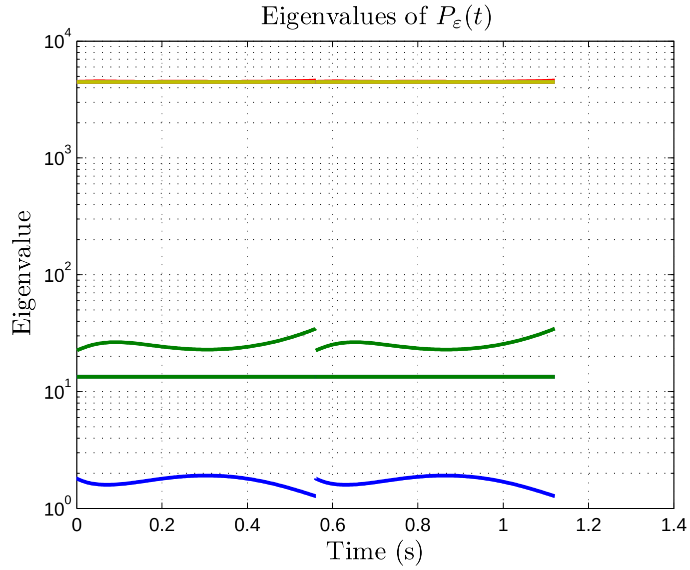

Figure 52: The eigenvalues of the solution $\mathbf{P}_\varepsilon(t)$ of (54), plotted for two steps. Due to the multiplicity of the eigenvalues, only four distinct eigenvalues among nine are plotted.

controller parameters to be used in (54) and (55) are chosen to enforce C1), C2), H1), and H4) through setting a positive value for ρ_3 and γ is set to the value found in the previous step. Also, it is important to consider that a higher value of ρ_3 provides faster stabilization (which is important so as to reach the smallest possible vicinity of the reference trajectory, fast enough before the next impact appears), but as it increases it also leads to increase the controller gain of $\mathbf{u}$. Variable ε in (54)-(55) is set to once again set to a small value, only to guarantee asymptotical stability. Using the value $\rho_3 = 100$, and setting $\varepsilon = 0.001$, and $\gamma = 10000$, (54)-(55) are verified to have a symmetric positive definite and periodic solution, and $\mathbf{u}$ is calculated from (62a)-(62b). The non-measured velocities needed for step 1, are estimated using (62a).

For every case in the following subsections, the reaction forces were verified so as to ensure that the legs do not slip nor take off. The simulations were performed using an event-driven algorithm, that is, integration of the continuous dynamics between events (impacts), and the application of algebraic conditions when an event occurs (Heemels and Brogliato, 2003).

7.4.1 Undisturbed case

Figure 53 presents the phase plane $\theta, \dot{\theta}$ for the undisturbed plant dynamics (150)-(151) ($\mathbf{w_0} = \mathbf{w_c} = \mathbf{w_d} = \mathbf{0}$), where the initial conditions of the plant (positions and velocities) were deviated 5% from the reference motion initial condition (the estimator (62a) initial conditions were the reference motion initial condition, so an initial estimation error also exists). It can be seen that the plant evolution converges asymptotically to a limit cycle (depicted in blue), which represents the reference motion limit cycle. This asymptotical convergence can also be appreciated from the Poincaré map presented in Fig. 54, where a Poincaré section is taken at $\theta = \pi/2\ rad$ (black line in Fig. 53), where it is clear that the plant dynamics evolves towards a fixed point, given by the blue line. It is important to remark that this Poincaré section is chosen instead of the predefined impact configuration ($\theta = \theta_f$), since in the disturbed scenario this configuration may be different due to the influence of the external disturbances.

When the dynamics of variable θ converge to the limit cycle, all of the joints positions will converge as well, as can be seen from Fig. 55 for the first four steps; after a short transitory response (evident during the first step, i.e. between $t = 0$, and $t = 0.55\ s$), all the joints attain a periodic behavior, as well as the torques depicted in Fig. 56. This fact will be taken into account to present the results of the following sections.

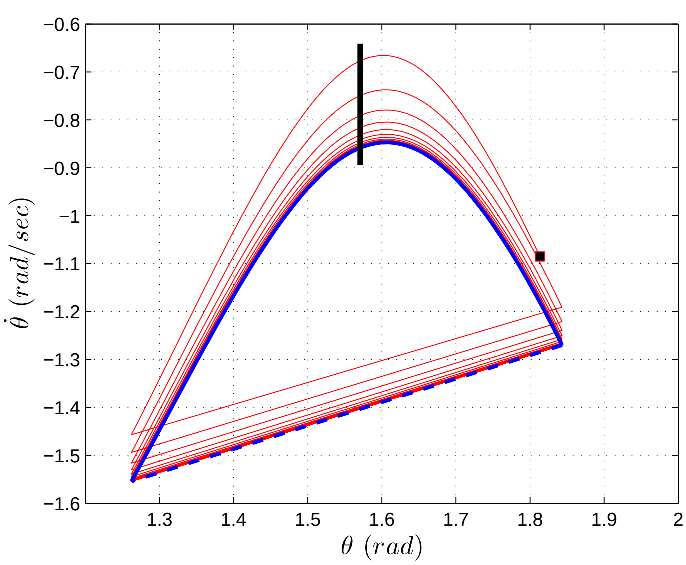

Figure 53: Phase plane of θ for the undisturbed plant dynamics, with non-zero initial conditions, for 18 steps. Red: Plant evolution converging to a limit cycle. Blue: Reference motion limit cycle. The initial point is indicated by the black square.

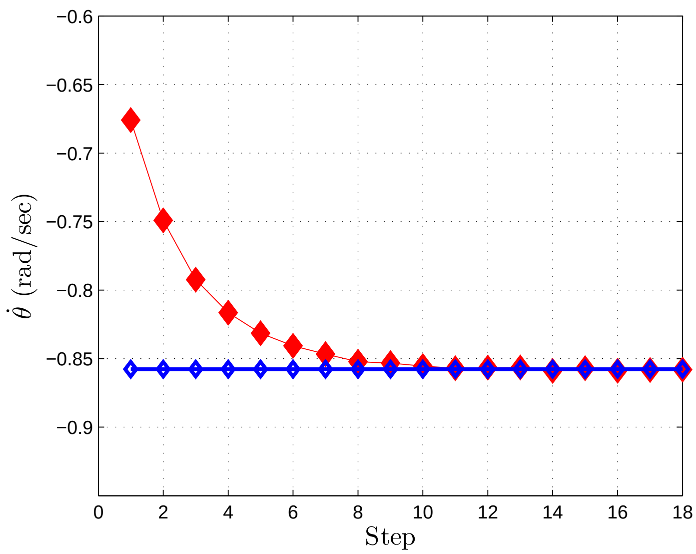

Figure 54: Poincaré Mapping at $\theta = \pi/2\ rad$, of the undisturbed plant dynamics, with non-zero initial tracking errors, for 18 steps. Red: Plant evolution converging to a fixed point. Blue: Reference motion fixed point.

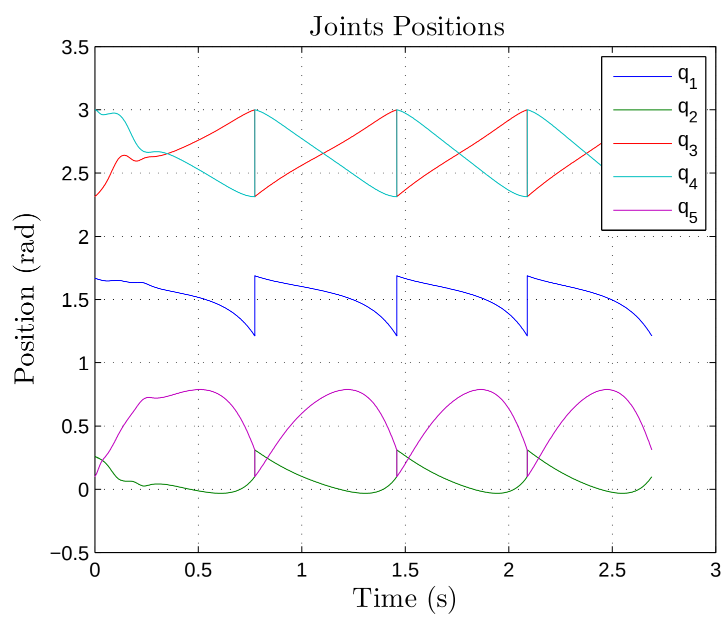

Figure 55: Joint positions for the undisturbed system, with non-zero initial conditions. After a transitory evolution, evident during the first step, all the joints converge to a periodic motion.

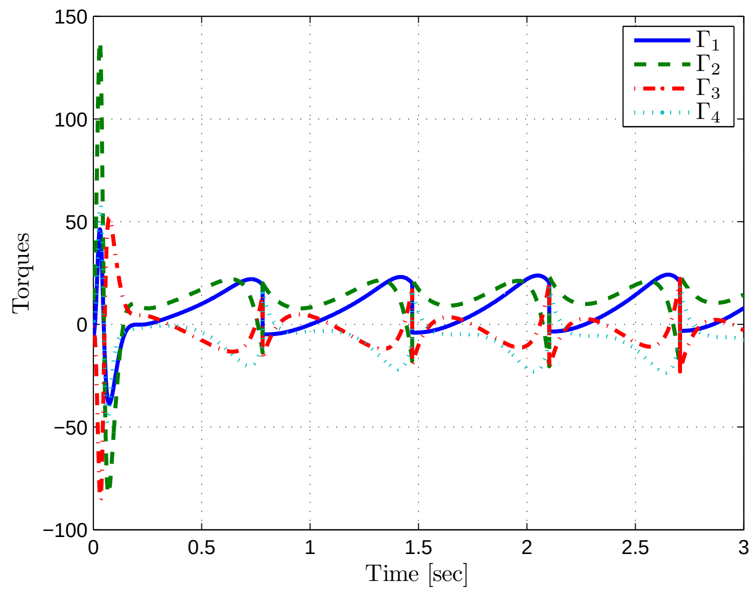

Figure 56: Joint torques for the undisturbed system, with non-zero initial conditions. After a transitory evolution, evident during the first step, all the joints converge to a periodic motion.

7.4.2 Noise in orientation measurement

In the case of the measurement of q_1, which is needed for developing the present algorithm, the biped Rabbit is not equipped with a sensor that measures this coordinate accurately (Chevallereau *et al.*, 2003). An alternative way to estimate q_1 would be from the measurement of orientation from an inertial measurement unit (IMU). IMUs are very useful sensors that can report measurements about three axes, reducing the number of independent sensors needed on the robot. However, the use of an IMU may present some problems rising from nonlinearities or systematic error in the sensor as well as random sensor noise (Angelosanto, 2008). While the Kalman filter has been used to reduce the effect of the noise in the measurements in many robotic applications (see for example the work from Alcaraz-Jiménez *et al.* (2013)), in this work the estimator (62a), included in the synthesis presented in theorem 2.1, was used.

By simulating an IMU similar to the presented at Alcaraz-Jiménez *et al.* (2013), with 1% precision in the range of $\pm 2G$ accelerations, the controller was tested (see Fig. 57) considering that the plant is started at the same initial conditions as the reference motion (so the effects of the disturbances introduced by the IMU are separately analyzed). The IMU is considered to be placed at the hip (as shown in Fig. 57); when the biped is in simple

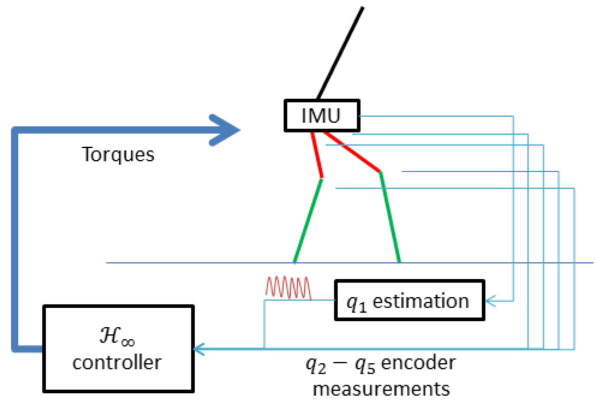

Figure 57: IMU connection to the $\mathcal{H}_\infty$-controller.

support, by considering the measurements of the horizontal and vertical accelerations, a_x and a_y, passing both by a double integrator, the unmeasurable coordinate q_1 (and in consequence, θ) is estimated using the knowledge of the geometrical relations (see Fig. 51) between the position of the IMU (hip), the lengths of the legs and the measurable angle q_2; then white noise was introduced to attain the desired precision. The dynamics of θ after several steps, achieve the cycle shown in Fig. 58. It can be seen that a stable cycle, around the nominal cycle, is attained even after 8 steps.

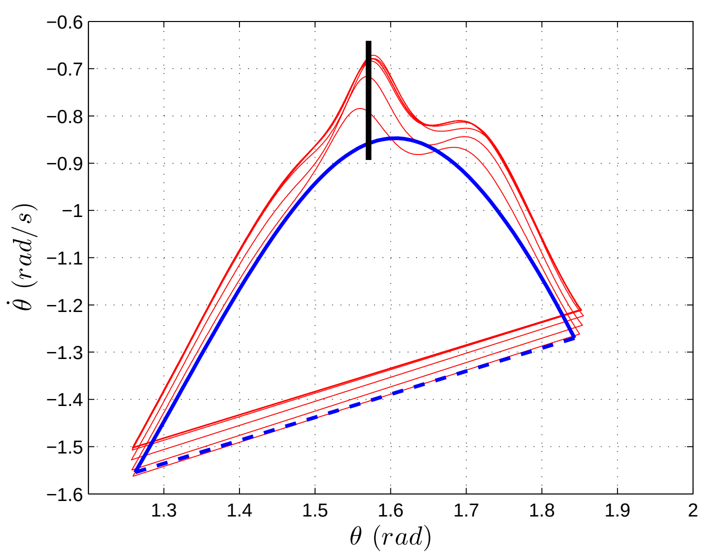

Figure 58: Phase plane of θ, $\dot{\theta}$, for the behavior obtained by estimating q_1 from an IMU with 1% precision, under the presence of white noise, for 8 steps. Blue: nominal cycle. Red: actual cycle.

Then, it was tested again, considering a 10% of error in the measurement considering again white noise. The behavior of the estimator (62a) is shown in Fig. 59, where it can clearly be seen the attenuation effect of the $\mathcal{H}_\infty$-estimator. The resulting Poincaré map after 8 steps of this disturbed system is shown in Fig. 60, where a maximum deviation of

$0.23\ rad/sec$ is obtained and stable walking is achieved.

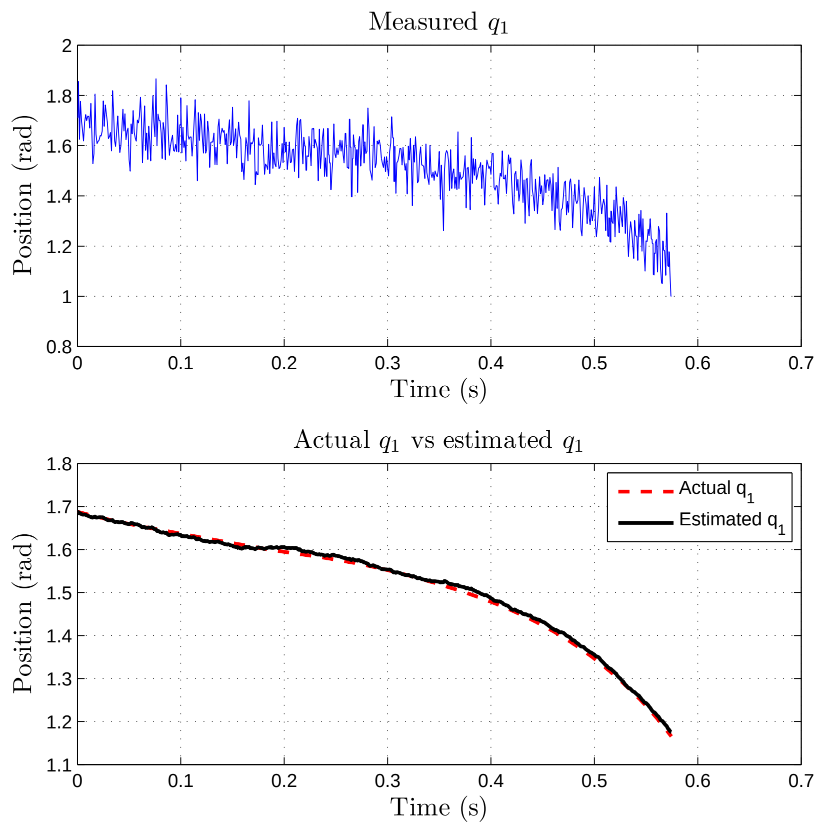

Figure 59: Estimation of q_1 using the $\mathcal{H}_\infty$-estimator (62a)**, along one step.**

7.4.3 Floor height variation

As it was done in the work by Dai and Tedrake (2013), an analysis of the biped walking over uneven terrain is made (see Fig. 61). In the former article, the virtual slope for the same biped robot was varied from $-2°$ to $2°$. Also, a perfect knowledge of the generalized positions and velocities was assumed. A direct comparison cannot be made for two reasons: first, the introduction of the estimator (62a) increases the minimum value of γ that can be achieved (in Dai and Tedrake (2013), a $\gamma \in [5000, 6000]$ is used, whereas in the present work a minimum value of $\gamma_{min} = 9800$ is obtained using the iterative process described at the beginning of Section 4.2). The second is that in (Dai and Tedrake, 2013), the authors do not use reference trajectories based on the virtual constraint approach, but rather trajectories defined as functions of time. It has been demonstrated that if trajectories defined as a function of time are compared against trajectories defined using the

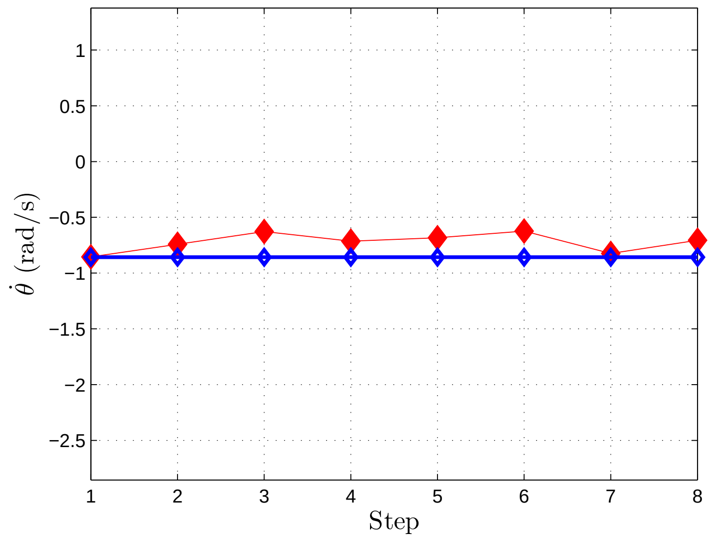

Figure 60: Poincaré Map for the system with noise measurements, for 8 steps, with 10% error in q_1. Blue: nominal cycle. Red: actual cycle.

virtual constraints approach, the latter exhibits better disturbance attenuation than the former, even without the use of a robust controller (Montano *et al.*, 2015b). Therefore, in this work, the combination of virtual constraints with the robust control synthesis, allows one to vary the slope up to $10°$, and stable walking is still achieved. The results are shown in Fig. 62 for three different cases: disturbance of the first step with a virtual slope of $5°$ (red); disturbance at the first two steps with virtual slopes of $-2°$ and $10°$ respectively (black); and alternating virtual slopes of $-5°$ and $5°$ (magenta). Again, as predicted by the theory, when the disturbances dissapear (black and red cases), the system returns to the reference cycle (blue line), whereas if the disturbance is sustained (magenta case), the systems will stay in a neighborhood of the reference cycle. The effect of these disturbances on the torques are illustrated in Figures 63-65, where the maximum effort occurs just after the slope changes.

7.4.4 Friction

Another important effect to consider is friction, specially at the knee joints, since the phasing variable θ depends on the behavior of q_2. Therefore, the Coulomb friction vector

$$\mathbf{F} = [F_1, \ldots, F_5]^\top \tag{215}$$

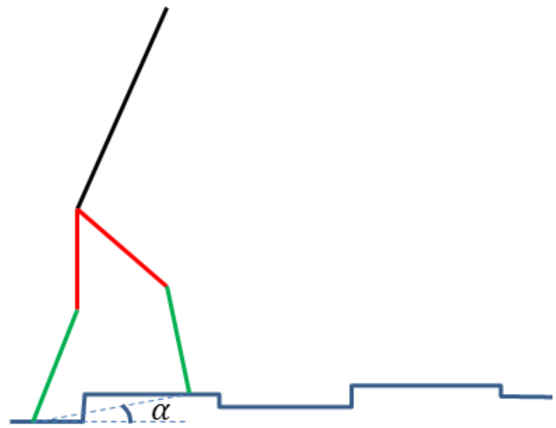

Figure 61: A simple humanoid walking over uneven terrain. α represents the virtual slope.

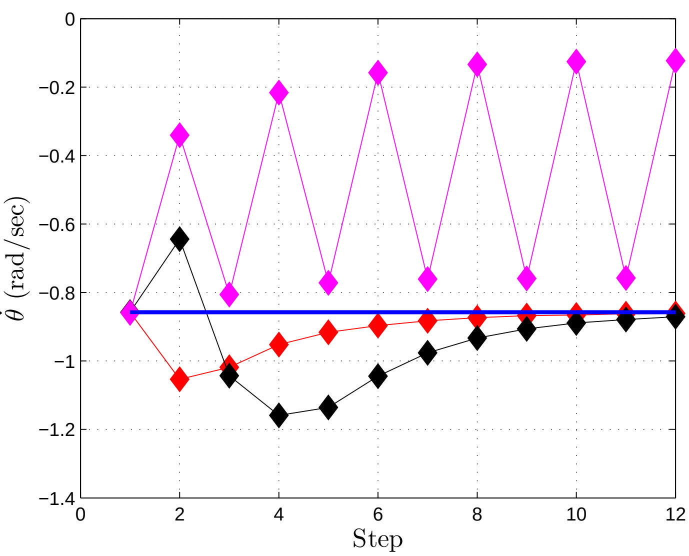

Figure 62: Poincaré Maps for the system under different virtual slopes, during 12 steps. Blue: nominal cycle (plain ground). Red: Virtual slope of $5°$ in the first step, $0°$ for the rest. Black: Virtual slope of $-2°$ for the first step, $10°$ for the second and $0°$ for the rest. Magenta: Alternating $-5°$ and $5°$.

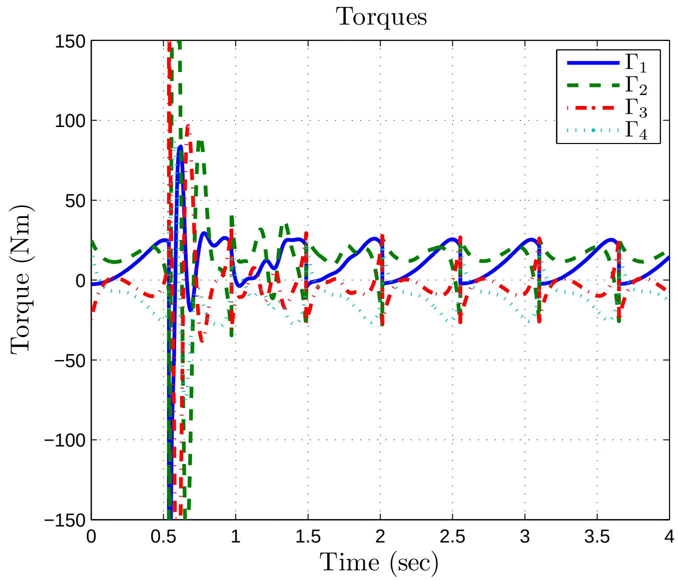

Figure 63: Joint torques for the system under a virtual slope of $5°$ in the first step, $0°$ for the rest.

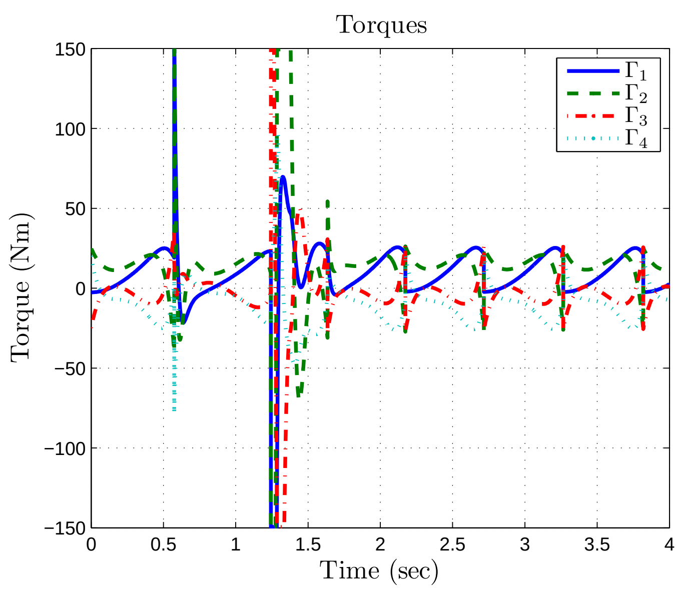

Figure 64: Joint torques for the system under a virtual slope of $-2°$ for the first step, $10°$ for the second and $0°$ for the rest.

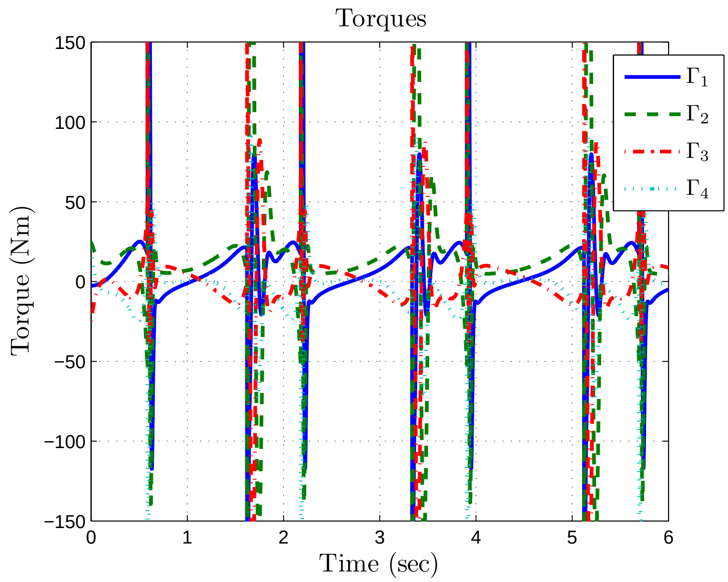

Figure 65: Joint torques for the system under an alternating virtual slope of $-5°$ and $5°$ each step.

is subtracted to the right side of (186), with

$$F_i = F_i^c \mathrm{sign}(\dot{q}_i), \quad i = 1, \ldots, 5. \tag{216}$$

The numerical tests were performed under an assumption that only the active joints $q_2, \ldots, q_5$ were affected by friction forces, which is why the friction coefficients were selected as $F_2^c = F_5^c = -2.1$, $F_3^c = F_4^c = -1.02$ and $F_1^c = 0$. The results are shown in Fig. 66. Even in the presence of the Coulomb friction, stable walking is still achieved after several steps, as can be seen from the phase plane of θ, where the evolution falls into a new orbit, represented in red. In Fig. 67, the torques can be seen to achieve a new periodic behavior as well.

7.4.5 Imperfect detection of the impact

Due to the practical implementation of the controller, there is an inherent delay between the moment of the impact and the switching of the control law, which won't occur at the same time. The effect that this generates increases as the time step used for implementation increases.

From Fig. 68 it can be seen that for a time step small enough, the walking cycle does not suffer an evident deviation from the nominal biped cycle. This deviation is mainly

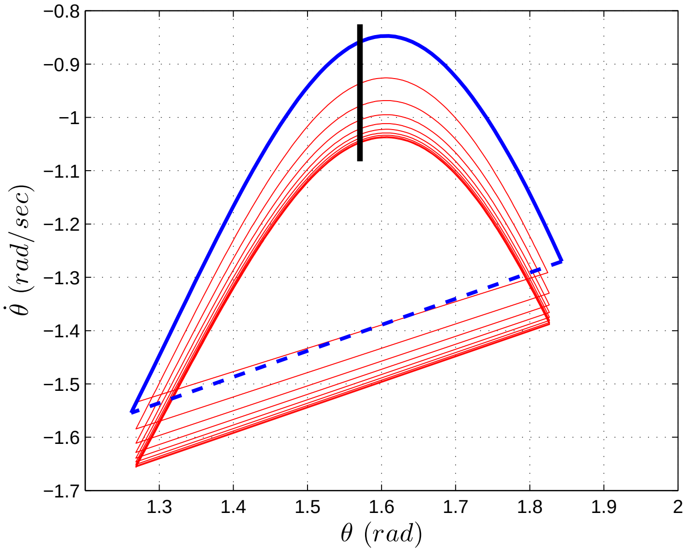

Figure 66: Phase plane of θ, $\dot{\theta}$ for the introduction of Coulomb friction at the actuated joints. Blue: nominal cycle. Red: actual cycle.

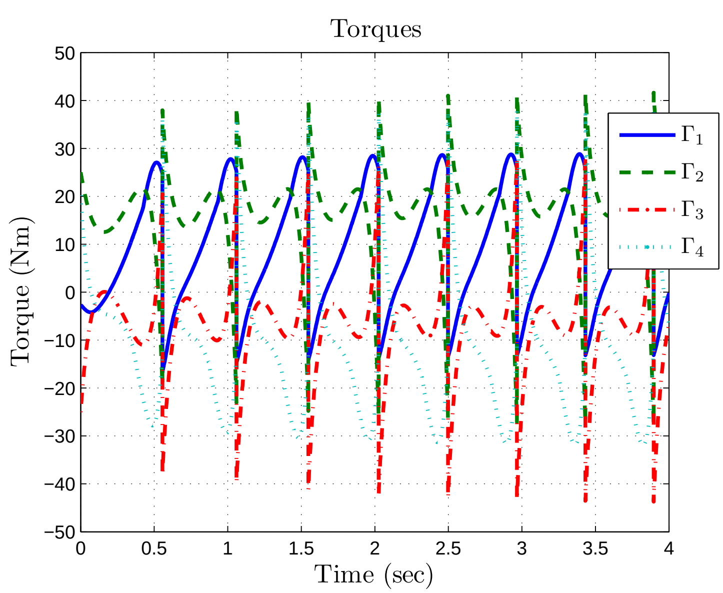

Figure 67: Join torques for the introduction of Coulomb friction at the actuated joints.

present due to the fact that the controller has not been switched, and the error begins to increase between the time the actual impact happens and the time the control law restarts. This effect becomes more and more evident as the time of detection increases: in Fig. 69, the sample time is increased ten times, so the degradation of the walking cycle becomes evident, but is still in a neighborhood around the nominal cycle, as shown in the figure.

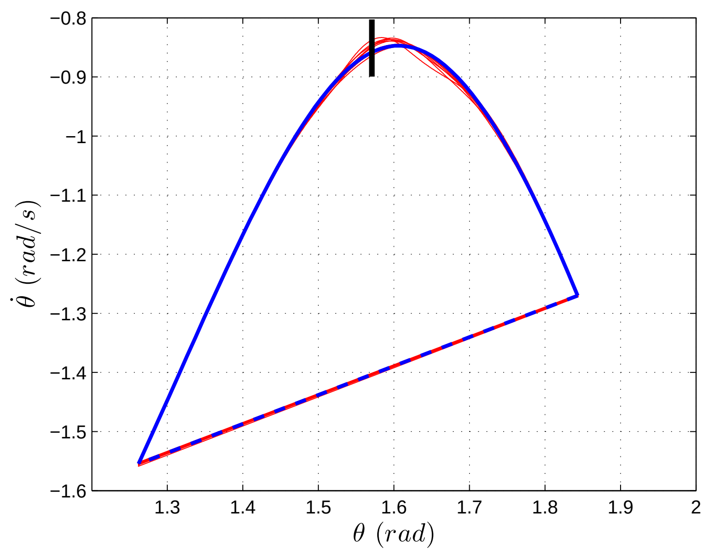

Figure 68: Phase plane of θ, $\dot{\theta}$ for a time step of $1\ ms$. Blue: nominal cycle. Red: actual cycle.

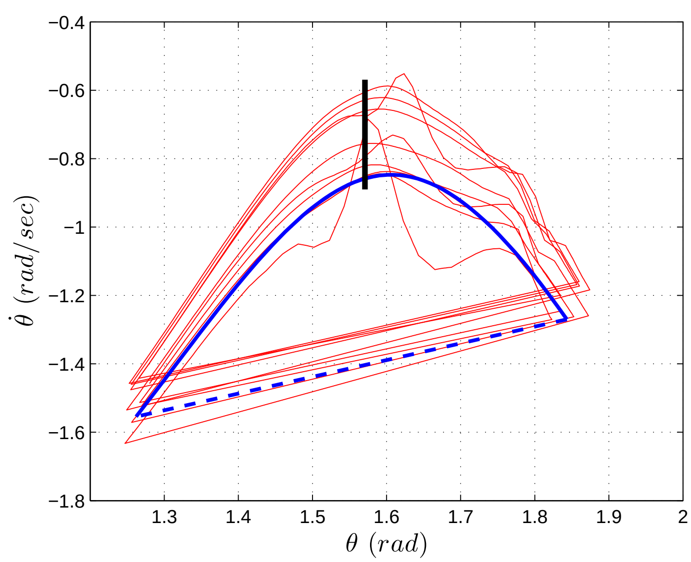

Figure 69: Phase plane of θ, $\dot{\theta}$ for a time step of $10\ ms$. Blue: nominal cycle. Red: actual cycle.

7.4.6 External forces and impact disturbances

As shown in Fig. 49, the system was tested under the application of a step disturbance ($5\ Nm$ at the hip, along the x axis) during the single support phase, starting from the first step; disturbances at each impact, modifying the impact function $\boldsymbol{\mu}$ in 5% from its original values, were applied as well. The measurements were disturbed by a sinusoidal disburbance of $0.05\sin(2t)\ rads$, and the initial estimation of the biped velocity is deviated 5% of its designed trajectory's initial velocity.

Just after the impact, the biggest error amplitude appears due to the disturbance in the impact phase, and this is rapidly attenuated to a lower level, where the new error is due to the disturbance on the continuous dynamics. The new orbit obtained is depicted in Fig. 70 by the red line. Due to the robustness of the controller, this new orbit is close to, and evolves around the nominal orbit. Even though the evolution of θ does not converge to a limit cycle, due to the effect of the persistent time-varying disturbances, it still remains oscillating in a neighborhood of the nominal cycle. Since the velocity was not measurable, Fig. 71 presents the behavior of the estimator (62a) while estimating the missing velocities, where it can be seen that in spite of the persistent time-varying disturbances in the measurements, the error does not diverge. The resulting joint torques are depicted in Fig. 72, where the peak efforts appear just after the impacts, due to the presence of the restitution law uncertainties.

Finally, the previous results were compared against the implementation of a PD-controller, similar to the one presented in the work of Hamed *et al.* (2014). To make a fair comparison, the same structure as (153) was used, but $\mathbf{u}$ was replaced with:

$$\dot{\boldsymbol{\xi}} = \mathbf{f}(\boldsymbol{\xi}, t) - \mathbf{g_2}(\boldsymbol{\xi}, t)\mathbf{K}\boldsymbol{\xi} + \mathbf{L}[\mathbf{y} - \mathbf{h_2}(\boldsymbol{\xi}, t)]$$

$$\boldsymbol{\xi}^{+} = \boldsymbol{\mu}(\boldsymbol{\xi}^{-}, t_i) \tag{217}$$

$$\mathbf{u} = -\mathbf{K}\boldsymbol{\xi} \tag{218}$$

where (217) has the form of a nonlinear Luenberger observer, and (218) of a standard PD-control, with $\mathbf{L}$ and $\mathbf{K} = (\mathbf{K_p}^{\top}, \mathbf{K_v}^{\top})^{\top}$ constant gain matrices. To obtain the values of both matrices, first the Differential Riccati Equations (54)-(55) are solved along the nom-

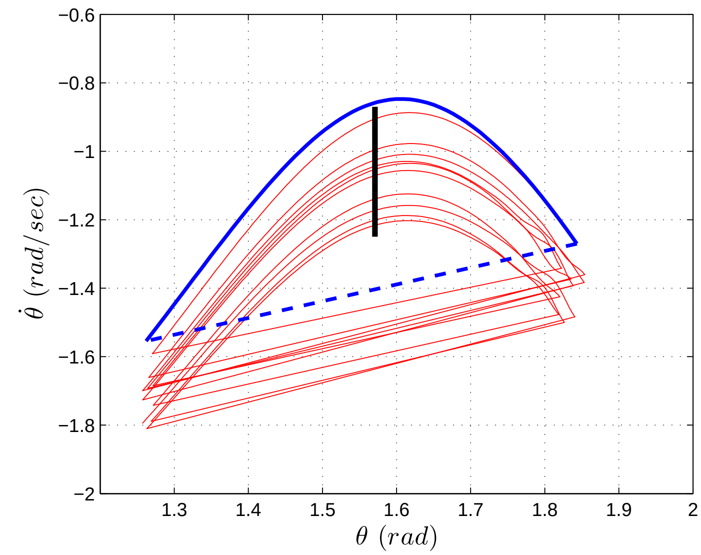

Figure 70: Phase plane of θ, $\dot{\theta}$ for the disturbed system with persistent perturbations. The blue line represents the limit cycle for the undisturbed system, whereas the red represents the orbit of the system under the perturbations. The black line indicates the Poincaré section.

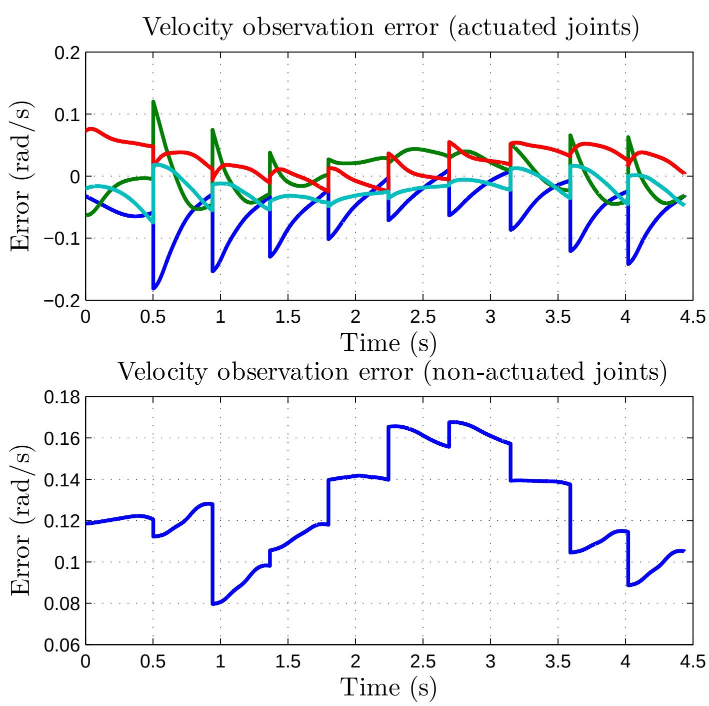

Figure 71: Velocity estimation errors $\boldsymbol{\xi_2} = (\xi_{21}, \ldots, \xi_{25})^\top$ for the estimator (62a), for the disturbed system with persistent perturbations. The estimation error does not diverge under the presence of disturbances in both the measurements and the plant dynamics.

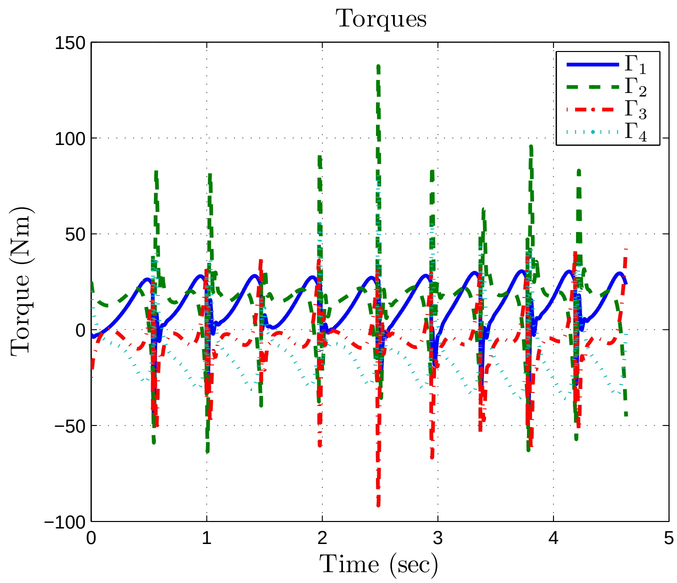

Figure 72: Joint torques for the disturbed system with persistent perturbations.

inal trajectory $\mathbf{q}_\star$, using the same method and parameters as in Sect. 7.4. Then, the undisturbed closed loop system (150)-(151), (153), (62a)-(62b) is simulated (with zero initial conditions) for just one step, that ends at time t_1. Thus, the gain matrices $\mathbf{L}$ and $\mathbf{K}$ for the PD-control are calculated as:

$$\mathbf{L} = \frac{1}{t_1}\int_0^{t_1} \mathbf{Z}_\varepsilon(t)\mathbf{C_2}^\top(t)\mathrm{d}t \tag{219}$$

$$\mathbf{K} = \frac{1}{t_1}\int_0^{t_1} \mathbf{B_2}^\top(t)\mathbf{P}_\varepsilon(t)\mathrm{d}t \tag{220}$$

so they become the average values of the time-varying gains of the $\mathcal{H}_\infty$-controller (62a)-(62b). The transversal control $\mathbf{v}$ in (192) is replaced by $\mathbf{v} = \mathbf{K}_\perp \mathbf{x}_\perp$, and $\mathbf{K}_\perp$ is obtained following the same idea. Once these values are obtained, the system is tested again with the same disturbances as the ones presented at the beginning of this section, but replacing (62a)-(62b) with (217)-(218), and the results were compared against the previously exposed.

Figure 73 compares the evolution of the Poincaré maps for both cases. It can be seen that the implementation of the proposed $\mathcal{H}_\infty$-control exhibits better velocity tracking, since its map evolution is closer to the nominal fixed point than in the case of the PD-controller. Also, Fig. 74 compares the cumulative tracking error for both implementations: after three steps, the $\mathcal{H}_\infty$-control performance is better than that of the PD-control, and stays better for successive steps. This is also reflected in the time shifting from the reference trajectory: whereas for the undisturbed case, it takes $5.6\ s$ to complete 10 steps, it took $4.6\ s$ to the $\mathcal{H}_\infty$ implementation, and $3.69\ s$ to the PD implementation, so the behavior of the former is closer to the nominal behavior than that of the latter. Thus, better performance can be concluded for the implementation of the proposed synthesis.

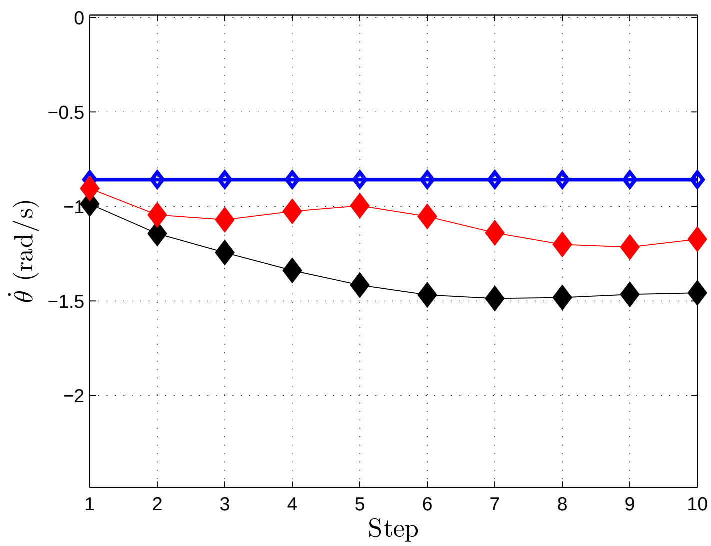

Figure 73: Comparison of the Poincare Maps for the $\mathcal{H}_\infty$ and PD-controller implementations, for the disturbed system under persistent disturbances. Red: $\mathcal{H}_\infty$. Black: PD; Blue: Nominal behavior

7.5 Conclusions

The controller synthesis presented in Chapter 6 was tested in the numerical study made for a five-link planar bipedal emulator to be stabilized around a periodic nominal trajectory. Good performance of the closed-loop system was obtained in spite of external disturbances, affecting the single support phase and the impact phase, and under imperfections in the position measurements.

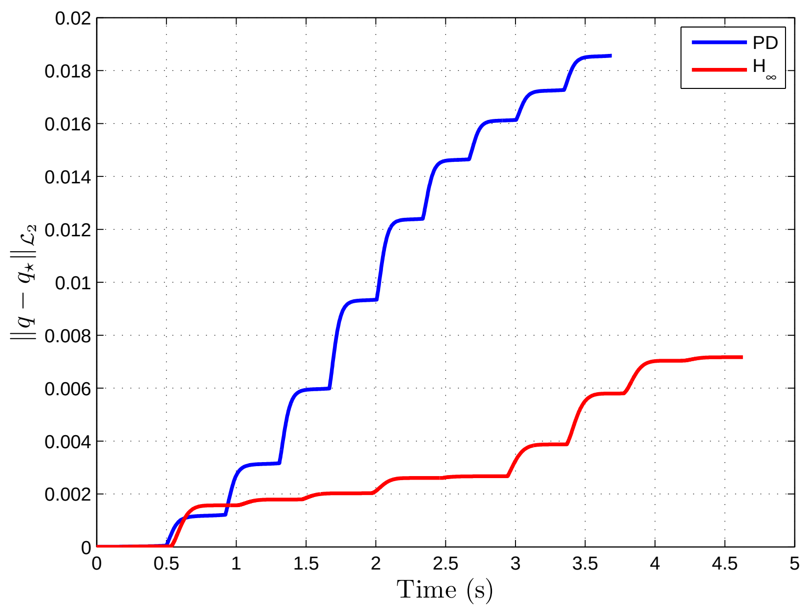

Figure 74: Comparison of the cumulative tracking errors of the $\mathcal{H}_\infty$ vs PD-controller, for the disturbed system under persistent disturbances.

Chapter 8. Conclusions

The $\mathcal{H}_\infty$-control problem is solved for mechanical systems under unilateral constraints via output and state feedback design. Sufficient conditions for the existence of a solution of the output feedback tracking problem are obtained in terms of the appropriate solvability of three coupled inequalities, involving two Hamilton-Jacobi-Isaacs inequalities which arise in the continuous time state-feedback and, respectively, output-injection designs, and an extra independent inequality on discrete disturbance factor that occurs in the restitution rule.

Arising from the need of an appropriate reference model, the Van der Pol oscillator is studied under unilateral constraints. This constrained oscillator is shown to be capable of exhibiting an unstable equilibrium point and asymptotically stable limit cycle, but also of degenerating its cycle to an asymptotically stable equilibrium; this is opposed to the unconstrained oscillator, where only an unstable equilibrium point and an asymptotically stable limit cycle co-exist. Sufficient conditions of an asymptotically stable limit cycle to exist are obtained and numerically validated via the Poincaré analysis. Under a change in the damping parameter of the oscillator, the Hopf bifurcation of the equilibrium to a limit cycle is then obtained. Thus, the limit cycle generation and its degeneration into an asymptotically stable equilibrium remain at the designer's will through an appropriate on-line modification of this oscillator parameter. Therefore, the constrained Van der Pol oscillator appears to be extremely attractive for its use as a reference model in mechanical control applications where desired periodic motions to be synthesized under unilateral constraints depend on the current control task that may vary in time.

Effectiveness of the proposed design procedure is supported in numerical studies made for three specific fully actuated mechanical systems: a pendulum impacting against a barrier, a seven-link biped, and a 32-DOF biped robot.

The impacting pendulum serves as an illustrative example, capturing all the essential features of the general treatment under unilateral constraints. The reference trajectory to follow is generated by an impact Van der Pol oscillator, possessing an asymptotically stable limit cycle. The desired disturbance attenuation is satisfactorily achieved under external disturbances during the free-motion phase and in the presence of uncertainties in the transition phase. To tackle the peaking phenomena appearing in the tracking of hybrid systems (Biemond *et al.*, 2013), the idea of an online model reset adaptation is introduced and additionally applied so as to synchronize the impacts of the plant with those of the reference model, thereby enhancing the performance of the closed-loop system.

The numerical studies, made side by side, for state and position feedback designs of stable gaits of a seven-link biped and a 32-DOF biped robot, further support the effectiveness of the developed synthesis. The desired disturbance attenuation is satisfactorily achieved under external disturbances during the free-motion phase and in the presence of uncertainty in the transition phase.

Finally, an extension of the proposed synthesis towards underactuated mechanical systems, of underactuation degree one, operating under unilateral constraints is presented. By analyzing the transversal dynamics, sufficient conditions for attenuating the plant disturbances around a prescribed trajectory are derived, provided that the reference periodic trajectory is feasible. The tests made for the five-link bipedal robot Rabbit, allowed to illustrate good performance of the closed-loop system, despite the disturbances introduced on the single support phase, the impact phase, and imperfections on the position measurements.

8.1 Contributions

The contribution of the paper into the existing literature is twofold. First, the nonlinear $\mathcal{H}_\infty$ approach is constructively generalized under unilateral constraints by means of incorporating an additional condition on the plant reset in the closed-loop. The resulting robust synthesis under both external disturbances and restitution uncertainties is then effectively applied to the afore-given impact testbeds for the purpose of generating periodic motions. Being numerically justified in the benchmark testbeds, the robustness features of the proposed synthesis form an important novelty of this work.

Furthermore, discovering the Hopf bifurcation of the constrained Van der Pol oscillator is one of the main contributions of the present work. This allows to generate on-line modifiable reference trajectories that either present a periodic behavior or degenerate to the origin, making this hybrid oscillator ideal as a reference model for mechanical systems operating under unilateral constraints.

The impact synchronization method introduced to suppress the peaking phenomena, is yet another contribution of this work. This allows to improve the closed-loop performance and to guarantee asymptotic stability.

An essential feature, adding value to the present investigation, is that standard external disturbances (such as environmental external forces, biped parameters uncertainty, etc.), their discrete-time counterparts (such as non-perfect inelastic contact between the floor and the foot at the impact, or floor height variations), and measurement imperfections are considered in combination and are attenuated with the proposed synthesis. This in contrast to the existing literature where the perfect knowledge of both the state vector, and of the impact equation at the collision time instants is assumed.

8.2 Productivity

Journals

- Montano, O., Orlov, Y., Aoustin, Y., and Chevallereau, C. (2016). Orbital stabilization of an underactuated bipedal gait via nonlinear $\mathcal{H}_\infty$-control using measurement feedback. *Autonomous Robots*, pp. 1–19.
- Montano, O., Orlov, Y. and Aoustin, Y. (2016). Nonlinear $\mathcal{H}_\infty$-control under unilateral constraints. *International Journal of Control*, pp. 1–35.
- Osuna, T., Montano, O. and Orlov, Y. (2016). Nonlinear $\mathcal{L}_2$-Gain Analysis of Hybrid Systems in the Presence of Sliding Modes and Impacts. *Mathematical Problems in Engineering*. Article ID 9074096.

Proceedings

- (Accepted) Orlov, Y., Montano, O., and Herrera, L. (2016). Hopf Bifurcation of Van der Pol Oscillators operating under Unilateral Constraints. *Proceedings of the Amer-*

ican Control Conference.

- Montano, O., Orlov, Y., and Aoustin, Y. (2015). Nonlinear output feedback $\mathcal{H}_\infty$-control of mechanical systems under unilateral constraints. *Proceedings of the 1st IFAC Conference on Modelling, Identification and Control of Nonlinear Systems*, pp. 284–289.

- Montano, O., Orlov, Y., Aoustin, Y., and Chevallereau, C. (2015). Nonlinear orbital $\mathcal{H}_\infty$-stabilization of underactuated mechanical systems with unilateral constraints. *Proceedings of the 14th European Control Conference*, pp. 800–805.

- Montano, O., Orlov, Y., and Aoustin, Y. (2014). Nonlinear $\mathcal{H}_\infty$-control of mechanical systems under unilateral constraints. *Proc. 9th World Congress of the International Federation of Automatic Control (IFAC 2014)*.

- Montano, O., Orlov, Y., and Aoustin, Y. (2013). Nonlinear $\mathcal{H}_\infty$-control of mechanical systems under unilateral constraints on the position. *Proc. of the Congreso Nacional de Control Automatico, AMCA*.

Chapter 9. Résumé en Français

9.1 Introduction

Les systèmes hybrides sont des systèmes à commutation dont le comportement est décrit par des équations de différentielles et des équations algébriques. Ces systèmes ont été l'objet de beaucoup d'attention en raison de la grande variété de leurs applications et en raison du besoin d'outils d'analyse spécifiques pour ce type de systèmes. Le lecteur intéressé peut se référer aux travaux pertinents de Goebel *et al.* (2009); Hamed and Grizzle (2013); Naldi and Sanfelice (2013); Nesic *et al.* (2013), pour ne citer que quelques exemples. En particulier, le problème d'atténuation des perturbations pour des systèmes dynamiques hybrides a été traité par Haddad *et al.* (2005); Nesic *et al.* (2013, 2008) où des entrées de commande impulsionnelles ont été admises pour compenser les perturbations / incertitudes à des instants de changement instantané de l'état. Cependant, il est important de noter que même pour la synthèse par retour d'état, il est nécessaire de résoudre deux équations de Riccati indépendantes qui apparaissent respectivement lors de la phase continue et à l'impact. La solution cherchée doit satisfaire ces deux équations. En outre, la mise en œuvre physique des entrées de commande impulsionnelles est impossible dans des nombreuses situations pratiques, par exemple, pour la commande de robots bipèdes lors de la marche.

Ainsi motivée, la présente recherche a pour objectif d'introduire une nouvelle stratégie de commande. Ce qui est réalisable sous certaines conditions et ce qui évite l'utilisation des entrées de commande impulsionnelles. L'objectif de commande en question est de stabiliser asymptotiquement le système hybride non perturbé, tout en atténuant les perturbations externes. Le travail se concentre sur les systèmes hybrides avec impact. Ils sont reconnus comme systèmes dynamiques sous contraintes unilatérales (Brogliato, 1999). Étant donné que les systèmes dynamiques soumis à des contraintes unilatérales possèdent des solutions non lisses, un problème difficile est d'étendre la bien connue approche $\mathcal{H}_\infty$ non linéaire (Basar and Bernhard, 1995; Isidori and Astolfi, 1992; Van Der Schaft, 1991) à ce type de systèmes dynamiques. Il convient de noter que la caractérisation de Lyapunov de la stabilité entrée-état intégrale (iISS), récemment mise au point par Hespanha *et al.* (2008) pour les systèmes impulsionnels avec des impacts indépendants de l'état, pourraient constituer une base pour une telle extension. Toutefois, le choix de cette stratégie exige la généralisation du concept de iISS aux systèmes hybrides avec des impacts dépendants de l'état.

L'approche $\mathcal{H}_\infty$, qui a récemment été développée par Orlov and Aguilar (2014) pour des applications mécaniques non lisses avec des forces difficiles à modéliser, comme les frottements de Coulomb et les jeux mécaniques, est étendue en section 2, en présence des contraintes unilatérales. Cette extension, est en plus généralisée aux systèmes mécaniques multi-corps soumis à des unilatérales contraintes de co-dimension 1. Le cas général des contraintes unilatérales de co-dimensions supérieurs, qui entraîne un comportement dynamique complexe (Brogliato, 1999; Bentsman *et al.*, 2012), n'est pas considéré dans l'étude présente.

Le cas où l'état est entièrement connu et celui ou l'état est partiellement connu avec des mesures corrompues sont traités pour des manipulateurs mécaniquement entièrement actionnés. Une caractéristique essentielle est que non seulement les perturbations exogènes standard lors de la phase continue ou lors de l'impact sont rejetées. Il convient de noter que ceci est en contraste avec les algorithmes de commande développés à ce jour (*e.g.*, celle de Ames *et al.* (2012)) où la parfaite connaissance de la règle de la restitution est supposée acquise aux instants de collision.

Afin de faciliter la présentation des capacités de la synthèse développée et de ses caractéristiques de robustesse, la section 4 illustre un simple système non linéaire avec 1-DDL; il s'agite d'un pendule qui frappe contre une barrière. Il présente toutes les caractéristiques des systèmes mécaniques hybrides soumis à des contraintes unilatérales. En plus de l'étude numérique, faite pour la régulation par retour de position de ce banc d'essai, deux scénarios sont imaginés et testés côte à côte pour le suivi d'un modèle de référence avec des impacts par retour de position, pour la génération d'un cycle limite stable. Lors du premier scénario, une sortie de référence à suivre est construite hors ligne. Elle est fondée sur l'oscillateur de Van der Pol hybride (qui sera commenté dans la sous-section suivante) (Akhmet and Turan, 2014). Dans le second scénario, la même sortie de référence est mise à jour en ligne pour synchroniser les instants des impacts avec ceux désirés lorsque le système atteint la contrainte unilatérale, tel qu'il évite le phénomène de ≪ peaking ≫ (Biemond *et al.*, 2013). Ce phénomène est observé sur les courbes des erreurs de poursuite dues à la désynchronisation des temps des impacts réels et ceux prévus par la trajectoire de référence. Comme prévu théoriquement, l'atténuation de la perturbation est effectivement observée et la bonne performance du système en boucle fermée est conclue à partir de l'étude numérique réalisée.

9.1.1 Oscillateurs d'impact

Un ingrédient essentiel de l'illustration de la section 4 réside dans la conception d'un modèle de référence hybride, capable de générer un mouvement périodique. La motivation derrière la conception d'un tel modèle de référence hybride peut être trouvée, par exemple, dans la robotique (Aoustin and Formalsky, 2003; Chevallereau *et al.*, 2004b) où il est nécessaire de générer une démarche cyclique stable sur le sol (considéré comme une contrainte unilatérale naturelle) pour un robot bipède.

L'intérêt pour la recherche de la stabilisation orbitale des systèmes mécaniques est inspiré par les applications où le mode de fonctionnement naturel est périodique. Pour ces systèmes, le paradigme de stabilisation orbitale diffère des formulations typiques de suivi de sortie où la trajectoire de référence à suivre est connue *a priori*. L'objectif de commande de la stabilisation orbitale (par exemple, l'équilibrage périodique d'un bipède pendant la marche (Chevallereau *et al.*, 2003) ou la planification de trajectoire pour des robots manipulateurs industriels (Ellekilde and Perram, 2005)), est double. Tout d'abord, le système en boucle fermée doit générer son propre cycle limite, similaire à celui produit par un oscillateur non-linéaire (par exemple, l'oscillateur de Van der Pol). En second lieu, il doit être capable de se déplacer d'une orbite à l'autre en modifiant les paramètres de l'orbite, comme la fréquence et / ou l'amplitude.

Les oscillateurs d'impact ont attiré un intérêt de recherche important, principalement dû à la variété de leurs applications, telles que celles présentées dans Goyder and Teh (1989); Hogan (1989); Ehrich (1991) pour n'en citer que quelques uns. Ce type de systèmes présente également différents types de phénomènes complexes (voir, par exemple (Bernardo *et al.*, 2008a, p.208); Kuznetsov (2013); Leine and Nijmeijer (2013); Makarenkov and Lamb (2012) et les références qui y sont citées). Pour le cas simple d'oscillateurs linéaires forcés, la méthode des sections de Poincaré a été utilisée avec succès en faisant varier l'un des paramètres du modèle hybride (typiquement, la fréquence d'une force externe) pour déterminer la frontière entre différents comportements dynamiques, telles que les bifurcations de double période et chaos (Lee, 2005; Ikeda *et al.*, 2012).

Section 3 vise à donner une idée plus précise sur le comportement de l'oscillateur (modifié) de Van Der Pol, soumis à une contrainte unilatérale qui a été utilisé *ad hoc* dans Montano *et al.* (2013); Dutra *et al.* (2003) pour générer des locomotions périodiques avec des impacts (en raison des contraintes au sol) pour robots bipèdes. En appliquant l'analyse de Poincaré sur la stabilité des orbites périodiques dans les systèmes mécaniques hybrides (Aoustin and Formalsky, 2003; Chevallereau *et al.*, 2004b; Grizzle *et al.*, 1999), il est numériquement révélé que, dépendant de la valeur d'amortissement ε, l'oscillateur hybride de Van der Pol conduit à une alternative. Soit il imite les caractéristiques de sa version sans contrainte, présentant à la fois un cycle limite hybride asymptotiquement stable et un équilibre instable, soit il ne possède qu'un équilibre asymptotiquement stable.

Une étude numérique est effectuée pour obtenir la valeur de bifurcation du paramètre d'amortissement ε pour lequel le cycle limite disparaît. Une fois que cette valeur est obtenue, un modèle de référence approprié est conçu et utilisé pour fournir une référence à suivre pour l'exemple numérique de la section 4.

9.1.2 Applications aux robots bipèdes

Les robots bipèdes forment une sous-classe des robots à pattes. Leur conception est naturellement inspirée de la mobilité du corps humain. Sur le plan pratique, l'étude de la locomotion mécanique à pattes a été motivée par son utilisation potentielle comme moyen de locomotion dans les terrains accidentés. L'intérêt découle de divers intérêts sociologiques et commerciaux, allant du désir de remplacer les humains pour effectuer des travaux dangereux, où la restauration du mouvement pour les handicapés (Westervelt *et al.*, 2007).

Pour la mise en œuvre pratique, une bonne conception mécanique et une bonne modélisation, jouent un rôle très important pour l'obtention d'une bonne performance. Cependant, pour les applications du monde réel, les robots bipèdes sont soumis à de nombreuses sources d'incertitude pendant la marche. Ceux-ci pourraient inclure une bousculade, une rafale inattendue de vent, des perturbations géométriques des hauteurs de terrain, ou des incertitudes paramétriques des forces de frottement non modélisé (Dai and Tedrake, 2013). Pour cette raison, la conception de systèmes de commande en boucle fermée, capable d'atténuer l'effet de ces incertitudes, est essentielle pour obtenir la marche souhaitée.

Par souci de simplicité, le modèle complet du robot bipède pris en compte dans ce travail se compose de deux parties: les équations différentielles qui décrivent la dynamique du robot lors de la phase d'appui simple (un pied sur l'air, l'autre restant en appui sur le terrain), et un modèle impulsionnel de l'événement de contact (l'impact entre la jambe oscillante et le sol, qui est modélisé comme un contact entre deux corps rigides comme dans l'ouvrage de Westervelt *et al.* (2007)). Ce modèle simplifié permet l'utilisation de la théorie développée dans la section 2 afin d'obtenir une atténuation des perturbations dans ces modèles complexes et hautement non linéaires.

En outre, l'actionnement au niveau des chevilles permet de définir deux problèmes différents: 1) si les chevilles sont actionnées, le bipède est **complètement actionnée** pendant la phase de simple appui, car il y aura autant d'actionneurs que de degrés de liberté au niveau des jambes (des rotations autour des pieds, rotations au niveau des genoux, et rotations autour de la hanche); 2) si les chevilles ne sont pas actionnées, le bipède est **sous-actionné** pendant la phase de simple appui, car il y aura moins d'actionneurs que de degrés de liberté, puisque la rotation autour du pied sur le sol n'est pas commandée directement par un actionneur. Ces deux problèmes seront abordés dans les sections 5 et 7, respectivement.

D'autres techniques de commande robustes, telles que la commande par modes glissantes, ont été conçues pour ce type de systèmes (voir Raibert *et al.* (1993), Manamani *et al.* (1997), Nikkhah *et al.* (2007), Aoustin *et al.* (2010), Oza *et al.* (2014). Tout en fournissant à la fois la convergence en temps fini à une trajectoire de référence et le rejet des perturbations, ces approches impliquent aussi le bien connu problème de commutation (chattering) pour les actionneurs. Ce problème motive l'étude des techniques de commande robustes telle que celle présentée dans ce travail, qui atténue l'effet des perturbations tout en évitant les effets indésirables et nuisibles tant sur les actionneurs comme sur les articulations.

9.1.3 Stabilisation orbitale de la locomotion d'un bipède

La stabilité de la locomotion des robots bipèdes est un sujet récent de recherche. Par exemple, dans l'ouvrage de Westervelt *et al.* (2004), les auteurs ont stabilisé un bipède sous-actionné autour d'une orbite périodique, mais au lieu d'un mode de glissement ou d'une loi de commande à convergence en temps fini, les auteurs ont préféré utiliser une loi de commande PD découplée pour sa robustesse vis-à-vis du bruit. Hamed *et al.* (2014) a proposé une stratégie de commande pour stabiliser de façon exponentielle un bipède sous-actionné en utilisant un correcteur continu invariant dans le temps. Cependant, les effets des perturbations externes ne sont pas explicitement pris en compte pour la synthèse du correcteur, et une parfaite connaissance du vecteur d'état complet a été supposée. Dans Chevallereau *et al.* (2009) et Hamed and Grizzle (2014), des correcteurs fondés sur événements ont été développés pour stabiliser des orbites périodiques pour les systèmes de bipèdes sous-actionnés. En outre, sur la base de la méthode de Poincaré, Hobbelen and Wisse (2007) introduisent la norme de sensibilité de démarche, en tant que mesure de robustesse pour les marcheurs bipèdes.

À cet égard, deux inconvénients majeurs doivent être mentionnés sur les méthodes fondées sur l'analyse de Poincaré. D'une part, il est difficile d'introduire des incertitudes dans la phase de simple appui, puisque l'analyse est faite uniquement sur la section de Poincaré sélectionnée. D'autre part, l'application de Poincaré est souvent analysée numériquement, car elle repose sur la solution analytique des équations différentielles qui décrivent le mouvement du système. Comme indiqué par Morris and Grizzle (2005), des schémas numériques peuvent être utilisés pour calculer l'application de Poincaré, trouver ses points fixes, et estimer les valeurs propres pour déterminer la stabilité exponentielle. Cependant, les calculs numériques sont généralement lourds, et les exécuter de manière itérative dans le cadre d'un processus de conception du système peut être fastidieux.

L'utilisation de la méthode de déplacement des sections de Poincaré (Leonov, 2006), couplée avec la méthode des contraintes virtuelles holonomes (voir Shiriaev *et al.* (2008); Freidovich *et al.* (2008); Shiriaev and Freidovich (2009); La Hera *et al.* (2013) et les références qui y sont citées), les sections 6 et 7 sont consacrées à la dérivation des conditions suffisantes pour une nouvelle stratégie de commande par retour de sortie, qui permet la stabilisation orbitale asymptotique du système hybride sous-actionné, tout en garantissant que la $\mathcal{L}_2$-Gain de sa version perturbée est inférieure à un niveau de perturbation appropriée γ.

L'approche $\mathcal{H}_\infty$, étendue aux systèmes entièrement actionnés sous contraintes unilatérales dans le chapitre 2, est généralisée dans le chapitre 6 aux systèmes mécaniques sous-actionnées avec des collisions. Afin d'illustrer les capacités de la synthèse proposée, dans la section 7 est développée la stabilisation orbitale d'un robot bipède plane sous-actionné sous des contraintes unilatérales au sol et soumis à des perturbations externes.

Finalement, il convient de mentionner que, dans Dai and Tedrake (2012) et Dai and Tedrake (2013), une approche de commande $\mathcal{H}_\infty$ hybride a été développée par la définition d'un $\mathcal{L}_2$-Gain, des perturbations au sol aux écarts par rapport au cycle limite nominale. Contrairement au travail de Dai and Tedrake (2013), le présent travail démontre de bonnes caractéristiques de robustesse de la synthèse orbitale développée par rapport aux deux perturbations externes, qui affectent la phase de mouvement sans collision, et contre les incertitudes qui se produisent lors de l'impact, tout en utilisant seulement les mesures de position disponibles. Avec le développement théorique de la synthèse $\mathcal{H}_\infty$ sous contraintes unilatérales, ces caractéristiques de robustesse, justifiées numériquement sur un simulateur du bipède (Aoustin *et al.*, 2010), forment la nouveauté de ce travail.

9.1.4 Objectifs

L'objectif principal de ce travail, est de développer la commande $\mathcal{H}_\infty$ non-linéaire pour les systèmes mécaniques sous contraintes unilatérales sur la position, avec des perturbations exogènes bornées sur la dynamique continue et lors de l'impact, et aussi sur les mesures.

9.1.4.1 Objectifs spécifiques

Afin d'atteindre l'objectif général mentionné ci-dessus, les objectifs spécifiques suivants ont été fixés:

- Synthèse des correcteurs $\mathcal{H}_\infty$ pour les systèmes mécaniques sous contraintes unilatérales, compte tenu de l'action de commande seulement entre les impacts.
- Le correcteur robuste sera synthétisé par retour de sortie.
- Validation du schéma proposé en utilisant des simulations numériques pour un robot bipède plan de six degrés de liberté.
- Extension du schéma proposé au scénario sous-actionné (degré de sous-actionnement 1), pour stabiliser une bipède plan sans pieds.
- Validation du schéma proposé en utilisant des simulations numériques pour un robot bipède de 32 degrés de liberté, Romeo, de l'entreprise Aldebaran Robotics.

9.1.5 Plan de la thèse

Dans la section 2, le problème de commande $\mathcal{H}_\infty$ est spécifié pour le modèle hybride considéré, qui est soumis à une contrainte unilatérale. Des conditions suffisantes pour l'existence d'une solution locale du problème sous-jacent sont dérivées, afin de synthétiser une commande par retour de sortie. La section 3 présente une étude de bifurcation d'une version hybride de l'oscillateur de Van der Pol, pour l'utiliser comme un modèle de référence pour les systèmes mécaniques soumis à des contraintes unilatérales. Les capacités de la synthèse développée sont illustrées dans la section 4, dans des expériences numériques faites pour la régulation et la stabilisation orbitale d'un pendule qui frappe contre une barrière. La section 5 présente les résultats de l'application de la synthèse sur un robot bipède plan avec des pieds. Un correcteur local $\mathcal{H}_\infty$, qui assure la stabilisation orbitale asymptotique et l'atténuation des perturbations pour les systèmes mécaniques soumis à des contraintes unilatérales, de degré de sous-actionnement 1, est présenté dans la section 6. Ce correcteur est ensuite généralisé dans la section 7, pour un bipède sous-actionné, qui marche dans le plan sagittal, et ses capacités sont illustrées par les essais de simulation. Finalement, les conclusions, les contributions et les travaux futurs sont recueillies section 8.

9.2 Synthèse $\mathcal{H}_\infty$ non linéaire sous contraintes unilatérales par retour de sortie

9.2.1 Énoncé du problème

Étant donné une contrainte unilatérale scalaire $F(\mathbf{x_1}, t) \geq 0$, nous allons considérer un système non linéaire, qui évolue au sein de la contrainte ci-dessus, et qui est régi par la dynamique continue de la forme

$$\begin{aligned} \dot{\mathbf{x}}_1 &= \mathbf{x}_2 \\ \dot{\mathbf{x}}_2 &= \mathbf{\Phi}(\mathbf{x}_1, \mathbf{x}_2, t) + \mathbf{\Psi}_1(\mathbf{x}_1, \mathbf{x}_2, t)\mathbf{w} + \mathbf{\Psi}_2(\mathbf{x}_1, \mathbf{x}_2, t)\mathbf{u} \end{aligned} \tag{221}$$

$$\mathbf{z} = \mathbf{h_1}(\mathbf{x}_1, \mathbf{x}_2, t) + \mathbf{k_{12}}(\mathbf{x}_1, \mathbf{x}_2, t)\mathbf{u} \tag{222}$$

$$\mathbf{y} = \mathbf{h_2}(\mathbf{x}_1, \mathbf{x}_2, t) + \mathbf{k_{21}}(\mathbf{x}_1, \mathbf{x}_2, t)\mathbf{w} \tag{223}$$

au-delà de la surface $F(\mathbf{x_1}, t) = 0$ où la contrainte est inactive, et pour les relations algébriques

$$\begin{aligned} \mathbf{x}_1(t_i^+) &= \mathbf{x}_1(t_i^-) \\ \mathbf{x}_2(t_i^+) &= \mu_0(\mathbf{x}_1(t_i), \mathbf{x}_2(t_i^-), t_i) + \omega(\mathbf{x}_1(t_i), \mathbf{x}_2(t_i^-), t_i)\mathbf{w_d^i} \end{aligned} \tag{224}$$

$$\mathbf{z_i^d} = \mathbf{x}_2(t_i^+) \tag{225}$$

à des instants *a priori* inconnus $t = t_i,\ i = 1, 2, \ldots$, lorsque la trajectoire du système frappe la surface $F(\mathbf{x_1}, t) = 0$. Dans les relations ci-dessus, $\mathbf{x}^\top = [\mathbf{x}_1^\top, \mathbf{x}_2^\top] \in \mathbb{R}^{2n}$ représentent le vecteur d'état, avec $\mathbf{x}_1 \in \mathbb{R}^n$ et $\mathbf{x}_2 \in \mathbb{R}^n$; $\mathbf{u} \in \mathbb{R}^n$ est l'entrée de commande de dimension n; $\mathbf{w} \in \mathbb{R}^l$ et $\mathbf{w_d^i} \in \mathbb{R}^q$ sont des signaux exogènes qui affectent le mouvement du système (des forces externes, y compris les forces impulsionnelles, ainsi que les imperfections du modèle). La variable $\mathbf{y} \in \mathbb{R}^p$ est la seule mesure disponible de l'état du système tandis que la variable $\mathbf{z} \in \mathbb{R}^s$ représente une composante en temps de la sortie du système à commander. La valeur après l'impact de la seule composante $\mathbf{x}_2(t)$ qui est soumise à la variation instantanée est pré-spécifiée comme la seule composante de la sortie discrète $\mathbf{z_i^d}$ à être commandée. L'ensemble du système dans la boucle fermée doit être dissipatif par rapport à la sortie ainsi déterminée. Tout au long de ce travail, les fonctions $\mathbf{\Phi}$, $\mathbf{\Psi_1}$, $\mathbf{\Psi}_2$, $\mathbf{h_1}$, $\mathbf{k_{12}}$, $\mathbf{h_2}$, $\mathbf{k_{21}}$, $\mathbf{F}$, μ_0, et ω sont de dimensions appropriées, et sont continuement différentiables et uniformément bornées en t. Ces fonctions sont variables dans le temps pour faire face au problème de suivi où la description du modèle est donnée en termes de déviation par rapport à une trajectoire de référence. L'origine est supposé être un point d'équilibre du système libre (221)-(225), $\mathbf{\Phi}(0,0,t) = 0$, $\mathbf{h_1}(0,0,t) = 0$, $\mathbf{h_2}(0,0,t) = 0$ pour tous les instants t et $\mu_0(0,0,0) = 0$.

Pour une utilisation ultérieure, considérons un correcteur de bouclage dynamique causale à construire de la même structure que celle du système

$$\begin{aligned}
\dot{\boldsymbol{\xi}}_{\mathbf{1}} &= \boldsymbol{\xi}_2, \quad \dot{\boldsymbol{\xi}}_2 = \boldsymbol{\eta}(\boldsymbol{\xi}_1, \boldsymbol{\xi}_2, \mathbf{y}, t) \\
\boldsymbol{\xi}_1(t_j^+) &= \boldsymbol{\xi}_1(t_j^-), \quad \boldsymbol{\xi}_2(t_j^+) = \boldsymbol{\nu}(\boldsymbol{\xi}_1(t_j), \boldsymbol{\xi}_2(t_j^-), t_j) \\
\mathbf{u} &= \boldsymbol{\theta}(\boldsymbol{\xi}, t)
\end{aligned} \tag{226}$$

et avec l'état interne $\boldsymbol{\xi} = [\boldsymbol{\xi}_1, \boldsymbol{\xi}_2]^\top \in \mathbb{R}^{2n}$ de la même dimension, avec les instants $t = t_i,\ i = 1, 2, \ldots,$ qui peuvent coïncider avec les instants d'impact des équations (221)-(225), et avec les fonctions $\boldsymbol{\eta}(\boldsymbol{\xi}, \mathbf{y}, t)$, $\boldsymbol{\nu}(\boldsymbol{\xi}, t)$, et $\boldsymbol{\theta}(\boldsymbol{\xi}, t)$ qui sont continues par morceaux et uniformément bornées par rapport à t, et de classe C^2 par rapport aux variables $\boldsymbol{\xi}$ et $\mathbf{y}$. Ces fonctions sont telles que $\boldsymbol{\eta}(\mathbf{0}, \mathbf{0}, t) = \mathbf{0}$, $\boldsymbol{\nu}(\mathbf{0}, t) = \mathbf{0}$, et $\boldsymbol{\theta}(\mathbf{0}, t) = \mathbf{0}$ pour tous les instants t.

Le problème d'atténuation des perturbations consiste à trouver un correcteur local (226), de telle sorte que le $\mathcal{L}_2$-gain du système en boucle fermée (221)–(226) soumis à des perturbations est inférieur à une certaine valeur $\gamma > 0$, choisie en fonction d'un niveau d'atténuation désiré. En d'autres termes, l'inégalité

$$\int_{t_0}^{T} \|\mathbf{z}(t)\|^2 \mathrm{d}t + \sum_{i=1}^{N_T} \|\mathbf{z_i^d}\|^2 \leq \gamma^2 \int_{t_0}^{T} \|\mathbf{w}(t)\|^2 \mathrm{d}t + \gamma^2 \sum_{i=1}^{N_T} \|\mathbf{w_i^d}\|^2 + \sum_{k=0}^{N_T} \beta_k(\mathbf{x}(t_k^-), \boldsymbol{\xi}(t_k^-), t_k) \tag{227}$$

doit être satisfaite pour certaines valeurs positives $\beta_k(\mathbf{x},\boldsymbol{\xi},t)$, $k=0,\ldots,N_T$, pour tous les segments $[t_0,T]$, et N_T tels que $t_{N_T} \leq T < t_{N_T+1}$, pour toutes les perturbations continues par morceaux $\mathbf{w}(t)$ et discrètes $\mathbf{w_i^d},\ i=1,2,\ldots,$ pour lesquelles la trajectoire $(\mathbf{x}(t),\boldsymbol{\xi}(t))$ du système en boucle fermée, à partir d'un point initial $(\mathbf{x}(t_0),\boldsymbol{\xi}(t_0)) = (\mathbf{x_0},\boldsymbol{\xi_0}) \in \mathcal{U}$ à l'intérieur d'un voisinage $\mathcal{U} \subset \mathbb{R}^{4n}$ de l'origine, reste dans $\mathcal{U}$ pour tous les instants $t \in [t_0,T]$. Les fonctions positives $\beta_k,\ k=1,2,\ldots$ sont incluses afin de considérer différentes conditions d'impact. Un tel correcteur est dit être un correcteur $\mathcal{H}_\infty$ non linéaire, si le système en boucle fermée est aussi asymptotiquement stable.

9.2.2 Synthèse sous contraintes unilatérales par retour de sortie

Pour une utilisation ultérieure, la dynamique continue (221) est réécrite sous la forme

$$\dot{\mathbf{x}} = \mathbf{f}(\mathbf{x},t) + \mathbf{g_1}(\mathbf{x},t)\mathbf{w} + \mathbf{g_2}(\mathbf{x},t)\mathbf{u} \tag{228}$$

alors que la règle de la restitution est représentée comme suit

$$\mathbf{x}(t_i^+) = \mu(\mathbf{x}(t_i^-),t_i) + \Omega(\mathbf{x}(t_i^-),t_i)\mathbf{w_d^i},\ i=1,2,\ldots \tag{229}$$

avec $\mathbf{x} = [\mathbf{x}_1^\top,\mathbf{x}_2^\top]^\top$, $\mathbf{f}(\mathbf{x},t) = [\mathbf{x}_2^\top,\boldsymbol{\Phi}^\top(\mathbf{x},t)]^\top$, $\mathbf{g_1}(\mathbf{x},t) = [\mathbf{0},\boldsymbol{\Psi}_1^\top(\mathbf{x},t)]^\top$, $\mathbf{g}_2(\mathbf{x},t) = [\mathbf{0},\boldsymbol{\Psi}_2^\top(\mathbf{x},t)]^\top$, $\mu(\mathbf{x},t) = [\mathbf{x}_1^\top,\mu_0^\top(\mathbf{x},t)]^\top$, et $\Omega(\mathbf{x},t) = [\mathbf{0},\omega(\mathbf{x},\mathbf{t})]^\top$. Afin de simplifier la synthèse à développer et à fournir des expressions raisonnables pour la conception du correcteur, les hypothèses suivantes

$$\begin{aligned} &\mathbf{h_1}^\top\mathbf{k_{12}} = \mathbf{0},\ \mathbf{k_{12}}^\top\mathbf{k_{12}} = \mathbf{I}, \\ &\mathbf{k_{21}}\mathbf{g_1}^\top = \mathbf{0},\ \mathbf{k_{21}}\mathbf{k_{21}}^\top = \mathbf{I}, \end{aligned} \tag{230}$$

qui sont la norme dans la littérature (voir, par exemple, Orlov (2009)) sont faites. Ces hypothèses peuvent être assouplies mais elles compliqueraient les formules à élaborer.

9.2.2.1 Solution non-locale dans l'espace d'état

Ci-dessous, nous listons les hypothèses dans lesquelles une solution au problème en question est dérivée. Soit $\gamma > 0$, dans une domaine $\mathbf{x} \in B_\delta^{2n}, \boldsymbol{\xi} \in B_\delta^{2n}, t \in \mathbb{R}$, où $B_\delta^{2n} \in \mathbb{R}^{2n}$ est une boule de rayon $\delta > 0,$ centrée en l'origine,

H1) la norme de la fonction matricielle $\boldsymbol{\omega}$ est délimitée par $\frac{\sqrt{2}}{2}\gamma$, i.e.,

$$\|\boldsymbol{\omega}(\mathbf{x},t)\| \leq \frac{\sqrt{2}}{2}\gamma. \tag{231}$$

H2) Il existe une fonction lisse, définie positive, et décroissante $V(\mathbf{x},t)$, et une fonction définie positive $R(\mathbf{x})$ telle que, si elle est calculée le long des trajectoires du système (221)-(225) avec des conditions initiales à l'intérieur B_δ^{2n}, pour tous les instants $t \in (t_{i-1}, t_i),\ i = 1, 2, \ldots$, avec t_0 étant le temps initial, et t_i les instants de collision du système perturbé (221)-(225), l'inégalité de Hamilton–Jacobi–Isaacs

$$\begin{aligned} \frac{\partial V}{\partial t} + \frac{\partial V}{\partial \mathbf{x}}(\mathbf{f}(\mathbf{x},t) + \mathbf{g_1}(\mathbf{x},t)\boldsymbol{\alpha_1} + \mathbf{g_2}(\mathbf{x},t)\boldsymbol{\alpha_2}) +& \\ \mathbf{h_1}^\top\mathbf{h_1} + \boldsymbol{\alpha_2}^\top\boldsymbol{\alpha_2} - \gamma^2\boldsymbol{\alpha_1}^\top\boldsymbol{\alpha_1} \leq -R(\mathbf{x})& \end{aligned} \tag{232}$$

est vraie, avec

$$\begin{aligned} \boldsymbol{\alpha_1}(\mathbf{x},t) &= \frac{1}{2\gamma^2}\mathbf{g}_1^\top(\mathbf{x},t)\left(\frac{\partial V}{\partial \mathbf{x}}\right)^\top \\ \boldsymbol{\alpha_2}(\mathbf{x},t) &= -\frac{1}{2}\mathbf{g}_2^\top(\mathbf{x},t)\left(\frac{\partial V}{\partial \mathbf{x}}\right)^\top; \end{aligned}$$

H3) il existe une fonction continue uniformément bornée $G(t)$, une fonction définie positive $Q(\mathbf{x},\boldsymbol{\xi})$ avec $Q(\mathbf{0},\boldsymbol{\xi})$ définie positive, et une fonction lisse, semi-définie positive et décroissante $W(\mathbf{x},\boldsymbol{\xi},t)$ avec $W(\mathbf{0},\boldsymbol{\xi},t)$ définie positive, et telle que calculée le long des trajectoires du système (221)-(225) avec des conditions initiales $(\mathbf{x}(t_0),\boldsymbol{\xi}(t_0)) \in B_\delta^{2n}$, pour tous les instants $t \in (t_{i-1}, t_i)$, l'inégalité de Hamilton-Jacobi-Isaacs

$$\begin{aligned} \frac{\partial W}{\partial t} + \begin{pmatrix} \frac{\partial W}{\partial \mathbf{x}} & \frac{\partial W}{\partial \boldsymbol{\xi}} \end{pmatrix} \mathbf{f_e}(\mathbf{x},\boldsymbol{\xi},t) + \mathbf{h_e}^\top\mathbf{h_e}& \\ -\gamma^2\boldsymbol{\psi}^\top\boldsymbol{\psi} \leq -Q(\mathbf{x},\boldsymbol{\xi})& \end{aligned} \tag{233}$$

est vraie avec

$$
\begin{aligned}
&\mathbf{f_e}(\mathbf{x},\boldsymbol{\xi},t) = \\
&\begin{pmatrix} \mathbf{f}(\mathbf{x},t) \\ \mathbf{f}(\boldsymbol{\xi},t)+\mathbf{g_1}(\boldsymbol{\xi},t)\boldsymbol{\alpha_1}(\boldsymbol{\xi},t) \end{pmatrix} + \begin{pmatrix} \mathbf{g_1}(\mathbf{x},t)\boldsymbol{\alpha_1}(\mathbf{x},t) \\ \mathbf{g_2}(\boldsymbol{\xi},t)\boldsymbol{\alpha_2}(\boldsymbol{\xi},t) \end{pmatrix} \\
&\quad + \begin{pmatrix} \mathbf{g_2}(\mathbf{x},t)\boldsymbol{\alpha_2}(\boldsymbol{\xi},t) \\ \mathbf{G}(t)(\mathbf{h_2}(\mathbf{x},t)-\mathbf{h_2}(\boldsymbol{\xi},t)) \end{pmatrix},
\end{aligned}
$$

$$\mathbf{h_e}(\mathbf{x},\boldsymbol{\xi},t) = \boldsymbol{\alpha_2}(\mathbf{x},t)-\boldsymbol{\alpha_2}(\boldsymbol{\xi},t),$$

$$\boldsymbol{\psi}(\mathbf{x},\boldsymbol{\xi},t) = \frac{1}{2\gamma^2}\mathbf{g_e}^\top(\mathbf{x},t)\begin{pmatrix} \left(\frac{\partial W}{\partial \mathbf{x}}\right)^\top \\ \left(\frac{\partial W}{\partial \boldsymbol{\xi}}\right)^\top \end{pmatrix},$$

$$\mathbf{g_e}(\mathbf{x},t) = \begin{pmatrix} \mathbf{g_1}(\mathbf{x},t) \\ \mathbf{G}(t)\mathbf{k_{21}}(\mathbf{x},t) \end{pmatrix};$$

H4) Les hypothèses H2) et H3) sont satisfaites avec les fonctions $V(\mathbf{x},t)$ et $W(\mathbf{x},\boldsymbol{\xi},t)$ qui décroissent suivant la direction $\boldsymbol{\mu}$ telles que les inégalités

$$V(\mathbf{x},t) \geq V(\boldsymbol{\mu}(\mathbf{x},t),t), \tag{234}$$

$$W(\mathbf{x},\boldsymbol{\xi},t) \geq W(\boldsymbol{\mu}(\mathbf{x},t),\boldsymbol{\mu}(\boldsymbol{\xi},t),t) \tag{235}$$

restent vraies dans les domaines de V et W.

Le premier des principaux résultats de ce travail est donné ci-dessous.

Théorème 9.1 *Considérons le système* (221)-(225)*, et soit $\gamma > 0$, supposons que les hypothèses H1)-H3) sont satisfaites dans les domaines $\mathbf{x} \in B_\delta^{2n}, \boldsymbol{\xi} \in B_\delta^{2n}, t \in \mathbb{R}$. Alors, le système en boucle fermée* (221)-(225)*, asservi par le correcteur dynamique*

$$
\begin{aligned}
\dot{\boldsymbol{\xi}} &= \mathbf{f}(\boldsymbol{\xi},t)+\mathbf{g_1}(\boldsymbol{\xi},t)\boldsymbol{\alpha_1}(\boldsymbol{\xi},t)+\mathbf{g_2}(\boldsymbol{\xi},t)\boldsymbol{\alpha_2}(\boldsymbol{\xi},t)+\mathbf{G}(t)(\mathbf{y}(t)-\mathbf{h_2}(\boldsymbol{\xi},t)) \\
\boldsymbol{\xi}(t_i^+) &= \boldsymbol{\nu}(\boldsymbol{\xi}(t_i^-),\mathbf{y}(t_i^+),t_i) \\
\mathbf{u} &= \boldsymbol{\alpha_2}(\boldsymbol{\xi},t),
\end{aligned}
\tag{236}
$$

possède localement un $\mathcal{L}_2$-gain inférieur à γ. En outre, le système en boucle-fermée sans *perturbations* (221)-(225)*,* (236) *est uniformément asymptotiquement stable à condition que la hypothèse H4) soit aussi satisfaite.*

9.2.3 Application aux systèmes mécaniques soumis a des impacts

La synthèse proposée est maintenant spécifiée pour le problème de suivi pour un manipulateur mécanique, composé de phases de mouvement libre régies par

$$\mathbf{D}(\mathbf{q})\ddot{\mathbf{q}} + \mathbf{H}(\mathbf{q}, \dot{\mathbf{q}}) = \mathbf{D}_{\boldsymbol{\tau}}\boldsymbol{\tau} + \mathbf{w_1} \tag{237}$$

au-delà de la contrainte $F_0(\mathbf{q}) = \mathbf{0}$ où

$$F_0(\mathbf{q}) > 0, \tag{238}$$

pendant que ces phases sont séparées par des transitions conformément à la règle de restitution

$$\mathbf{q}(t_i^+) = \mathbf{q}(t_i^-) \tag{239}$$

$$\dot{\mathbf{q}}(t_i^+) = \phi(\mathbf{q}(t_i))\dot{\mathbf{q}}(t_i^-) + \mathbf{w_i^d} \tag{240}$$

lorsque la trajectoire de l'état frappe la surface

$$F_0(\mathbf{q}(t_i)) = 0, \;\; i = 1, 2, \ldots. \tag{241}$$

Ci-après, $\mathbf{q}, \dot{\mathbf{q}} \in \mathbb{R}^n$ sont les vecteurs généralisés de position et de vitesse, l'entrée de commande $\boldsymbol{\tau} \in \mathbb{R}^n$ est un vecteur de couples externes, $\mathbf{w_1} \in \mathbb{R}^n$ est une perturbation externe, $\mathbf{w_i^d}, \; i = 1, 2, \ldots$ sont des perturbations discrètes de la règle de restitution de vitesse (240) aux instants t_i. La fonction $\phi(\mathbf{q}) \in \mathbb{R}^{n\times n}$ est la matrice de restitution, qui dépend de la position; $\mathbf{H}(\mathbf{q}, \dot{\mathbf{q}}) \in \mathbb{R}^n$ est le vecteur de couples centrifuges, gravitationnels et de Coriolis, la matrice d'inertie $\mathbf{D}(\mathbf{q})$ et la matrice d'actionnement $\mathbf{D}_\tau$ sont de dimension appropriée de telle sorte que $\mathbf{D}(\mathbf{q})$ est symétrique et définie positive, et $\mathbf{D}_\tau$ est inversible et est composée de 1 et 0 (considérant ainsi que des systèmes mécaniques entièrement actionnés); la fonction scalaire $F_0(\mathbf{q})$ est la contrainte unilatérale imposée sur le robot. En fait, $\mathbf{D}(\mathbf{q})$, $\mathbf{H}(\mathbf{q},\dot{\mathbf{q}})$, et $\phi(\mathbf{q})$ sont des fonctions lisses.

Dans ce qui suit, la recherche est limitée au problème de commande de suivi, où la sortie à commander est donnée en termes de l'écart d'état à partir d'une trajectoire de référence $\mathbf{q^r}(t)$, et elle est définie par

$$\mathbf{z} = \begin{bmatrix} \mathbf{0} \\ \rho_p(\mathbf{q}-\mathbf{q^r}) \\ \rho_v(\dot{\mathbf{q}}-\dot{\mathbf{q}}^\mathbf{r}) \end{bmatrix} + \begin{bmatrix} \mathbf{I} \\ \mathbf{0} \\ \mathbf{0} \end{bmatrix} \mathbf{u} \tag{242}$$

avec des coefficients de pondération positifs ρ_p, ρ_v, et son équivalent discret

$$\mathbf{z_i^d} = \dot{\mathbf{q}}(t_i^+) - \dot{\mathbf{q}}^\mathbf{r}(t_i^+) \tag{243}$$

alors que la mesure disponible

$$\mathbf{y} = \mathbf{q} - \mathbf{q^r} + \mathbf{w_0} \tag{244}$$

est affecté par l'erreur de mesure $\mathbf{w_0}(t)$.

La trajectoire de référence à suivre $\mathbf{q^r}(t)$ est une trajectoire périodique soumise à un impact qui apparaît lorsque la trajectoire atteint la surface $F_0(\mathbf{q^r}) = 0$. La loi de restitution pendant la phase d'impact est donnée par

$$\dot{\mathbf{q}}^\mathbf{r}(t_i^+) = \phi(\mathbf{q^r}(t_i))\dot{\mathbf{q}}^\mathbf{r}(t_i^-), \quad i = 1, 2, \ldots. \tag{245}$$

Cette trajectoire peut être construite hors ligne avec des instants d'impact connus $t_i, \ i = 1, 2, \ldots$.

9.2.3.1 Erreur de la dynamique du système hybride

Introduisons le vecteur d'erreur $\mathbf{x} = (\mathbf{x}_1, \mathbf{x}_2)^\top$ où $\mathbf{x}_1(t) = \mathbf{q}(t) - \mathbf{q^r}(t)$ et $\mathbf{x}_2(t) = \dot{\mathbf{q}}(t) - \dot{\mathbf{q}}^\mathbf{r}(t)$. Puis, en réécrivant les équations d'état (237)-(241),(242)-(244) en fonction des erreurs $\mathbf{x_1}$

and $\mathbf{x_2}$ on obtient la dynamique d'erreur

$$\begin{aligned}\dot{\mathbf{x}}_\mathbf{1} &= \mathbf{x_2}\\ \dot{\mathbf{x}}_\mathbf{2} &= \mathbf{D^{-1}}(\mathbf{x_1}+\mathbf{q}^\mathrm{r})[-\mathbf{H}(\mathbf{x_1}+\mathbf{q}^\mathrm{r},\mathbf{x_2}+\dot{\mathbf{q}}^\mathrm{r})+\mathbf{D}_{\boldsymbol{\tau}}\boldsymbol{\tau}+\mathbf{w_1}]-\ddot{\mathbf{q}}^\mathrm{r}.\end{aligned} \tag{246}$$

Les transitions se produisent dans la dynamique d'erreur selon les scénarios suivants:

T1) La trajectoire de référence atteint son instant d'impact prédéfini $t=t^k,\ k=1,2,\dots$ quand elle frappe la contrainte unilatérale alors que le système reste au-delà de cette contrainte, i.e., $F_0(\mathbf{q}^\mathrm{r}(t^k))=0$, $F_0(\mathbf{x_1}(t^k)+\mathbf{q}^\mathrm{r}(t^k))\neq 0$;

T2) Le système atteint la contrainte unilatérale à $t=t^j,\ j=1,2,\dots$ alors que la trajectoire de référence reste au-delà de la contrainte, i.e., $F_0(\mathbf{q}^\mathrm{r}(t^j))\neq 0$, $F_0(\mathbf{x_1}(t^j)+\mathbf{q}^\mathrm{r}(t^j))=0$;

T3) Tant que la trajectoire de référence et le système frappent la contrainte unilatérale en même temps $t=t^l,\ l=1,2,\dots$ (ce qui peut être exécuté en modifiant la trajectoire de référence pré-spécifiée en ligne), i.e., $F_0(\mathbf{q}^\mathrm{r}(t^l))=0$, $F_0(\mathbf{x_1}(t^l)+\mathbf{q}^\mathrm{r}(t^l))=0$.

Nous pouvons écrire les scénarios ci-dessus dans la forme de (224), comme suit

$$\boldsymbol{\mu}_\mathbf{0}(\mathbf{x},t)=\begin{cases}\boldsymbol{\mu}^1(\mathbf{x},t)\text{ if }F_0(\mathbf{q}^\mathrm{r}(t))=0,\quad F_0(\mathbf{x_1}+\mathbf{q}^\mathrm{r})\neq 0\\ \boldsymbol{\mu}^2(\mathbf{x},t)\text{ if }F_0(\mathbf{q}^\mathrm{r}(t))\neq 0,\quad F_0(\mathbf{x_1}+\mathbf{q}^\mathrm{r})=0\\ \boldsymbol{\mu}^3(\mathbf{x},t)\text{ if }F_0(\mathbf{q}^\mathrm{r}(t))=0,\quad F_0(\mathbf{x_1}+\mathbf{q}^\mathrm{r})=0.\end{cases} \tag{247}$$

avec

$$F(\mathbf{x},t)=F_0(\mathbf{x_1}+\mathbf{q}^\mathrm{r}(t)),\quad \boldsymbol{\omega}(\mathbf{x},t)=\mathbf{I} \tag{248}$$

et où les fonctions $\boldsymbol{\mu}^1$, $\boldsymbol{\mu}^2$, et $\boldsymbol{\mu}^3$ sont données par

$$\boldsymbol{\mu}^1(\mathbf{x},t)=\mathbf{x_2}+[\mathbf{I}-\phi(\mathbf{q}^\mathrm{r}(t))]\dot{\mathbf{q}}^\mathrm{r}(t^-) \tag{249}$$

$$\boldsymbol{\mu}^2(\mathbf{x},t)=\phi(\mathbf{x_1}+\mathbf{q}^\mathrm{r}(t))[\mathbf{x_2}+\dot{\mathbf{q}}^\mathrm{r}(t^-)]-\dot{\mathbf{q}}^\mathrm{r}(t^-) \tag{250}$$

$$\boldsymbol{\mu}^3(\mathbf{x},t)=\phi(\mathbf{x_1}+\mathbf{q}^\mathrm{r}(t)[\mathbf{x_2}+\dot{\mathbf{q}}^\mathrm{r}(t^-)]-\phi(\mathbf{q}^\mathrm{r}(t))\dot{\mathbf{q}}^\mathrm{r}(t^-). \tag{251}$$

9.2.3.2 Conception du pré-compensateur et synthèse du correcteur

Dans le cas où les positions généralisées du système mécanique sont les seules disponibles pour la mesure, le pré-compensateur suivant est considéré:

$$\boldsymbol{\tau} = \mathbf{D_{\boldsymbol{\tau}}}^{-1}[\mathbf{D}(\mathbf{q^r})\ddot{\mathbf{q}}^{\mathbf{r}} + \mathbf{H}(\mathbf{q^r}, \dot{\mathbf{q}}^{\mathbf{r}}) + \mathbf{u}]. \tag{252}$$

Par conséquent, le correcteur de position à construire se compose d'un atténuateur de perturbations $\mathbf{u}$, la responsable de la stabilisation interne du bipède autour de la trajectoire désirée, et le reste, qui est responsable de la compensation de la trajectoire de référence et les couples associés avec cette trajectoire.

En substituant (252) dans (246) on obtient la dynamique d'erreur sans impact sous la forme

$$\begin{aligned} \dot{\mathbf{x}}_{\mathbf{1}} &= \mathbf{x_2} \\ \dot{\mathbf{x}}_{\mathbf{2}} &= \mathbf{D^{-1}}(\mathbf{x_1}+\mathbf{q^r})[-\mathbf{H}(\mathbf{x_1}+\mathbf{q^r}, \mathbf{x_2}+\dot{\mathbf{q}}^{\mathbf{r}}) + \mathbf{D}(\mathbf{q^r})\ddot{\mathbf{q}}^{\mathbf{r}} + \mathbf{H}(\mathbf{q^r}, \dot{\mathbf{q}}^{\mathbf{r}}) + \mathbf{u} + \mathbf{w_1}] - \ddot{\mathbf{q}}^{\mathbf{r}} \end{aligned} \tag{253}$$

Ces dynamiques d'erreur représentent une forme particulière du système générique (222)-(223), (228)-(229), spécifiée par (248)-(247) et

$$\mathbf{f}(\mathbf{x}, t) = \begin{bmatrix} \mathbf{x}_2 \\ \mathbf{D^{-1}}(\mathbf{x_1}+\mathbf{q^r})[-\mathbf{H}(\mathbf{x_1}+\mathbf{q^r}, \mathbf{x_2}+\dot{\mathbf{q}}^{\mathbf{r}}) + \mathbf{D}(\mathbf{q^r})\ddot{\mathbf{q}}^{\mathbf{r}} + \mathbf{H}(\mathbf{q^r}, \dot{\mathbf{q}}^{\mathbf{r}})] - \ddot{\mathbf{q}}^{\mathbf{r}} \end{bmatrix} \tag{254}$$

$$\mathbf{g_1}(\mathbf{x}, t) = \begin{bmatrix} \mathbf{0} & \mathbf{0} \\ \mathbf{0} & \mathbf{D^{-1}}(\mathbf{x_1}+\mathbf{q^r}) \end{bmatrix}, \ \mathbf{h_1}(\mathbf{x}, t) = \begin{bmatrix} \mathbf{0} \\ \rho_p \mathbf{x}_1 \\ \rho_v \mathbf{x}_2 \end{bmatrix}, \tag{255}$$

$$\mathbf{g_2}(\mathbf{x}, t) = \begin{bmatrix} \mathbf{0} \\ \mathbf{D^{-1}}(\mathbf{x_1}+\mathbf{q^r}) \end{bmatrix}, \ \mathbf{k_{12}}(\mathbf{x}, t) = \begin{bmatrix} \mathbf{1} \\ \mathbf{0} \\ \mathbf{0} \end{bmatrix} \tag{256}$$

$$\mathbf{h_2}(\mathbf{x}, t) = \begin{bmatrix} \mathbf{x_1}^\top & \mathbf{0} \end{bmatrix}^\top, \ \mathbf{k_{21}}(\mathbf{x}, t) = \begin{bmatrix} \mathbf{I} & \mathbf{0} \end{bmatrix}, \ \boldsymbol{\omega}(\mathbf{x}, t) = \mathbf{I}, \ \mathbf{w} = [\mathbf{w_0}^\top \mathbf{w_1}^\top]^\top. \tag{257}$$

Dans la suite, la synthèse $\mathcal{H}_\infty$ non linéaire générique du théorème 9.1 est spécifiée pour le suivi par retour de sortie du manipulateur mécanique unilatéralement contraint. Il est donné en termes de solutions locales appropriées des inégalités HJI (232), (233).

9.2.3.3 Solution locale dans l'espace d'état

La difficulté de résoudre les inégalités Hamilton-Jacobi-Isaacs (232), (233) est contournée en approchant leurs solutions locales par celles des équations de Riccati correspondantes. Les dernières équations apparaissent dans la résolution du problème de commande $\mathcal{H}_\infty$ pour le système linéarisé qui est donné par

$$\dot{\mathbf{x}} = \mathbf{A}(t)\mathbf{x} + \mathbf{B_1}(t)\mathbf{w} + \mathbf{B_2}(t)\mathbf{u}, \tag{258}$$

$$\mathbf{z} = \mathbf{C_1}(t)\mathbf{x} + \mathbf{D_{12}}(t)\mathbf{u}, \tag{259}$$

$$\mathbf{y} = \mathbf{C_2}(t)\mathbf{x} + \mathbf{D_{21}}(t)\mathbf{w}, \tag{260}$$

à l'intérieur des intervalles de temps sans impact (t_{i-1}, t_i) où t_0 est l'instant de temps initial et $t_i,\ i = 1, 2, \ldots$ sont les temps de collision, alors que

$$\begin{aligned} \mathbf{A}(t) &= \left.\frac{\partial \mathbf{f}(\mathbf{x}, t)}{\partial \mathbf{x}}\right|_{\mathbf{x}=\mathbf{0}},\ \mathbf{B_1}(t) = \mathbf{g_1}(0, t), \mathbf{B_2}(t) = \mathbf{g_2}(0, t),\ \mathbf{C_1}(t) = \left.\frac{\partial \mathbf{h_1}(\mathbf{x}, t)}{\partial \mathbf{x}}\right|_{\mathbf{x}=\mathbf{0}}, \\ \mathbf{C_2}(\mathbf{x})(t) &= \begin{bmatrix} \mathbf{x_1} & \mathbf{0} \end{bmatrix}, \mathbf{D_{12}}(t) = \mathbf{k_{12}}(0, t),\ \mathbf{D_{21}}(\mathbf{x})(t) = \begin{bmatrix} \mathbf{I} & \mathbf{0} \end{bmatrix}. \end{aligned} \tag{261}$$

Par le lemme de stricte bornitude (Orlov and Aguilar, 2014, p.46), les conditions suivantes sont nécessaires et suffisantes pour l'existence d'une solution au problème de commande linéaire $\mathcal{H}_\infty$ (258)-(260):

Soit $\gamma > 0$,

C1) il existe une constante positive ε_0 telle que l'équation différentielle de Riccati

$$\begin{aligned} -\dot{\mathbf{P}}_\varepsilon(t) &= \mathbf{P}_\varepsilon(t)\mathbf{A}(t) + \mathbf{A}^\top(t)\mathbf{P}_\varepsilon(t) + \mathbf{C_1}^\top(t)\mathbf{C_1}(t) \\ &+ \mathbf{P}_\varepsilon(t)[\frac{1}{\gamma^2}\mathbf{B_1}\mathbf{B_1}^\top - \mathbf{B_2}\mathbf{B_2}^\top](t)\mathbf{P}_\varepsilon(t) + \varepsilon\mathbf{I} \end{aligned} \tag{262}$$

a une solution symétrique, uniformément bornée et définie positive $\mathbf{P}_\varepsilon(t)$ pour chaque $\varepsilon \in (0, \varepsilon_0)$;

C2) tout en étant couplée à (262), l'équation différentielle de Riccati

$$\begin{aligned}\dot{\mathbf{Z}}_\varepsilon(t) = \mathbf{A}_\varepsilon(t)\mathbf{Z}_\varepsilon(t) + \mathbf{Z}_\varepsilon(t)\mathbf{A}_\varepsilon^\top(t) + \mathbf{B_1}(t)\mathbf{B_1}^\top(t) \\ +\mathbf{Z}_\varepsilon(t)[\frac{1}{\gamma^2}\mathbf{P}_\varepsilon\mathbf{B_2}\mathbf{B_2}^\top\mathbf{P}_\varepsilon - \mathbf{C_2}^\top\mathbf{C_2}](t)\mathbf{Z}_\varepsilon(t) + \varepsilon\mathbf{I},\end{aligned} \tag{263}$$

a une solution symétrique, uniformément bornée et définie positive $\mathbf{Z}_\varepsilon(t)$ avec $\mathbf{A}_\varepsilon(t) = \mathbf{A}(t) + \frac{1}{\gamma^2}\mathbf{B_1}(t)\mathbf{B_1}^\top(t)\mathbf{P}_\varepsilon(t)$.

Le résultat suivant affirme que ces conditions, couplées à une certaine condition de monotonie, sont également suffisantes pour l'existence d'une solution locale au problème de commande $\mathcal{H}_\infty$ non linéaire sous contraintes unilatérales.

Théorème 9.2 *Considérons le système non linéaire* (221)-(225)*, spécifié avec* (254)-(257)*. Si les conditions C1) et C2) sont satisfaites avec une certaine $\gamma > 0$, alors les hypothèses H2) et H3) restent vraies localement autour de l'origine $(\mathbf{x}, \boldsymbol{\xi}) = (0, 0)$ avec*

$$V(\mathbf{x}, t) = \mathbf{x}^\top\mathbf{P}_\varepsilon(t)\mathbf{x} \tag{264}$$

$$R(\mathbf{x}) = \frac{\varepsilon}{2}\|\mathbf{x}\|^2 \tag{265}$$

$$W(\mathbf{x}, \boldsymbol{\xi}, t) = \gamma^2(\mathbf{x} - \boldsymbol{\xi})^\top\mathbf{Z}_\varepsilon^{-\mathbf{1}}(t)(\mathbf{x} - \boldsymbol{\xi}) \tag{266}$$

$$Q(\mathbf{x}, \boldsymbol{\xi}) = \frac{\varepsilon}{2}\gamma^2 \inf_{t\in\mathbb{R}^1} \|\mathbf{Z}_\varepsilon^{-\mathbf{1}}(t)\|^2\|\mathbf{x} - \boldsymbol{\xi}\|^2 \tag{267}$$

$$G(t) = \mathbf{Z}_\varepsilon(t)\mathbf{C_2}^\top(t) \tag{268}$$

$$\boldsymbol{\nu}(\xi, \mathbf{y}, t) = \begin{bmatrix} \mathbf{y}^\top & \boldsymbol{\mu}_0^\top(\xi, t) \end{bmatrix}^\top \tag{269}$$

et le système en boucle fermée, asservi par le retour de sortie

$$\dot{\boldsymbol{\xi}} = \mathbf{f}(\boldsymbol{\xi}, t) + \mathbf{Z}_\varepsilon(t)\mathbf{C_2}^\top(t)[\mathbf{y}(t) - \mathbf{h_2}(\boldsymbol{\xi}, t)] + \left[\frac{1}{\gamma^2}\mathbf{g_1}(\boldsymbol{\xi}, t)\mathbf{g_1}^\top(\boldsymbol{\xi}, t) - \mathbf{g_2}(\boldsymbol{\xi}, t)\mathbf{g_2}^\top(\boldsymbol{\xi}, t)\right]\mathbf{P}_\varepsilon(t)\boldsymbol{\xi}$$

$$\boldsymbol{\xi}(t_i^+) = \boldsymbol{\nu}(\boldsymbol{\xi}(t_i^-), \boldsymbol{y}(t_i^-), t_i) \tag{270a}$$

$$\mathbf{u} = -\mathbf{g_2}(\boldsymbol{\xi}, t)^\top\mathbf{P}_\varepsilon(t)\boldsymbol{\xi}, \tag{270b}$$

possède localement un $\mathcal{L}_2$-gain inférieur à γ à condition que l'hypothèse H1) reste vraie.

En outre, le système en boucle fermée sans perturbations (221)-(225)*,* (270) *est uniformément asymptotiquement stable à condition que l'hypothèse H4) soit satisfaite avec les fonctions quadratiques* (264) *et* (266)*.*

9.2.4 Synthèse par retour d'état

Dans le cas de l'information complète où la mesure de l'état parfait est disponible, un pré-compensateur de la forme

$$\boldsymbol{\tau} = \mathbf{D}_{\boldsymbol{\tau}}{}^{-1}[\mathbf{D}(\mathbf{q})(\ddot{\mathbf{q}}^{\mathbf{r}} + \mathbf{u}) + \mathbf{H}(\mathbf{q}, \dot{\mathbf{q}})] \tag{271}$$

est conçu de manière à simplifier la synthèse par retour d'état ultérieur. Le correcteur est constitué d'un atténuateur de perturbations $\mathbf{u}$, responsable pour la stabilisation interne du bipède autour de la trajectoire désirée, et le reste, qui est responsable de la compensation de la trajectoire.

En substituant (271) dans (246), la dynamique d'erreur entre les impacts sont simplifiées, comme suit

$$\begin{aligned} \dot{\mathbf{x}}_{\mathbf{1}} &= \mathbf{x}_{\mathbf{2}} \\ \dot{\mathbf{x}}_{\mathbf{2}} &= \mathbf{D}^{-\mathbf{1}}(\mathbf{x}_{\mathbf{1}} + \mathbf{q}^{\mathbf{r}})\mathbf{w}_{\mathbf{1}} + \mathbf{u} \end{aligned} \tag{272}$$

Ainsi, la dynamique de l'erreur est représentée sous la forme générique (221)-(225), spécifiée avec

$$\mathbf{f}(\mathbf{x}, t) = \begin{bmatrix} \mathbf{x}_2 \\ \mathbf{0} \end{bmatrix},\ \mathbf{g}_{\mathbf{1}}(\mathbf{x}, t) = \begin{bmatrix} \mathbf{0} \\ \mathbf{D}^{-\mathbf{1}}(\mathbf{x}_{\mathbf{1}} + \mathbf{q}^{\mathbf{r}}) \end{bmatrix}, \tag{273}$$

$$\mathbf{g}_{\mathbf{2}}(\mathbf{x}, t) = \begin{bmatrix} \mathbf{0} \\ \mathbf{1} \end{bmatrix},\ \mathbf{h}(\mathbf{x}) = \begin{bmatrix} \mathbf{0} \\ \rho_p \mathbf{x}_1 \\ \rho_v \mathbf{x}_2 \end{bmatrix},\ \mathbf{k}_{\mathbf{12}}(\mathbf{x}) = \begin{bmatrix} \mathbf{I} \\ \mathbf{0} \\ \mathbf{0} \end{bmatrix}. \tag{274}$$

Enfin, le théorème 9.2 est simplifié à la conception du bouclage statique

$$\mathbf{u} = -\mathbf{g}_{\mathbf{2}}(\mathbf{x}, t)^{\top} \mathbf{P}_{\varepsilon}(t) \mathbf{x} \tag{275}$$

et il se résume comme suit.

Théorème 9.3 *Supposons que l'hypothèse H1) et la condition C1) soient satisfaites par un certain* $\gamma > 0$*. En conséquence, le système en boucle fermée* (221)-(225)*, spécifié avec* (273)-(274) *et asservi par le retour d'état* (275)*, possède localement une* $\mathcal{L}_2$*-gain inférieur à* γ*. En outre, le système en boucle fermée sans perturbation est uniformément asymptotiquement stable à condition que la fonction* $V(\mathbf{x}, t) = \mathbf{x}^\top \mathbf{P}_\varepsilon(t)\mathbf{x}$ *satisfait localement l'inégalité* (234)*.*

9.3 Génération des mouvements périodiques sous contraintes unilatérales : l'oscillateur hybride de Van der Pol

Le objectif de cette section est de concevoir un oscillateur hybride pour l'utiliser comme un modèle de référence qui pourrait générer un cycle limite stable sous contraintes unilatérales. Comme dans le cas sans contraintes, un tel modèle peut aider pour synthétiser un système en boucle fermée qui produit son propre cycle limite.

Nous allons étudier la modification de l'oscillateur de Van der Pol suivant

$$\dot{x}_1 = x_2, \quad \dot{x}_2 = -\varepsilon \left[\left(x_1^2 + \frac{x_2^2}{\mu^2} \right) - \rho^2 \right] x_2 - \mu^2 x_1 \tag{276}$$

qui a été proposée par Roup and Bernstein (2001) où le vecteur $x = (x_1, x_2)^T$ consiste en la position x_1 de l'oscillateur et sa vitesse x_2. Il a été montré par Orlov *et al.* (2004) qu'il possède un cycle limite stable qui attire toutes les autres solutions, sauf celles initialisées au point d'équilibre $(x, \dot{x}) = (0, 0)$. Ce cycle limite est gouverné par l'équation d'ellipse

$$x_1^2 + \frac{x_2^2}{\mu^2} = \rho^2, \tag{277}$$

et il est produit par l'oscillateur harmonique

$$\dot{x}_1 = x_2, \; \dot{x}_2 = -\mu^2 x_1, \tag{278}$$

initialisé sur l'ellipse (277).

Tout en étant initialisé en dehors de l'origine, l'oscillateur de Van der Pol modifié (276) produit des oscillations harmoniques stables d'amplitude ρ et de fréquence μ, avec un amortissement ε. En raison des caractéristiques ci-dessus, la modification de Van der Pol (276) est devenue extrêmement adaptée pour son utilisation dans la commande adaptative par modèle de référence de Roup and Bernstein (2001); Orlov *et al.* (2008); Santiesteban *et al.* (2008) où l'amplitude désirée et la fréquence de l'oscillation résultant peuvent être modifiées en ligne.

9.3.1 L'oscillateur de Van der Pol sous contraintes

Dans la suite, la dynamique de l'oscillateur de Van der Pol modifié (276) sont étudiés sous la contrainte unilatérale $x_1 \geq 0$. Le présente étude a pour but de savoir si un tel oscillateur de Van der Pol sous contrainte unilatérale est encore capable de générer un cycle limite. L'analyse numérique réalisée pour vérifier l'existence d'un cycle limite, a révélé l'existence d'une bifurcation de type Hopf pour la modification de Van der Pol sous contrainte unilatérale, pour une valeur non négligeable du paramètre ε.

Comme nous l'avons souligné, l'oscillateur de Van der Pol modifié fonctionne sous la contrainte de position unilatérale $x_1 \geq 0$. Une fois qu'une trajectoire arrive à la surface de contrainte

$$S = \{x \in \mathbb{R}^2 : x_1 = 0 \cup x_2 \leq 0\} \tag{279}$$

à un instant de collision t, le modèle sous-jacent réinitialise instantanément sa vitesse en fonction de la loi de la restitution élastique

$$x_1(t^+) = x_1(t^-), \;\; x_2(t^+) = -ex_2(t^-), \text{ iff } \; x(t) \in S \tag{280}$$

avec le paramètre de restitution $e \in (0, 1)$. Ci-après, $x_1(t^-)$ et $x_2(t^-)$ représentent les états avant l'impact (position et vitesse, respectivement), avant de frapper la surface de contrainte (279), tandis que $x_1(t^+)$ et $x_2(t^+)$ représentent les états après l'impact. Au-delà de la contrainte, la dynamique continue est régie par (276) pour $x \notin S$.

9.3.2 Existence d'un cycle limite sous contraintes

Sans perte de généralité, l'analyse de stabilité du modèle hybride de Van der Pol(276), (279), (280) est limitée aux conditions initiales $x^0 = (0, v_0)^T$ avec $v_0 > 0$; sinon, on pourrait facilement ré-initialiser le modèle avec les conditions initiales en reconstituant la dynamique continue pour les instants passés. A partir de là on peut laisser $x(v_0; t) = (x_1(v_0; t), x_2(v_0; t))^T$ dénoter une trajectoire de (276), (279), (280), initialiser à $x_1(v_0; 0) = 0, x_2(v_0; 0) = v_0 > 0$ et laisser t_k, $k = 1, 2, \ldots$ indiquer les instants de collision lorsque cette trajectoire réinitialise sa vitesse. En fonction des valeurs des paramètres de l'oscillateur, les scénarios alternatifs suivants sont heuristiquement dans l'ordre.

S1) Les inégalités

$$x_2(v_0; t_1^+) < v_0,\ x_2(v_0; t_{k+1}^+) < x_2(v_0; t_k^+) \tag{281}$$

restent vraies pour $k = 1, 2, \ldots$ et tous les $v_0 > 0$.

S2) Il existe un scalaire $x^* > 0$ tel que les inégalités (281) restent vraies pour tous les $k = 1, 2, \ldots$ et tous les $v_0 > x^*$ tandis que les inégalités inverses

$$x_2(v_0; t_1^+) > v_0,\ x_2(v_0; t_{k+1}^+) > x_2(v_0; t_k^+) \tag{282}$$

restent vraies pour tous les $k = 1, 2, \ldots$ et tous les $v_0 \in (0, x^*)$.

Le résultat suivant peut être considéré comme une contrepartie du critère de Poincaré-Bendixson pour l'oscillateur sous contraintes (276), (279), (280).

Théorème 9.4 *Considérons l'oscillateur hybride de Van der Pol* (276)*,* (279)*,* (280) *avec les paramètres $\rho, \mu, \varepsilon > 0$ et $e \in (0, 1)$ fixés a priori. Si le scénario S1) est valide, alors* (276)*,* (279)*,* (280) *est globalement asymptotiquement stable à l'origine. Au contraire, si le scénario S2) est valide, alors* (276)*,* (279)*,* (280) *possède un cycle limite stable γ^* généré par la trajectoire $x(x^*; t)$ avec $x^0 = (0, x^*)^\top$ de telle sorte que toute trajectoire de* (276)*,* (279)*,* (280)*, initialisée au-delà de l'origine, converge vers γ^*.*

Ces deux scénarios sont illustrés Fig. 75, où les convergences vers l'origine où vers le cycle limite sont claires.

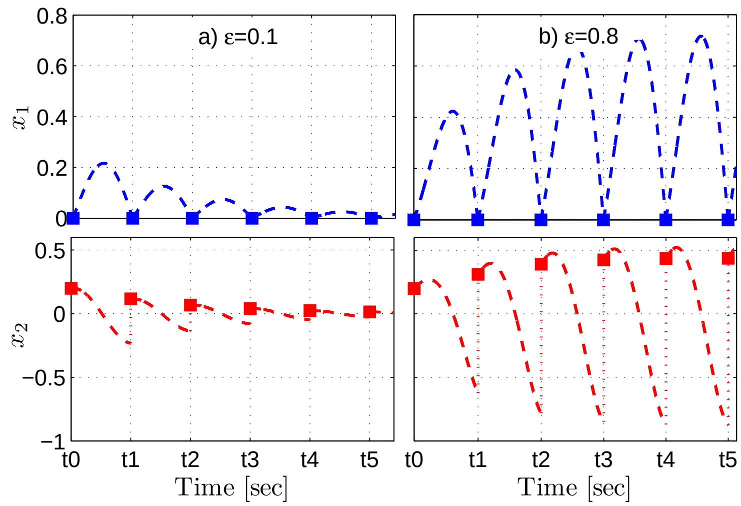

Figure 75: La dynamique de l'état en vertu d'une condition initiale $x^0 = (0, 0, 2)^T$. Les carrés indiquent les positions et les vitesses après impact à des instants t_k. Pour $\varepsilon = 0,1$, la séquence de $x_2(0, 2; t_k^+)$ tombe dans le scénario S1). Au contraire, pour $\varepsilon = 0,8$, Scénario S2) est mis en jeu.

Le Théorème 9.4 admet une interprétation utile en termes de l'application de Poincaré des trajectoires de (276), (279), (280) où la section de Poincaré est fixée à chaque instant juste après la réinitialisation. A partir de ceci la variable $x(t_k^+)$ après chaque réinitialisation peut être considérée comme un système discret de la forme

$$x_2(t_{k+1}^+) = F(x_2(t_k^+)) \tag{283}$$

où F représente l'application de l'état après-impact précédente au suivante. A partir du théorème 9.4, les inégalités (281)-(282) assurent l'existence d'un point fixe x^* pour l'application (283), et assurent aussi que les valeurs propres du gradient ∇F de cette application sont toutes à l'intérieur du cercle unité, et aucune valeur propre n'a de partie imaginaire parce que la séquence $x_2(t_k^+),\ k = 1, 2, \ldots$ ne peut pas traverser x^*. Dans la section suivante cette observation sera numériquement appliquée à l'analyse de la stabilité d'un cycle limite généré par l'oscillateur hybride de Van der Pol (276), (279), (280).

9.3.3 Bifurcation de cycles limites

Après plusieurs expériences numériques, (voir par exemple Fig. 76), la valeur de bifurcation est trouvé entre les valeurs $0,4 < \varepsilon_c < 0,5$.

Motivé par ces résultats, la section suivante applique numériquement la méthode de

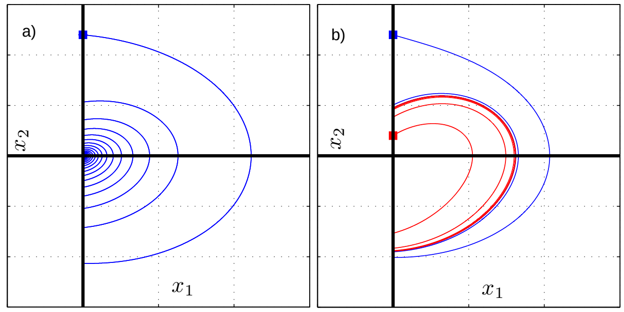

Figure 76: Trajectoires de phase de (80)**,** (83)**,** (84) **pour deux valeurs du paramétré** ε**: a)** $\varepsilon = 0,3$**, b)** $\varepsilon = 1$**. Les carrés indiquent la condition initiale de chaque trajectoire.**

Poincaré pour mieux approcher la valeur du paramètre critique ε_c, lorsque la bifurcation de Hopf a lieu.

9.3.4 Analyse de la stabilité des cycles limites par l'application de Poincaré

Dans cette section, la méthode de Poincaré est appliquée afin d'analyser le scénario qui est en jeu. La section de Poincaré (283) est déterminée juste après une réinitialisation du système (276), (279), (280) pour la prise en compte à la fois de la dynamique continue et discrète. Cette application comprend la solution de l'équation différentielle de la dynamique continue (276) et la loi de restitution (280). Étant donné que le premier est quasiment impossible à obtenir, le développement actuel repose sur une méthode d'intégration numérique pas à pas, comme celle de Goswami *et al.* (1996).

Afin de vérifier que (276), (279), (280) possède une solution périodique, seulement l'application unidimensionnelle x_2 est analysée parce que la valeur post-impact de la position x_1 est toujours nulle en raison du choix de la surface de restitution.

Les paramètres $e = 0,5, \mu = 1, \rho = 1$ sont considérés, et la stabilité du cycle limite montrée dans Fig. 76b, est analysée avec $\varepsilon = 1$. Le graphique de Cobweb, qui est bien connu comme un outil utile pour étudier sur le comportement qualitatif des applications à une dimension Waugh (1964), est presenté dans la Fig. 77a pour la même valeur de ε. Les points fixes de (283) sont normalement obtenus comme les intersections entre cette application et l'application identité.

En plus de l'équilibre instable $x_2 = 0$, il y a une autre intersection, qui correspond à un

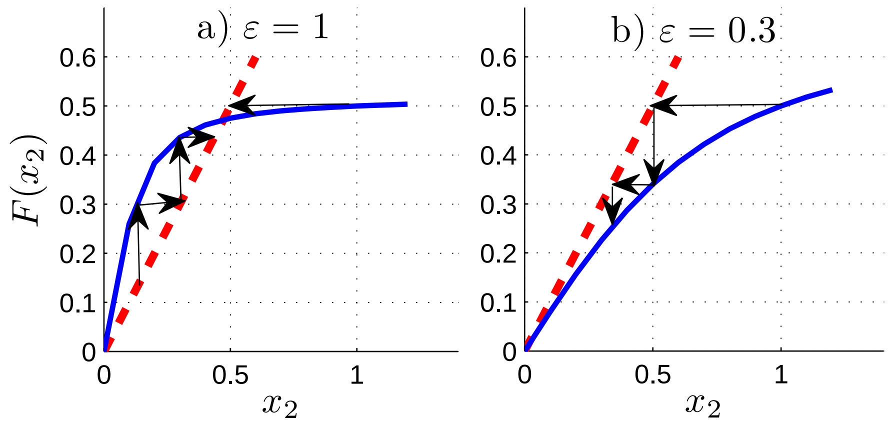

Figure 77: Les graphiques de Cobweb de l'application de Poincaré (283) **avec** $\varepsilon = 1$ **et** $\varepsilon = 0,3$**. La ligne continue est pour l'application de Poincaré** $F(x_2)$**, tandis que la ligne en pointillés est pour l'application identité. les flèches illustrent a) l'attractivité du point fixe (carré noir) pour** $\varepsilon = 1$**, et b) l'attractivité de l'origine pour** $\varepsilon = 0,3$**.**

point fixe asymptotiquement stable x^*, indiqué sur la Figure 77a par le carré noir. En effet, les flèches sur la graphique de Cobweb indiquent l'évolution de l'application de Poincaré à partir d'une condition initiale arbitraire $x_2(t_0) = v_0 > 0$, et il est montré que toutes les trajectoires évoluent loin de zéro et se rapprochent au point fixe x^*. Ainsi, le scénario S2) est en ordre et le théorème 9.4 assure l'existence et de la stabilité asymptotique du cycle limite, généré par la trajectoire, initialisée à $x_1 = 0, x_2 = x^*$. Pour analyser localement la stabilité du point fixe x^*, les valeurs propres du gradient de l'application de Poincaré F sont numériquement calculées comme suit (Goswami *et al.*, 1996)

$$\nabla F = [F(x^* + \delta x^*) - x^*] = \Upsilon\Omega^{-1}(\delta x^*)^{-1}. \tag{284}$$

Alors, ∇F est calculé en fonction de (284) en appliquant un écart Ω du point fixe (par l'intermédiaire d'écarter la valeur initiale de x_2) pour le calcul numérique de la valeur résultante $\Upsilon = x_2(t^+_{k+1})$.

En suivant cette procédure avec un certain écart $\Omega = 0,228$, la valeur $\Upsilon = 0,018$ est obtenue pour $\varepsilon = 1$. Comme la valeur propre $\lambda(\nabla F) = 0,079$ est à l'intérieur du cercle unité, la stabilité asymptotique de x^* est établie. En outre, en raison du fait que $\lambda(\nabla F)$ a une partie imaginaire nulle, le scénario S2) est valide, de sorte que le théorème 9.4 assure que le cycle limite de l'oscillateur hybride de Van der Pol (276), (279), (280), illustré dans la Fig. 76b, est asymptotiquement stable aussi.

La stabilité asymptotique de l'origine est illustrée sur la Fig. 76a pour $\varepsilon = 0,3$ et elle est analysée au moyen du graphique de Cobweb de (283), représentée Fig. 77b. Dans ce cas, le seul point de la carte fixe est à l'origine, et, comme indiqué par les flèches noires, la carte évolue vers l'origine, conduisant ainsi à la stabilité asymptotique de l'origine. La même conclusion est obtenue à partir de la valeur propre de ∇F, à l'intérieur du cercle unité centré en l'origine.

L'analyse proposée révèle que l'existence d'un point fixe de (283) assure l'existence d'un cycle limite. La figure 78 montre les intersections de l'application de Poincaré (283) et l'application identité, pour plusieurs valeurs de ε. On peut observer que, tout en diminuant ε vers zéro, il n'y a plus une intersection de l'application de Poincaré avec l'application identité. Donc il n'y a pas de point fixe de (283) autre que l'origine. En utilisant les mêmes outils que précédemment, la graphique de Cobweb démontre que l'origine est attractive, comme prévu sur la base des valeurs propres de ∇F, situées à l'intérieur du cercle unité pour les petites valeurs de ε. Ainsi, le scénario S1) est valide, et la stabilité asymptotique de l'origine est déduite par le théorème 9.4.

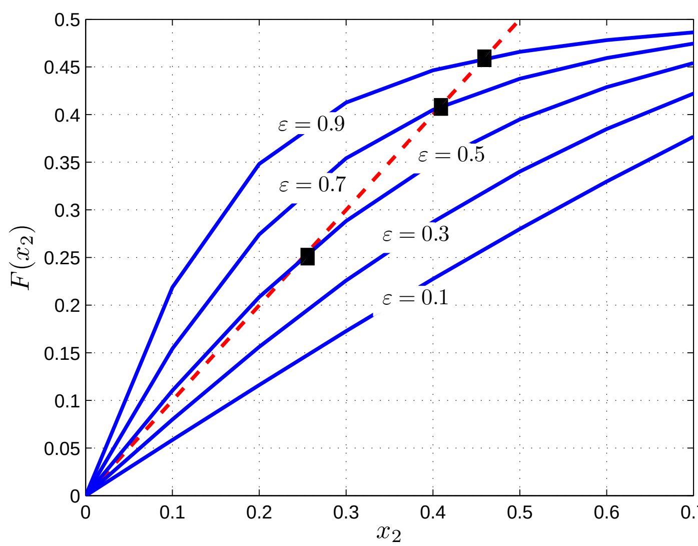

Figure 78: Intersections de l'application de Poincaré (283) **et l'application identité pour plusieurs valeurs de** ε**. La ligne pointillée est pour l'application identité, et les carrés noirs pour les points fixes des applications.**

La Fig. 79 trace le point fixe x^*, calculé pour plusieurs valeurs de ε. Cette figure illustre la bifurcation de Hopf de (276), (279), (280) se produisant à la valeur critique $\varepsilon_c \approx 0,43$.

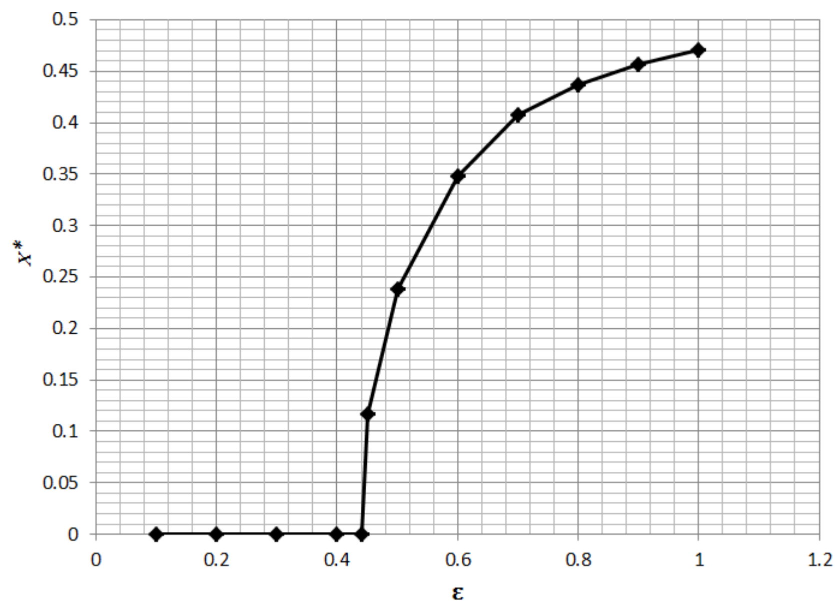

Figure 79: Diagramme de bifurcation pour l'oscillateur hybride de Van der Pol : point fixe x^* de l'application de Poincaré (283) **vs ε. La bifuraction de Hopf se produit à $\varepsilon \approx 0,43$.**

9.4 Suivi d'un cycle limite par modèle de référence : Étude de cas

9.4.1 Modèle d'un pendule soumis à une contrainte unilatérale

Un simple banc d'essai d'un pendule qui frappe contre une barrière est représenté sur la Fig. 80 où le mouvement libre du pendule est confinée par la barrière située à l'axe vertical positif. Pour la dynamique de mouvement libre $q \in (0, 2\pi)$, l'équation du système est donnée par

$$(ml^2 + J)\ddot{q} = -mgl\sin(q) - k\dot{q} + \tau + w_1 \tag{285}$$

où q est l'angle formé par le pendule avec la verticale, m est la masse du pendule, l est la distance au centre de masse, J est le moment d'inertie du pendule autour du centre de masse, g est l'accélération de la gravité, k est un coefficient de frottement visqueux, τ est le couple de commande, et w_1 représente les forces externes non modélisés (frottement sec, par example). Pour la transition à l'équilibre instable $q = 0$, la loi de restitution est donnée par

$$q^+ = q^-, \quad \dot{q}^+ = -e\dot{q}^- + w_i^d, \quad e \in [0, 1]. \tag{286}$$

Les variables $w_i^d,\ i = 1, 2, \ldots$ sont introduites pour tenir compte des incertitudes de modèle et des incertitudes à l'impact. Une vitesse de restitution similaire se produit à

$q = 2\pi$. La synthèse locale se limitera ultérieurement au mouvement libre dans le domaine $q \in (0, \pi)$.

Afin d'aborder le problème de suivi d'une trajectoire de référence $q^r(t)$, les variables d'erreur

$$x_1 = q - q^r, \; x_2 = \dot{q} - \dot{q}^r \tag{287}$$

et la mesure de position

$$y = x_1 + w_0 \tag{288}$$

sont introduites, où w_0 est le bruit de mesure. Inspirée de (252), la loi de commande

$$\tau = (ml^2 + J)\ddot{q}^r + k\dot{q}^r + mgl \sin q^r + (ml^2 + J)u, \tag{289}$$

est composée d'un correcteur u à déterminer et le reste forme un compensateur de trajectoire. Ensuite, en définissant $\mathbf{x} = (x_1, x_2)^\top$, $\mathbf{w} = (w_0, w_1)^\top$, et en réécrivant le système (285)-(289) en fonction des variables d'erreur de suivi, on obtient

La dynamique d'erreur de la phase de mouvement libre

$$\dot{\mathbf{x}} = \underbrace{\begin{bmatrix} x_2 \\ -\frac{mgl}{ml^2+J}\sin(x_1 + q^r) - \frac{k}{ml^2+J}x_2 + \frac{mgl}{ml^2+J}\sin(q^r) \end{bmatrix}}_{\mathbf{f}(\mathbf{x},t)} + \underbrace{\begin{bmatrix} 0 & 0 \\ 0 & \frac{1}{m} \end{bmatrix}}_{\mathbf{g_1}} \mathbf{w} + \underbrace{\begin{bmatrix} 0 \\ 1 \end{bmatrix}}_{\mathbf{g_2}} u \tag{290}$$

au-delà de la contrainte $F_0(\mathbf{x}, t) = x_1 + q^r(t) > 0$ et

le système d'erreur de la transition

$$\mathbf{x}^+ = \begin{bmatrix} x_1^- \\ \mu_0(\mathbf{x}, t) \end{bmatrix} + \begin{bmatrix} 0 \\ 1 \end{bmatrix} w_i^d \tag{291}$$

sous la contrainte $F_0(\mathbf{x}, t) = x_1 + q^r(t) = 0$ où

$$\mu_0(\mathbf{x}, t) = \begin{cases} x_2 + (1+e)\dot{q}^r & \text{if } F_0(q^r(t)) = 0, \quad F_0(x_1 + q^r) \neq 0 \\ -e(x_2 + \dot{q}^r) - \dot{q}^r & \text{if } F_0(q^r(t)) \neq 0, \quad F_0(x_1 + q^r) = 0 \\ -ex_2 & \text{if } F_0(q^r(t)) = 0, \quad F_0(x_1 + q^r) = 0, \end{cases} \tag{292}$$

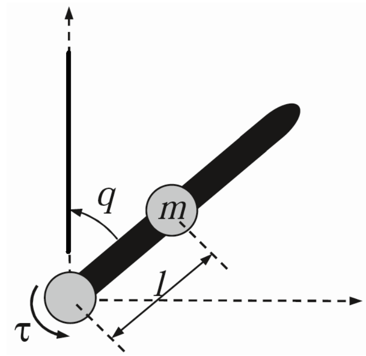

Figure 80: Le système pendule-barrière

est obtenu en spécifiant (245)-(247).

En ce qui concerne les erreurs de suivi, les variables à commander sont spécifiées sous la forme

$$\mathbf{z} = \underbrace{\begin{bmatrix} 0 & 0 \\ \rho_p & 0 \\ 0 & \rho_v \end{bmatrix}}_{\mathbf{h_1}} \mathbf{x} + \underbrace{\begin{bmatrix} 1 \\ 0 \\ 0 \end{bmatrix}}_{\mathbf{D_{12}}} u \tag{293}$$

$$z_i^d = -ex_2^- + w_i^d, \tag{294}$$

qui respecte (230).

9.4.2 Régulation par retour de la sortie

Le suivi du système pendule-barrière est traité dans un cas particulier de la trajectoire de référence trivial dégénérée à l'origine $q^r = 0$, $\dot{q}^r = 0$, $\ddot{q}^r = 0$, tandis que la commande (289) est simplifiée sous la forme $\tau = (ml^2 + J)u$, sans compensation de la trajectoire. L'application du Théorème 9.2 au système d'erreur(290)-(294), pour obtenir la régulation robuste désirée, est vérifiée comme suit.

Premièrement, les termes invariants en temps (261) dans les équations de Riccati (262)-(263) sont spécifiées en fonction de (290)-(294), et les conditions C1) et C2) du Théorème 9.2 sont vérifiées en effectuant une itération sur γ afin d'approcher la valeur minimale $\gamma_{min} \approx 1,01$. La valeur $\gamma = 2$ est sélectionnée pour éviter la définition d'un correcteur à gain élevé indésirable qui apparaît pour une valeur de γ proche du infimale $\gamma_{min} \approx 1,01$. Avec $\gamma = 2$, la valeur $\varepsilon = 0,01$ est obtenue par itération sur ε pour assurer que l'équation de Riccati perturbée correspondant (262) possède la solution définie positive suivante

$$\mathbf{P}_\varepsilon = \begin{bmatrix} 3,6682 & 0,1020 \\ 0,1020 & 0,7234 \end{bmatrix}, \quad \mathbf{Z}_\varepsilon = \begin{bmatrix} 0,0678 & -0,0027 \\ -0,0027 & 0,3306 \end{bmatrix} \tag{295}$$

qui est obtenue avec MATLAB.

Après cela, l'inégalité (231) de l'hypothèse H1), requise par le Théorème 9.2, est vérifiée pour la valeur $\gamma = 2$.

Afin de vérifier l'hypothèse H4) du Théorème 9.2 il suffit de noter que seulement le scénario T3 est valide pour la régulation par retour de position. A partir de cela, en utilisant (292) nous obtenons la loi de restitution de l'état suivant

$$\begin{bmatrix} x_1^+ \\ x_2^+ \end{bmatrix} = \mu(x_1^-, x_2^-) = \begin{bmatrix} 0 \\ -ex_2^- \end{bmatrix}, \begin{bmatrix} \xi_1^+ \\ \xi_2^+ \end{bmatrix} = \nu(\xi_1^-, \xi_2^-, y) = \begin{bmatrix} 0 \\ -e\xi_2^- \end{bmatrix} \tag{296}$$

dans le cas sans perturbation lorsque le pendule touche la contrainte $x_1 = 0$. Ainsi, les inégalités (234) et (235) de l'hypothèse H4) sont simplifiées telles que

$$V(\mathbf{x}^-) = P_{22}(x_2^-)^2 \geq P_{22}e^2(x_2^-)^2 = V(\mu(\mathbf{x}^-)) \tag{297}$$

$$\begin{aligned} W(\mathbf{x}^-, \boldsymbol{\xi}^-) = \gamma^2 \left[Y_{11}(x_1^- - \xi_1^-)^2 + 2Y_{12}(x_1^- - \xi_1^-)(x_2^- - \xi_2^-) + Y_{22}(x_2^- - \xi_2^-)^2\right] \geq \\ \gamma^2 Y_{22} e^2 (x_2^- - \xi_2^-)^2 = W(\boldsymbol{\mu}(\mathbf{x}^-), \boldsymbol{\nu}(\boldsymbol{\xi}^-, \mathbf{y}^-)), \end{aligned} \tag{298}$$

avec les fonctions quadratiques

$$V(\mathbf{x}, t) = \mathbf{x}^\top \mathbf{P}_\varepsilon \mathbf{x} = [\ x_1 \quad x_2\ ] \begin{bmatrix} P_{11} & P_{12} \\ P_{12} & P_{22} \end{bmatrix} \begin{bmatrix} x_1 \\ x_2 \end{bmatrix} = x_1^2 P_{11} + 2P_{12}x_1x_2 + P_{22}x_2^2 \tag{299}$$

$$\begin{aligned} W(\mathbf{x}, \boldsymbol{\xi}, t) = \gamma^2(\mathbf{x} - \boldsymbol{\xi})^\top \mathbf{Z}_\varepsilon^{-\mathbf{1}}(\mathbf{x} - \boldsymbol{\xi}) = \gamma^2 \begin{bmatrix} x_1 - \xi_1 & x_2 - \xi_2 \end{bmatrix} \begin{bmatrix} Y_{11} & Y_{12} \\ Y_{12} & Y_{22} \end{bmatrix} \begin{bmatrix} x_1 - \xi_1 \\ x_2 - \xi_2 \end{bmatrix} \\ = \gamma^2 \left[Y_{11}(x_1 - \xi_1)^2 + 2Y_{12}(x_1 - \xi_1)(x_2 - \xi_2) + Y_{22}(x_2 - \xi_2)^2\right]. \end{aligned} \tag{300}$$

Table 4: Paramétrés de la simulation de régulation

Paramètres	**Valeurs**	**Paramètres**	**Valeurs**
g	$9,81\ Nm/s^2$	J	1
k	$1\ N/rad/s$	ε	$0,01$
m	$1\ kg$	l	$1\ m$
e	0.5	w_1	$0,1q_2 + 0,1\text{sign}(q_2)\ Nm$
ρ_p	1	w_2	$0,1\sin(1,5t)\ rad$
ρ_v	1	w_i^d	$0,2q_2\ rad/s$
$q(0)$	$1\ rad$	$\dot{q}(0)$	$-0,2\ rad/s$
$\xi_1(0)$	$0,1\ rad$	$\xi_2(0)$	$-0,1\ rad/s$

spécifiées avec (295). Les deux inégalités sont satisfaites pour

$$e^2 < 0,9997. \tag{301}$$

Dans les simulations numériques de la section suivante, la valeur de la restitution $e = 0,5$ est pré-spécifiée pour satisfaire la condition (301), et le théorème 9.2 est alors appliqué à la stabilisation robuste du pendule sous la contrainte unilatérale.

9.4.2.1 Résultats numériques

La performance du système en boucle fermée, piloté par le correcteur, conçu selon le théorème 9.2, est numériquement illustrée dans la suite. Les paramètres utilisés dans la simulation, sont présentés dans le Tableau 4.

La Fig. 81 représente les erreurs de régulation libres de toute perturbation, et l'erreur d'estimation de vitesse, convergent vers zéro. Par conséquent on conclut que le pendule est effectivement régulée à la barrière. La Fig. 82 montre que si bien le système est affecté par une force de frottement w_1, par un perturbation de la mesure w_2 et par un écart w_i^d sur le coefficient de restitution, ces perturbations sont effectivement atténuées par le correcteur conçu.

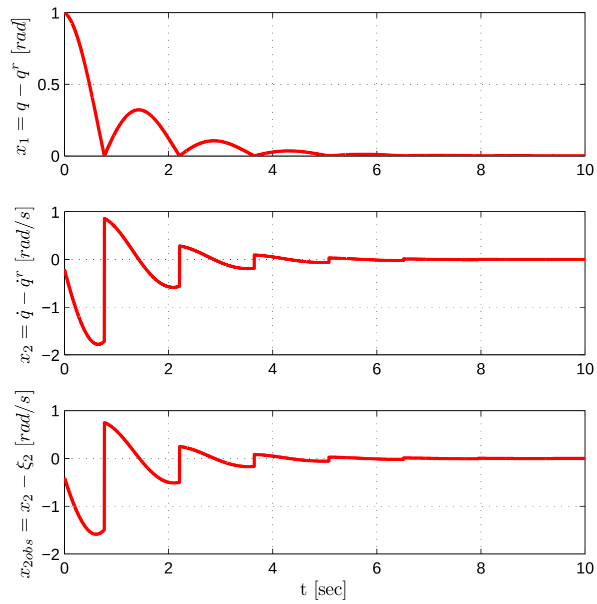

Figure 81: Erreurs de position, vitesse et estimation de vitesse pour le problème de régulation (cas non perturbé).

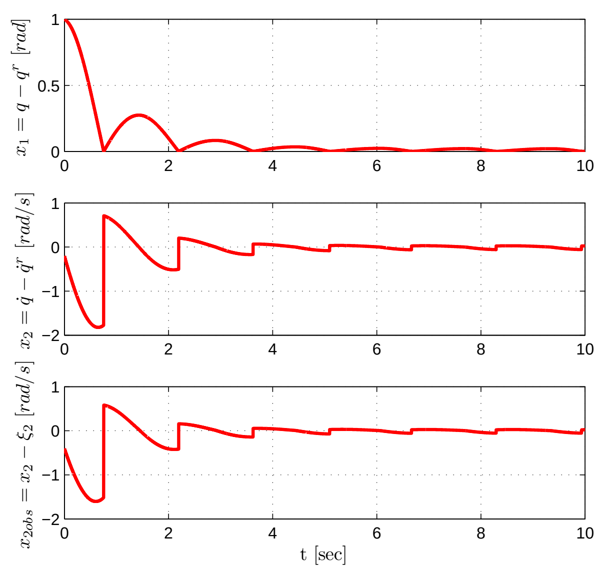

Figure 82: Erreurs de position, vitesse et estimation de vitesse pour le problème de régulation (cas perturbé).

9.4.3 Suivi du pendule par retour de la sortie

Dans la suite, la synthèse $\mathcal{H}_\infty$ pour la stabilisation orbitale par retour de sortie est développé en utilisant la version hybride du l'oscillateur de Van der Pol oscillateur, générant un cycle limite stable à suivre.

Cette trajectoire est générée en spécifiant l'oscillateur hybride de Van der Pol (80), (83), (84) de la section précédente, comme suit

Phase de mouvement libre ($q^r > 0$)

$$\ddot{q}^r = -\left[(q^r)^2 + (\dot{q}^r)^2 - 1\right]\dot{q}^r - q^r \tag{302}$$

Phase de transition ($q^r = 0$)

$$q^r(t_i^+) = q^r(t_i^-), \quad \dot{q}^r(t_i^+) = -e\dot{q}^r(t_i^-) \tag{303}$$

où q^r représente la position désirée, $\dot{q}^r$ la vitesse, $t_i,\ i = 1, 2, \ldots$ sont des instants d'impact lorsque l'oscillateur atteint la contrainte $q^r = 0$, et les paramètres de l'oscillateur ont été mis à $\varepsilon = 1$, $\mu = 1$ and $\rho = 1$.

Selon les résultats de la section 9.3, cet oscillateur génère un cycle limite asymptotiquement stable. En le simulant numériquement, ce cycle limite présente une période de

$$T_r = 3,183. \tag{304}$$

9.4.3.1 Synthétises de la commande

La synthèse de retour de position est fondée sur le Théorème 9.2, appliqué à la dynamique d'erreur (288), (290)-(294), asservi par (289), pour assurer le suivi robuste de la trajectoire souhaitée, régie par (302)-(303). En substituant le côté droit de (302) dans (289) pour $\ddot{q}^r$, le pré-compensateur (289), guidé par la sortie de l'oscillateur hybride de

Van der Pol (302)-(303), est représenté sous la forme

$$\tau = (ml^2 + J)[-\left((q^r)^2 + (\dot{q}^r)^2 - 1\right)\dot{q}^r - q^r] + k\dot{q}^r + mgl\sin q^r + (ml^2 + J)u. \tag{305}$$

Quant à la règle de restitution de l'erreur, elle est donnée par (292).

L'applicabilité du Théorème 9.2 au cas présent est vérifiée en suivant la même ligne du raisonnement utilisé dans le cas de régulation. Étant couplé à (261), les équations de Riccati (262)-(263) spécifiées par $\mathbf{A}(t)$, $\mathbf{B_1}(t)$, $\mathbf{B_2}(t)$, $\mathbf{C_1}(t)$, $\mathbf{C_2(t)}$, identifiées des équations du système (290)-(294), (288). Dans les relations ci-dessus, la trajectoire de référence $q_r(t)$ à suivre est une fonction périodique, qui est numériquement calculée sur l'intervalle de temps $[0, T_r]$, où T_r est donné par (304), en résolvant les équations de l'oscillateur hybride de Van der Pol (302)-(303), initialisée au point fixe de l'application de Poincaré correspondante.

Afin de vérifier les Conditions C1) et C2) dans le cas périodique, une solution T_r-périodique, définie positive $\mathbf{P}_\varepsilon(t)$, $\mathbf{Z}_\varepsilon(t)$ du système périodique (262)-(263) est obtenue en effectuant une itération sur les conditions initiales $\mathbf{P}_\varepsilon(0)$, $\mathbf{Z}_\varepsilon(0),$ pour une valeur suffisamment grande γ et pour une valeur suffisamment petite ε. Les règles de restitution suivantes

$$\mathbf{P}_\varepsilon(T_r^+) = \begin{bmatrix} P_{11}(T_r^-) & -\frac{1}{e}P_{12}(T_r^-) \\ -\frac{1}{e}P_{12}(T_r^-) & \frac{1}{e^2}P_{22}(T_r^-) \end{bmatrix} \tag{306}$$

$$\mathbf{Z}_\varepsilon(T_r^+) = Y^{-1}(T_r^+) = \begin{bmatrix} Y_{11}(T_r^-) & -\frac{1}{e}Y_{12}(T_r^-) \\ -\frac{1}{e}Y_{12}(T_r^-) & \frac{1}{e^2}Y_{22}(T_r^-) \end{bmatrix}^{-1} \tag{307}$$

sont délibérément imposées sur les solutions périodiques à l'instant de la période T_r pour assurer que les relations (234)-(235) de l'hypothèse H4) restent vraies.

Par itération sur γ, le niveau minimum $\gamma_{min} \approx 10$ est approché. La valeur $\gamma = 15$ est cependant choisie pour éviter une conception de correcteur à gain élevé indésirable, qui peut apparaître pour une valeur de γ proche de l'optimum $\gamma_{min} \approx 10$. Avec $\gamma = 15$, les équations de Riccati correspondantes (262)-(263), spécifiées par (261) et respectant (306), (307), sont correctement résolues avec des solutions périodiques définies positives $\mathbf{P}_\varepsilon$, $\mathbf{Z}_\varepsilon$ sous $\varepsilon = 0,01$ qui sont obtenues en effectuant une itération sur ε.

Après cela, la valeur $\gamma = 15$ est vérifiée pour satisfaire l'hypothèse H1) avec $\omega = 1$, correspondant à la présente enquête. Ainsi, le théorème 9.2 assure que le système en boucle fermée possède un $\mathcal{L}_2$-gain inférieur à $\gamma = 15$.

Étant donné que les instants d'impact de la trajectoire de référence ne sont pas en général synchronisés avec les instants d'impact du système (à moins que l'état initial de référence coïncide avec celle du système), quelque soit les scénarios T1) -T3) qui peuvent se produire, en fonction de la règle de restitution d'erreur adoptée (292). Par conséquent, l'hypothèse H4) est généralement exclue par la synthèse résultante, qui reste incapable de stabiliser asymptotiquement le système en boucle fermée, même dans le cas sans perturbation, comme il est bien connu de Biemond *et al.* (2013). Néanmoins, le correcteur proposé atténue les perturbations externes, de restitution, et le bruit de mesure, comme établi par le Théorème 9.2, et tout en étant numériquement testé, la performance du système en boucle fermée observé est acceptable.

9.4.3.2 Résultats numériques

Les résultats de simulation présentés sur la Fig. 83, ont été réalisées dans les mêmes circonstances de la section 2 9.4.2.1, en utilisant les paramètres du Tableau 4 et des paramètres supplémentaires du Tableau 5, où l'on peut noter que la trajectoire de référence est initialisée sur le cycle limite. Le cas sans perturbation est présenté dans la Fig. 83. Les pics de la figure d'erreur apparaissent puisque les sauts de vitesse du système ne correspondent pas aux sauts de vitesse de la trajectoire de référence, tombant ainsi dans le scénario soit T1) ou T2) de la section 9.2.3.1. Par conséquent, la preuve de stabilité asymptotique n'est plus applicable dans le cas sans perturbation pour ces deux scénarios. Malgré la différence dans les instants d'impact du système et de la référence, l'inegalité (227) ($\mathcal{L}_2$-gain) est toujours garantie par le théorème 9.2, et un bon comportement du système en boucle fermée, avec les erreurs de suivi se rapprochant de zéro entre les instants d'impact, est déduit de la Fig. 83 dans le cas sans perturbation. La figure 84 montre qu'une bonne performance est également conclue pour la synthèse de suivi en dépit des perturbations supplémentaires, affectant le mouvement libre (due au frottement) et les transitions (en raison de l'incertitude du coefficient de restitution).

Table 5: Paramétrés de la simulation de suivi

Param	**Valeur**	**Param**	**Valeur**
$q(0)$	$0,1\ rad$	$\dot{q}(0)$	$-0,1\ rad/s$
$\xi_1(0)$	$0,1\ rad$	$\xi_2(0)$	$0,1\ rad/s$
$q^r(0)$	$0\ rad$	$\dot{q}^r(0)$	$1,012\ rad/s$

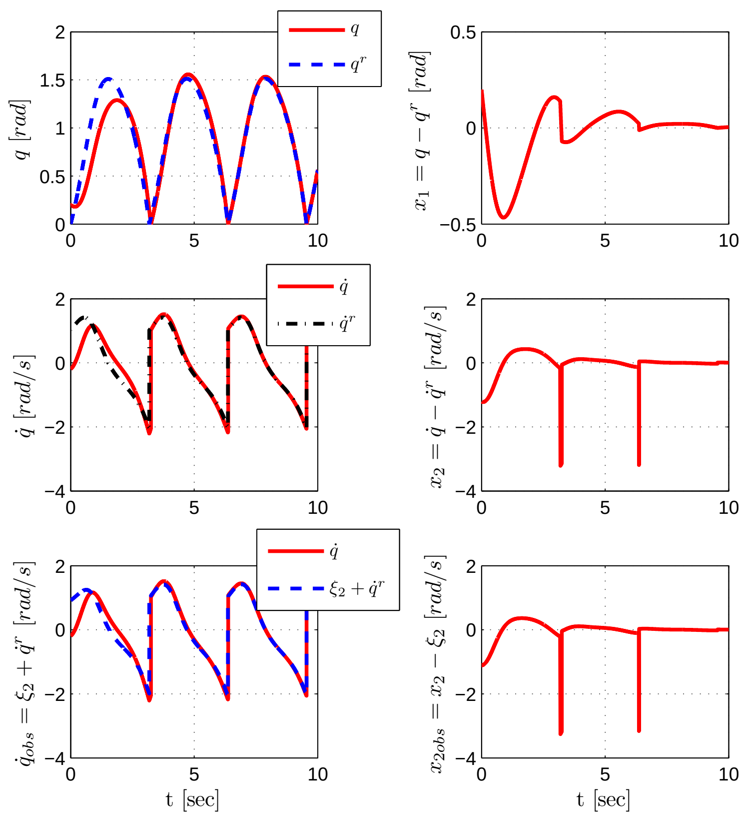

Figure 83: Graphiques de la position, la vitesse du pendule, la vitesse estimée, les erreurs de suivi, et l'erreur d'estimation de vitesse dans le cas sans perturbation.

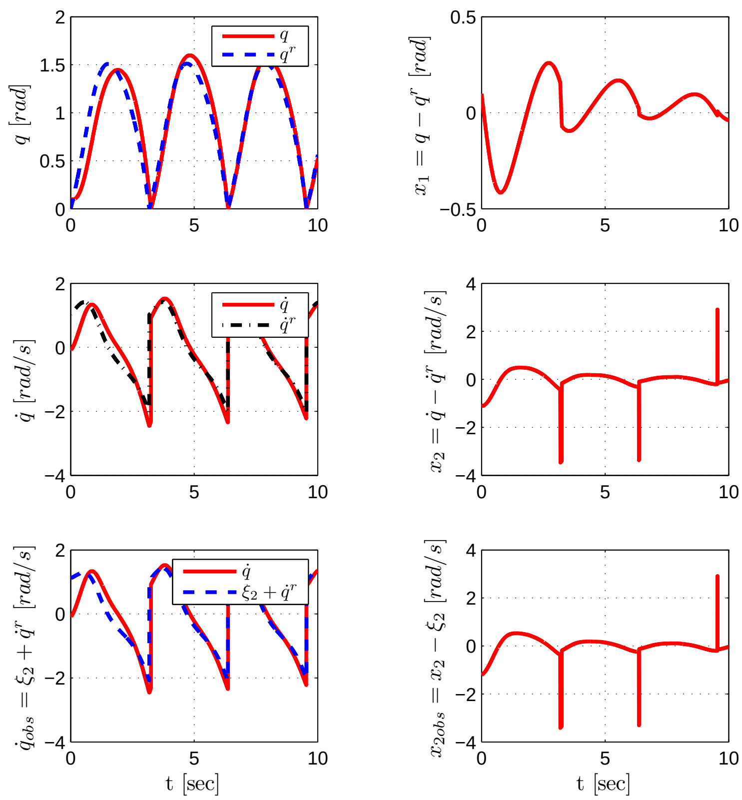

Figure 84: Graphiques de la position, la vitesse du pendule, la vitesse estimée, les erreurs de suivi, et l'erreur d'estimation de vitesse dans le cas perturbé.

9.4.3.3 Synchronisation des impacts par la ré-initialisation du modèle de référence en ligne

Afin de supprimer les pics montrés sur la Fig. 83 qui détruisent la stabilité asymptotique du système en boucle fermée sans perturbation, le modèle de référence est maintenant réinitialisé en ligne, comme il est indiqué dans le bloc-diagramme de la Fig. 85, où l'événement de ré-initialisation est synchronisé avec l'impact du système ($q = 0$). Ainsi, la loi de restitution (303) est modifiée comme suit

$$q^r(t_i^+) = 0, \quad \dot{q}^r(t_i^+) = -e\dot{q}^r(t_i^-), \quad \text{iff } q(t_i) = 0. \tag{308}$$

Le pré-compensateur (305) et le même correcteur u, synthétisé dans la section 9.4.3.1, sont désormais couplés au modèle de référence Van der Pol ainsi modifié. Les hypothèses H1) - H3) sont encore une fois valides, et il reste à montrer que H4) est satisfaite dans ce cas. Étant donné que la trajectoire de référence est remise à zéro lorsque le système atteint la contrainte, le scénario T3) est maintenant valide, et en raison de (292), la transition d'erreur est régie par $x_2^+ = -ex_2^-$. Puisque les solutions de (262)-(263) sont choisies pour se conformer aux conditions limites (306) - (307), H4) est ainsi établie avec les fonctions quadratiques V et W. Cela permet de vérifier l'applicabilité du Théorème 9.2, en vertu duquel, le correcteur dynamique (270) permet au pendule sous impacts de suivre asymptotiquement la trajectoire de référence, tout en atténuant les perturbations externes.

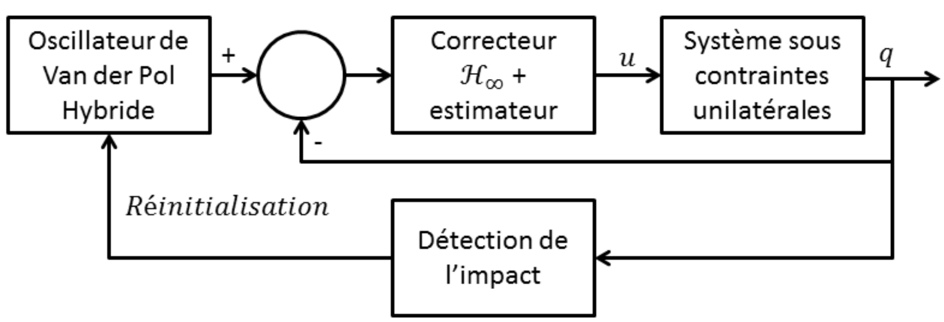

Figure 85: Schéma du modèle de référence de Van der Pol réinitialisé en ligne

.

Afin de démontrer que le système en boucle fermée, (285), (286), (302), (308), (270) génère un cycle limite asymptotiquement stable, l'analyse de la section de Poincaré 9.3.4

Table 6: Paramétrés de la simulation de suivi avec synchronisation des impacts

Param	Valeur	Param	Valeur
$q(0)$	$0,1\ rad$	$\dot{q}(0)$	$-0,2\ rad/s$
$\xi_1(0)$	$0,1\ rad$	$\xi_2(0)$	$-0,1\ rad/s$
$q^r(0)$	$0,2\ rad$	$\dot{q}^r(0)$	$1,5\ rad/s$

est revisitée, en utilisant l'application de Poincaré

$$\tilde{\Gamma}(\zeta_k) = \zeta_{k+1} \tag{309}$$

associée à la section de Poincaré $q = 0$, qui considère les valeurs après l'impact $\zeta_k = [q_k, \dot{q}_k, \xi_k, q_k^r, \dot{q}_k^r]$ aux instants d'impact t_k, $k = 1, 2, \ldots$. Le point fixe $\zeta^* = [0\ \ 1,012\ \ 0\ \ 0\ \ 0\ \ 1,012]$ de l'application de Poincaré $\tilde{\Gamma}$ et les valeurs propres $eig(\nabla\tilde{\Gamma}) = [0\ \ 0,6961\ \ 0\ \ 0,0045\ \ 0\ \ -0,7706]$ du gradient $\nabla\tilde{\Gamma}$ autour du point fixe sont calculées numériquement. La stabilité asymptotique du cycle limite est établie en observant que les valeurs propres du gradient $\nabla\tilde{\Gamma}$ sont toutes dans le cercle unité.

9.4.3.4 Résultats numériques

Les Figures 86-87 montrent les résultats numériques effectuées en utilisant les paramètres des tableaux 4 et 6, tandis que le correcteur de suivi synthétisé est couplé au modèle de référence de Van der Pol, dont l'adaptation de la ré-initialisation en ligne est synchronisée avec les impacts du système, qui est initialisée à une valeur hors du cycle limite. On peut voir d'après la Fig. 86 que dans le cas sans perturbation, les erreurs de position, de vitesse et d'estimation échappent à zéro, indépendamment des conditions initiales non nulles.

Les simulations réalisées pour le cas perturbé, sont montrées Fig. 87 qui présente les graphiques des erreurs de position et de suivi de vitesse ainsi que la trace de l'erreur d'estimation de vitesse. On voit qu'après le transitoire, les erreurs restent petites et bornées.

Il est important de noter que dans les deux cas, perturbé et non perturbé, les pics présents Fig. 83, qui correspondent aux instants d'impact désynchronisés du système et du modèle de référence, disparaîtraient sur les courbes d'erreurs de suivi de la vitesse et

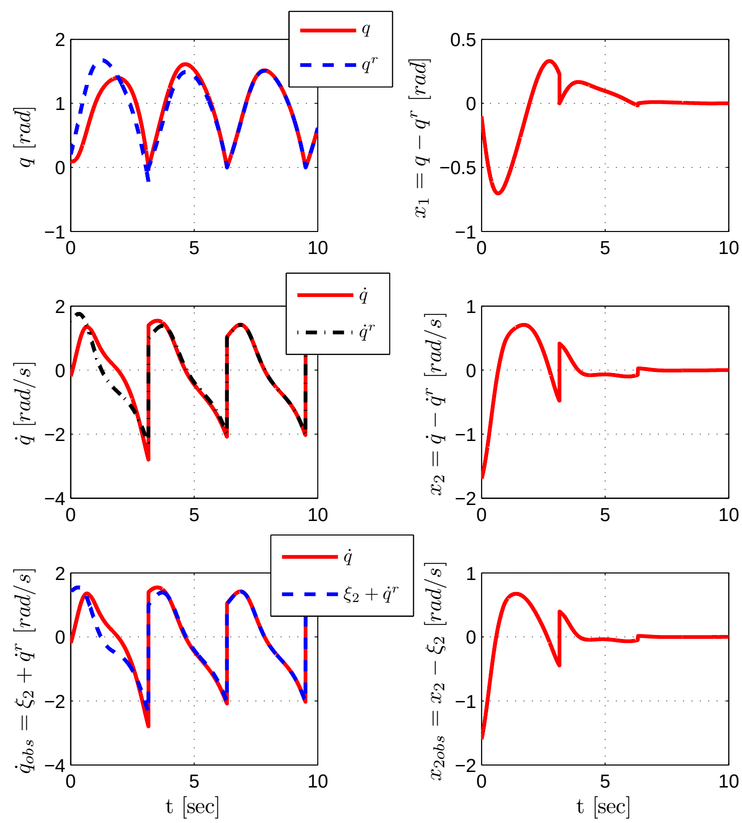

Figure 86: Graphiques de la position, vitesse, estimation de la vitesse, erreurs de suivi, et erreur de l'estimation de la vitesse dans le cas non perturbé, avec l'adaptation en ligne du modèle de Van der Pol.

de l'erreur d'estimation de vitesse des Figs. 86 et 87, où la ré-initialisation du modèle de référence est synchronisé avec les instants d'impact du système. Ainsi, la supériorité de la synthèse avec l'adaptation en ligne du modèle de référence est conclue.

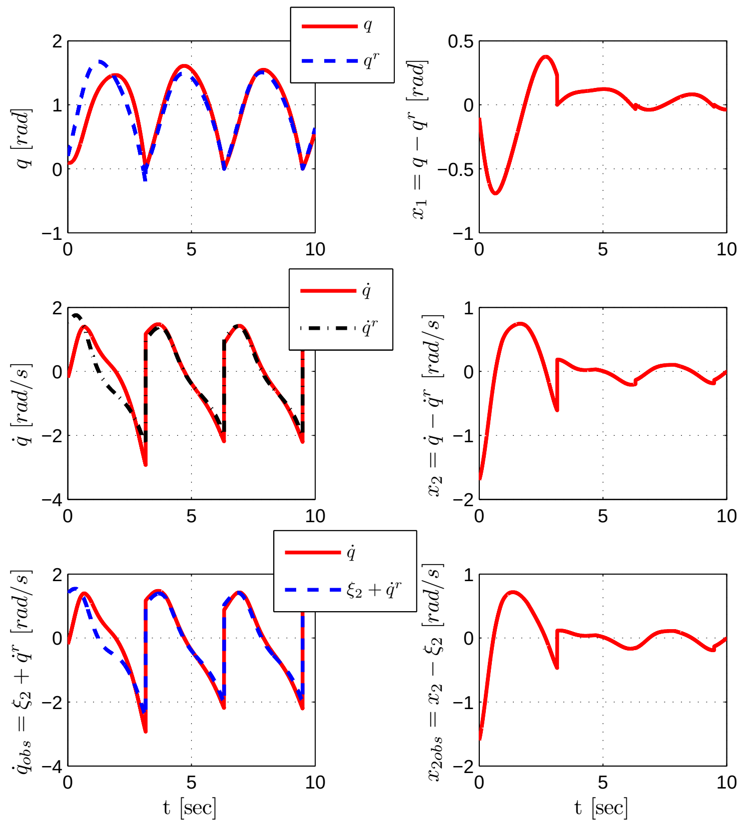

Figure 87: Graphiques de la position, vitesse, estimation de la vitesse, erreurs de suivi, et erreur de l'estimation de la vitesse dans le cas perturbé, avec l'adaptation en ligne du modèle de Van der Pol.

9.5 Locomotion périodique d'un bipède avec des pieds

Les résultats théoriques développés sont désormais corroborés par l'étude numérique faite pour le suivi robuste de la trajectoire d'un robot bipède plan, et pour un robot bipède de 32-DDL.

9.5.1 Suivi de la trajectoire d'un robot bipède plan avec des pieds

Le robot bipède considéré dans cette section marche sur une surface rigide et horizontale. Il est modélisé sous la forme d'un bipède plan, qui se compose d'un torse, des hanches, de deux jambes avec des genoux et des pieds. L'allure de marche a lieu dans le plan sagittal et se compose de phases de simple appui et des impacts, qui se produisent entre deux corps rigides (le pied et le sol).

9.5.1.1 Modèle dynamique en simple appui

Dans la phase d'appui unique, étant donné un contact de pied à plat (par exemple, il n'y a pas de décollage, pas de basculement, et pas de glissement pendant cette phase), le modèle dynamique du bipède peut être écrit comme suit:

$$\mathbf{D}(\mathbf{q})\ddot{\mathbf{q}} + \mathbf{H}(\mathbf{q}, \dot{\mathbf{q}}) = \mathbf{D}_{\tau}\boldsymbol{\tau} + \mathbf{w_1} \tag{310}$$

avec $\mathbf{q} = (q_1, q_2, q_3, q_4, q_5, q_6)^{\top}$ le vecteur 6×1 de coordonnées généralisées, $\mathbf{D}$ est la matrice 6×6 d'inertie, qui est symétrique et définie positive, $\mathbf{D}_{\tau}$ est une matrice 6×6 constante et inversible; $\boldsymbol{\tau} = (\boldsymbol{\tau}_1, \boldsymbol{\tau}_2, \boldsymbol{\tau}_3, \boldsymbol{\tau}_4, \boldsymbol{\tau}_5, \boldsymbol{\tau}_6)^{\top}$ est le vecteur 6×1 de couples; $\mathbf{H}(\mathbf{q}, \dot{\mathbf{q}})$ est le vecteur 6×1 des forces de Coriolis, centrifuges et de gravité; et $\mathbf{w_1}$ est le vecteur 6×1 de perturbations externes.

9.5.1.2 Modèle d'impact

Si nous supposons un impact pied à plat, la phase de double appui est instantanée et peut être modélisée par des équations d'impact passif (Formalskii (2009)). Un impact apparaît à $t = T_I$, lorsque la jambe en mouvement touche le sol. Nous supposerons que l'impact est passif, absolument inélastique, et que les jambes ne glissent pas (Tlalolini *et al.*, 2010). Cela signifie que la vitesse du pied qui frappe le sol est égale à zéro après l'impact. Après un impact, le précédent pied d'appui décolle du sol, de sorte que la composante verticale de la vitesse du pied en décollage juste après un impact doit être dirigée vers le haut et la réaction impulsionnelle du sol sur ce pied est égale à zéro. Ainsi, le modèle dynamique d'impact peut être représenté sous la forme (Haq *et al.*, 2012):

$$\dot{\mathbf{q}}^{+} = \phi(\mathbf{q})\dot{\mathbf{q}}^{-} + \mathbf{w_d} \tag{311}$$

où $\dot{\mathbf{q}}^-$ est la vitesse du robot juste avant l'impact et $\dot{\mathbf{q}}^+$ est la vitesse juste après l'impact; $\phi(\mathbf{q})$ représente la loi de restitution qui détermine les relations entre les vitesses avant et après l'impact; $\mathbf{q}$ est la configuration du robot au moment de l'impact. Le terme additif $\mathbf{w_d}$ est introduit pour tenir compte des incertitudes sur cette loi de restitution.

La contrainte unilatérale peut être définie comme $\mathbf{F}(\mathbf{q})$, ce qui représente la hauteur du pied en mouvement, en fonction des coordonnées généralisées du modèle de contact implicite (310). Dans la section suivante, une trajectoire spécifique pour générer un mouvement cyclique du modèle non perturbé (310)-(311), est conçue de sorte qu'elle peut être utilisée dans notre problème de suivi comme une trajectoire de référence.

9.5.1.3 Planification du mouvement périodique

À l'aide d'une optimisation hors ligne (Haq *et al.*, 2012), l'allure de marche, qui est composée de phases de simple appui et des impacts, est déterminée par la trajectoire de référence dont la position $\mathbf{q^r}(t)$ et de la vitesse $\dot{\mathbf{q}}^\mathbf{r}(t)$ satisfont les conditions de contact.

La tâche de commande est de conduire le bipède de telle manière que chaque variable articulaire suit sa propre trajectoire de référence. Selon l'optimisation adoptée hors ligne (Haq *et al.*, 2012), la référence périodique minimise l'intégrale de la norme du vecteur de couples pour une distance donnée. Pour le bipède sous-jacent avec les paramètres obtenus de Haq *et al.* (2012), la vitesse de marche a été prise égale à $0,5\ m/s$ avec une durée de pas de $0,53\ s$. Étant donné que l'impact est instantané et passif, le correcteur agit pendant la phase d'appui uniquement. La loi de restitution de cette trajectoire de référence est régie par (245).

9.5.1.4 Étude numérique

La synthèse proposée est testée sur un simulateur du bipède (Haq *et al.*, 2012), où l'approche bien connue de complémentarité (Rengifo *et al.*, 2011; Acary and Brogliato, 2008; Brogliato, 2000) est utilisée pour simuler le contact avec le sol. Cette dernière approche appartient à la famille des approches de capture d'événements (voir, par exemple Van Zutven *et al.* (2010); Hurmuzlu *et al.* (2004); Yunt and Glocker (2005)).

Afin de simuler une perturbation discrète, les vitesses après un impact sont modifiées de $5\ \%$ par rapport aux valeurs données par la règle de restitution (240).

Synthèse de commande $\mathcal{H}_\infty$ par retour d'état, avec une adaptation de la trajectoire de référence

La synthèse de suivi de trajectoire de référence de la section 9.2.3, appliquée au bipède plan, est d'abord testé avec la connaissance complète du vecteur d'état. Le Théorème 9.3 est appliqué au système hybride (310) - (311). La condition C1 est vérifiée en suivant la procédure $\mathcal{H}_\infty$ standard (voir, par exemple, (Orlov and Aguilar, 2014, Section 6.2.1)), avec les paramètres $\rho_p = 500$, $\rho_v = 1$, $\gamma = 470$ et $\epsilon = 0,01$. Ensuite, l'hypothèse H1) est vérifiée avec $\boldsymbol{\omega}$ étant une matrice d'identité. Enfin, pour se conformer à la dernière condition du théorème 9.3, l'inégalité (234) est vérifiée en utilisant la méthode d'adaptation de trajectoire décrit ci-dessous.

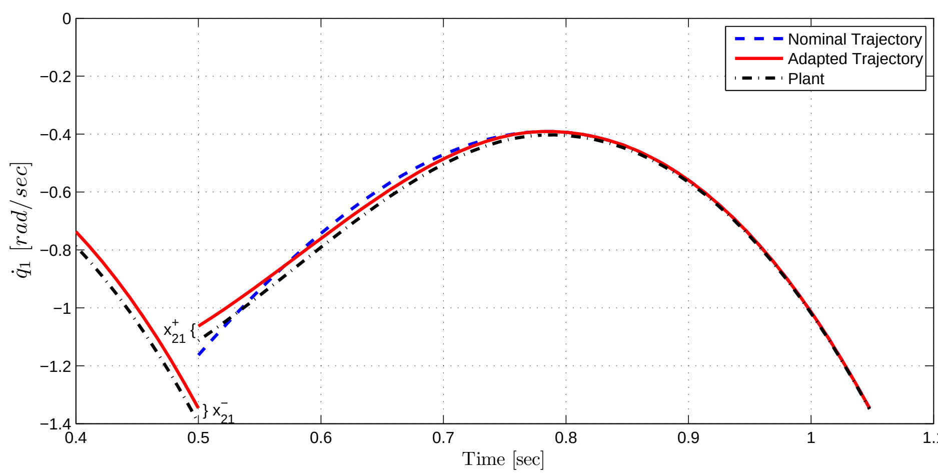

Figure 88: Adaptation de la référence de vitesse pour la première articulation, avec un impact à $t^l = 0,5$. Après l'impact, la valeur initiale de la vitesse adaptée est telle que les erreurs de suivi ($x_{21}(t^l-) = \dot{q}_1(t^l-) - \dot{q}_1^r(t^l-)$) et ($x_{21}(t^l+) = \dot{q}_1(t^l+) - \dot{q}_1^r(t^l+)$) sont égales, et au milieu du pas, la vitesse de référence adaptée atteint la nominale.

L'idée de l'adaptation est présentée Fig.88 pour la première articulation q_1. La trajectoire de référence est redémarrée en ligne une fois que la collision du pied avec le sol est détectée (forçant ainsi le scénario T3). Les erreurs de suivi de position et de vitesse sont mesurées, et une fois que l'impact du robot est détecté, la trajectoire adaptée est mise à jour en ligne de telle sorte que la nouvelle erreur après l'impact, x_{21}^+ dans la Fig.88, coïncide avec l'erreur mesurée avant l'impact ($x_{21}(t^l-)$ dans la Fig.88). Suite à l'idée de

Grishin *et al.* (1994), un nouveau polynôme est défini pour la trajectoire adaptée, qui commence à partir de cette condition imposée, et rejoint la trajectoire nominale de référence au milieu du pas avec la même vitesse, et continuera à être la même jusqu'à la fin du pas.

Résultats numériques

Le système non perturbé est ensuite simulé, en utilisant des conditions initiales à une distance de la trajectoire de référence. En utilisant la méthode d'adaptation de la trajectoire de référence proposée, l'erreur de vitesse est lisse et tend vers zéro, au lieu de présenter le phénomène de pics décrit dans Biemond *et al.* (2013). Ceci est clairement observé sur la Fig.89). Comme il n'y a pas de sauts dans l'erreur de vitesse, la fonction de Lyapunov diminue de façon monotone vers zéro, comme représenté sur la Fig. 90). La Fig. 91 représente les hauteurs des pieds qui en résultent. La périodicité de ces hauteurs est un bon indicateur d'un mouvement stable pour l'allure de marche. Dans la Fig.91, les légendes ”P1” et ”P3” représentent le ”doigt de pied” du pied droit et du pied gauche, respectivement; de façon similaire, ”P2” et ”P4” représentent le ”talon” du pied droit et du pied gauche.

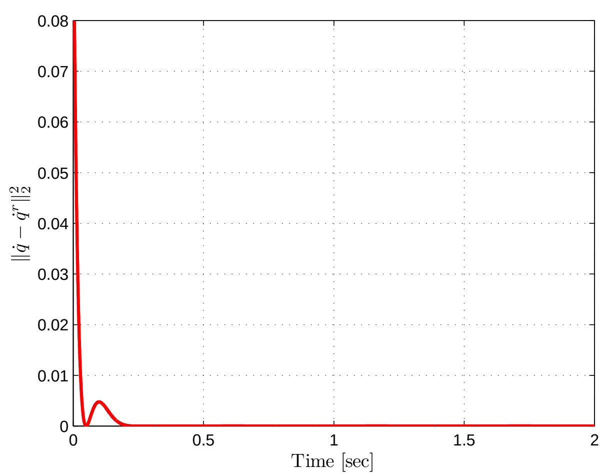

Figure 89: Erreur de vitesse $\|\dot{\mathrm{q}} - \dot{\mathrm{q}}^{\mathrm{r}}\|^2$ pour le système non perturbé.

La robustesse du correcteur de suivi (275) a été testée en utilisant une force de perturbation résultante $F_{xw} = 80\ N$ dans le plan horizontal, appliquée à la hanche du robot. Une telle force a été utilisée pendant une durée de $0,07\ s$ pour simuler un effet de perturbation. Cette force, appliquée à $0,8\ s$ dans le premier pas du bipède, représente une perturbation

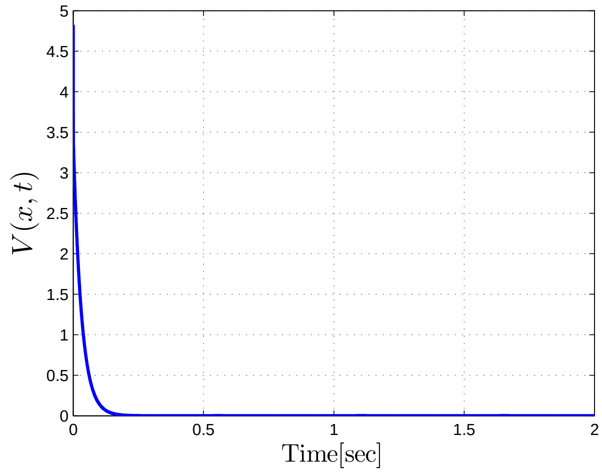

Figure 90: Fonction de Lyapunov pour le système non perturbé.

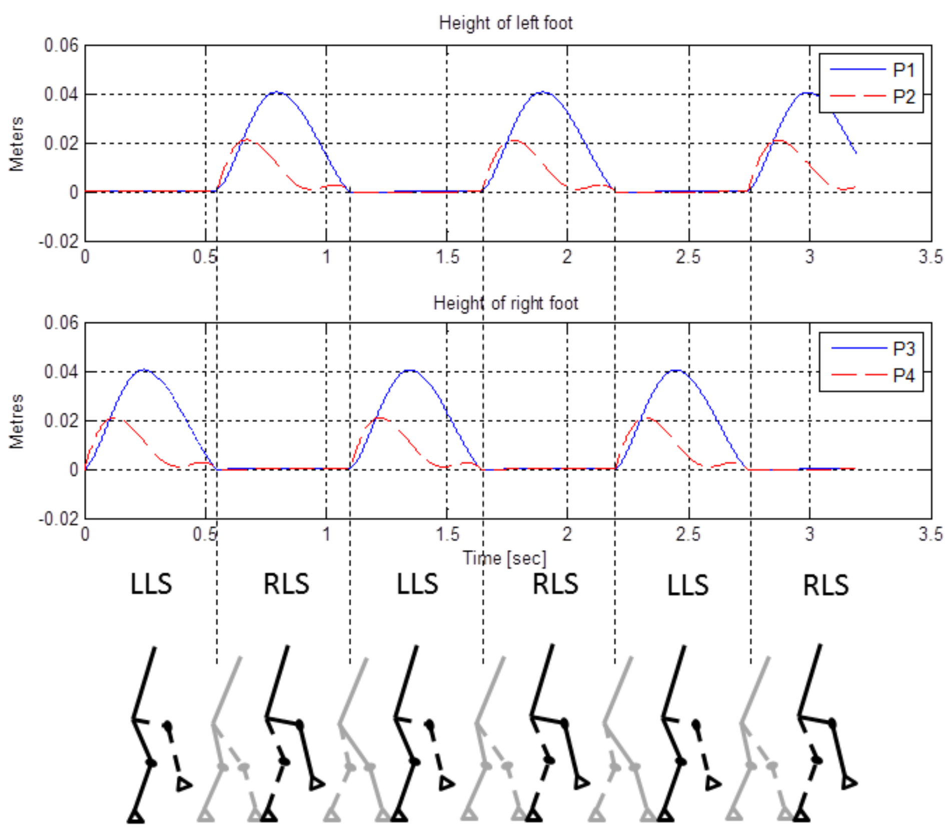

Figure 91: Hauteurs des pieds dans l'allure de marche, ceux qui représentent un mouvement stable avec les phases d'appui de la jambe gauche (LLS), suivies des phases d'appui de la jambe droite (RLS), séparées par des impacts.

dans la phase continue de la dynamique (237).

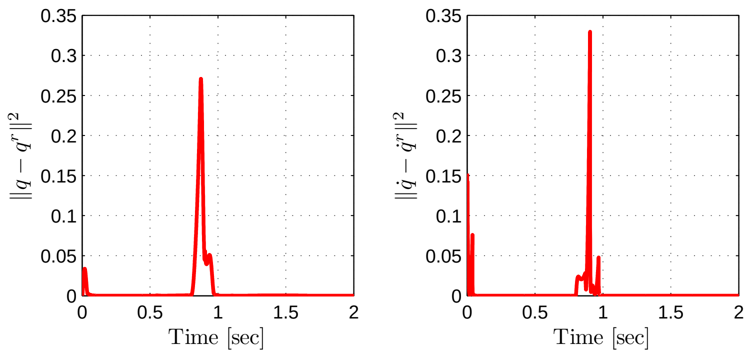

Figure 92: Erreurs de position et vitesse $\|\mathbf{q}-\mathbf{q}^{\mathrm{r}}\|^2$ et $\|\dot{\mathbf{q}}-\dot{\mathbf{q}}^{\mathrm{r}}\|^2$ du système perturbé. L'effet de la perturbation est évident à $0,8\ sec$, et il est rapidement atténué par le correcteur.

L'atténuation de la perturbation est facilement déduite de la Fig.92 lorsque l'effet de la perturbation est rapidement atténué par le correcteur.

9.5.2 Suivi de la trajectoire d'un robot bipède 3D avec des pieds

Le robot bipède considéré dans cette section marche sur une surface rigide et horizontale. Il s'agit d'un robot de 32-DDL, le robot bipede Romeo, d'Aldebaran Robotics compose du 32-DOF robots Romeo. Comme pour le bipède plan de la section précédente, l'allure de marche a lieu dans le plan sagittal et se compose de phases de simple appui et des impacts.

9.5.2.1 Modèle dynamique en simple appui

La configuration du robot bipède en simple appui peut être décrite par le vecteur $\mathbf{q} = (q_0, q_1, \ldots, q_{32})^\top$. Dans cette phase, compte tenu d'un contact de pied à plat du pied d'appui avec le sol, et en supposant un non décollage, un non glissement et une non rotation du pied d'appui, le modèle du bipède peut être représenté par:

$$\mathbf{D}(\mathbf{q})\ddot{\mathbf{q}} + \mathbf{H}(\mathbf{q}, \dot{\mathbf{q}}) = \mathbf{D}_\tau \boldsymbol{\tau} + \mathbf{w_1} \tag{312}$$

où $\mathbf{D}_\tau$ est la matrice 32×32 d'inertie, symétrique et définie positive, $\boldsymbol{\tau} = (\boldsymbol{\tau}_1, \ldots, \boldsymbol{\tau}_{32})^\top$ est le vecteur 32×1 de couples; $\mathbf{H}(\mathbf{q}, \dot{\mathbf{q}})$ est le vecteur 32×1 de couples centrifuges, gravitationnels et de Coriolis; et $\mathbf{w_1}$ est le vecteur 32×1 de perturbations externes.

En raison de la difficulté du calcul analytique du modèle dynamique (312), il est numériquement calculé au moyen de l'algorithme de Newton-Euler (Luh *et al.*, 1980), qui est fondée sur des calculs récursifs associés au choix des repères de référence utilisés pour obtenir le modèle géométrique du robot. Ensuite, les matrices $\mathbf{D}$, $\mathbf{C}(\mathbf{q}, \dot{\mathbf{q}})$ et $\mathbf{G}(\mathbf{q})$ peuvent être facilement et rapidement calculées selon la méthode de Walker and Orin (1982).

9.5.2.2 Modèle d'impact

Nous supposerons que l'impact est passif, absolument inélastique, et que les jambes ne glissent pas (Tlalolini *et al.*, 2010). Si nous supposons un impact pied à plat, la phase de double appui est instantanée et peut être modélisée par des équations d'impact passifs (Formalskii (2009)). Un impact apparaît à $t = T_I$, lorsque la jambe en mouvement touche le sol. Cela signifie que la vitesse du pied qui impact avec le sol est égale à zéro après l'impact. Après un impact, le précédent pied d'appui décolle du sol, de sorte que la composante verticale de la vitesse du pied en décollage juste après un impact doit être dirigée vers le haut et la réaction impulsionnelle du sol dans ce pied est égale à zéro. Similaire au cas planaire, le modèle dynamique d'impact peut être représenté sous la forme:

$$\dot{\mathbf{q}}^{+} = \phi(\mathbf{q})\dot{\mathbf{q}}^{-} + \mathbf{w_i^d} \tag{313}$$

La contrainte unilatérale invariant dans le temps $F_0(\mathbf{q}) \geq 0$ est déterminée par la hauteur de la plante du pied en transfert.

Les équations (312), (313) définissent un système hybride qui peut être commandé en utilisant la méthodologie développée dans ce travail.

9.5.2.3 Planification du mouvement

Comme une allure de marche est un phénomène périodique, notre objectif est de concevoir une allure cyclique. Un cycle de marche complet se compose de deux phases :

une phase d'appui simple et un double appui instantané qui est modélisé par une équation d'impact passif. La phase de simple appui commence avec un pied qui reste sur le sol tandis que l'autre pied balance de l'arrière vers l'avant. Cela signifie que lorsque la jambe en mouvement touche le sol et la jambe d'appui décolle. Les trajectoires de référence, ceux qui permettent une marche symétrique, sont obtenues par une optimisation hors ligne, ce qui minimise un critère sthénique, présenté dans le travail de Tlalolini *et al.* (2010).

9.5.2.4 Synthèse de commande $\mathcal{H}_\infty$ par retour d'état, avec une adaptation de la trajectoire de référence

Étant donné que la structure du modèle simplifié (312) est identique à un manipulateur mécanique soumis à des contraintes unilatérales (présentées à la section 9.2), les résultats de la section 9.2.4 peuvent être utilisés, en dépit la complexité du modèle du bipède. Par conséquent, le pré-compensateur (271) et le Théorème 9.3 sont appliqués au système hybride (312), (313) afin de concevoir un correcteur robuste, capable d'atténuer les perturbations externes autour de la allure de marche de référence. Les paramètres de régulation utilisés sont $\rho_p = 3500$, $\rho_v = 500$, $\gamma = 200$ et $\epsilon = 0,01$. En outre, l'idée de l'adaptation de la trajectoire présentée dans la section 9.5.1.4 est mise en œuvre de la conception de commande, afin de supprimer le phénomène de pics et de garantir la stabilité asymptotique.

9.5.2.5 Résultats numériques

Les paramètres pour la simulation ont été tirés de la documentation d'Aldebaran sur Romeo. Le simulateur est fondé sur (Rengifo *et al.*, 2011).

La Figure 93 présente les hauteurs des pieds pour le cas non perturbé. Comme pour le bipède plan, la périodicité de ces hauteurs est un bon indicateur d'un mouvement stable pour l'allure de marche. Dans la Fig.93, les légendes "P1" et "P4" représentent les coins correspondants aux doigts du pied, alors que "P2" et "P3" représentent les coins du talon.

Dans une prochaine étape, une perturbation persistante égale à $10 \sin(t)\ Nm$ a été appliquée à la hanche, tandis que les vitesses après l'impact sont déviées de $5\ \%$ par rapport à ses valeurs nominales (données par (313)), considérant ainsi des perturbations sur la phase de simple appui et sur l'impact. L'effet de ces perturbations sur six articulations représentatives (les chevilles, les genoux et les articulations de la hanche) peut être observé Fig. 94, où l'erreur est faible et bornée, et le robot maintient une allure de marche stable. Malgré les perturbations, une bonne performance de la dynamique d'erreur en boucle fermée, asservie par la commande $\mathcal{H}_\infty$ non linéaire par retour d'état, est encore conclue.

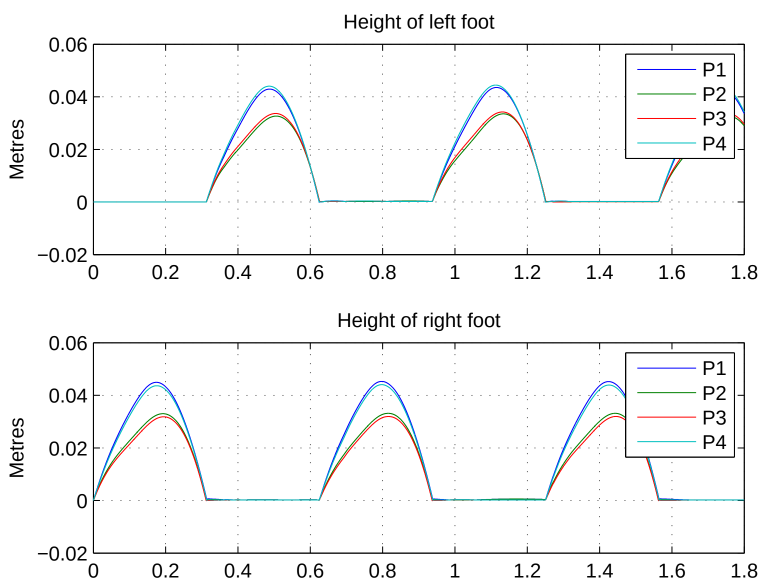

Figure 93: Hauteurs des pieds pour 6 pas de Romeo, ceux qui représentent un mouvement stable.

9.6 Commande $\mathcal{H}_\infty$ non linéaire des systèmes mécaniques sous-actionnes soumis à des contraintes unilatérales

Étant donné une contrainte unilatérale scalaire $F(q) \geq 0$, considérons un système non linéaire, évoluant au-delà de la contrainte ci-dessus, qui est régi par la dynamique continue de la forme

$$\mathbf{D}(\mathbf{q})\ddot{\mathbf{q}} + \mathbf{C}(\mathbf{q}, \dot{\mathbf{q}})\dot{\mathbf{q}} + \mathbf{G}(\mathbf{q}) = \mathbf{B}\boldsymbol{\Gamma} + \mathbf{w_c} \tag{314}$$

hors de la surface $F(q) = 0$ où la contrainte est inactive, et par les relations algébriques

$$\begin{bmatrix} \mathbf{q}^+ \\ \dot{\mathbf{q}}^+ \end{bmatrix} = \psi(\mathbf{q}^-, \dot{\mathbf{q}}^-) + \boldsymbol{\omega}(\mathbf{q}^-, \dot{\mathbf{q}}^-)\mathbf{w_d} \tag{315}$$

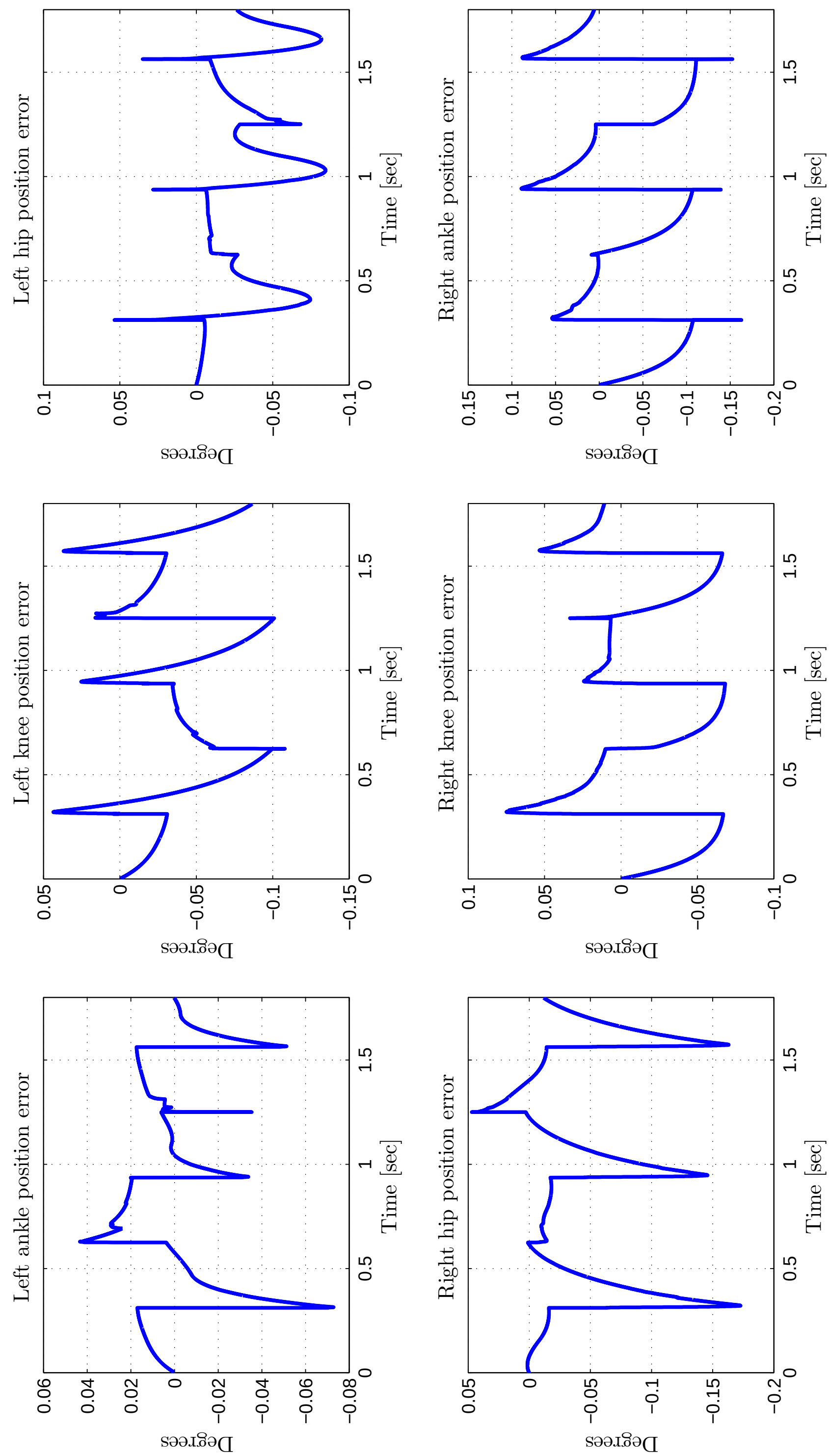

Figure 94: Erreurs des articulations des chevilles, genoux et articulations de la hanche, sous une perturbation continue persistante ($10\sin(t)\ Nm$) appliquée à la hanche.

lorsque la trajectoire du système frappe la surface $F(q) = 0$. Les vecteurs $\mathbf{q} \in \mathbb{R}^n$ et $\dot{\mathbf{q}} \in \mathbb{R}^n$ sont les vecteurs positions et vitesses généralisés, respectivement, $\mathbf{D}$ est une matrice $n \times n$ symétrique, définie positive d'inertie, $\mathbf{B}$ est une matrice constante $n \times (n-k)$ composé de 0 et 1, qui définit les variables actionnées et sous-actionnées, alors que $\mathbf{\Gamma} \in \mathbb{R}^{n-k}$ avec $1 \leq k < n$ est le vecteur de couples actionnés (étudiant ainsi les systèmes sous-actionnés); ψ représente l'équation d'impact; $\mathbf{w_c} \in \mathbb{R}^n$ représente les perturbations externes qui affectent la dynamique continue, tandis que $\mathbf{w_d} \in \mathbb{R}^s$ représente les perturbations qui affectent l'équation d'impact (315). Le vecteur $\mathbf{C}(\mathbf{q}, \dot{\mathbf{q}})\dot{\mathbf{q}}$ désigne les forces centrifuges et de Coriolis, tandis que $\mathbf{G}(\mathbf{q})$ désigne les forces gravitationnelles. Nous allons nous concentrer dans les systèmes mécaniques de degré de sous-actionnement 1 au cours de leur locomotion, de sorte que $k = 1$.

Considérons qu'une certaine tâche est réalisée par l'obtention d'une trajectoire faisable $\mathbf{q}_\star$ du système mécanique hybride (314)-(315), et cette trajectoire faisable décrira une orbite périodique, donnée par

$$\mathcal{O}_\star = \{(\mathbf{q}, \dot{\mathbf{q}}) \in \mathbb{R}^{2n} : \mathbf{q} = \mathbf{q}_\star(\theta), \dot{\mathbf{q}} = \dot{\mathbf{q}}_\star(\theta, \dot{\theta})\} \tag{316}$$

où θ est appelée une variable de phase, qui est une quantité scalaire, strictement monotone sur l'orbite périodique. Soit $\theta_\star$ qui dénote l'évolution de θ correspondant à l'orbite périodique $\mathcal{O}_\star$, alors $\theta_\star|_t = \theta_\star|_{(t+T_s)}$, où $T_s > 0$ représente la période de la motion.

Par conséquent, le problème de la stabilisation orbitale en question est de trouver une action de commande $\mathbf{\Gamma}$ telle que les solutions de la version non perturbée de (314), (315), initialisées dans un voisinage de l'orbite souhaitée $\mathcal{O}_\star$, donnée par (316), tendent asymptotiquement vers $\mathcal{O}_\star$; et pour la version perturbée, le correcteur atténue l'effet des perturbations sur la dynamique continue (314) et sur la loi de restitution (315).

9.6.1 Matériel de référence

Dans cette section, l'approche de contraintes virtuelles est présentée, ainsi que les notions de coordonnées transversales et linéarisation transversales. Couplés ensemble, ces résultats constituent une base d'atténuation des perturbations pour les systèmes mécaniques de degré de sous-actionnement 1 ($k = 1$).

9.6.1.1 L'approche de contraintes virtuelles et coordonnées transversales

L'approche des contraintes virtuelles (CV) est un puissant outil d'analyse pour la planification de mouvements périodiques dans les systèmes mécaniques sous-actionnés Shiriaev *et al.* (2005). En plus de la représentation du système (314)-(315) avec les coordonnées généralisées

$$q_1 = q_1(t), \dots, q_n = q_n(t), \quad t \in [0, T_s], \tag{317}$$

on peut utiliser une représentation indépendante du temps alternative du système, donnée sous la forme paramétrique

$$q_1 = \phi_1(\theta), \dots, q_n = \phi_n(\theta), \quad \theta \in [\theta_0, \theta_f] \tag{318}$$

qui est valable le long de l'orbite souhaitée, spécifié avec des fonctions $\phi_i(\cdot)$, $i = 1, \dots, n$, qui sont des fonctions d'une paramètre θ. Les identités (318) sont connues comme des contraintes virtuelles car elles expriment des relations algébriques entre les coordonnées généralisées. La variable θ peut être choisie parmi les coordonnées généralisées (Shiriaev *et al.*, 2005) ou comme une combinaison linéaire d'entre eux (Westervelt *et al.*, 2007).

La dynamique de (314) dans les nouvelles coordonnées (318) peut maintenant être obtenue en introduisant les dérivées temporelles $\dot{q}_i = \phi_i'\dot{\theta}$, $\ddot{q}_i = \phi_i''\dot{\theta}^2 + \phi_i'\ddot{\theta}$, $i = 1, \dots, n$ dans l'équation d'Euler-Lagrange (314), où $\phi_i' = \frac{\partial \phi_i}{\partial \theta}$ et $\phi_i'' = \frac{\partial^2 \phi_i}{\partial \theta^2}$. L'équation résultante est alors régie par la dynamique du second ordre réduit le long des contraintes virtuelles (318):

$$\bar{\alpha}(\theta)\ddot{\theta} + \bar{\beta}(\theta)\dot{\theta}^2 + \bar{\gamma}(\theta) = 0 \tag{319}$$

oú

$$\bar{\alpha}(\theta) = \mathbf{B}^{\perp}(\mathbf{\Phi}(\theta))\mathbf{D}(\mathbf{\Phi}(\theta))\mathbf{\Phi}'(\theta) \tag{320}$$

$$\bar{\beta}(\theta) = \mathbf{B}^{\perp}(\mathbf{\Phi}(\theta))[\mathbf{C}(\mathbf{\Phi}(\theta), \mathbf{\Phi}'(\theta)\dot{\theta}) + \mathbf{D}(\mathbf{\Phi}(\theta))\mathbf{\Phi}''] \tag{321}$$

$$\bar{\gamma}(\theta) = \mathbf{B}^{\perp}(\mathbf{\Phi}(\theta))\mathbf{G}(\mathbf{\Phi}(\theta)), \tag{322}$$

$\mathbf{B}^{\perp}(\mathbf{q})$ est une matrice telle que $\mathbf{B}^{\perp}(\mathbf{q})\mathbf{B}(\mathbf{q}) = \mathbf{0}$ et

$$\mathbf{\Phi}(\theta) = [\phi_1(\theta), \ldots, \phi_n(\theta)]^{\top}, \quad \mathbf{\Phi}'(\theta) = [\phi_1'(\theta), \ldots, \phi_n'(\theta)]^{\top}, \quad \mathbf{\Phi}''(\theta) = [\phi_1''(\theta), \ldots, \phi_n''(\theta)]^{\top}. \tag{323}$$

Pour les systèmes mécaniques sous contraintes unilatérales, l'équation (319) doit être accompagnée de la loi de réinitialisation

$$\begin{bmatrix} \theta^+ \\ \dot{\theta}^+ \end{bmatrix} = \Delta_\theta(\theta^-, \dot{\theta}^-) \tag{324}$$

où Δ_θ il convertit les sauts du système mécanique (314), (315) aux sauts de la dynamique réduite (319).

Le système réduit (319), (324) est désigné comme la dynamiques de zéro hybride (Westervelt *et al.*, 2003; Ames *et al.*, 2012), et ses solutions (si elles existent) représentent les mouvements que, sous certaines hypothèses techniques, peuvent être imposées sur le système par une synthèse de retour adéquate. Ces solutions peuvent être obtenues, par exemple, par l'utilisation d'une optimisation dynamique non linéaire (voir, par exemple Aoustin and Formalsky (2003); Westervelt *et al.* (2007)).

Il est clair que la connaissance de $\mathbf{q}_\star(t)$ permet de construire n fonctions scalaires $\phi_1(\theta), \ldots, \phi_n(\theta)$ qui permettent de paramétrer la même solution périodique $\mathbf{q}_\star(\mathbf{t})$ par la variable scalaire θ. Compte tenu de ces $n+1$ quantités

$$\theta, \quad \eta_1 = q_1 - \phi_1(\theta), \ldots, \eta_n = q_n - \phi_n(\theta) \tag{325}$$

peuvent être considérées comme coordonnées généralisées redondantes pour le système sous-actionné (314)-(315) de telle sorte que l'une d'entre elles, peut être exprimée en fonction des autres coordonnées. Sans la perte de généralité, nous supposons que ces coordonnées est η_n, et les nouvelles coordonnées indépendantes sont

$$\boldsymbol{\eta} = \eta_1, \ldots, \eta_{n-1}{}^{\top} \in \mathbb{R}^{n-1} \quad \text{and} \quad \theta \in \mathbb{R} \tag{326}$$

tandis que la dernière égalité dans (325) peut être réécrite comme

$$q_n = \phi_n(\theta) + h(\boldsymbol{\eta}, \theta) \tag{327}$$

avec une certaine fonction scalaire lisse $h(\boldsymbol{\eta}, \theta)$. L'utilisation d'une transformation de coordonnées appropriée Shiriaev *et al.* (2005), permet d'écrire les équations d'état qui régissent la dynamique de $\boldsymbol{\eta}$, comme suit

$$\ddot{\boldsymbol{\eta}} = \mathbf{R}(\boldsymbol{\eta}, \dot{\boldsymbol{\eta}}, \theta, \dot{\theta}) + \mathbf{N_1}(\boldsymbol{\eta}, \theta)\mathbf{w} + \mathbf{N_2}(\boldsymbol{\eta}, \theta)\boldsymbol{\Gamma}. \tag{328}$$

En outre, on peut introduire une transformation de commande

$$\boldsymbol{\Gamma} = \mathbf{v} + \boldsymbol{\Gamma}_\star \tag{329}$$

où $\boldsymbol{\Gamma}_\star$ est l'entrée nominale le long de la trajectoire nominale $\theta = \theta_\star$, $\dot{\theta} = \dot{\theta}_\star$, $\boldsymbol{\eta} = 0$, $\dot{\boldsymbol{\eta}}$. Alors, en combinant (328) et (329) on obtient la dynamique de $\boldsymbol{\eta}$ sous la forme

$$\ddot{\boldsymbol{\eta}} = \bar{\mathbf{R}}(\boldsymbol{\eta}, \dot{\boldsymbol{\eta}}, \theta, \dot{\theta}) + \mathbf{N_1}(\theta, \boldsymbol{\eta})\mathbf{w} + \mathbf{N_2}(\theta, \boldsymbol{\eta})\mathbf{v} \tag{330}$$

où la fonction $\bar{\mathbf{R}} = \mathbf{R}(\boldsymbol{\eta}, \dot{\boldsymbol{\eta}}, \theta, \dot{\theta}) + \mathbf{N_2}(\theta, \boldsymbol{\eta})\boldsymbol{\Gamma}_\star$ est annulée le long de l'orbite désirée. Afin de décrire complètement la dynamique dans les nouvelles coordonnées (325), il reste à intégrer la dynamique de θ. En suivant le méthode de (Shiriaev *et al.*, 2005), les dynamiques locales de (314) sont données par

$$\begin{aligned} \bar{\alpha}(\theta)\ddot{\theta} + \bar{\beta}(\theta)\dot{\theta}^2 + \bar{\gamma}(\theta) = g_I(\boldsymbol{\eta}, \dot{\boldsymbol{\eta}}, \theta, \dot{\theta}, \ddot{\theta})I \\ + g_\eta(\boldsymbol{\eta}, \dot{\boldsymbol{\eta}}, \theta, \dot{\theta}, \ddot{\theta})\boldsymbol{\eta} + g_{\dot{\eta}}(\boldsymbol{\eta}, \dot{\boldsymbol{\eta}}, \theta, \dot{\theta}, \ddot{\theta})\dot{\boldsymbol{\eta}} + g_v(\boldsymbol{\eta}, \dot{\boldsymbol{\eta}}, \theta, \dot{\theta}, \ddot{\theta})\mathbf{v} \\ + g_w(\boldsymbol{\eta}, \dot{\boldsymbol{\eta}}, \theta, \dot{\theta}, \ddot{\theta})\mathbf{w} \end{aligned} \tag{331}$$

$$\ddot{\boldsymbol{\eta}} = \bar{\mathbf{R}}(\boldsymbol{\eta}, \dot{\boldsymbol{\eta}}, \theta, \dot{\theta}) + \mathbf{N_1}(\theta, \boldsymbol{\eta})\mathbf{w} + \mathbf{N_2}(\theta, \boldsymbol{\eta})\mathbf{v} \tag{332}$$

où les fonctions $g_I(\cdot)$, $g_\eta(\cdot)$, $g_{\dot{\eta}}(\cdot)$, $g_v(\cdot)$ et $g_w(\cdot)$ sont des fonctions matricielles lisses de dimensions appropriées, et elles sont annulées pour $\boldsymbol{\eta} = \dot{\boldsymbol{\eta}} = \mathbf{0}$, tandis que I est la solution de l'équation différentielle

$$\dot{I} = \dot{\theta}\left[\frac{2}{\alpha(\theta)}g - \frac{2\beta(\theta)}{\alpha(\theta)}I\right] \tag{333}$$

with $g(\cdot) = g_I(\cdot)I + g_\eta(\cdot)\boldsymbol{\eta} + g_{\dot{\eta}}(\cdot)\dot{\boldsymbol{\eta}} + g_v(\cdot)\mathbf{v} + g_w(\cdot)\mathbf{w}$.

Les *coordonnées transversales* au mouvement périodique sont données par le vecteur de dimension $(2n-1)$

$$\mathbf{x}_\perp = [I, \boldsymbol{\eta}, \dot{\boldsymbol{\eta}}]^\top, \tag{334}$$

qui peut être introduite dans le voisinage de la solution

$$\eta_1 = \eta_{\star 1} = 0, \ldots, \eta_{n-1} = \eta_{\star(n-1)} = 0, \quad \theta = \theta_\star. \tag{335}$$

Le choix de ces coordonnées transversales permet d'introduire une section de Poincaré mobile $S(\tau)$, qui est déterminée dans un intervalle de temps $[0, T_s]$. Ces sections sont transversales à la trajectoire cible à chaque instant et à chaque point de la trajectoire (voir (Leonov, 2006) pour plus de détails sur les sections de Poincaré mobiles). En particulier, la quantité conservée I, qui joue un rôle important dans la dynamique transversale, se rapporte directement à la distance euclidienne de l'orbite générée par la trajectoire de référence $\theta_\star(t)$, à la trajectoire réelle du système pour chaque $t \in [0, T_s]$ (Shiriaev *et al.*, 2008).

Le problème de stabilisation orbitale pour les systèmes sous-actionnés peut maintenant être traité, en utilisant la synthèse de commande $\mathcal{H}_\infty$ développée pour les systèmes entièrement actionnés soumis à des contraintes unilatérales dans la section 9.2.

9.6.2 Synthèse orbitale par commande $\mathcal{H}_\infty$ non linéaire

Entre impacts, la combinaison de (333), (330), permet d'obtenir les dynamiques non linéaires des coordonnées généralisées (334), données par un système variant dans le temps non linéaire de la forme

$$\dot{\mathbf{x}}_\perp = \mathbf{f}(\mathbf{x}_\perp, t) + \mathbf{g_1}(\mathbf{x}_\perp, t)\mathbf{w} + \mathbf{g_2}(\mathbf{x}_\perp, t)\mathbf{v} \tag{336}$$

Pour compléter ce modèle, il faut compléter (336) avec l'équation d'impact correspondant. Ceci peut être effectué en appliquant la transformation instantanée proposée par (Freidovich *et al.*, 2008), qui permet d'introduire la loi d'impact comme

$$\mathbf{x}_\perp^+ = \mathcal{F}\mathbf{x}_\perp^- + \mathbf{w}_\perp^{\mathbf{d}} \tag{337}$$

où $\mathcal{F}$ est l'application des états avant l'impact $\mathbf{x}_\perp^-$ aux états après l'impact $\mathbf{x}_\perp^+$, T_s est la période de la trajectoire cible, $\mathbf{I}$ est une matrice d'identité des dimensions appropriées (à ne pas confondre avec le scalaire I, qui est la solution de (333)), $w_\perp^d$ considère des inexactitudes dans la loi sur la restitution. Pour plus de détails sur cette formulation, voir Freidovich *et al.* (2008); Freidovich and Shiriaev (2009).

Clairement, (336)-(337) représente un système non lineaire hybride qui peut être stabilisée à l'aide de la synthèse $\mathcal{H}_\infty$ non linéaire présentée auparavant. Le résultat suivant s'ensuit.

Théorème 9.5 *Considérons le système hybride variant dans le temps non linéaire* (336)-(337)*. Soient l'hypothèse H1), l'inégalité* (234) *et la condition C1) satisfaites avec* $\gamma > 0$ *(voir les sections 9.2.2.1 et 9.2.3.3). Alors, le système transversal* (336)-(337) *asservi par le retour d'état*

$$\mathbf{v} = -\mathbf{g_2}^\top \mathbf{P}_\varepsilon(s(\theta))\mathbf{x}_\perp \tag{338}$$

possède localement un $\mathcal{L}_2$*-gain inférieur à* γ*, où*$s(\theta)$ *est un indice du paramétrage de la feuille particulière de la section de Poincaré mobile, dans laquelle le vecteur* $x_\perp$ *appartient à des moments de temps* t*, i.e. une fonction lisse qui satisfait l'identité* $s(\theta_\star) = t$ *pour tous les instants* $t \in [0, T_s]$*. En outre, le système transversal en boucle fermée sans perturbations* (336)-(337)*,* (338) *est uniformément asymptotiquement stable, ce qui rend l'orbite souhaitée* (316) *orbitalement asymptotiquement stable.*

9.7 Commande $\mathcal{H}_\infty$ pour la stabilisation orbitale d'un bipède sous-actionné

Le robot bipède considéré dans cette section marche sur une surface rigide et horizontale. Il est modélisé sous la forme d'un bipède plan, qui se compose d'un torse, des hanches, des deux jambes avec des genoux, mais pas de chevilles actionnées. L'allure de marche se compose de phases de simple appui et des impacts. L'objectif est la stabilisation orbitale robuste de ce robot bipède sous-actionné, étant donné que seulement les mesures de position imparfaites sont disponibles.

9.7.1 Modèle du robot bipède plan

Le modèle complet du robot bipède se compose de deux parties : les équations différentielles qui décrivent la dynamique du robot pendant la phase de simple appui, et un modèle impulsionnel de l'événement de contact (l'impact entre la jambe oscillante et le sol est modélisé comme un contact entre deux corps rigides comme dans Chevallereau *et al.* (2003)). Il est supposé que les seules mesures disponibles sont les positions des articulations.

Au cours de la phase simple appui, le degré de sous-actionnement est égal à 1. Supposons que le point d'appui de la jambe agit comme un pivot sur le sol, *i.e.*, il n'y a pas de glissement et aucun décollage de la pointe de la jambe d'appui. Ensuite, le modèle bipède en phase de simple appui entre les impacts successifs peut être écrit comme

$$\begin{pmatrix} D_{11} & \mathbf{D_{12}} \\ \mathbf{D_{21}} & \mathbf{D_{22}} \end{pmatrix} \begin{pmatrix} \ddot{q}_1 \\ \ddot{\mathbf{q}}_\mathbf{a} \end{pmatrix} + \begin{pmatrix} H_1 \\ \mathbf{H_2} \end{pmatrix} = \begin{pmatrix} 0 \\ \mathbf{\Gamma} \end{pmatrix} + \begin{pmatrix} w_1 \\ \mathbf{w_2} \end{pmatrix} \tag{339}$$

où $\mathbf{q} = (q_1, q_2, q_3, q_4, q_5)^\top$ est le vecteur de dimension 5×1 de cordonnées généralisées, $\mathbf{q_a} = (q_2, q_3, q_4, q_5)^\top$ est le vecteur de dimension 4×1 des angles articulaires actionnés, $\mathbf{\Gamma} = (\Gamma_1, \Gamma_2, \Gamma_3, \Gamma_4)^\top$ est le vecteur de dimension 4×1 de couples, $\mathbf{H} = \mathbf{C}(\mathbf{q}, \dot{\mathbf{q}})\dot{\mathbf{q}} + \mathbf{G}(\mathbf{q}) = [H_1, \mathbf{H_2}^\top]^\top$ et $\mathbf{w_c}$ est le vecteur de dimension 5×1 de perturbations, avec les composantes w_1 et $\mathbf{w_2}$ qui représentent les perturbations dans les sous-systèmes actionnés et sous-actionnés, respectivement. D_{11} et H_1 sont quantités scalaires, $\mathbf{D_{12}}$ est un vecteur 1×4, $\mathbf{D_{21}}$ et $\mathbf{H_2}$ sont vecteurs de dimension 4×1 et $\mathbf{D_{22}}$ est une matrice 4×4.

Les considérations de la phase de double appui instantanée ont été décrites dans la section (9.5.1.2). Alors, le modèle global du robot bipède peut être exprimé sous la forme d'un système non linéaire avec des effets d'impulsion (314)-(315), oú $F(q)$ est l'altitude de la pointe de la jambe en mouvement, et $\mathbf{w_d}$ représente des perturbations externes à l'impact, telles que les erreurs de modélisation, terrain accidenté, etc.

9.7.2 Planification du mouvement périodique

La commande de l'allure de marche d'un bipède pendant la marche, consiste à suivre une trajectoire de référence $(\mathbf{q}_\star(\theta)^\top, \dot{\mathbf{q}}_\star(\theta, \dot{\theta})^\top)^\top$. La caractéristique de sous-actionnement du bipède en phase de simple appui doit être pris en compte car il est impossible de prescrire les cinq coordonnées généralisées indépendamment avec seulement quatre couples. La phase de double appui est considérée instantanée. La trajectoire est alors obtenue en utilisant une optimisation de la dynamique non linéaire (Aoustin and Formalsky, 1999; Chevallereau *et al.*, 2003; Miossec and Aoustin, 2006; Tlalolini *et al.*, 2011)

Un ensemble de contraintes virtuelles sont imposées comme les trajectoires de référence sur les coordonnées actionnées $\mathbf{q_a}$, et ils sont choisis pour être fonctions de la variable géométrique

$$\theta = q_1 + 0,5q_2 \tag{340}$$

au lieu du temps (Chevallereau and Aoustin, 2001). La variable θ représente l'angle de la ligne reliant l'extrémité de la jambe d'appui à la hanche contre le sol, et elle est strictement monotone le long de chaque pas.

Ces fonctions sont choisies comme polynômes Bézier de cinquième ordre (Bezier, 1972). Les coefficients sont choisis pour minimiser l'énergie des moteurs et pour assurer une marche périodique. Pour plus de détails, le lecteur intéressé peut consulter Westervelt *et al.* (2004).

9.7.3 Synthèse de commande $\mathcal{H}_\infty$

9.7.3.1 Synthèse par retour de l'état

L'objectif de commande pour le robot bipède est de concevoir un correcteur $\mathcal{H}_\infty$ non linéaire qui suit le mouvement périodique donné par

$$\mathbf{q}_\star(\theta) = \mathbf{\Phi}(\theta) = [\phi_1(\theta), \phi_2(\theta), \phi_3(\theta), \phi_4(\theta), \phi_5(\theta)]^\top \tag{341}$$

$$\dot{\mathbf{q}}_\star(\theta, \dot{\theta}) = \mathbf{\Phi}'(\theta) = \frac{\partial \mathbf{\Phi}(\theta)}{\partial \theta}\dot{\theta} \tag{342}$$

$$\ddot{\mathbf{q}}_\star(\theta, \dot{\theta}, \ddot{\theta}) = \mathbf{\Phi}''(\theta) = \frac{\partial \mathbf{\Phi}(\theta)}{\partial \theta}\dot{\theta}^2 + \frac{\partial^2 \mathbf{\Phi}(\theta)}{\partial \theta^2}\ddot{\theta}. \tag{343}$$

Nous définissons les variables d'erreur $\eta_1 = q_2 - \phi_2(\theta), \ldots \eta_4 = q_5 - \phi_5(\theta)$ et le vecteur d'erreur $\boldsymbol{\eta} = [\eta_1, \ldots, \eta_4]^\top$. En introduisant la transformation de commande

$$\mathbf{\Gamma} = \left(\mathbf{H_2} - \frac{\mathbf{D_{21}}}{D_{11}} H_1\right) + \mathbf{D_T}(\mathbf{\Phi_a''}(\theta) + \mathbf{v}), \tag{344}$$

spécifiée avec $\mathbf{D_T} = \mathbf{D_{22}} - \frac{\mathbf{D_{21}}\mathbf{D_{12}}}{D_{11}}$ et $\mathbf{\Phi_a''}(\theta) = [\phi_2''(\theta), \ldots, \phi_5''(\theta)]^\top$, la dynamique (330) peut être représentée sous la forme du double intégrateur perturbé

$$\ddot{\boldsymbol{\eta}} = \mathbf{v} + \mathbf{D_T^{-1}} \mathbf{w_2}, \tag{345}$$

où $\mathbf{w_2}$ est la perturbation qui affecte le fonctionnement du sous-système actionné de (339).

Ensuite, on peut obtenir l'équation des zéros dynamiques (319), (324) comme suit

$$\ddot{\theta} = \frac{-\left(\dfrac{D_{11}}{2}\dfrac{\partial^2 \phi_2(\theta)}{\partial \theta^2} + \mathbf{D_{12}}\dfrac{\partial^2 \mathbf{\Phi_a}(\theta)}{\partial \theta^2}\right)\dot{\theta}^2 - H_1}{D_{11}\left(1 - \dfrac{1}{2}\dfrac{\partial \phi_2(\theta)}{\partial \theta}\right) + \mathbf{D_{12}}\dfrac{\partial \mathbf{\Phi_a}(\theta)}{\partial \theta}} \tag{346}$$

$$\begin{bmatrix} \theta^+ \\ \dot{\theta}^+ \end{bmatrix} = \Delta_\theta(\theta^-, \dot{\theta}^-) = \theta \circ \psi(\mathbf{q}_\star(\theta)^-, \dot{\mathbf{q}}_\star(\theta)^-) \tag{347}$$

avec $\mathbf{\Phi_a}(\theta) = [\phi_2(\theta), \ldots, \phi_5(\theta)]^\top$.

Par conséquent, en utilisant les coordonnées transverses $\mathbf{x}_\perp = [I.\boldsymbol{\eta}^\top, \dot{\boldsymbol{\eta}^\top}]^\top$, on peut réécrire la dynamique du bipède sous la forme (336), (337), spécifiée par

$$\mathbf{f}(\mathbf{x}_\perp,t) = \begin{bmatrix} -\frac{2\dot{\theta}\bar{\beta}(\theta)}{\bar{\alpha}(\theta)} I \\ \dot{\boldsymbol{\eta}} \\ \mathbf{0} \end{bmatrix}, \quad \mathbf{g_1}(\mathbf{x}_\perp,t) = \begin{bmatrix} \frac{2\dot{\theta}}{\bar{\alpha}(\theta)} & \mathbf{0_{1\times 4}} \\ \mathbf{0_{4\times 1}} & \mathbf{0_{4\times 4}} \\ \mathbf{0_{4\times 1}} & \mathbf{D_T^{-1}} \end{bmatrix}, \tag{348}$$

$$\mathbf{g_2}(\mathbf{x}_\perp,t) = \begin{bmatrix} \frac{2\dot{\theta}}{\bar{\alpha}(\theta)}(D_{11}\mathbf{K}_\perp - \mathbf{D_{12}}) \\ \mathbf{0_{4\times 4}} \\ \mathbf{I_{4\times 4}} \end{bmatrix}, \quad \mathbf{K}_\perp = \left[\frac{1}{2}, 0, 0, 0\right], \quad \mathcal{F} = \mathbf{P}^{+}_{\mathbf{n(0)}} \mathrm{d}\psi(\mathbf{q},\dot{\mathbf{q}}) \mathbf{P}^{-}_{\mathbf{n(T_s)}} \tag{349}$$

avec les fonctions $\bar{\alpha}$, $\bar{\beta}$ données par (320)-(321), et θ, $\dot{\theta}$ pris le long de la solution prédéfinie (346).

Inspiré par le travail de Isidori and Astolfi (1992), la sortie à commander (222) peut être écrite comme suit

$$\mathbf{z} = \begin{bmatrix} \mathbf{0_{1\times 4}} & \rho_0 I & \rho_1 \boldsymbol{\eta}^\top & \rho_2 \dot{\boldsymbol{\eta}}^\top \end{bmatrix}^\top + \mathbf{v}^\top \begin{bmatrix} \mathbf{I_{4\times 4}} & \mathbf{0}^\top_{\mathbf{9\times 4}} \end{bmatrix}^\top \tag{350}$$

qui satisfait (230), où ρ_0, ρ_1, ρ_2 sont des valeurs scalaires. Enfin, le correcteur $\mathbf{v}$ est synthétisé en appliquant le théorème 9.5 au système transversal (336), (337) specifié par (348)-(349), et avec la sortie(350).

9.7.3.2 Synthèse par retour de la sortie

Selon (314)-(315), le mouvement périodique souhaité correspondant à l'orbite $\mathcal{O}_\star$ est régi par

$$\mathbf{D}(\mathbf{q}_\star)\ddot{\mathbf{q}}_\star + \mathbf{H}(\mathbf{q}_\star, \dot{\mathbf{q}}_\star) = \mathbf{B}\boldsymbol{\Gamma}^{\mathrm{s}}_\star. \tag{351}$$

Le couple d'entrée $\boldsymbol{\Gamma}^{\mathrm{s}}_\star$ est égal à (344). Ce couple oblige aux trajectoires de (314), (315), (329), (338) à rester sur l'orbite périodique $\mathcal{O}_\star$ lorsque le système est démarré sur $\mathcal{O}_\star$. Comme $\boldsymbol{\Gamma}^{\mathrm{s}}_\star$ dépend de la mesure des positions et des vitesses généralisées (ces dernières sont supposées non mesurables), $\boldsymbol{\Gamma}$ est remplacée par le correcteur dynamique

$$\boldsymbol{\Gamma} = \boldsymbol{\Gamma}^{\mathrm{s}}_\star + \mathbf{u}(\boldsymbol{\xi}, t) \tag{352}$$

où $\mathbf{u}(\boldsymbol{\xi},t)$ est défini par (226), et son état interne $\boldsymbol{\xi}$ donne une estimation des variables non mesurées. Ceci est effectué en définissant les vecteurs d'état $\mathbf{x_1} = \mathbf{q} - \mathbf{q}_\star$, $\mathbf{x_2} = \dot{\mathbf{q}} - \dot{\mathbf{q}}_\star$, et en combinant (314), (352) et (351), la dynamique de l'erreur peut être réécrite comme

$$\begin{aligned} \dot{\mathbf{x}}_\mathbf{1} &= \mathbf{x_2} \\ \dot{\mathbf{x}}_\mathbf{2} &= \mathbf{D}(\mathbf{x_1}+\mathbf{q}_\star)^{-1}[\mathbf{D}(\mathbf{q}_\star)\ddot{\mathbf{q}}_\star + \mathbf{H}(\mathbf{q}_\star,\dot{\mathbf{q}}_\star) - \mathbf{H}(\mathbf{x_1}+\mathbf{q}_\star,\mathbf{x_2}+\dot{\mathbf{q}}_\star) + \mathbf{B}\mathbf{u} + \mathbf{w_c}] - \ddot{\mathbf{q}}_\star \end{aligned} \tag{353}$$

avec une sortie à commander

$$\mathbf{z} = \rho_3 \left[\begin{array}{ccccc} \mathbf{0_{1\times4}} & x_{1_2} & x_{1_3} & x_{1_4} & x_{1_5} \end{array} \right]^\top + \mathbf{u}^\top \left[\begin{array}{cc} \mathbf{I_{4\times4}} & \mathbf{0_{4\times4}} \end{array} \right]^\top \tag{354}$$

où $x_{1_i} = q_i - q_{i\star}$, $i = 2,3,4,5$, ρ_3 est une valeur scalaire positif, et avec les mesures

$$\mathbf{y} = \mathbf{x_1} + \mathbf{w_y} \tag{355}$$

où $\mathbf{w_y}$ est un vecteur de perturbations de mesure de dimension 5×1. Ainsi, le système générique (221)-(225) est spécifié avec

$$\begin{aligned} \mathbf{f}(\mathbf{x},t) = & \left[\begin{array}{c} \mathbf{x}_2 \\ \mathbf{D}(\mathbf{x_1}+\mathbf{q}_\star)^{-1}[\mathbf{H}(\mathbf{q}_\star,\dot{\mathbf{q}}_\star) + \mathbf{D}(\mathbf{q}_\star)\ddot{\mathbf{q}}_\star] \end{array} \right] \\ & + \left[\begin{array}{c} \mathbf{0_{5\times1}} \\ -\mathbf{D}(\mathbf{x_1}+\mathbf{q}_\star)^{-1}[\mathbf{H}(\mathbf{x_1}+\mathbf{q}_\star,\mathbf{x_2}+\dot{\mathbf{q}}_\star)] - \ddot{\mathbf{q}}_\star \end{array} \right] \end{aligned} \tag{356}$$

$$\mathbf{g_1}(\mathbf{x},t) = \left[\begin{array}{cc} \mathbf{0_{5\times5}} & \mathbf{0_{5\times5}} \\ \mathbf{0_{5\times5}} & \mathbf{D}(\mathbf{x_1}+\mathbf{q}_\star)^{-1} \end{array} \right], \tag{357}$$

$$\mathbf{g_2}(\mathbf{x},t) = \left[\begin{array}{c} \mathbf{0_{5\times4}} \\ \mathbf{D}(\mathbf{x_1}+\mathbf{q}_\star)^{-1}\mathbf{B} \end{array} \right], \ \mathbf{h_1}(\mathbf{x}) = \left[\begin{array}{c} \mathbf{0_{4\times1}} \\ \rho_1 \mathbf{K_o} \mathbf{x}_1 \end{array} \right], \tag{358}$$

$$\mathbf{k_{12}}(\mathbf{x}) = \left[\begin{array}{c} \mathbf{I_{4\times4}} \\ \mathbf{0_{4\times4}} \end{array} \right], \ \mathbf{K_o} = \left[\begin{array}{cc} \mathbf{0_{4\times1}} & \mathbf{I_{4\times4}} \end{array} \right], \tag{359}$$

$$\mathbf{h_2}(\mathbf{x}) = \mathbf{x_1}, \ \mathbf{k_{21}}(\mathbf{x}) = \left[\begin{array}{cc} \mathbf{I_{5\times5}} & \mathbf{0_{5\times5}} \end{array} \right], \tag{360}$$

$$\boldsymbol{\mu}(\mathbf{x},t) = \psi(\mathbf{x_1}+\mathbf{q}_\star,\mathbf{x_2}+\dot{\mathbf{q}}_\star) - \psi(\mathbf{q}_\star,\dot{\mathbf{q}}_\star), \tag{361}$$

$$F(\mathbf{x}, t) = F_0(\mathbf{x_1} + \mathbf{q}_\star), \quad \boldsymbol{\omega}(\mathbf{x}, t) = \mathbf{I_{5\times 5}} \tag{362}$$

où la fonction $F_0(\mathbf{q})$ est donnée par la hauteur du pied en mouvement.

Enfin, le dernier théorème de ce travail est présenté ci-dessous.

Théorème 9.6 *Supposons que les conditions C1)-C2) et les hypothèses H1) et H4) (voir section 9.2) soient satisfaites pour le système hybride* (221)-(225)*, specifié avec* (356)-(362)*. En conséquence le correcteur dynamique* (270a)-(270b) *est une solution au problème de commande $\mathcal{H}_\infty$ pour le système mécanique à boucle fermée* (314)-(315)*,* (352)*.*

Il est important de remarquer que $\dot{\theta}$ et $\ddot{\theta}$, qui sont nécessaires pour obtenir les vitesses $\dot{\mathbf{q}}_\star$ et accélérations $\ddot{\mathbf{q}}_\star$, doivent être estimées, puisque seulement les mesures de position sont disponibles. Cette estimation est faite en utilisant les états de (270a).

Ce résultat sera utilisé dans la prochaine section pour stabiliser un robot bipède sous-actionné sur une orbite périodique souhaitée.

9.7.4 Étude numérique

Les paramètres du robot utilisés pour les simulations sont ceux de ”Rabbit” (Chevallereau *et al.*, 2003). L’application de la loi de commande (352) est considérée pour suivre une trajectoire géométrique de référence définie à l’aide de l’approche de contraintes virtuelles. La période et la longueur de l’allure de marche nominale, qui est obtenue par optimisation, sont $0,56\ s$ et $0,45\ m$. La vitesse de marche moyenne est $0,80\ m \cdot s^{-1}$. Cette allure de marche a été testée en boucle fermée pour plusieurs pas.

Pour tous les cas dans les paragraphes suivants, les forces de réaction ont été vérifiées afin de veiller que les jambes ne glissent pas, et qu’elles ne décollent pas. Les simulations sont effectuées en utilisant un algorithme de détection d’événements (Heemels and Brogliato, 2003).

9.7.4.1 Cas non perturbé

La Figure 95 présente le plan de phase $\theta, \dot{\theta}$ pour le système sans perturbations (314)-(315) ($\mathbf{w_0} = \mathbf{w_c} = \mathbf{w_d} = \mathbf{0}$), où les conditions initiales du système (positions et vitesses) sont déviées 5% par rapport aux conditions initiales de la trajectoire de référence (les conditions initiales de l'estimateur (270a) sont égales aux conditions initiales du mouvement de référence, donc il y a une erreur d'estimation initiale aussi). On peut constater que l'évolution du système converge asymptotiquement à un cycle limite (représentée en bleu), qui représente le cycle limite du mouvement de référence.

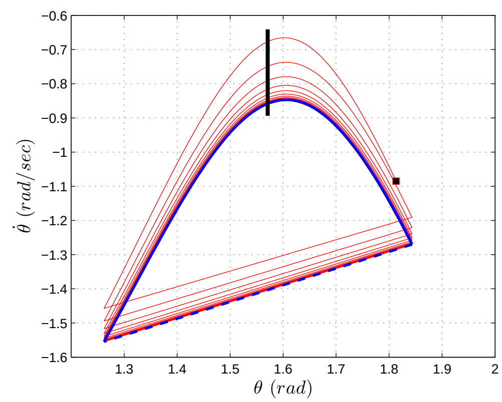

Figure 95: Le plan de phase de θ pour le système sans perturbations, sous conditions initiales non nulles, pour 18 pas. Red: Évolution du système. Blue: Cycle limite de la référence. La condition initiale du système est indiquée par le carré noir.

9.7.4.2 Terrain accidenté

Une analyse du bipède marchant sur un terrain accidenté est faite. Les résultats sont présentés sur la Fig. 96 pour trois cas différents : une perturbation du premier pas donné par une inclinaison virtuelle de $5°$ (rouge); perturbation lors des deux premiers pas par inclinaisons virtuelles de $-2°$ et $10°$ respectivement (noire); et inclinaisons virtuelles alternantes de$-5°$ et $5°$ (magenta). Comme prédit par la théorie, lorsque les perturbations disparaissent (cas noir et rouge), le système retourne au cycle de référence (ligne bleue), alors que si la perturbation est soutenue (cas magenta), les systèmes vont rester au voisinage du cycle de référence.

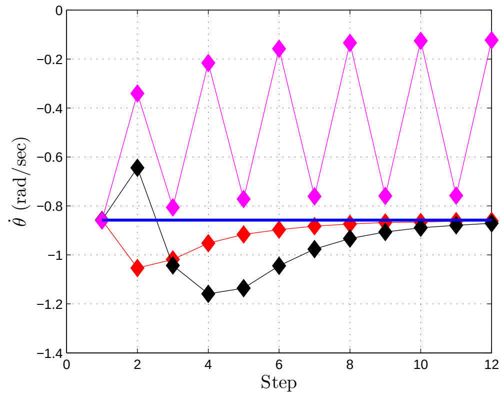

Figure 96: Applications de Poincaré pour le système sous plusieurs inclinaisons virtuelles, pendant 12 pas. Bleu: cycle nominal. Rouge: Inclinaison virtuelle de $5°$ pour le premier pas, $0°$ pour le reste. Noir: Inclinaison virtuelle de $-2°$ pour le premier pas, $10°$ pour le deuxième pas et $0°$ pour le reste. Magenta: Alternance de $-5°$ et $5°$.

9.7.4.3 Frottement

Un effet important à considérer est le frottement, surtout au niveau des articulations du genou, car θ dépend du comportement de q_2. Par conséquent, le vecteur de frottement de Coulomb

$$\mathbf{F} = [F_1, \ldots, F_5]^\top \tag{363}$$

est soustrait du membre de droite de l'équation (339), avec

$$F_i = F_i^c \mathrm{sign}(\dot{q}_i), \quad i = 1, \ldots, 5. \tag{364}$$

Les tests numériques ont été réalisés sous l'hypothèse que les articulations actionnées sont soumises aux forces de frottement. C'est pour ça que les coefficients de frottement $F_2^c = F_5^c = -2,1$, $F_3^c = F_4^c = -1,02$ et $F_1^c = 0$ sont choisis. Les résultats sont présentés sur la Fig. 97. Même en présence du frottement de Coulomb, la marche est encore stable après plusieurs pas, comme on peut le voir dans le plan de phase de θ, où l'évolution du système se rapproche d'une nouvelle orbite, représentée en rouge.

9.7.4.4 Forces externes et perturbations de l'impact

Les Fig. 98-99, montrent les résultats de simulation pour le système testé sous l'application d'une force externe ($5\ Nm$ à la hanche, le long de l'axe x) pendant la phase de sim-

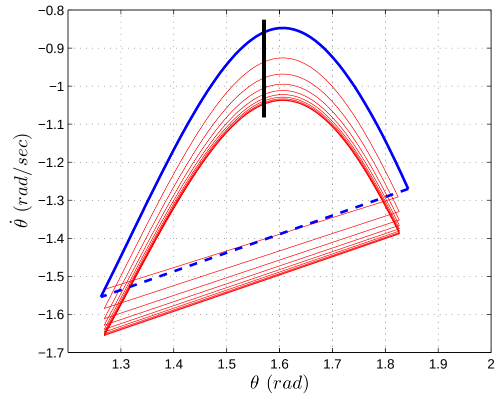

Figure 97: Le plan de phase de θ, $\dot{\theta}$ pour le cas perturbé par frottement de Coulomb. Bleu: cycle nominal. Rouge: cycle réel.

ple appui, à partir du premier pas; la fonction d'impact $\boldsymbol{\mu}$ est déviée 5% par rapport des valeurs nominales. Les mesures ont été perturbées par la perturbation sinusoïdale $0,05\sin(2t)\ rads$, et l'estimation initiale de la vitesse du bipède est dévié 5% par rapport à la trajectoire de référence.

La nouvelle orbite obtenue est représentée sur la Fig. 98 par la ligne rouge. En raison de la robustesse du correcteur, cette nouvelle orbite est proche de l'orbite nominale. Même si l'évolution de θ ne converge pas vers un cycle limite, en raison de l'effet des perturbations variant dans le temps, il oscille dans un voisinage du cycle nominal.

Comme la vitesse est non mesurable, Fig. 99 présente le comportement de l'estimateur (270a) lors de l'estimation des vitesses manquantes, où l'on peut constater que, malgré des perturbations persistantes dans les mesures, l'erreur ne diverge pas.

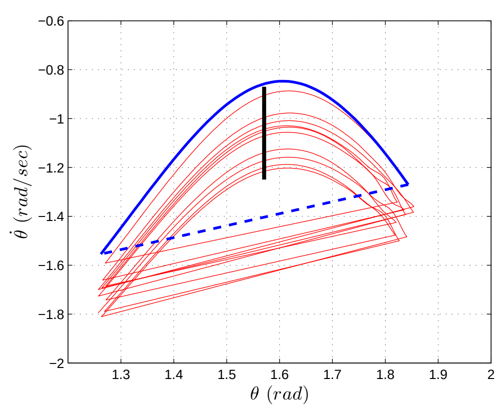

Figure 98: Le plan de phase de θ, $\dot{\theta}$ pour le système affecté par perturbations persistantes. La ligne bleue représente le cycle limite pour le système non perturbé, alors que la rouge représente l'orbite du système sous les perturbations. La ligne noire indique la section de Poincaré.

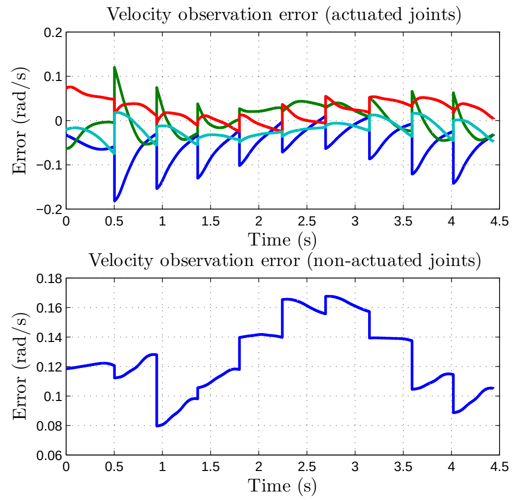

Figure 99: Erreurs d'estimation de la vitesse $\boldsymbol{\xi_2} = (\xi_{21}, \ldots, \xi_{25})^\top$ pour l'estimateur (270a), pour le système affecté par perturbations persistantes. L'erreur d'estimation ne diverge pas sous la présence de perturbations sur les mesures ainsi que la sur la dynamique du système.

9.8 Conclusions générales

Le problème de commande $\mathcal{H}_\infty$ est résolu pour les systèmes mécaniques sous contraintes unilatérales via la conception par retour de sortie et par retour d'état. Des conditions suffisantes pour l'existence d'une solution du problème de suivi par retour de sortie sont obtenues par la résolution de trois inégalités couplées : deux inégalités Hamilton-Jacobi-Isaacs, et une inégalité indépendante supplémentaire qui est due à la loi de restitution.

L'oscillateur de Van der Pol est étudié sous contraintes unilatérales, à cause de la nécessité d'un modèle de référence approprié. Cet oscillateur hybride est capable de présenter un point d'équilibre instable et une cycle limite asymptotiquement stable, et sous une variation du paramètre d'amortissement, il présente un équilibre asymptotiquement stable. Des conditions suffisantes pour l'existence d'un cycle limite asymptotiquement stable sont obtenues et numériquement validées par l'analyse de Poincaré. En outre, la valeur de bifurcation de Hopf est calculée avec précision. Par conséquent, l'oscillateur de Van der Pol hybride est extrêmement attrayant pour son utilisation comme modèle de référence dans les applications de commande mécanique.

L'efficacité de la procédure de synthèse proposée est démontrée par les études numériques réalisées pour trois systèmes mécaniques complètement actionnés: un pendule qui frappe contre une barrière, un bipède de 7 corps, et un robot bipède de 32 degrés de liberté. Pour les trois cas, l'atténuation de perturbation souhaitée est atteinte de manière satisfaisante dans la présence de perturbations externes pendant la phase de mouvement libre et en présence d'incertitudes dans la transition. Afin de lutter contre le phénomène de pics qui apparaît pour le suivi des systèmes hybrides (Biemond *et al.*, 2013), l'idée d'une adaptation en ligne de la ré-initialisation du modèle est introduite. Cette idée est appliquée afin de synchroniser les impacts du système avec ceux du modèle de référence, améliorant ainsi la performance du système en boucle fermée.

Enfin, une extension de la synthèse proposée vers des systèmes mécaniques sous-actionnés, soumis à des contraintes unilatérales, est présentée. En analysant les dynamiques transversales, des conditions suffisantes pour atténuer les perturbations du système autour d'une trajectoire prescrite sont dérivées, sous réserve que la trajectoire de référence périodique est réalisable. Les tests effectués pour le robot bipède "Rabbit", illustrent la bonne performance du système en boucle fermée, malgré les perturbations introduites sur la phase de simple appui, sur la phase d'impact, et les imperfections sur les mesures de position.

9.8.1 Contributions

La contribution du papier dans la littérature existante est double. D'abord, l'approche $\mathcal{H}_\infty$ non linéaire est généralisée sous contraintes unilatérales, par l'incorporation d'une condition supplémentaire sur la ré-initialisation du système dans la boucle fermée. La synthèse robuste résultant est ensuite appliquée efficacement aux bancs d'essai ci-données, dans le but de générer des mouvements périodiques. Les caractéristiques de robustesse de la synthèse proposée, justifiées par les simulations dans les bancs d'essai, constituent une nouveauté importante de ce travail.

Par ailleurs, la découverte de la bifurcation de Hopf pour l'oscillateur hybride de Van der Pol est l'une des principales contributions du présent travail. Cela permet de générer des trajectoires de référence, modifiables en ligne, qui soit présentent un comportement périodique ou tendent vers l'origine. C'est pour ça que cet oscillateur hybride est idéal comme un modèle de référence pour les systèmes mécaniques soumis à des contraintes unilatérales.

La méthode de synchronisation d'impact introduit afin de supprimer le phénomène de pics, est encore une autre contribution de ce travail. Ceci permet d'améliorer la performances en boucle fermée et pour garantir la stabilité asymptotique.

Une caractéristique essentielle est que non seulement les perturbations exogènes standard lors de la phase continue (telles que les forces externes, l'incertitude de paramètres du bipède, etc.) sont rejetées. Celles de l'impact (comme le contact inélastique non-parfaite entre le sol et le pied à l'impact, ou des variations de hauteur du sol) et les imperfections de mesure sont atténuées avec la synthèse proposée.

List of References

Acary, V. and Brogliato, B. (2008). *Numerical methods for nonsmooth dynamical systems: applications in mechanics and electronics*, Vol. 35. Springer.

Aghabalaie, P., Hosseinzadeh, M., Talebi, H., and Shafiee, M. (2010). Nonlinear robust control of a biped robot. En: *Industrial Electronics (ISIE), 2010 IEEE International Symposium on*. IEEE, pp. 1907–1912.

Akhmet, M. (2005). Perturbations and hopf bifurcation of the planar discontinuous dynamical system. *Nonlinear Analysis: Theory, Methods & Applications*, **60**(1): 163–178.

Akhmet, M. and Turan, M. (2014). Bifurcation of discontinuous limit cycles of the van der pol equation. *Mathematics and Computers in Simulation*, **95**: 39–54.

Alcaraz-Jiménez, J., Herrero-Pérez, D., and Martínez-Barberá, H. (2013). Robust feedback control of zmp-based gait for the humanoid robot nao. *The International Journal of Robotics Research*, **32**(9-10): 1074–1088.

Ames, A., Galloway, K., and Grizzle, J. (2012). Control lyapunov functions and hybrid zero dynamics. En: *Decision and Control (CDC), 2012 IEEE 51st Annual Conference on*. IEEE, pp. 6837–6842.

Angelosanto, G. (2008). *Kalman filtering of IMU sensor for robot balance control*. Tesis de doctorado, Massachusetts Institute of Technology.

Antsaklis, P. (2000). A brief introduction to the theory and applications of hybrid systems. En: *Proc IEEE, Special Issue on Hybrid Systems: Theory and Applications*. Citeseer.

Aoustin, Y. and Formalsky, A. (1999). Design of reference trajectory to stabilize desired nominal cyclic gait of a biped. En: *Robot Motion and Control, 1999. RoMoCo'99. Proceedings of the First Workshop on*. IEEE, pp. 159–164.

Aoustin, Y. and Formalsky, A. (2003). Control design for a biped: reference trajectory based on driven angles as functions of the undriven angle. *Journal of Computer and Systems Sciences International*, **42**(4): 645–662.

Aoustin, Y. and Hamon, A. (2013). Human like trajectory generation for a biped robot with a four-bar linkage for the knees. *Robotics and Autonomous Systems*, **61**(12): 1717–1725.

Aoustin, Y., Chevallereau, C., and Formalsky, A. (2006). Numerical and experimental study of the virtual quadrupedal walking robot-semiquad. *Multibody System Dynamics*, **16**(1): 1–20.

Aoustin, Y., Chevallereau, C., and Orlov, Y. (2010). Finite time stabilization of a perturbed double integrator-part ii: applications to bipedal locomotion. En: *Decision and Control (CDC), 2010 49th IEEE Conference on*. IEEE, pp. 3554–3559.

Arai, H., Tanie, K., and Shiroma, N. (1998). Time-scaling control of an underactuated manipulator. En: *Robotics and Automation, 1998. Proceedings. 1998 IEEE International Conference on*. IEEE, Vol. 3, pp. 2619–2626.

Baras, J. and James, M. (1993). Robust output feedback control for discrete-time nonlinear systems: The finite-time case. En: *Decision and Control, 1993., Proceedings of the 32nd IEEE Conference on*. IEEE, pp. 51–55.

Basar, T. and Bernhard, P. (1995). $\mathcal{H}_\infty$-optimal control and related minimax design problems: a dynamic game approach. *Systems & control*.

Bentsman, J., Miller, B. M., Rubinovich, E. Y., and Mazumder, S. K. (2012). Modeling and control of systems with active singularities under energy constraints: Single-and multi-impact sequences. *Automatic Control, IEEE Transactions on*, **57**(7): 1854–1859.

Bernardo, M., Budd, C., Champneys, A., and Kowalczyk, P. (2008a). *Piecewise-smooth dynamical systems: theory and applications*, Vol. 163. Springer Science & Business Media.

Bernardo, M., Budd, C., Champneys, A., Kowalczyk, P., Nordmark, A., Tost, G., and Piiroinen, P. (2008b). Bifurcations in nonsmooth dynamical systems. *SIAM review*, pp. 629–701.

Bezier, P. (1972). *Numerical control: Mathematics and applications*. Wiley and Sons.

Biemond, J., van de Wouw, N., Heemels, W., and Nijmeijer, H. (2013). Tracking control for hybrid systems with state-triggered jumps. *Automatic Control, IEEE Transactions on*, **58**(4): 876–890.

Branicky, M., Borkar, V., and Mitter, S. (1998). A unified framework for hybrid control: Model and optimal control theory. *Automatic Control, IEEE Transactions on*, **43**(1): 31–45.

Brogliato, B. (1999). *Nonsmooth Mechanics.: Models, Dynamics and Control*. Springer.

Brogliato, B. (2000). *Impacts in mechanical systems: analysis and modelling*, Vol. 551. Springer Verlag.

Brogliato, B., Niculescu, S., and Orhant, P. (1997). On the control of finite-dimensional mechanical systems with unilateral constraints. *Automatic Control, IEEE Transactions on*, **42**(2): 200–215.

Bullo, F. and Lynch, K. (2001). Kinematic controllability for decoupled trajectory planning in underactuated mechanical systems. *Robotics and Automation, IEEE Transactions on*, **17**(4): 402–412.

Chardonnet, J.-R., Miossec, S., Kheddar, A., Arisumi, H., Hirukawa, H., Pierrot, F., and Yokoi, K. (2006). Dynamic simulator for humanoids using constraint-based method with static friction. En: *Robotics and Biomimetics, 2006. ROBIO'06. IEEE International Conference on*. IEEE, pp. 1366–1371.

Chen, B., Lee, T., and Feng, J. (1994). A nonlinear h_∞ control design in robotic systems under parameter perturbation and external disturbance. *International Journal of Control*, **59**(2): 439–461.

Chevallereau, C. and Aoustin, Y. (2001). Optimal reference trajectories for walking and running of a biped robot. *Robotica*, **19**(5): 557–569.

Chevallereau, C., Abba, G., Aoustin, Y., Plestan, F., Westervelt, E., Canudas De Wit, C., and Grizzle, J. (2003). Rabbit: A testbed for advanced control theory. *IEEE Control Systems Magazine*, **23**(5): 57–79.

Chevallereau, C., Formalsky, A., and Djoudi, D. (2004a). Tracking a joint path for the walk of an underactuated biped. *Robotica*, **22**(1): 15–28.

Chevallereau, C., Westervelt, E., and Grizzle, J. (2004b). Asymptotic stabilization of a five-link, four-actuator, planar bipedal runner. En: *Decision and Control, 2004. CDC. 43rd IEEE Conference on*. IEEE, Vol. 1, pp. 303–310.

Chevallereau, C., Grizzle, J., and Shih, C. (2009). Asymptotically stable walking of a five-link underactuated 3-d bipedal robot. *Robotics, IEEE Transactions on*, **25**(1): 37–50.

Chillingworth, D. (2002). Discontinuity geometry for an impact oscillator. *Dynamical Systems*, **17**(4): 389–420.

Dai, H. and Tedrake, R. (2012). Optimizing robust limit cycles for legged locomotion on unknown terrain. En: *Decision and Control (CDC), 2012 IEEE 51st Annual Conference on*. IEEE, pp. 1207–1213.

Dai, H. and Tedrake, R. (2013). $\mathcal{L}_2$-gain optimization for robust bipedal walking on unknown terrain. En: *Robotics and Automation (ICRA), 2013 IEEE International Conference on*. IEEE, pp. 3116–3123.

Djoudi, D. (2007). *Contribution à la commande d'un robot bipède*. Tesis de doctorado, Nantes.

Djoudi, D., Chevallereau, C., and Aoustin, Y. (2005). Optimal reference motions for walking of a biped robot. En: *Robotics and Automation, 2005. ICRA 2005. Proceedings of the 2005 IEEE International Conference on*. IEEE, pp. 2002–2007.

Dutra, M. S., de Pina Filho, A. C., and Romano, V. F. (2003). Modeling of a bipedal locomotor using coupled nonlinear oscillators of van der pol. *Biological Cybernetics*, **88**(4): 286–292.

Ehrich, F. (1991). Some observations of chaotic vibration phenomena in high-speed rotordynamics. *Journal of Vibration and Acoustics*, **113**(1): 50–57.

El-Farra, N. H., Mhaskar, P., and Christofides, P. D. (2005). Output feedback control of switched nonlinear systems using multiple lyapunov functions. *Systems & Control Letters*, **54**(12): 1163–1182.

Ellekilde, L. and Perram, J. (2005). Tool center trajectory planning for industrial robot manipulators using dynamical systems. *The International Journal of Robotics Research*, **24**(5): 385–396.

Foale, S. and Bishop, S. (1994). Bifurcations in impact oscillations. *Nonlinear Dynamics*, **6**(3): 285–299.

Formalskii, A. M. (2009). Ballistic walking design via impulsive control. *Journal of Aerospace Engineering*, **23**(2): 129–138.

Forni, F., Teel, A. R., and Zaccarian, L. (2011). Tracking control in billiards using mirrors without smoke, part i: Lyapunov-based local tracking in polyhedral regions. En: *Decision and Control and European Control Conference (CDC-ECC), 2011 50th IEEE Conference on*. IEEE, pp. 3283–3288.

Fredriksson, M. and Nordmark, A. (1997). Bifurcations caused by grazing incidence in many degrees of freedom impact oscillators. En: *Proceedings of the Royal Society of London A: Mathematical, Physical and Engineering Sciences*. The Royal Society, Vol. 453, pp. 1261–1276.

Freidovich, L. and Shiriaev, A. (2009). Transverse linearization for mechanical systems with passive links, impulse effects, and friction forces. En: *Decision and Control, 2009 held jointly with the 2009 28th Chinese Control Conference. CDC/CCC 2009. Proceedings of the 48th IEEE Conference on*. IEEE, pp. 6490–6495.

Freidovich, L., Shiriaev, A., and Manchester, I. (2008). Stability analysis and control design for an underactuated walking robot via computation of a transverse linearization. En: *Proc. 17th IFAC World Congress, Seoul, Korea*. pp. 10–166.

Goebel, R., Sanfelice, R., and Teel, A. (2009). Hybrid dynamical systems. *Control Systems, IEEE*, **29**(2): 28–93.

Goswami, A., Espiau, B., and Keramane, A. (1996). Limit cycles and their stability in a passive bipedal gait. En: *Robotics and Automation, 1996. Proceedings., 1996 IEEE International Conference on*. IEEE, Vol. 1, pp. 246–251.

Goyder, H. and Teh, C. (1989). A study of the impact dynamics of loosely supported heat exchanger tubes. *Journal of pressure vessel technology*, **111**(4): 394–401.

Grishin, A., Formalsky, A., Lensky, A., and Zhitomirsky, S. (1994). Dynamic walking of a vehicle with two telescopic legs controlled by two drives. *The International Journal of Robotics Research*, **13**(2): 137–147.

Grizzle, J., Plestan, F., and Abba, G. (1999). Poincare's method for systems with impulse effects: application to mechanical biped locomotion. En: *Decision and Control, 1999. Proceedings of the 38th IEEE Conference on*. IEEE, Vol. 4, pp. 3869–3876.

Grizzle, J., Abba, G., and Plestan, F. (2001). Asymptotically stable walking for biped robots: Analysis via systems with impulse effects. *Automatic Control, IEEE Transactions on*, **46**(1): 51–64.

Grizzle, J., Choi, J., Hammouri, H., and Morris, B. (2007). On observer-based feedback stabilization of periodic orbits in bipedal locomotion. *Proc. Methods and Models in Automation and Robotics*.

Grizzle, J., Chevallereau, C., Ames, A., and Sinnet, R. (2010). 3d bipedal robotic walking: models, feedback control, and open problems. En: *IFAC Symposium on Nonlinear Control Systems*. Vol. 2, p. 8.

Haddad, W., Kablar, N., Chellaboina, V., and Nersesov, S. (2005). Optimal disturbance rejection control for nonlinear impulsive dynamical systems. *Nonlinear Analysis: Theory, Methods & Applications*, **62**(8): 1466–1489.

Haddad, W., Chellaboina, V., and Nersesov, S. (2006). *Impulsive and hybrid dynamical systems: stability, dissipativity, and control*. Princeton University Press.

Hale, J. and Koçak, H. (2012). *Dynamics and bifurcations*, Vol. 3. Springer Science & Business Media.

Hamed, K. and Grizzle, J. (2013). Robust event-based stabilization of periodic orbits for hybrid systems: Application to an underactuated 3d bipedal robot. En: *Proceedings of the 2013 American Control Conference*.

Hamed, K. and Grizzle, J. (2014). Event-based stabilization of periodic orbits for underactuated 3-d bipedal robots with left-right symmetry. *Robotics, IEEE Transactions on*, **30**(2): 365–381.

Hamed, K., Sadati, N., Gruver, W., and Dumont, G. (2012). Stabilization of periodic orbits for planar walking with noninstantaneous double-support phase. *Systems, Man and Cybernetics, Part A: Systems and Humans, IEEE Transactions on*, **42**(3): 685–706.

Hamed, K., Buss, B., and Grizzle, J. (2014). Continuous-time controllers for stabilizing periodic orbits of hybrid systems: Application to an underactuated 3d bipedal robot. *Proceedings of the 53rd IEEE Conderence on Decision and Control.*.

Haq, A., Aoustin, Y., and Chevallereau, C. (2012). Effects of knee locking and passive joint stiffness on energy consumption of a seven-link planar biped. En: *Robotics and Automation (ICRA), 2012 IEEE International Conference on*. IEEE, pp. 870–876.

Heemels, W. and Brogliato, B. (2003). The complementarity class of hybrid dynamical systems. *European Journal of Control*, **9**(2): 322–360.

Hespanha, J. P., Liberzon, D., and Teel, A. R. (2008). Lyapunov conditions for input-to-state stability of impulsive systems. *Automatica*, **44**(11): 2735–2744.

Hill, D. and Moylan, P. (1980). Connections between finite-gain and asymptotic stability. *Automatic Control, IEEE Transactions on*, **25**(5): 931–936.

Hobbelen, D. G. and Wisse, M. (2007). A disturbance rejection measure for limit cycle walkers: The gait sensitivity norm. *Robotics, IEEE Transactions on*, **23**(6): 1213–1224.

Hogan, S. (1989). On the dynamics of rigid-block motion under harmonic forcing. En: *Proceedings of the Royal Society of London A: Mathematical, Physical and Engineering Sciences*. The Royal Society, Vol. 425, pp. 441–476.

Hurmuzlu, Y., Génot, F., and Brogliato, B. (2004). Modeling, stability and control of biped robots—a general framework. *Automatica*, **40**(10): 1647–1664.

Ikeda, G., Asahara, H., Aihara, K., and Kousaka, T. (2012). A search algorithm of bifurcation point in an impact oscillator with periodic threshold. En: *Circuits and Systems (APCCAS), 2012 IEEE Asia Pacific Conference on*. IEEE, pp. 200–203.

Isidori, A. and Astolfi, A. (1992). Disturbance attenuation and $\mathcal{H}_\infty$-control via measurement feedback in nonlinear systems. *Automatic Control, IEEE Transactions on*, **37**(9): 1283–1293.

Kajita, S., Hirukawa, H., Harada, K., and Yokoi, K. (2008). *Introduction à la commande des robots humanoïde : De la modélisation à la génération du mouvement*. Springer-Verlag.

Khalil, H. (2002). *Nonlinear Systems*. Prentice Hall.

Khalil, W. and Kleinfinger, J. (1986). A new geometric notation for open and closed-loop robots. En: *Robotics and Automation. Proceedings. 1986 IEEE International Conference on*. IEEE, Vol. 3, pp. 1174–1179.

Kuznetsov, Y. (2013). *Elements of applied bifurcation theory*, Vol. 112. Springer Science & Business Media.

La Hera, P., Shiriaev, A., Freidovich, L., Mettin, U., and Gusev, S. (2013). Stable walking gaits for a three-link planar biped robot with one actuator. *Robotics, IEEE Transactions on*, **29**(3): 589–601.

Lee, J. (2005). Motion behavior of impact oscillator. *J. Marine Sci. Technol*, **13**: 89–96.

Leine, R. and Nijmeijer, H. (2013). *Dynamics and bifurcations of non-smooth mechanical systems*, Vol. 18. Springer Science & Business Media.

Leonov, G. (2006). Generalization of the andronov-vitt theorem. *Regular and chaotic dynamics*, **11**(2): 281–289.

Li, Y., Li, T., and Jing, X. (2014). Indirect adaptive fuzzy control for input and output constrained nonlinear systems using a barrier lyapunov function. *International Journal of Adaptive Control and Signal Processing*, **28**(2): 184–199.

Liberzon, D. (2003). *Switching in Systems and Control*. Birkhauser:Boston.

Lin, W. and Byrnes, C. (1996). $\mathcal{H}_\infty$-control of discrete-time nonlinear systems. *Automatic Control, IEEE Transactions on*, **41**(4): 494–510.

Luh, J., Walker, M., and Paul, R. (1980). Resolved-acceleration control of mechanical manipulators. *Automatic Control, IEEE Transactions on*, **25**(3): 468–474.

Mabrouk, M. (1998). A unified variational model for the dynamics of perfect unilateral constraints. *European Journal of Mechanics-A/Solids*, **17**(5): 819–842.

Makarenkov, O. and Lamb, J. (2012). Dynamics and bifurcations of nonsmooth systems: a survey. *Physica D: Nonlinear Phenomena*, **241**(22): 1826–1844.

Manamani, N., Gauthier, N., and MSirdi, N. (1997). Sliding mode control for pneumatic robot leg. En: *Proceedings European Control Conference*.

Menini, L. and Torambe, A. (2000). Asymptotic tracking of periodic trajectories for a simple mechanical system subject to non-smooth impacts. En: *Decision and Control, 2000. Proceedings of the 39th IEEE Conference on*. IEEE, Vol. 5, pp. 5059–5064.

Menini, L. and Tornambè, A. (2002). Velocity observers for non-linear mechanical systems subject to non-smooth impacts. *Automatica*, **38**(12): 2169 – 2175.

Mettin, U., La Hera, P., Freidovich, L., and Shiriaev, A. (2007). Planning human-like motions for an underactuated humanoid robot based on the virtual constraints approach. *In Proc. 13th International Conference on Advanced Robotics, Jeju, Korea,*, pp. 585–590.

Meza-Sanchez, I., Aguilar, L., Shiriaev, A., Freidovich, L., and Orlov, Y. (2011). Periodic motion planning and nonlinear $\mathcal{H}_\infty$ tracking control of a 3-dof underactuated helicopter. *International Journal of Systems Science*, **42**(5): 829–838.

Mhaskar, P., El-Farra, N. H., and Christofides, P. D. (2006). Stabilization of nonlinear systems with state and control constraints using lyapunov-based predictive control. *Systems & Control Letters*, **55**(8): 650–659.

Miossec, S. and Aoustin, Y. (2005). A simplified stability study for a biped walk with underactuated and overactuated phases. *The International Journal of Robotics Research*, **24**(7): 537–551.

Miossec, S. and Aoustin, Y. (2006). Dynamical synthesis of a walking cyclic gait for a biped with point feet. En: *Fast motions in biomechanics and robotics*. Springer, pp. 233–252.

Montano, O., Orlov, Y., and Aoustin, Y. (2013). Nonlinear $\mathcal{H}_\infty$-control of mechanical systems under unilateral constraints on the position. *Proc. of the Congreso Nacional de Control Automatico, AMCA*.

Montano, O., Orlov, Y., and Aoustin, Y. (2014). Nonlinear $\mathcal{H}_\infty$-control of mechanical systems under unilateral constraints. *Proc. 9th World Congress of the International Federation of Automatic Control (IFAC 2014)*.

Montano, O., Orlov, Y., and Aoustin, Y. (2015a). Nonlinear output feedback $\mathcal{H}_\infty$-control of mechanical systems under unilateral constraints. *Proceedings of the 1st IFAC Conference on Modelling, Identification and Control of Nonlinear Systems*, pp. 284–289.

Montano, O., Orlov, Y., Aoustin, Y., and Chevallereau, C. (2015b). Nonlinear orbital $\mathcal{H}_\infty$-stabilization of underactuated mechanical systems with unilateral constraints. *Proceedings of the 14th European Control Conference*, pp. 800–805.

Montano, O., Orlov, Y., Aoustin, Y., and Chevallereau, C. (2016). Orbital stabilization of an underactuated bipedal gait via nonlinear $\mathcal{H}_\infty$-control using measurement feedback. *Autonomous Robots*, pp. 1–19.

Morarescu, I. and Brogliato, B. (2010). Trajectory tracking control of multiconstraint complementarity lagrangian systems. *Automatic Control, IEEE Transactions on*, **55**(6): 1300–1313.

Morimoto, J. and Atkeson, C. (2002). Minimax differential dynamic programming: An application to robust biped walking. En: *NIPS*. pp. 1539–1546.

Morris, B. and Grizzle, J. (2005). A restricted poincaré map for determining exponentially stable periodic orbits in systems with impulse effects: Application to bipedal robots. En: *Decision and Control, 2005 and 2005 European Control Conference. CDC-ECC'05. 44th IEEE Conference on*. IEEE, pp. 4199–4206.

Morris, B. and Grizzle, J. (2009). Hybrid invariant manifolds in systems with impulse effects with application to periodic locomotion in bipedal robots. *Automatic Control, IEEE Transactions on*, **54**(8): 1751–1764.

Naldi, R. and Sanfelice, R. G. (2013). Passivity-based control for hybrid systems with applications to mechanical systems exhibiting impacts. *Automatica*, **49**(5): 1104 – 1116.

Nesic, D., Zaccarian, L., and Teel, A. (2008). Stability properties of reset systems. *Automatica*, **44**(8): 2019–2026.

Nesic, D., Teel, A. R., Valmorbida, G., and Zaccarian, L. (2013). Finite-gain stability for hybrid dynamical systems. *Automatica*, **49**(8): 2384 – 2396.

Nguang, S. and Shi, P. (2000). Nonlinear $\mathcal{H}_\infty$ filtering of sampled-data systems. *Automatica*, **36**(2): 303–310.

Nikkhah, M., Ashrafiuon, H., and Fahimi, F. (2007). Robust control of underactuated bipeds using sliding modes. *Robotica*, **25**(03): 367–374.

Niu, B. and Zhao, J. (2013a). Barrier lyapunov functions for the output tracking control of constrained nonlinear switched systems. *Systems & Control Letters*, **62**(10): 963–971.

Niu, B. and Zhao, J. (2013b). Tracking control for output-constrained nonlinear switched systems with a barrier lyapunov function. *International Journal of Systems Science*, **44**(5): 978–985.

Orlov, Y. (2009). *Discontinuous systems–Lyapunov analysis and robust synthesis under uncertainty conditions*. Springer.

Orlov, Y. and Acho, L. (2001). Nonlinear $\mathcal{H}_\infty$-control of time-varying systems: a unified distribution-based formalism for continuous and sampled-data measurement feedback design. *Automatic Control, IEEE Transactions on*, **46**(4): 638–643.

Orlov, Y. and Aguilar, L. (2014). *Advanced $\mathcal{H}_\infty$ Control–Towards Nonsmooth Theory and Applications*. Birkhauser:Boston.

Orlov, Y., Acho, L., and Solis, V. (1999). Nonlinear h∞-control of time-varying systems. En: *Decision and Control, 1999. Proceedings of the 38th IEEE Conference on*. IEEE, Vol. 4, pp. 3764–3769.

Orlov, Y., Acho, L., and Aguilar, L. (2004). Quasihomogeneity approach to the pendubot stabilization around periodic orbits. En: *Proc. 2nd IFAC Symposium on Systems, Structure and Control*. pp. 448–453.

Orlov, Y., Aguilar, L., Acho, L., and Ortiz, A. (2008). Asymptotic harmonic generator and its application to finite time orbital stabilization of a friction pendulum with experimental verification. *International Journal of Control*, **81**(2): 227–234.

Orlov, Y., Montano, O., and Herrera, L. (2016). Hopf bifurcation of van der pol oscillators operating under unilateral constraints. *Proceedings of the 2016 American Control Conference*, pp. 1–6.

Ortega, R., Perez, J. A., Nicklasson, P., and Sira-Ramirez, H. (2013). *Passivity-based control of Euler-Lagrange systems: mechanical, electrical and electromechanical applications*. Springer Science & Business Media.

Oza, H., Orlov, Y., Spurgeon, S., Aoustin, Y., and Chevallereau, C. (2014). Finite time tracking of a fully actuated biped robot with pre-specified settling time: a second order sliding mode synthesis. En: *Robotics and Automation (ICRA), 2014 IEEE International Conference on*. IEEE, pp. 2570–2575.

Park, H. W. (2012). *Control of a bipedal robot walker on rough terrain*. Tesis de doctorado, The University of Michigan.

Raibert, M., Tzafestas, S., and Tzafestas, C. (1993). Comparative simulation study of three control techniques applied to a biped robot. En: *Systems, Man and Cybernetics, 1993.'Systems Engineering in the Service of Humans', Conference Proceedings., International Conference on*. IEEE, pp. 494–502.

Rengifo, C., Aoustin, Y., Plestan, F., Chevallereau, C., *et al.* (2011). Contact forces computation in a 3d bipedal robot using constrained-based and penalty-based approaches. *Proceedings of Multibody Dynamics*.

Richter, H. (2011). A multi-regulator sliding mode control strategy for output-constrained systems. *Automatica*, **47**(10): 2251–2259.

Robles, M. and Sanfelice, R. (2011). Hybrid controllers for tracking of impulsive reference state trajectories: a hybrid exosystem approach. En: *Proceedings of the 14th international conference on Hybrid systems: computation and control*. ACM, pp. 231–240.

Rodrigues, L. and Boukas, E.-K. (2006). Piecewise-linear $\mathcal{H}_\infty$ controller synthesis with applications to inventory control of switched production systems. *Automatica*, **42**(8): 1245–1254.

Roup, A. V. and Bernstein, D. S. (2001). Adaptive stabilization of a class of nonlinear systems with nonparametric uncertainty. *Automatic Control, IEEE Transactions on*, **46**(11): 1821–1825.

Sanfelice, R., Biemond, J., Wouw, N., and Heemels, W. (2014). An embedding approach for the design of state-feedback tracking controllers for references with jumps. *International Journal of Robust and Nonlinear Control*, **24**(11): 1585–1608.

Santiesteban, R., Floquet, T., Orlov, Y., Riachy, S., and Richard, J. (2008). Second-order sliding mode control of underactuated mechanical systems ii: Orbital stabilization of an inverted pendulum with application to swing up/balancing control. *International Journal of Robust and Nonlinear Control*, **18**(4-5): 544–556.

Savkin, A. and Evans, R. (2002). *Hybrid dynamical systems: controller and sensor switching problems*. Springer.

Shih, C., Grizzle, J., and Chevallereau, C. (2012). From stable walking to steering of a 3d bipedal robot with passive point feet. *Robotica*, **30**(07): 1119–1130.

Shiriaev, A., Perram, J., and Canudas-de Wit, C. (2005). Constructive tool for orbital stabilization of underactuated nonlinear systems: Virtual constraints approach. *Automatic Control, IEEE Transactions on*, **50**(8): 1164–1176.

Shiriaev, A., Freidovich, L., and Manchester, I. (2008). Can we make a robot ballerina perform a pirouette? orbital stabilization of periodic motions of underactuated mechanical systems. *Annual Reviews in Control*, **32**(2): 200–211.

Shiriaev, A., Freidovich, L., and Gusev, S. (2010). Transverse linearization for controlled mechanical systems with several passive degrees of freedom. *Automatic Control, IEEE Transactions on*, **55**(4): 893–906.

Shiriaev, A. S. and Freidovich, L. B. (2009). Transverse linearization for impulsive mechanical systems with one passive link. *Automatic Control, IEEE Transactions on*, **54**(12): 2882–2888.

Su, Q., Wang, M., Dimirovski, G. M., Dong, X., and Zhao, J. (2012). Tracking of output-constrained switched nonlinear systems in strict-feedback form. En: *Control Conference (CCC), 2012 31st Chinese*. IEEE, pp. 367–372.

Tlalolini, D., Aoustin, Y., and Chevallereau, C. (2010). Design of a walking cyclic gait with single support phases and impacts for the locomotor system of a thirteen-link 3d biped using the parametric optimization. *Multibody System Dynamics*, **23**(1): 33–56.

Tlalolini, D., Chevallereau, C., and Aoustin, Y. (2011). Human-like walking: Optimal motion of a bipedal robot with toe-rotation motion. *Mechatronics, IEEE/ASME Transactions on*, **16**(2): 310–320.

Van Der Schaft, A. J. (1991). On a state space approach to nonlinear $\mathcal{H}_\infty$ control. *Systems & Control Letters*, **16**(1): 1–8.

Van Zutven, P., Kostic, D., and Nijmeijer, H. (2010). On the stability of bipedal walking. *Simulation, Modeling, and Programming for Autonomous Robots*, p. 521.

Vukobratović, M. and Borovac, B. (2004). Zero-moment point—thirty five years of its life. *International Journal of Humanoid Robotics*, **1**(01): 157–173.

Walker, M. and Orin, D. (1982). Efficient dynamic computer simulation of robotic mechanisms. *Journal of Dynamic Systems, Measurement, and Control*, **104**(3): 205–211.

Wang, T. and Chevallereau, C. (2010). Stability of time-varying control for an underactuated biped robot based on choice of controlled outputs. En: *Intelligent Robots and Systems (IROS), 2010 IEEE/RSJ International Conference on*. IEEE, pp. 4083–4088.

Waugh, F. (1964). Cobweb models. *Journal of Farm Economics*, **46**(4): 732–750.

Westervelt, E., Buche, G., and Grizzle, J. (2004). Experimental validation of a framework for the design of controllers that induce stable walking in planar bipeds. *The International Journal of Robotics Research*, **23**(6): 559–582.

Westervelt, E., Grizzle, J., Chevallereau, C., Choi, J., and Morris, B. (2007). *Feedback control of dynamic bipedal robot locomotion*. CRC press Boca Raton.

Westervelt, E. R., Grizzle, J. W., and Koditschek, D. E. (2003). Hybrid zero dynamics of planar biped walkers. *Automatic Control, IEEE Transactions on*, **48**(1): 42–56.

Willems, J. (1972). Dissipative dynamical systems part 1: General theory. *Archive for rational mechanics and analysis*, **45**(5): 321–351.

Yuliar, S., James, M., and Helton, J. (1998). Dissipative control systems synthesis with full state feedback. *Mathematics of Control, Signals and Systems*, **11**(4): 335–356.

Yunt, K. and Glocker, C. (2005). Trajectory optimization of mechanical hybrid systems using sumt. En: *9th IEEE International Workshop on Advanced Motion Control*. IEEE, pp. 665–671.

Zhang, X., Zhao, J., and Dimirovski, G. M. (2012). L 2-gain analysis and control synthesis of uncertain switched linear systems subject to actuator saturation. *International Journal of Systems Science*, **43**(4): 731–740.